Observational Tests of the Cosmological Paradigm and the Phenomenology of its Extensions

Enrico Specogna

A Thesis Submitted to the
School of Mathematical and Physical Sciences of
the University of Sheffield in Candidacy for
the Degree of Doctor of Philosophy

Supervised by Dr Eleonora Di Valentino

March 2026



Abstract

As we usher in the era of precision cosmology, the inconsistencies that afflict the cosmological paradigm, also known as the "ΛCDM model", prompt us to question its validity as a description of the universe and challenge its foundations. This Thesis explores different ways of tackling three present and persistent issues: the lensing anomaly, the Hubble tension and the value of the spatial curvature of the universe. This is done, respectively, by introducing extensions from the standard picture in the form of modifications of gravity, dark energy and deviations from spatial flatness. After introducing the basic tools needed to understand the theoretical underpinnings of the ΛCDM model, along with the observational and statistical methods required to test its robustness against the state-of-the-art cosmological datasets, five chapters present a series of five papers that make up the bulk of this Thesis. The results of these works are, in order, a proof that the lensing anomaly can be recast in terms of modified gravity, an alleviation of the Hubble tension and an improvement in the currently available constraints of the spatial curvature. In retrospect, these results offer new and original takes on the limits of our standard model of the universe, which the upcoming cosmological surveys are set to constrain more precisely than ever before.

To Kita.
Without you I simply would not have made it.

Acknowledgments

It is hard to capture in the space of just a few lines all the support that countless ones have given to me, both in the best and the worst moments of my time as a PhD student in Sheffield. But here is my best try.
Thank you Eleonora, for your wisdom, guidance and endless patience for me: yours really are the makings of a true Saint!
Thank you Carsten and Steffen for all the chats and coffees we shared.
Thank you Ethan for always being a friend I could truly rely on.
Thank you Yuejia for your amazingly helpful scientific (and gastronomical!) suggestions.
Thank you Daniel, Sofie, Rita, Kavin, Dong Ha, Abhinove and Adam for your kindness, wittiness and great company.
Thank you Mum, Elettra and Dad for always being there for me.
Thank you Beatrice and Fugo for your unwavering friendship, hospitality and (some) great archery moments.
Thank you Zurul Cafe on Glossop Road, wonderful refuge and unparalleled curries.
And finally, thank you too Weather Report, Boards of Canada and Labi Siffre.

Relation to Published Work

The first three chapters of this Thesis serve as an introduction to the fundamental cosmology tools needed to navigate through the papers presented in the later chapters. In particular, chapter I is an outline of the motivations behind the works completed during the PhD that is given alongside a brief historical account of the field of cosmology and its current status, while chapter II entails a description of the theoretical framework underpinning the ΛCDM model. To conclude this introductory part of the Thesis, chapter III summarises the observational and statistical methods that are used in the later chapters to test the cosmological paradigm (and its extensions) with the state-of-the-art cosmological measurements. These initial chapters stem from the knowledge about cosmology gained by the Author through textbooks, summer school materials and pedagogical papers on this subject read during the course of the PhD period, which is why the equations presented do not technically count as original derivations. However, the pages making up the entirety of these first chapters have been written solely by the Author. The same is true for both the preambles and afterwords to the papers included in this Thesis, and also for chapter IX, which summarises the works presented once more and concludes the whole Thesis.

Chapters IV-VIII make up the bulk of this Thesis. All of these chapters contain papers that have been both peer-reviewed and published; they entail analyses of different standard model extensions [1–5]. Since all the papers presented here were the result of a collaborative effort, the following lines are dedicated to sketch the contribution given by the Author and each co-author, along with the papers' proper citations.

- **Chapter IV: "Exploring the growth index γ_L: Insights from different CMB dataset combinations and approaches".**
  E. Specogna, E. Di Valentino, J. Levi Said, and N.-M. Nguyen, Phys. Rev. D 109, 043528 (2024), arXiv:2305.16865.

  In this chapter, the Author conducted the whole data analysis and contributed to the writing of substantial parts of Secs. IV.A, IV.B, IV.D and IV.E of the paper. The appendix was compiled by N.-M. Nguyen, along with Sec. IV.C. E. Di Valentino and J. Levi-Said both contributed to the refinement of the results interpretation in Sec. IV.E and to the final Sec. IV.F. All of the figures in the main body were produced by the Author, while the graphics in Appendix A were made by N.-M. Nguyen.

- **Chapter V: "Planck-PR4 anisotropy spectra show better consistency with general relativity".**

E. Specogna, W. Giarè, and E. Di Valentino, Phys. Rev. D 111, 103510 (2025), arXiv:2411.03896.

This chapter contains an article for which the Author conducted all of the MCMC analysis and wrote Secs. V.B and V.C, along with substantial parts of Secs. V.A, V.D and V.E in coordination with W. Giarè. E. Di Valentino contributed to the results interpretation in Sec. V.D. All of the figures were produced by W. Giarè.

- **Chapter VI: "Neutrino mass tension or suppressed growth rate of matter perturbations?".**
  W. Giarè, O. Mena, E. Specogna, and E. Di Valentino, Phys. Rev. D 112, 103520 (2025), arXiv:2507.01848.

  This chapter includes an investigation for which the Author conducted all of the MCMC analysis and wrote Secs. VI.B and VI.C. W. Giarè completed Secs. VI.A and VI.E. Sec. VI.D was produced by a joint effort of W. Giarè, the Author and E. Di Valentino. All of the figures were plotted by W. Giarè, except for Fig. VI.2, which was produced by the Author.

- **Chapter VII: "Updated Constraints on Omnipotent Dark Energy: A Comprehensive Analysis with CMB and BAO Data".**
  E. Specogna, S. A. Adil, E. Ozulker, E. Di Valentino, R. C. Nunes, O. Akarsu, and A. A. Sen, Phys. Rev. D 113, 103549 (2026), arXiv:2504.17859.

  This chapter contains the update to a work in which the Author also took part [6], but that is not listed in this Thesis. All of the data analysis for this work, including all figures and tables, was completed by the Author, who also completed Secs. VII.D and VII.E jointly with A. Adil. While the Author wrote all of Sec. VII.C, A. Adil completed Secs. VII.A and VII.B. The remaining authors helped with the final interpretation of the results.

- **Chapter VIII: "Slow-rolling down the curvature: a reassessment of the Planck constraints on ϕ^2 inflation in a closed universe".**
  E. Specogna, T. Vardanyan, W. Giarè, and E. Di Valentino, Phys. Rev. D 113, 123526 (2026), arXiv:2509.26263.

  This final paper entails an MCMC analysis that has been carried out entirely by the Author, also thanks to an insightful suggestion about the implementation of this model into code by W. Giarè, who wrote Sec. VIII.E. Secs. VIII.A and VIII.C were written entirely by the Author. Sec. VIII.B has been written jointly by T. Vardanyan and the Author, while Sec. VIII.D was completed by the Author and, partly, by W. Giarè and E. Di Valentino. All of the figures in this paper have been produced by the Author.

Contents

Abstract iii

Acknowledgments vi

Relation to Published Work vii

List of Figures xiii

List of Tables xv

I Introduction 1

II The ΛCDM Model: A Cosmological Paradigm 7

II.A The Homogeneous (and Isotropic and Flat) Universe 8
II.B The Inhomogeneous (but Isotropic and Flat) Universe 12
II.C Inflation, or the Initial Conditions of the Universe 16

III Observables and Statistics 23

III.A The Cosmic Microwave Background 24
III.A.1 The temperature fluctuations of the CMB 27
III.A.2 The polarization of the CMB 28
III.A.3 Secondary anisotropies: CMB lensing 29
III.A.4 Secondary anisotropies: the Sunyaev-Zel'dovich effect 30
III.A.5 Estimating cosmology with the CMB: H_0 31
III.B Baryon Acoustic Oscillations 33
III.C Type-Ia Supernovae 35
III.D Bayesian Inference and the MCMC Algorithms 37

IV Exploring the Growth Index γ_L: Insights from Different CMB Dataset Combinations and Approaches 41

Preamble to the Paper 41
IV.A Introduction 44

IV.B Structure Formation and the Growth Index . . . 46
IV.C Mapping the growth index into observables: MGCAMB and CAMB_GammaPrime_Growth . . . 47
IV.D Datasets and Methodology . . . 49
IV.E Results . . . 51
IV.E.1 MGCAMB Results . . . 51
IV.E.2 CAMB_GammaPrime_Growth Results . . . 54
IV.F Conclusions . . . 58
IV.G Acknowledgments . . . 59
Appendix A . . . 60
Afterword . . . 63

V Planck-PR4 Anisotropy Spectra Show Better Consistency with General Relativity 65

Preamble to the Paper . . . 65
V.A Introduction . . . 67
V.B Parametric Modified Gravity and Perturbation Theory . . . 71
V.B.1 The (μ, Σ) Framework . . . 72
V.B.2 The growth index γ . . . 72
V.C Likelihoods and Sampling Methodology . . . 73
V.D Results . . . 76
V.D.1 Constraints on the (μ, Σ) framework . . . 77
V.D.2 Constraints on the growth index γ . . . 81
V.E Discussion And Conclusion . . . 84
V.F Acknowledgments . . . 86
Afterword . . . 88

VI Neutrino Mass Tension or Suppressed Growth Rate of Matter Perturbations? 89

Preamble to the Paper . . . 89
VI.A Introduction . . . 91
VI.B Growth index and neutrinos . . . 94
VI.C Methodology and datasets . . . 100
VI.D Results . . . 103
VI.E Summary . . . 110
VI.F Acknowledgments . . . 112
Appendix A . . . 113

Afterword . . . 116

VII Updated Constraints on Omnipotent Dark Energy: a Comprehensive Analysis with CMB and BAO Data 117

Preamble to the Paper . . . 117
VII.A Introduction . . . 119
VII.B Omnipotent Dark Energy: a review . . . 122
VII.C Data and Methodology . . . 124
VII.D Results and Discussion . . . 127
VII.E Conclusion . . . 138
VII.F Acknowledgments . . . 139
Afterword . . . 140

VIII Slow-rolling Down the Curvature: a Reassessment of the Planck Constraints on ϕ^2 Inflation in a Closed Universe 141

Preamble to the Paper . . . 141
VIII.A Introduction . . . 143
VIII.B The Gauge-invariant Primordial power Spectrum in a Closed Universe . . . 147
VIII.C Methodology and datasets . . . 151
VIII.C.1 Re-expressing P_ζ^c . . . 151
VIII.C.2 Planck Likelihoods and Data . . . 154
VIII.D Results . . . 158
VIII.E Discussion and Conclusion . . . 160
VIII.F Acknowledgments . . . 163
Appendix A . . . 163
Appendix B . . . 164
Afterword . . . 167

IX Conclusions 169

Bibliography 171

List of Figures

I.1 The thermal spectrum of the CMB. 2
II.1 DESI's rendition of the large-scale structure. 12
III.1 CMB temperature and polarisation anisotropies: theory *vs* data. 25
III.2 CMB lensing spectrum: theory *vs* data. 31
III.3 The effect of changing H_0 on the CMB. 33
III.4 Baryonic acoustic oscillations: theory *vs* data. 35
III.5 Supernovae-Ia: theory *vs* data. 36
IV.1 Contours for `MGCAMB` (no BAO). 54
IV.2 Contours for `MGCAMB`. 55
IV.3 Contours for `CAMB_GammaPrime_Growth` (no BAO). 57
IV.4 Contours for `CAMB_GammaPrime_Growth`. 58
IV.5 Unlensed CMB TT angular power spectrum with `MGCAMB`. 60
IV.6 Unlensed CMB TT angular power spectrum with `CAMB_GammaPrime_Growth` 61
IV.7 Lensing potential with `MGCAMB`. 61
IV.8 Lensing potential with `CAMB_GammaPrime_Growth`. 62
V.1 1D and 2D posteriors of μ_0, Σ_0. 77
V.2 1D and 2D posteriors of Σ_0/γ_0 against A_L. 78
V.3 2D posteriors of μ_0, Σ_0 and S_8. 79
V.4 1D posteriors of γ_0. 82
V.5 2D posteriors of γ_0 and S_8. 83
VI.1 Effects of massive neutrinos on the CMB. 95
VI.2 Effects of massive neutrinos on the matter power spectrum. 96
VI.3 1D and 2D posteriors of γ and $\sum m_\nu$. 105
VI.4 1D and 2D posteriors of γ, H_0 and S_8. 107
VI.5 Full analysis posteriors for $\sum m_\nu$ (Plik). 113
VI.6 Full analysis posteriors for $\sum m_\nu$ (Camspec). 114
VII.1 ODE's equation of state. 125
VII.2 1D and 2D ODE posteriors (post-filtered). 127
VII.3 1D and 2D ODE posteriors (full-prior). 128
VII.4 $H(z)$ in the ODE model. 129
VII.5 $\rho_{\rm DE}$ and $w_{\rm DE}$ in the ODE model (SPT, post-filtered). 130
VII.6 $\rho_{\rm DE}$ and $w_{\rm DE}$ in the ODE model (SPT, full-prior). 131
VII.7 $\rho_{\rm DE}$ and $w_{\rm DE}$ in the ODE model (Planck, post-filtered). 132
VII.8 $\rho_{\rm DE}$ and $w_{\rm DE}$ in the ODE model (Planck, full-prior). 133
VIII.1 Variations of C_ℓ^{TT} with the slow-roll parameters. 148
VIII.2 Variations of C_ℓ^{TT} with curvature. 152

VIII.3 2D posteriors for the closed universe model. 156
VIII.4 1D posteriors on $\Omega_{\mathcal{K}}$. 157
VIII.5 Classic *vs* new curvature parametrization, CMB low-ℓ comparison. 157
VIII.6 2D posteriors for the closed universe model with late time data. 164
VIII.7 Fractional difference between the approximated and non-approximated theoretical predictions of the closed universe model. 165
VIII.8 Predictions of the closed universe model against Planck data. 165

List of Tables

IV.1 γ-parametrisation priors. . . . 50
IV.2 Fiducial values for the Planck-like dataset. . . . 51
IV.3 Results for the Planck-like dataset. . . . 51
IV.4 Planck results with `MGCAMB`. . . . 52
IV.5 ACT results with `MGCAMB`. . . . 52
IV.6 SPT results with `MGCAMB`. . . . 53
IV.7 Planck results with `CAMB_GammaPrime_Growth`. . . . 55
IV.8 ACT results with `CAMB_GammaPrime_Growth`. . . . 56
IV.9 SPT results with `CAMB_GammaPrime_Growth`. . . . 56
V.1 Priors on μ_0, Σ_0 and γ_0. . . . 75
V.2 Posteriors of μ_0, Σ_0 (fixed A_L). . . . 76
V.3 Posteriors of μ_0, Σ_0. . . . 77
V.4 Posteriors of γ_0 (fixed A_L). . . . 81
V.5 Posteriors of γ_0. . . . 82
VI.1 Priors on the total neutrinos mass. . . . 102
VI.2 Posteriors of the total neutrino mass. . . . 103
VI.3 Full analysis results for $\sum m_\nu$. . . . 115
VII.1 Priors on the Omnipotent model. . . . 124
VII.2 Posteriors of the ODE model (SPT, post-filtered). . . . 133
VII.3 Posteriors of the ODE model (SPT, full-prior). . . . 134
VII.4 Posteriors of the ODE model (Planck, post-filtered). . . . 134
VII.5 Posteriors of the ODE model (Planck, full-prior). . . . 135
VII.6 w_0 values for the ODE model. . . . 137
VIII.1 Flat priors for the closed universe model. . . . 154
VIII.2 1D posteriors for the closed universe model. . . . 155
VIII.3 1D posteriors for the ΛCDM+$\Omega_\mathcal{K}$ model. . . . 156
VIII.4 Posteriors for the closed universe model with late time data. . . . 163

I Introduction

The cosmological paradigm, better known for the past 30 years or so as the "ΛCDM" model, is a remarkably precise physical description of the largest scales of the universe [I.1], its dynamics and its history. Notably, the predictive breadth of this "standard model" of the universe rests upon a relatively small number of building blocks that were gradually incorporated into it over the course of the last century.

The first pillar of the standard model is the assumption of a gravitational theory, as gravity is the only fundamental long-range force that matters at cosmological scales. In the ΛCDM model, this role is occupied by general relativity - GR. By further postulating that the universe is homogeneous, isotropic and flat (or "Euclidean"), Einstein's theory is able to predict the so-called "Big Bang", or the observation that the universe is expanding in nature and, by extrapolation, that it must have been extremely hot and dense during the early epochs of its existence. In the same way the word "Impressionism" was coined as a derisory term by art critics in late 19th–century France to deny the innovative power of what went on to become one of the first truly modern movements in western art, dubbing the birth of the universe as a *big bang* was an attempt at discrediting a series of observations made in the first decades of the 20th century that were gradually ruling out the outdated and prejudicial idea that our universe would have to be a static one. The expansion of the universe is now an observationally established fact. One of its most notable proofs is found in the observation of the relic radiation known as the "cosmic microwave background" - CMB, which we can measure isotropically in the sky. The energy distribution of the CMB photons is expected to follow a thermal (or "blackbody") spectrum [8, 9], which is exactly what we observe, and very precisely so: we can see in Fig. I.1 that the root mean square of the deviations from the predicted blackbody spectrum with temperature $T_0 = 2.7260\,\mathrm{K}$ is extremely small, less than 5 parts in 10^5.

The second set of fundamental ingredients of the ΛCDM model can be readily found in its very name. "Λ" and "CDM", respectively the "cosmological constant" and "cold dark matter", are postulated to be the two main protagonists of the total energy budget of our universe (today), roughly making up 95% of its contents. Unlike the remaining 5%, made of relativistic particles and ordinary (or, somewhat improperly, *baryonic*) matter, the exact nature of Λ and CDM still eludes us: we have yet to find direct proof of their existence. Interestingly though, as our measurements get more numerous and precise, the indirect evi-

[I.1] Here, by *very large* or *cosmological* scales, we mean distances in the universe that are much greater than the size of a black hole, our solar system or even our own galaxy, the Milky Way. In order to understand the distance range of interest to cosmologists, the unit length that we have to pick needs to stretch all the way to a distance of at least ~ 100 Megaparsecs (Mpc) [7], with 1 Mpc roughly amounting to the separation between our galaxy and our closest neighbour, Andromeda (!).

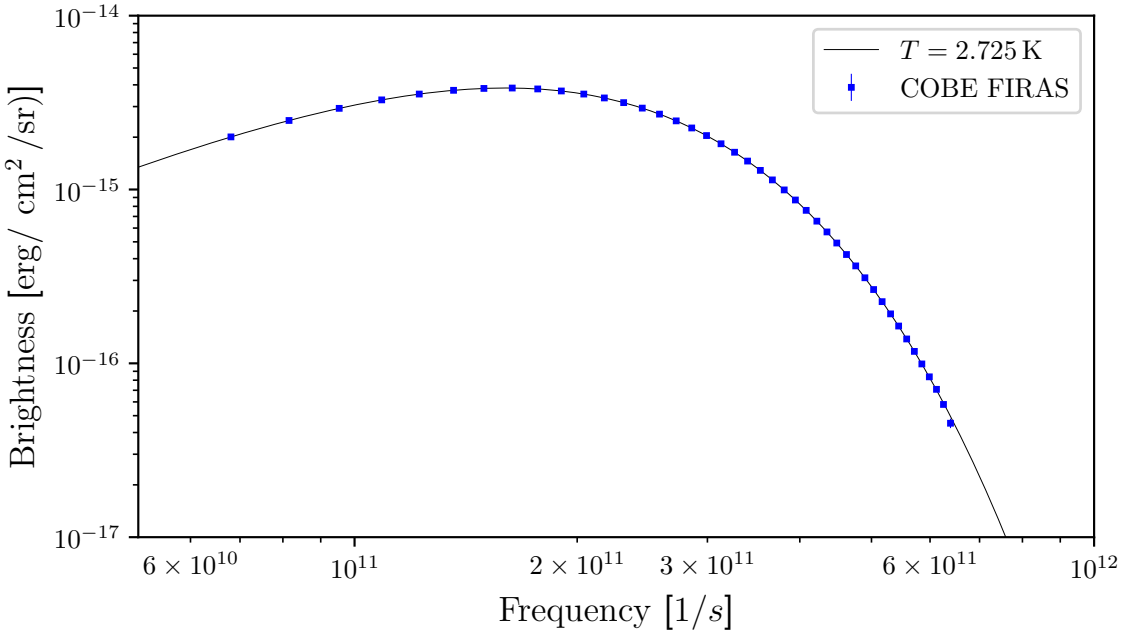


FIG. I.1. Blackbody spectrum of CMB as measured by COBE (blue squares with error bars) and its predicted curve for $T = 2.7260\,\mathrm{K}$ (black line). This was measured by the FIRAS instrument of the COBE mission [10] and it is, to date, the most precise measurement of the CMB blackbody spectrum. Future probes like BISOU [11], PIXIE [12] and FOSSIL [13] are set out to measure it again, with the goal of using the expected but tiny deviations in the blackbody shape of this curve, which are known as *spectral distortions*, to further constrain the cosmological paradigm.

dence for the existence of CDM is getting stronger, while the case for Λ, according to some of the most recent developments in observational cosmology, is actually getting weaker, at least for a cosmological constant with an equation of state such that $w_\Lambda = -1$ (the meaning of w_Λ will be defined in Eq.(II.5)). One of the strongest clues prompting us to reconsider the robustness of the introduction of Λ in our model of the universe is given by DESI, a spectroscopic survey which, by virtue of a combination of the measurements it made about another prediction of the standard model known as the "baryonic acoustic oscillations" - BAO - and CMB data, seemingly shows that we stand 3.1 *standard deviations* - σ - away from a universe that includes a cosmological constant [14]. Interestingly, the hints for dynamical dark energy have remained strong with the newer data release by DESI [15], confirming the deviation from $w_\Lambda = -1$ as one of the most enticing avenues in current cosmological research.

Finally, the ΛCDM model also includes a mechanism for the origin of its contents: the theory of "inflation". While originally devised as a way to explain the fact that we observe regions in space that, despite not being in causal contact, look remarkably similar (this is the well-known "horizon problem" [16]), inflation also turned out as a framework that traces

the origin of CDM and all the other components of the universe back to the fluctuations (or inhomogeneities) in the distribution of a common ancestor, the "inflaton" field. In addition to this, inflation also explains why we observe no magnetic monopoles in the current universe, even though they are expected to be produced in large amounts by those theories that seek to unify the interactions of the standard model of particle physics at energies greater than $\sim 10^{16}$ GeV (also known as "grand unified theories" - GUT). This discrepancy between theory and observations is also known as the "monopole problem". Inflation can also show why the universe appears to be essentially flat and mostly homogeneous at present. It is the observed flatness that prompted James Peebles, who was also the first physicist to advocate for the need of CDM in the cosmological context [17], to include Λ in the standard model. This changed the Einstein-de Sitter prescription that dominated our picture of the universe until the mid-1980s, when various experiments indicated that ordinary and dark matter could only account for about 30% of our universe's total energy budget [18, 19]. This stance was definitively consolidated in 1998 by two independent experiments, the "High-Z Supernova Search Team" and the "Supernova Cosmology Project". By using "type-Ia supernovae" - SNIa (a type of supernova that is particularly regular in the time evolution of its thermonuclear explosion's light-curve) - to measure cosmological distances, both of these research teams delivered the observational proof that the universe is not just expanding, but that it is doing so at an accelerated rate [20, 21], making the introduction of Λ inevitable if our picture of a flat, homogeneous and isotropic universe governed by GR is to survive.

The turn of the millenium gave way to a rapid increase in the amount and quality of the available cosmological data: we are now in the "age of precision cosmology". Experiments such as WMAP, Planck, ACT, SPT, BICEP, the SDSS survey, DESI, HST, HSC, DES, KiDS and many others enormously improved our capability of testing the ΛCDM model predictions in independent ways, further corroborating its validity. However, such a quick rise in the quantity of cosmological data also meant that the underlining flaws that plague the standard model could rise above the gradually decreasing noise in the data, unveiling several issues that still require an explanation.

Firstly, as it was just mentioned, the case for Λ has become much weaker, especially in light of the recent results by DESI, which instead seem to favour what is arguably the most straightforward extension of the cosmological constant: "dark energy", or a time-varying form of the energy that is responsible for the accelerated expansion of the universe. What is more, we find that measuring the current rate of this expansion, quantified through a parameter known as H_0 or the "Hubble constant", yields different values depending on the type of observable used. This is an open problem known as the "H_0 tension", and it reflects the fact that estimates of H_0 differ depending on whether we use early time data, such as

CMB data, or late time expansion measurements found by distance indicators such as SNIa, reaching a 7.1σ significance with the latest combinations of these two kinds of dataset [22]. Another important issue is the so-called *lensing anomaly*, which, like the problem with H_0, is another prime example of the tensions that riddle the standard cosmological model. It refers to an excess in the amount of CMB lensing that we can measure from the suppression of the acoustic oscillations in the spectra of Planck, reaching a 2.8σ significance in the experiment's 2018 data release (PR3, [23]). Interestingly, this evidence for excessive lensing of the CMB can also be re-interpreted as a deviation from spatial flatness, yet another challenge posed to the ΛCDM model's validity. The H_0 tension and the lensing anomaly are both topics of primary interest in the Thesis presented here, as it will be made clear in the ensuing chapters. While the most recent reanalysis of Planck's data (PR4) showed the lensing anomaly to be weaker than previously thought, lowering to a less than 1σ discrepancy [24], the combination of CMB data with DESI continues to favour a deviation as large as 3.5σ in magnitude [25]. This prompts us to still regard the lensing anomaly as an interesting problem which, while not intrinsic to CMB data, can reveal details about how parameters correlate in the standard model when different data like BAO and CMB measurements are combined.

One further problem that has been puzzling cosmologists in the recent years is the "S_8 tension", which relates to the discrepancy in the measurement of S_8, a standard model parameter that quantifies the current magnitude of matter perturbations. As in the case of the Hubble tension, once again we find a discrepancy between early and late time cosmological probes. In fact, S_8 has been estimated to be consistently different across CMB and weak lensing datasets, with the discrepancy being larger than three standard deviations for certain data combinations [26]. Recently, however, this issue has become much less statistically significant, as the deviation has been shown in [27] to decrease to less than 1σ when a combination of cosmic shear measurements by the KiDS and DES surveys is compared to Planck's CMB data. Arguably, this makes the S_8 tension less prominent in the current debate on the validity of the ΛCDM model.

Finally, the number of models proposed as an alternative to the cosmological paradigm is still much greater than the available data that could be used to test them, despite the enormous progress that led up to the best observations of the universe currently in our hands. In other words, at present, cosmology suffers from *underdetermination*, meaning that our datasets are still not precise enough to resolve the microphysical details of dark energy [28–30].

In summary, this Thesis is a collection of five published works that aim to tackle the issues outlined above by testing three different classes of ΛCDM model extensions against the state-of-the-art cosmological data.

In what follows, these three modification classes are schematically introduced, along with the issues they intend to address and their respective locations in this document.

- **Modified gravity - MG**: with a very broad and qualitative definition, this class can be defined as entailing the modification of the equations that are obtained from GR for the standard cosmological model. In particular, in this Thesis we look at the modifications induced by two parametrisations of gravity on the equations describing the *perturbations* in the homogeneous distribution of non-relativistic matter and its time evolution only; for this reason, the "modified gravity" definition is not exactly strict, but will be used for the remainder of this Thesis for simplicity. The papers produced on this topic are presented in Secs.(IV, V and VI), and they all aim, in similar ways, to address the same issue: the lensing anomaly of the CMB.

- **Dark energy - DE**: in this case, what changes are the homogeneous equations of motion for the ΛCDM model rather than its perturbations, thanks to the introduction of a parametrisation for the density and pressure of the DE component. This is what is done in the paper presented in Sec.(VII), where it is shown how both the H_0 tension and the evidence for dynamical dark energy found by DESI can, under certain conditions, be explained under the cosmological model dubbed "omnipotent dark energy".

- **A closed universe**: in this final analysis, we shift our focus from the late time modifications considered in the previous two extension categories to a deviation from the standard picture happening during the inflationary era. Precisely, we leverage the lensing anomaly once more, by re-assessing Planck's evidence for non-zero spatial curvature under the assumption of a new, gauge-invariant parametrisation for the perturbations of the early-universe. The paper describing this investigation is presented in Sec.(VIII).

All of the scenarios presented above share one common factor: the use of parametrisations. This reflects the fact that the works constituting the main body of this Thesis always follow a *phenomenological* approach, in the sense that it is never a specific model that is being tested against the data, but rather a *class* or *collection* of models expressed through a model-independent parametrisation. A similar choice is forced on us by all the problems that the underdetermination of DE models poses to our fundamental understanding of observations, such as the expanding universe or the evidence for dynamical DE. The problem of underdetermination then prompts us to study the universe by letting data guide our intuition about the cosmological paradigm, as our datasets are just not, either now or in the foreseeable future, good enough to resolve the microphysical details of the true cosmological model.

These paper–chapters also include a preamble presenting the models that were analysed in each manuscript, detailing in which ways they deviate from the observable predictions of the ΛCDM picture and why they were chosen to tackle the problems of the standard model in the first place, while levelling any notation differences between the papers and the three introductory chapters of this Thesis. The afterword following each of these paper–chapters serves as an update on how new developments that came after the respective paper was written might have changed the interpretation of its results.

The next three chapters contain an introduction about the most important theoretical, observational and statistical concepts that are not already covered by the articles presented in chapters IV-VIII, but are still essential for their full comprehension. Specifically, chapter II introduces the homogeneous and non-homogeneous equations of the ΛCDM model. Chapter III describes the observables that have been used to test the parametrisations presented here, while bridging the gap between theory and observation, explaining how we can constrain cosmological models through the principles of Bayesian statistics and Markov chain Monte Carlo algorithms. Finally, we conclude with chapter IX, where we draw a summary of the results that came from testing the models and the new ideas presented throughout this Thesis, while keeping an eye on some novel and exciting directions for future work.

II The ΛCDM Model: A Cosmological Paradigm

In chapter I it is said that one of the foundational concepts that stand at the heart of the current cosmological paradigm, the ΛCDM model, is the combination of two assumptions about the distribution of matter in the universe and its kinematics: spatial isotropy and homogeneity. This combination takes the name of "cosmological principle". By applying the cosmological principle to GR it is possible to derive a set of two equations known as the "Friedmann equations". These two equations are (almost) all that we need in order to paint the macroscopic picture of the dynamics of an isotropic and homogeneous universe, while connecting its geometry to the matter and energy it contains, namely baryons, photons, neutrinos, Λ and CDM. In GR and the Friedmann equations, the universe's contents are expressed in terms of macroscopic thermodynamical quantities such as density, pressure or entropy. In particular, we are interested in their time–dependence, at least as long as we care for the cosmological principle to hold. However, such time-dependence has to be sought from the microscopic properties of these contents, specifically from their *distribution function* $f(\boldsymbol{x}, \boldsymbol{p}, t)$, a description of how the particles that make up e.g., dark matter are distributed in the phase space of position $\boldsymbol{x}$ and momentum $\boldsymbol{p}$ at time t. This is explained in detail in Sec.II.A, where another fundamental tool, which is needed to work out what $f(\boldsymbol{x}, \boldsymbol{p}, t)$ should look like for different energy components, is introduced: the "Boltzmann equations".

In Sec.II.B, we stray away from the cosmological principle assumptions and introduce the basic tools needed to describe the inhomogeneous part of the universe: its "large-scale structure" - LSS, made of galaxies, galaxy clusters and the filaments connecting them in the complex structure known as the "cosmic web". These tools are the equations fixing the time and space evolution of a new type of variable: the cosmological perturbations, consisting of functions designed to quantify the deviations from the simple scheme about the contents and the spacetime geometry of the universe devised in Sec.II.A.

Finally, in Sec.II.C, we will touch on inflation, the theory that forms another essential building block of the ΛCDM model by setting the initial conditions of the universe. These are represented, ultimately, by the perturbations of the primordial field known as the *inflaton* which, in turn, will go on to create the perturbations in matter and light that we observe today in the universe.

All of the equations outlined and developed in this chapter are implemented and solved in practice by codes known as "Boltzmann solvers". The code that is used the most for the theoretical calculations of the papers in chapters IV-VIII is `CAMB` [31, 32], along with its MG patches `MGCAMB` [33–37] and `CAMB_GammaPrime_Growth` [38, 39].

II.A The Homogeneous (and Isotropic and Flat) Universe

The centrepiece of the cosmological paradigm, as mentioned in chapter I, can be identified with the theory of gravity that we adopt to describe the universe at the largest scales: general relativity. Similarly to how electromagnetism, a classical theory like Einstein's, offers a complete description of the connections between charges, currents, electric and magnetic fields in the form of the "Maxwell equations", GR ties the geometry of spacetime to its matter and energy contents. This is a connection that can be succinctly summarised with a set of equations known as "Einstein field equations":

$$G_{\mu\nu} = 8\pi G\, T_{\mu\nu} - \Lambda g_{\mu\nu}. \tag{II.1}$$

G is Newton's universal constant of gravitation while Λ is, of course, the same cosmological constant introduced in chapter I. The left-hand side of Eq.(II.1), $G_{\mu\nu}$, is the "Einstein tensor", which defines the geometry of spacetime through its dependence on the "metric tensor" and its derivatives. The metric tensor, or "$g_{\mu\nu}$", is the tool that we use to describe how observer-dependent coordinates can be turned into invariant quantities in GR. The metric is essential to understand, when GR is applied to the largest scales, what we mean when we refer to the universe as "expanding". To show why this is the case, let us take an infinitesimal displacement in observer-dependent, or "comoving", coordinates - dx^μ - and the observer-independent, or "invariant", interval - ds. The metric then becomes the link between these two quantities:

$$ds^2 = g_{\mu\nu}\, dx^\mu dx^\nu, \tag{II.2}$$

where μ and ν denote the indices for one temporal ($\mu/\nu = 0$) and three spatial ($\mu/\nu = 1, 2, 3$) coordinates. In general, every coordinate system has its own $g_{\mu\nu}$; this is the case for an isotropically expanding (or contracting) Euclidean universe, for which the metric looks like

$$g_{\mu\nu} = \mathrm{diag}\left(-1, \delta_{\alpha\beta}\, a^2(t)\right). \tag{II.3}$$

Here, α and β are indices spanning through the spatial coordinates only, so that $a(t)$, a function of time t known as the "scale factor", affects distances but not time intervals. Each spatial dimension in Eq.(II.3) is scaled by the same factor $a(t)$: this is how spatial isotropy is translated in the mathematics of GR. In addition to the scale factor, another unit of measurement that cosmologists often use to describe the passage of time is the "redshift" - z, a monotonically decreasing function of time that quantifies the predictable change in the frequency of a photon that lives in the expanding universe.

As it turns out, we can relate z to the scale factor as:

$$a = \frac{1}{1+z}. \tag{II.4}$$

In order to complete the dynamical picture of a homogeneous and isotropic universe, we also need to apply the cosmological principle to the right-hand side of Eq.(II.1), specifically to $T_{\mu\nu}$ or the "energy-momentum tensor". Much in the way that the metric tensor is used to define the spacetime geometry of a gravitational system, $T_{\mu\nu}$ includes all that we need to know about the matter and energy that is contained in such system. In the context of the standard cosmological model, $T_{\mu\nu}$ encodes information about any of the universe's contents, like e.g., baryonic matter. Interestingly, the assumption of the cosmological principle allows for $T_{\mu\nu}$ to take the form of a perfect fluid, where each energy component i can be fully characterised in terms of its density $\rho_i(t)$ and pressure $P_i(t)$ or their ratio, the so-called "equation of state":

$$w_i = \frac{P_i}{\rho_i}. \tag{II.5}$$

In this Thesis, the index i will take the following "values", depending on the type of matter/energy considered: "c" for CDM, "b" for baryons, "CMB" for photons, "ν" for neutrinos and, of course, "Λ" for the cosmological constant. Eq.(II.5) can be seen as a simple tool to tell the energy components of the universe apart by means of their properties. For instance, non-relativistic matter yields $w_{b,c} = 0$, meaning that it cannot exert any pressure on itself, while photons, with $w_{\rm CMB} = 1/3$, can. Both of these forms of energy satisfy the strong energy condition: $w_i \geq -1/3$. However, within the standard model, two notable cases break this condition: Λ and, as we will see in, the scalar field that is responsible for the exponential growth of the newborn universe, ϕ, known as the "inflaton". In fact, both the cosmological constant and the inflaton field, at least during the expanding phase in the latter case, yield $w_{\Lambda,\phi} = -1$.

Finally, and in the limit of the validity of the cosmological principle, the stress-energy tensor for the ΛCDM model can then be expressed in the following, simple way:

$$T_{\mu\nu} = \sum_i \mathrm{diag}(-\rho_i, \delta_{\alpha\beta} P_i). \tag{II.6}$$

One can now fully resolve Einstein's equations for a universe where the cosmological principle holds. As it turns out, the highly symmetric nature of Eqs.(II.3,II.6) (i.e., the absence of any non-zero off-diagonal components) means that instead of having to deal with ten possible equations, the most that one could obtain in principle for an arbitrary choice of the metric

and the stress-energy tensors, we just find two, the "Friedmann equations":

$$\left(\frac{\dot{a}}{a}\right)^2 = \frac{8\pi G}{3}\sum_i \rho_i + \frac{\Lambda}{3}, \tag{II.7}$$

$$\frac{\ddot{a}}{a} = -\frac{4\pi G}{3}\sum_i (\rho_i + 3P_i) + \frac{\Lambda}{3}. \tag{II.8}$$

They are obtained from the $\mu=\nu=0$ and $\mu=\nu=1,2,3$ components of Einstein's equations respectively.

It can be now clarified, by looking at Eq.(II.7), why the cosmological principle applied to GR is able to predict an expanding universe. In particular, we need to look at the ratio on the left-hand side: this is the variation rate of the scale factor at time t, also known as the "Hubble function" or "$H(t)$", of which H_0, the Hubble parameter seen in chapter I, is the value at present. The right-hand side of Eq.(II.7) is always positive, as $\rho_i(t) > 0$ at all times, while Λ is a constant and a positive value as well. Therefore $H(t)$ will also need to be greater than zero, meaning that $a(t)$ has to be a monotonically growing function of time and that, as a consequence, the universe described by Eq.(II.7) must be an expanding one. While Λ does not need to be introduced at all in order to accommodate for an expanding universe, we still require it to take a non-zero value to explain why we observe this expansion to be *accelerating*. In fact, contrarily to Eq.(II.7), the right-hand side Eq.(II.8) is not necessarily positive and neither is $\ddot{a}$, which expresses the "acceleration/deceleration" of the expansion. However, with a non-vanishing value of the cosmological constant, $\ddot{a}$ can turn positive and the expansion can indeed be accelerating, provided that $\sum_i(\rho_i(t) + 3P_i(t))$ is large enough.

Now, by combining Eqs.(II.7, II.8) it is possible to obtain a third equation that, while not independent from the two Friedmann equations above, provides us with a useful relation for the time evolution of $\rho_i(t)$:

$$\dot{\rho}_i + 3\frac{\dot{a}}{a}(\rho_i + P_i) = 0. \tag{II.9}$$

By setting $P_i = w_i\rho_i$ (from Eq.(II.5)) and assuming w_i to be time-independent, it is possible to integrate Eq.(II.9) and work out a convenient expression for the scale factor evolution of the energy density:

$$\rho_i \propto a^{-3(1+w_i)}. \tag{II.10}$$

So how do we know what $\rho_i(t)$ and $P_i(t)$ should look like *in general*, at least for the case of an homogeneous universe? The answer relies on knowing, as mentioned above, the "distribution

function" of a matter/energy component: $f_i(x^\alpha, p^\alpha, t)$. The distribution function is related to $\rho_i(t)$ and $P_i(t)$ through the following two relations [40]:

$$\rho_i(t) = g_i \int \frac{d^3p}{(2\pi)^3} f_i(x^\alpha, p^\alpha, t) E_i(p), \tag{II.11}$$

$$P_i(t) = g_i \int \frac{d^3p}{(2\pi)^3} f_i(x^\alpha, p^\alpha, t) \frac{p^2}{3E_i(p)}. \tag{II.12}$$

The above expressions include, on top of the component's distribution function, the square root of $p^2 = \delta_{\alpha\beta}\, p^\alpha\, p^\beta$, the magnitude of its 3-momentum, g_i, its degeneracy factor, and $E_i(p)$, its energy. Both expressions hold for either relativistic or non-relativistic particles, with $E_i(p)$ changing according to either case. All that remains to be established to solve for Eqs.(II.11,II.12) is $f_i(x^\alpha, p^\beta, t)$: this is where the Boltzmann equation comes in. For an expanding universe described by the metric in Eq.(II.3), and neglecting any "collisions" or non-gravitational interactions between different energy components, the Boltzmann equation needed to work out $f_i(x^\alpha, p^\alpha, t)$ takes the following form:

$$\dot{f}_i - Hp\frac{\partial f_i}{\partial p} = 0, \tag{II.13}$$

where the absence of any derivative with respect to the spatial coordinates x^α is a consequence of the assumption of spatial homogeneity. By integrating Eq.(II.13) it is possible, in principle, to obtain the time evolution for the distribution of any energy component i.

Let us try this, as an example, for the case of CDM. The attribute "cold" in the name "cold dark matter" refers to the fact that the only interaction between this type of non-relativistic particles and any other energy component of the universe is purely gravitational, so that the collisionless approximation of Eq.(II.13) holds perfectly well and can be employed to find the number density of CDM, $n_c(t)$. To do this, we start by taking the zeroth momentum of (II.13), which means that we multiply both sides of the Boltzmann equation by $d^3p/(2\pi)^3$ and integrate them. This leads us to the following expression for $n_c(t)$:

$$\dot{n}_c + 3Hn_c = 0, \tag{II.14}$$

which can be easily solved to yield $n_c \propto a^{-3}(t)$, a well-known result for non-relativistic particles. Calculations of this type can lead to similar results for other particle species as well, such as photons or baryons.

In summary, the set of equations given by Eqs.(II.7-II.13) is, in essence, all that is needed to fully describe a universe ruled by the cosmological principle and often, throughout this

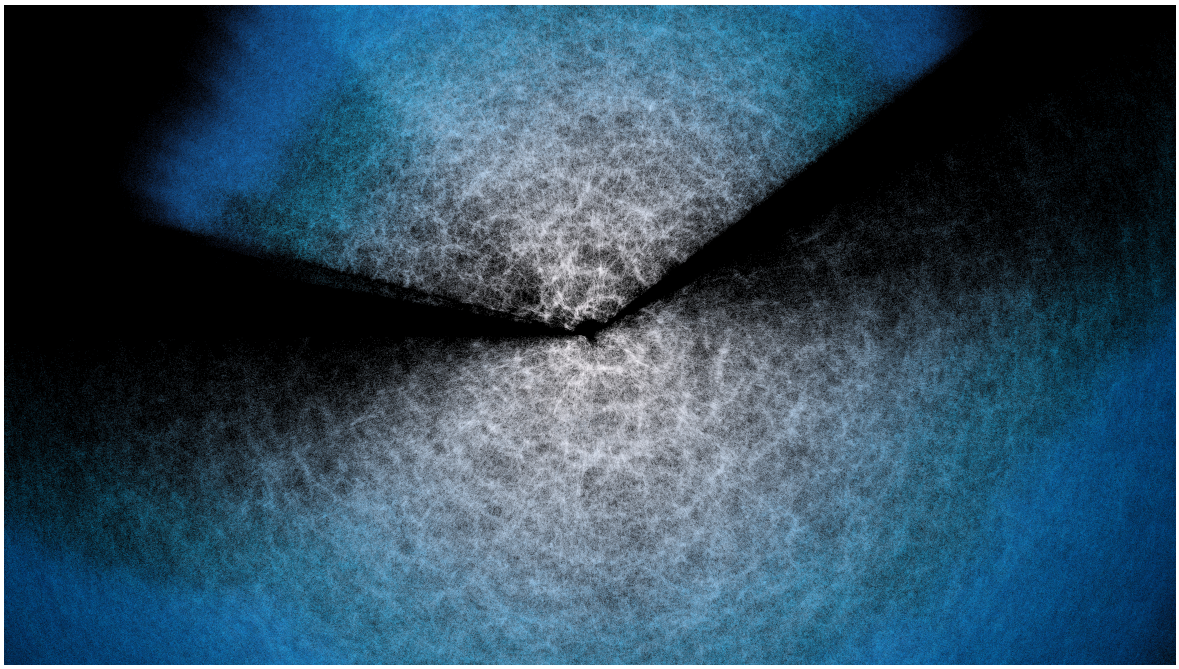


FIG. II.1. The two main sections of the sky scoped by DESI in its first three years of operation [15, 41], which included the observation of a very large number of objects like galaxies and quasars. It is possible to discern the net-like pattern that these objects, represented here as a myriad of tiny dots, form as part of a network of more and less crowded areas known as the "cosmic web", an informal definition of the large-scale structure of the universe.

Thesis, they will be referred to as the "background equations" of the ΛCDM model. We know, however, that the assumption of perfect spatial homogeneity cannot lead to an accurate representation of the real universe, since we observe clear deviations from such a simplistic picture in the form of galaxies and clusters. In other words, the cosmological principle cannot account for the LSS of the universe, which we can visualise from Fig.II.1. In order to accommodate for the LSS, we need to break free from the idealised geometry provided by the metric tensor in Eq.(II.3).

We can do so by introducing *perturbations* to this picture, which amounts to adding a spatial dependence to both the geometric and the energy quantities introduced thus far.

II.B The Inhomogeneous (but Isotropic and Flat) Universe

In order to describe the LSS of the universe we have to give up spatial homogeneity, but can still regard isotropy as a valid assumption. The same scale factor $a(t)$ that was introduced in Eq.(II.3) is in fact still applied to all the non-zero metric elements of $g_{\mu\nu}$, but we now also need to introduce a spatial dependence in the metric. While in principle this could be done

using scalar, vector and tensor perturbations, which we can distinguish mathematically by the way they change under transformations like a coordinates transformation, in this Thesis we will only focus on *scalar* perturbations. In particular, we choose to work in the so-called "conformal Newtonian" gauge, where the addition of two perturbative functions known as the "Newtonian potential", $\Psi(x^\alpha, t)$, and the "perturbation to the spatial curvature", $\Phi(x^\alpha, t)$, results in the following extension of the metric in Eq.(II.3):

$$g_{\mu\nu} = \text{diag}\left(-(1+2\Psi),\, \delta_{\alpha\beta}\, a^2(t)(1+2\Phi)\right). \tag{II.15}$$

With the two new functions just introduced, we are now able to describe a universe with a geometry that allows for slight deviations from the perfect smoothness postulated by the cosmological principle. In particular, the application of Eq.(II.15) leads to a generalization of the Boltzmann equation that includes Φ and Ψ. Consistently with the line of reasoning carried forward up to this point, here we only report the collisionless Boltzmann equation for non-relativistic particles, precisely that for CDM. Its form would of course change if we were to consider interactions with other species or relativistic particles. With this in mind, we can now describe the time evolution of the distribution function of CDM in a perturbed universe as follows:

$$\dot{f}_c + \frac{p}{E}\frac{\hat{p}^\alpha}{a(t)}\frac{\partial f_c}{\partial x^\alpha} - \left[H + \dot{\Phi} + \frac{E}{a(t)p}\hat{p}^\alpha\frac{\partial \Psi}{\partial x^\alpha}\right] p\frac{\partial f_c}{\partial p} = 0, \tag{II.16}$$

where $\hat{p}^\alpha$ is defined so that $p^\alpha = p\,\hat{p}^\alpha$.
The introduction of inhomogeneities leads to the appearance of the spatial divergence of f_c in the second term of the right-hand side of the expression above, along with contributions by Φ and Ψ in the third. Similarly to what was done for the homogeneous case, we can now take the zeroth momentum of Eq.(II.16):

$$\dot{n_c} + \frac{1}{a(t)}\frac{\partial(n_c u_c^\alpha)}{\partial x^\alpha} + 3(H + \dot{\Phi})n_c = 0. \tag{II.17}$$

The expression above is the perturbed version of Eq.(II.13) and, since here and throughout all of this Thesis we only deal with *linear* perturbations, we are able to easily separate the homogeneous contributions from the non-homogeneous ones by introducing two new perturbative variables:

- $\delta_c(x^\alpha, t)$, the perturbation in the density of dark matter, defined as $\delta_c(x^\alpha, t) = n_c(x^\alpha, t)/\bar{n}_c(t) - 1$, where $\bar{n}_c(t)$ is the homogeneous number density of CDM particles (a re-definition of the same variable used in Eq.(II.13)) and $n_c(x^\alpha, t)$ is an extension

of $\bar{n}_c(t)$ that includes a spatial dependence;

- $u_c^\alpha(x^\alpha, t)$, the bulk velocity of CDM, which is defined as:

$$u_c^\alpha = \frac{1}{n_c}\int \frac{d^3p}{(2\pi)^3} f_c \frac{p\hat{p}^\alpha}{E(p)}. \tag{II.18}$$

By taking advantage of the two newly defined variables, δ_c and u_c^α, we can extract the non-homogeneous part of Eq.(II.17) to find the evolution of δ_c:

$$\dot{\delta_c} - \frac{1}{a(t)}\frac{\partial u_c^\alpha}{\partial x^\alpha} + 3\dot{\Phi} = 0. \tag{II.19}$$

Here, δ_c can also be interpreted as the perturbation of the CDM *density* instead of its *number density*, given that ρ_i and n_i are proportional to each other in the case of non-relativistic matter.

The same procedure above can be repeated by taking the *first* moment of Eq.(II.16), namely by multiplying both sides of that equation by $\frac{d^3p}{(2\pi)^3}\frac{p}{E}\hat{p}^\alpha$ and integrating. This, in turn, provides us with an equation for the time evolution of $u_c^\alpha(x^\alpha, t)$:

$$\dot{u_c^\alpha} + \frac{1}{a(t)}\frac{\partial \Psi}{\partial x^\alpha} + H u_c^\alpha = 0. \tag{II.20}$$

Eqs.(II.19,II.20) are fundamental to solve for the dynamics of CDM perturbations, but they do not form a complete set of equations quite yet. To close this system, we also need two equations for the evolution of the perturbative potentials Φ and Ψ, which can be obtained by applying the perturbed metric defined above to Einstein's field equations. In particular, the $\mu = \nu = 0$ component of Eq.(II.1) yields the Poisson equation for the cosmology represented by the metric in Eq.(II.15):

$$k^2\Phi = 4\pi G a^2(t)[\rho_c\delta_c + \rho_b\delta_b]. \tag{II.21}$$

We note that Eq.(II.21) also includes δ_b, the density perturbation of baryons, because, along with CDM, this is the main energy component of the universe at late times (on top of Λ of course). Now, for the equation closing this system one can arbitrarily pick any other non-trivial component of the perturbed Einstein equations. Here, we choose the following:

$$k^2(\Phi + \Psi) = 0. \tag{II.22}$$

In a way, Eqs.(II.21,II.22) can be thought of as the Friedmann equations for a perturbed universe, even though the quantities at play are actually quite different from the homogeneous densities and pressures seen in the previous section.

A number of clarifications have to be made about Eqs.(II.21,II.22). Firstly, compared to all the equations presented up to this point, they are expressed in Fourier space, where the wavenumber k, defined as $k^2 = k^\alpha k_\alpha$, takes the stead of the spatial coordinates as the main variable, other than time, on which perturbative quantities like Φ and Ψ depend. The reason for this choice is that the Fourier form for these equations is closer to the notation used in the papers on MG presented in chapters IV, V and VI of this Thesis. The Fourier notation also makes it much easier to connect theoretical perturbative quantities like Φ and Ψ to the cosmological observables that will be presented in chapter III.
Secondly, Eqs.(II.21,II.22) are just an approximated version of the full Poisson equations derived from perturbation theory. In particular, they are only valid at late cosmological times (define here as $a \gtrsim a_{eq}$, where a_{eq} is the value of the scale factor at matter-radiation equality) and for sub-horizon scales (defined here as $k \gtrsim aH$). This is, however, not a problem in the context of this Thesis, as the modifications introduced by the MG models presented in chapters IV, V, VI and the DE model in chapter VII only affect the late-time universe and perturbation modes within the horizon.

Interestingly, in the late-time limit and at sub-horizon scales, it is possible to express the time dependence of the perturbations of non-relativistic species with one simple equation. In fact, in this approximation regime, the equations describing the time evolution of δ_b and u_b are identical to Eqs.(II.19,II.20), which describe dark matter perturbations. By then defining δ_m, the perturbation of all non-relativistic matter as $\rho_m \delta_m = \rho_b \delta_b + \rho_c \delta_c$, one can obtain the following equation of motion:

$$\ddot{\delta}_m + 2H\dot{\delta}_m - 4\pi G \rho_m \delta_m = 0. \tag{II.23}$$

This equation will be quite useful in the discussions of chapters IV and VI, as they both include analyses of an MG model that modifies it directly: the "γ parametrisation".

To summarise, we now have a complete set of equations for CDM in a inhomogeneous universe described by Eq.(II.15), namely the combination of Eqs.(II.19-II.22). The equations for the density perturbations of baryons, photons and neutrinos are not included here; the reader is referred [40, 42] for a complete account of their derivation. The CDM case was chosen simply as the neatest component to treat in this review of cosmological perturbations, given that it only interacts gravitationally with all the other components.

And what about Λ? By definition, the energy density of Λ is constant in time and space, so that all perturbations for this component are effectively zero. This picture, in general, is bound to change once we consider models of dark energy though. In fact, when the cosmological constant is "promoted" to a time-dependent form of energy, we are required to introduce new equations to describe the perturbations of DE: $\delta_{\rm DE}$ and $u^{\alpha}_{\rm DE}$. However, these perturbative quantities for DE are never really used in the paper presented in chapter VII, as in that work the only equations that change with respect to the standard theory are the homogeneous equations outlined in Sec. II.A.

II.C Inflation, or the Initial Conditions of the Universe

Finding a solution to the equations for the homogeneous and non-homogeneous universe, which were presented in the previous two sections of this chapter, is the first important step that needs to be taken in order to constrain the standard model of cosmology. The same goes, of course, for its extensions. While the equations for the background and the perturbations of these models might differ from their "homonymous" expressions in the ΛCDM model, the goal remains the same: obtaining the time and scale (if any) evolution of quantities such as ρ_i, δ_i, u^a_i, Ψ or Φ. These solutions are in fact essential to then compute the observables, such as the distances and spectra that will be introduced in chapter III, that are needed to compare cosmological models with data. However, as it is the case for any other differential equation in physics, to find a solution to an equation like Eq.(II.23) one needs the initial conditions for its key quantities, in this case δ_m. The theory of "inflation" is the framework that, in the context of the cosmological paradigm, provides us with the initial conditions that we require to compute exactly that. Before delving into how inflation accomplishes this though, it is important to spend a few lines on why inflation was developed in the first place. Doing this will serve as an introduction to its most fundamental constituent: the primordial scalar field known as "inflaton", ϕ.

Another important result of inflation is the mechanism it provides to explain why we observe no magnetic monopoles in the current universe, despite the fact that GUT theories clearly predict their existence: this is referred to as the "monopole problem". A simple way to motivate this "absence" is to postulate that, at very early times, the universe underwent a brief period of exponential expansion that suppressed the number density of these monopoles to an undetectable amount by pushing them beyond the comoving or *particle* horizon. This can be achieved by introducing a scalar field known as the "inflaton", characterised by a minimal coupling to gravity and a potential $V(\phi)$. With these characteristics in mind, it is possible to show that the density and pressure of the inflaton field, ρ_ϕ and P_ϕ respectively,

take the following form:

$$\rho_\phi = \frac{1}{2}\dot{\phi}^2 + V(\phi), \tag{II.24}$$

$$P_\phi = \frac{1}{2}\dot{\phi}^2 - V(\phi). \tag{II.25}$$

According to these results, one can now also define the equation of state of the inflaton field, w_ϕ:

$$w_\phi = \frac{\frac{1}{2}\dot{\phi}^2 - V(\phi)}{\frac{1}{2}\dot{\phi}^2 + V(\phi)}. \tag{II.26}$$

For inflation to be successful at solving the monopole problem, we need ϕ to obey the so-called "slow-roll" condition, which requires that the kinetic part of ρ_ϕ and P_ϕ (i.e., the term containing $\dot{\phi}^2/2$) be subdominant compared to the potential: $\dot{\phi}^2 \ll V(\phi)$. This is a condition that must be satisfied throughout the whole duration of inflation and, as one can gather from Eq.(II.26), it can be translated into a condition for the equation of state of ϕ:

$$w_\phi \approx -1. \tag{II.27}$$

By substituting the equation above in Eq.(II.10), it becomes clear that ρ_ϕ has to be a nearly constant value during inflation. Given that the inflaton field is also the dominating energy component in this very early phase of the universe, it is possible to show that, by virtue of Eq.(II.7), $H(t)$ must be almost perfectly fixed in time like ρ_ϕ. Here, we denote this fixed value for $H(t)$ as $H_{\rm infl}$. Finally, by taking advantage of the Friedmann equation (Eq.(II.7)) once more, it is possible to prove that the scale factor does indeed grow exponentially fast in time during inflation:

$$a \propto e^{H_{\rm infl}(t_f - t_i)}, \tag{II.28}$$

where t_f and t_i are the times at which inflation starts and ends respectively. In other words, the inflationary universe is a quasi-de Sitter universe. The monopole problem is then solved by recalling that, as derived in Sec.II.A, the number density of non-relativistic matter scales as $n_{b,c} \propto a^{-3}$, so that the number of monopoles $n_{\rm mono}$ will decrease exponentially fast:

$$n_{\rm mono} \propto a^{-3H_{\rm infl}(t_f - t_i)}. \tag{II.29}$$

Eq.(II.29) implies that, if inflation lasts for long enough, the number density of the magnetic monopoles in the (observable) universe can be reduced to virtually zero.

The duration of the inflationary phase of the universe is determined by the slow-roll condition and, ultimately, by the potential that we choose for ϕ. To better quantify this condition, it is often useful to introduce the so-called "slow-roll parameters", two dimensionless numbers that fix the shape of $V(\phi)$, defined as:

$$\epsilon_V = \frac{1}{16\pi G}\left(\frac{V_\phi}{V}\right)^2, \tag{II.30}$$

$$\eta_V = \frac{1}{8\pi G}\left(\frac{V_{\phi\phi}}{V}\right), \tag{II.31}$$

where the subscript notation (e.g., V_ϕ) denotes derivatives with respect to ϕ. In particular, inflation lasts for as long as $\epsilon_V, |\eta_V| \ll 1$, which is equivalent to the original slow-roll condition requiring $\dot{\phi}^2 \ll V(\phi)$. However, Eqs.(II.30,II.31) are not the only choices that we can make for the slow-roll parameters, as instead we can introduce two new quantities that are more closely related to the background evolution (i.e., to $H(t)$) rather than $V(\phi)$.
We call them "Hubble slow-roll parameters", and define them as follows [43]:

$$\epsilon = -\frac{\dot{H}}{H^2}, \tag{II.32}$$

$$\delta = \frac{d\ln(\epsilon)}{d\ln(a)} = -\frac{\ddot{\phi}}{H\dot{\phi}}. \tag{II.33}$$

Just like ϵ_V and η_V, which are known as the "potential slow-roll parameters", ϵ and δ also need to satisfy $\epsilon, |\delta| \ll 1$ for inflation to happen. In particular, given that $H(t)$ is required to be nearly constant during this phase, a small value for ϵ guarantees an accelerated expansion, while a small value for δ allows for inflation to last for long enough to solve the monopole problem. In the slow-roll approximation, these two sets of parameters can be related as $\epsilon \approx \epsilon_V$ and $\delta \approx \eta_V - \epsilon_V$.

In addition to equipping us with a solution for the monopole problem, inflation also does a pretty good job at explaining why the spatial curvature of the current universe looks so close to zero. The reason why this should seem weird at first consideration is that we expect the curvature's contribution to the Friedmann equations, which we define here as $\Omega_\mathcal{K}$, to grow as the universe expands. However, the majority of CMB experiments tells us that our universe must be flat to sub-percent precision [24, 25, 44, 45]: $\Omega_{\mathcal{K},0} \approx 0$, where the $\Omega_{\mathcal{K},0}$ is the value of $\Omega_\mathcal{K}$ today. This implies that, in the very early universe, $\Omega_\mathcal{K}$ must have been even closer to zero

than it is now, approximately 10^{60} times smaller than now if we take the Friedmann equation to work all the way back to when the universe was one "Planck time" old, the earliest epoch in which gravity can still be treated with GR. This seems like an extremely fine-tuned initial condition that just cannot be taken as a mere assumption about the initial curvature of the universe. To understand why curvature grows in time (in a matter or radiation-dominated universe at least), we need to rewrite Eq.(II.7) to include a spatial curvature contribution, as in Sec.II.A the Friedmann equations where presented under the assumption of a flat universe. This generalised version of the first Friedmann equation will look like the following:

$$H^2 = \frac{8\pi G}{3}\sum_i \rho_i - \frac{\mathcal{K}}{a^2} + \frac{\Lambda}{3}, \tag{II.34}$$

where $\mathcal{K} \in \{-1, 0, 1\}$, the curvature parameter, describes a universe that is geometrically open, flat and closed respectively. If we multiply both sides of Eq.(II.34) by H^2 and follow the general definition for the density parameter Ω_i of the energy component i (i.e., $\Omega_i = 3H^2\rho_i/(8\pi G)$), we can rewrite the Friedmann equation including curvature as follows [7]:

$$1 - \sum_i \Omega_i = -\frac{\mathcal{K}}{a^2H^2}. \tag{II.35}$$

The right-hand side of this equation quantifies the departure from flatness (i.e., when $\sum_i \Omega_i \neq 1$) and it can be expressed simply as $\Omega_\mathcal{K}$. Eq.(II.35) can be easily tweaked to link $\Omega_{\mathcal{K},0}$ to the past values of the spatial curvature:

$$\Omega_\mathcal{K} = \frac{H_0^2}{H^2a^2}\Omega_{\mathcal{K},0}. \tag{II.36}$$

In a matter-dominated universe, namely a universe where the main energy component is non-relativistic matter, the value of the Hubble function drops with the expansion as $H^2 \propto a^{-3}$, so that the spatial curvature increases as $\Omega_\mathcal{K} \propto a$. However, for a ϕ-dominated universe the scale factor was shown to grow exponentially in time, which results in the following time evolution for $\Omega_\mathcal{K}$:

$$\Omega_\mathcal{K} \propto e^{-2H_{\text{infl}}(t_f - t_i)}, \tag{II.37}$$

which means that, if again $t_f - t_i$ is a long enough duration for the inflationary phase of the universe, the curvature parameter is reduced to essentially zero, crushing even the 10^{60} factor separating the value of $\Omega_\mathcal{K}$ between t_f and today. To better quantify what we mean when we say that the inflationary phase needs to last for "long enough", it is useful to introduce the "e-folds" of inflation - N. This is the number of times by which the universe grew during inflation as a factor of e; it is defined as $dN = Hdt$. With this relation, Eq.(II.28) can be

easily rewritten as $a \propto e^N$, where $N = H_{\rm infl}(t_f - t_i)$. It can be shown that a "long enough" inflation requires $N \gtrsim 60$ in order to satisfy the monopole and flatness problems at once.

Finally, as noted above, inflation also sets the initial conditions for the perturbations around the homogeneous background of the universe, the same perturbations that go on to form its LSS at late times. Similarly to the treatment adopted for the perturbations in Sec.II.B, we split the field under investigation, the inflaton, into an homogeneous part, $\bar{\phi}$, and its perturbation, $\delta\phi$:

$$\phi = \bar{\phi} + \delta\phi. \tag{II.38}$$

Analogously to the other perturbation quantities like δ_m, which we can evolve in time by solving Eq.(II.23), the inflaton perturbation $\delta\phi$ can also be associated to its own equation of motion, the "Mukhanov-Sasaki" equation [46, 47]:

$$\delta\phi'' + 2aH\delta\phi' + k^2\delta\phi = 0, \tag{II.39}$$

which describes the dynamics of the (massless) inflaton perturbation field for an expanding universe given by Eq.(II.3) and where the "prime" notation (e.g., $\delta\phi'$) denotes derivatives with respect to the conformal time η, defined as $d\eta = dt/a(t)$. There is, however, a fundamental difference that sets the inflaton overdensity apart from other types of perturbation. $\delta\phi$ is in fact a quantum fluctuation, meaning that it can be turned into a quantum operator of which we can calculate the expectation value and, most importantly, the variance. The variance of $\delta\phi$ can in turn be used to define a fundamental quantity for the inflaton perturbations, the "spectrum of primordial perturbations":

$$P_{\delta\phi} = \frac{H^2}{4\pi^2}. \tag{II.40}$$

In inflation, it is often convenient to redefine $\delta\phi$ through a different variable termed as "curvature perturbation", $\mathcal{R}$:

$$\mathcal{R} = -\frac{aH}{\bar{\phi}'}\delta\phi, \tag{II.41}$$

which has the advantage of being a quantity that, unlike $\delta\phi$, is conserved once the exponential expansion pushes the perturbation modes of $\delta\phi$ to super-horizon scales (i.e., $\dot{\mathcal{R}} = 0$ for modes smaller than $k \sim aH$) and can thus be used as a proper, time-independent initial condition that fixes the starting point for the evolution of all other perturbations in the universe. In particular, with this redefinition, the spectrum of primordial perturbations now takes the

following form:

$$P_{\mathcal{R}} = \frac{GH^2}{\pi\epsilon}, \tag{II.42}$$

where we also gain a dependence on the slow-roll parameter ϵ. Notably, Eqs.(II.40,II.42) do not contain any scale dependence, at least in good approximation. This is why $P_{\mathcal{R}}$ is often parametrised with the following expression for the primordial spectrum:

$$P_{\mathcal{R}} = A_s \left(\frac{k}{k_*}\right)^{n_s-1}, \tag{II.43}$$

where k_* is a pivot scale that can be arbitrarily chosen depending on the scales that are probed by the cosmological observables like the CMB; the standard choice used by the Planck mission is $k_* = 0.05\,\mathrm{Mpc}^{-1}$ [23, 48]. A_s and n_s, respectively the amplitude and spectral index of the primordial scalar perturbations, are parameters that need to be constrained by the observations. The (near) scale-invariance of Eq.(II.43), guaranteed when $n_s \approx 1$, is another important consequence of the inflationary theory, representing a prediction that is observed with high precision [23, 48].
Now, by drawing $\mathcal{R}$ from a distribution with a variance defined by $P_{\mathcal{R}}$, one can initialise the perturbation equations outlined in Sec.(II.B) because of two crucial reasons. Firstly, it can be shown that, at the end of inflation, $\mathcal{R}$ and the metric perturbation Ψ are actually connected:

$$\mathcal{R} = -\frac{3}{2}\Psi. \tag{II.44}$$

Secondly, inflation also predicts the perturbations of the energy components of the universe, δ_i, to be *adiabatic*, meaning that, as soon inflation ends, they need to satisfy the following relation:

$$\frac{\delta\rho_i}{\dot{\rho}_i} = \frac{\delta\phi}{\dot{\phi}}\,. \tag{II.45}$$

In particular, $\delta\phi$ is thought to decay into all of the known matter and energy species through a post-inflation process known as "reheating", which means that Eq.(II.45) must be taken literally as "before" (right-hand side) and "after" (left-hand side) inflation. Thanks to Eq.(II.45), the inflaton perturbation $\delta\phi$ can be recast as an initial value of Ψ which, in turn, can be used as the initial condition for all the other perturbations.

The picture for the evolution of the homogeneous and non-homogeneous universe is then complete. We can now introduce how all the theoretical framework developed thus far can be tested against the data, a connection that is laid out by presenting, in the next chapter, the fundamental observables of cosmology.

III Two More Tools to Understand the Universe: Observables and Statistics

As Blake Sherwin noted in the opening of his PhD dissertation [49], "*a striking fact about our universe is how much of it we cannot see*". In fact, not only do we have no direct observational evidence of either CDM or DE, quite literally $\sim 95\%$ of the energy contained in the observable universe, but we also have yet to observe most of the matter that is actually "visible", baryonic matter. He then goes on to say that, despite this apparent deficit, "*advances in the study of the CMB ... allowed us (in combination with observations of the cosmic expansion history) to determine the precise amount of the universe that consists of dark matter and dark energy*". This is indeed one of the most remarkable achievements of WMAP, Planck, ACT and SPT, the telescopes that have and continue to measure the "anisotropies" of the CMB, allowing us to use this relic radiation from the early universe as a tool to seize the densities of DE and CDM. Chapter I portrayed the observation of the CMB blackbody spectrum (also known as the CMB "monopole") as one of the strongest proofs of the validity of the ΛCDM model. However, the same can be said about the measurement of the anistropies of the CMB, that is to say the small fluctuations around the uniform temperature of its photons, which we measure to be $T_0 \approx 2.7260\,\mathrm{K}$. The spectrum of these fluctuations is shown in Fig. III.1. The precision of the match between the ΛCDM predictions and the measurements by the ACT telescope is, once more, astounding. In fact, the orange, blue and green dots displayed in the figure follow the best-fit prediction found by the combination of ACT, SPT and Planck data almost perfectly well, with error bars so small they can hardly be spotted.

The main part of this chapter is dedicated to explaining the meaning of these "anisotropies", represented in the form of their power spectrum "wiggles" in Fig.(III.1), and sketching some of the ways in which we can do cosmology with them. In particular, Sec. III.A treats the "temperature" and "polarisation" anisotropies of the CMB, two fundamental cosmological observables. The main CMB datasets used in this Thesis will be introduced chapter by chapter in each of the papers presented. However, we can anticipate that they will include the temperature, polarisation and lensing spectra from the data releases by WMAP [50], Planck [23, 51–53], ACT [54, 55] and SPT [56, 57]. Since the time that these papers were written, new datasets came out for ACT and SPT, which are not employed in the analyses presented here, respectively [58] and [25].

The remainder of this chapter will instead be dedicated to two observables of the cosmic expansion history: the BAO and SNIa distance measurements. In this Thesis, these types of

data will be treated purely as background measurements (i.e., as observations pinning down the expansion of the universe rather than the evolution of its perturbations). Both probes, however, are also essential tools that we need to constrain the standard model in its entirety. In fact, it is thanks to the complementarity of BAO and SNIa data with CMB measurements that certain correlations between cosmological parameters, like the "geometric degeneracy" between H_0 and w_Λ which cannot be resolved by employing CMB data alone [59], are broken.

III.A The Cosmic Microwave Background

When the universe was ~ 380000 years old, long after the inflationary phase described in the previous chapter, its contents consisted of a hot and dense plasma of photons, protons, electrons and some very short-lived light nuclei like hydrogen. Until then, the temperature was much higher than the $\sim 13.6\,\text{GeV}$ required to ionise hydrogen, which meant that hydrogen atoms could never really form stably and that the main type of particle interaction was the Compton scattering between photons and electrons. However, the universe kept expanding and the photons' temperature lowered as $T \sim a^{-1}$, getting closer to $\sim 13.6\,\text{GeV}$. As the universe reached this point, protons and electrons could start bonding stably into hydrogen atoms: this was the start of the "recombination era". The number of free electrons - n_e - started plummeting while they "recombined" with protons and the interaction rate - Γ - between photons and electrons also decreased. Once Γ became lower than $H(t)$, the photons could start to stream freely and effectively "decoupled" from baryonic matter. This is how the CMB was formed. Today, we still observe the same photons released during recombination, but their current temperature, T_0, is now much lower and the frequency at which their blackbody spectrum is peaking lies, as given away by the name "cosmic microwave background", in the microwave band of the electromagnetic spectrum.

However, not all CMB photons share the same temperature T_0. In fact, there exist some extremely small temperature variations that can be measured from photons coming from different directions in the sky - $\hat{n}^\alpha$. These variations, which we refer to as *anisotropies* in the case of the CMB and define as $\delta T(x^\alpha, \hat{n}^\alpha, t)$, are a direct product of the curvature fluctuations - $\mathcal{R}$ - that were generated during inflation. Owing to the homogeneity of the universe, we can drop the dependence of δT on x^α and, since we need to compute its value today, we can also drop its time dependence [60]. Then, the temperature fluctuations can be seen as just depending on the direction in which we observe them: $\delta T \equiv \delta T(\hat{n}^\alpha)$.

To simplify their treatment, we decompose δT into modes of $Y_{\ell m}(\hat{n}^\alpha)$, the spherical harmonics of $\hat{n}^\alpha$ that are often used to describe vibration modes on the surface of a sphere (which, in

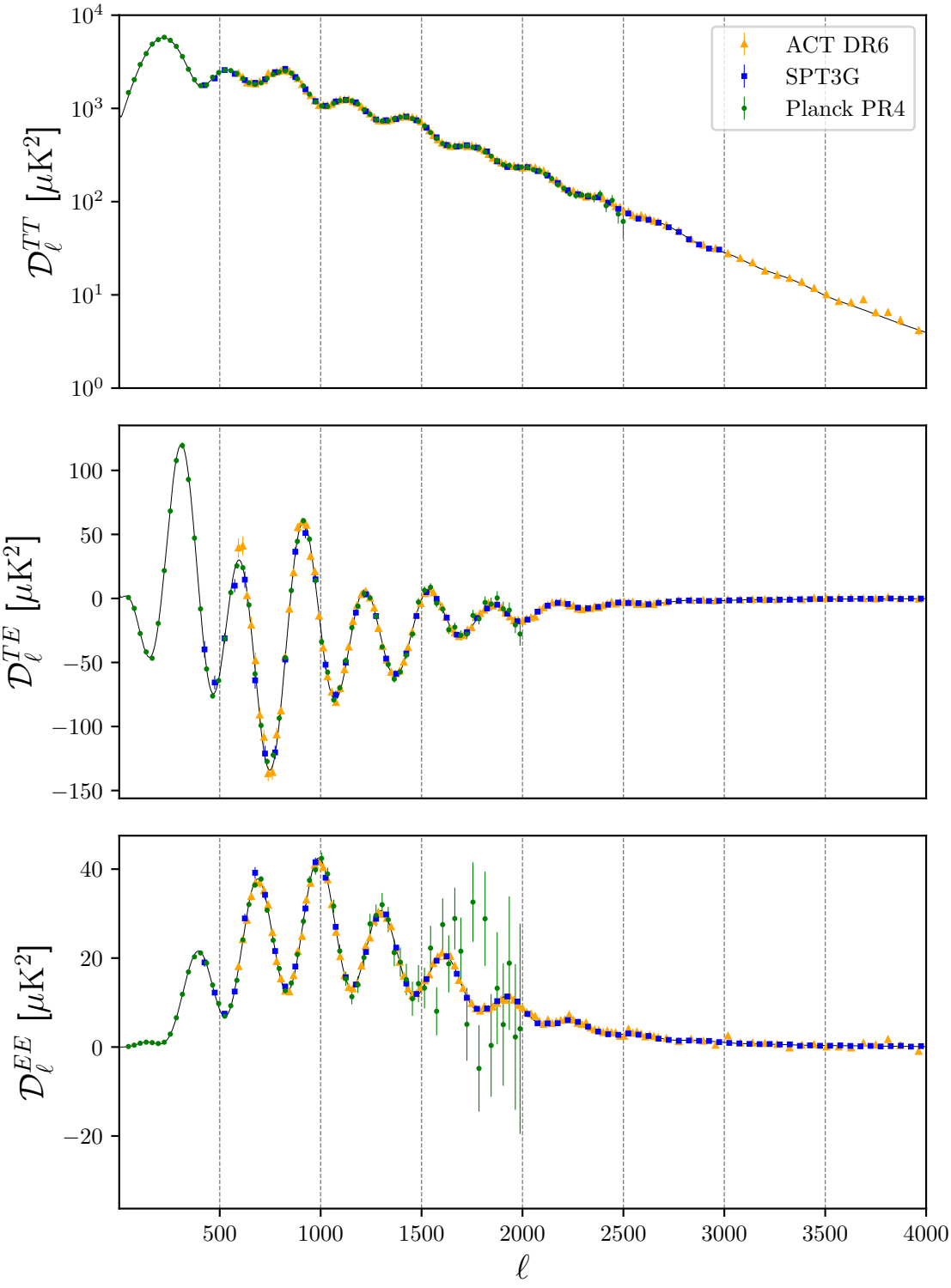


FIG. III.1. Best-fit temperature and polarisation spectra from the Planck PR4 measurements [53], in conjunction with the latest data by ACT [58] and SPT [25], where $\mathcal{D}_\ell = \ell(\ell+1)C_\ell/2\pi$.

this case, is the surface of last scattering):

$$\delta T(\hat{n}^\alpha) = \sum_{\ell m} \delta T_{\ell m} Y_{\ell m}(\hat{n}^\alpha). \tag{III.1}$$

Here, the indices ℓ, m are defined so that $0 < \ell < \infty$ and $-\ell < m < \ell$; each mode contains $2\ell + 1$ terms. While useful for what comes next, the decomposition in Eq.(III.1) is not something that can actually be observed, as our physical theories of the universe (including, of course, the ΛCDM model) cannot predict the evolution of each mode of $\delta T(\hat{n}^\alpha)$. What they can do instead is allow us to compute their statistical properties, like their "two-point function":

$$\langle \delta T(\hat{n}^\alpha) \delta T(\hat{n}'^\alpha) \rangle = \sum_{\ell m} \sum_{\ell' m'} \langle \delta T_{\ell m} \delta T_{\ell' m'} \rangle \,. \tag{III.2}$$

The prime notation, in the case of temperature perturbations only, is used to denote an arbitrarily different sky direction $\hat{n}'^\alpha$ as opposed to $\hat{n}^\alpha$. Now, if we take into consideration the second and last main assumption of the cosmological principle, that of spatial isotropy, we can uncorrelate the ℓ, m modes of $\delta T(\hat{n}^\alpha)$. This in turn leads to a major simplification of the term inside the sums of the right-hand side of Eq.(III.2) [60, 61]:

$$\langle \delta T(\hat{n}^\alpha) \delta T(\hat{n}'^\alpha) \rangle = \sum_{\ell m} \sum_{\ell' m'} \delta_{\ell m} \delta_{\ell' m'} C_\ell^{TT}, \tag{III.3}$$

where $\delta_{\ell m}$ is the Dirac delta function.

C_ℓ^{TT} is the most fundamental quantity in the observations of the CMB that will be considered in this Thesis. It is the "power spectrum" of the CMB temperature anisotropies or, equivalently, the variance of each ℓ-mode. The curve traced by C_ℓ^{TT} is represented by the continuous black curve shown in Fig. III.1: this is the point of connection between CMB theory and CMB data. In fact, the values of C_ℓ^{TT} at different "multipoles" ℓ are exactly what CMB surveys measure and, since we can compute this power spectrum from the ΛCDM theory outlined thus far, we can also fit our model's parameters by taking advantage of the statistical methods presented later in this chapter. The next paragraph will be dedicated to outlining the physical mechanisms that contribute to the origin of the CMB anisotropies $\delta T(\hat{n}^\alpha)$, which are what we need to compute the C_ℓ^{TT} modes. The same definition for the spectrum of the temperature anisotropies also applies to the case of CMB polarization, as shown in paragraph III.A.5.

One could wonder if the variance of the modes of $\delta T(\hat{n}^\alpha)$, C_ℓ^{TT}, is enough to fully describe

their statistical properties. It could be possible, in fact, to stray further from the two-point statistics above and calculate things like the three-point function, $\langle \delta T(\hat{n}^\alpha) \delta T(\hat{n}'^\alpha) \delta T(\hat{n}''^\alpha) \rangle$, or an even higher n-point statistics. However, if we take the fluctuations in temperature to be near-Gaussian fields like $\mathcal{R}$, any correlation function other than the two-point function can be neglected and we can safely take C_ℓ^{TT} as the complete description of $\delta T(\hat{n}^\alpha)$. While a good approximation for the CMB anisotropies computed at recombination, the near-Gaussianity of the temperature perturbations field does not quite hold for the late universe. In fact, the "weak lensing" effect that will be introduced below induces non-Gaussianities in the CMB, precisely in its four-point correlation function (also known as "trispectrum"), which in turn can be used to reconstruct the lensing contribution to the CMB spectrum that we measure in practice.

III.A.1 The temperature fluctuations of the CMB

Like all the perturbations treated in Sec. II.B, the temperature fluctuations are also associated to a Boltzmann equation. In the case of the CMB anisotropies, this equation describes the time evolution of $\delta T(\hat{n}^\alpha, t)$, where we have momentarily re-introduced t as a variable. The full form of the Boltzmann equation for the CMB photons is quite cumbersome and we refer the reader to [42, 60] for its complete derivation. Instead, here we present its integration along the line of sight, which is tantamount to integrating both sides of that equation with respect to time from t_*, the time of recombination, until t_0, the present. The final result of this operation is as follows [42, 60, 61]:

$$\delta T(\hat{n}^\alpha) = \frac{\delta_{\rm CMB}}{4} + u_b^\alpha n_\alpha + (\Phi + \Psi) + \int_{t_*}^{t_0} (\dot{\Phi} + \dot{\Psi}) dt, \tag{III.4}$$

where the first three terms are all evaluated at t_*.

Now, each of the terms in Eq.(III.4) has a physical meaning, which can be unpacked in the following way.

- $\delta_{\rm CMB}/4$: this is the *energy density* perturbation of the CMB photons.
- $u_b^\alpha n_\alpha$: this is called the "Doppler" term, owing to the fact that it contributes to $\delta T(\hat{n}^\alpha)$ through a frequency shift induced by the bulk velocity of baryons u_b^α, to which photons are tightly coupled at t_*.
- $\Phi + \Psi$: this is the "Weyl potential" and it describes the frequency shift induced by the gravity of a potential well on the photons. This term's contribution is also known as the "Sachs-Wolfe effect" [62].

- $\int_{t_*}^{t_0}(\dot{\Phi}+\dot{\Psi})dt$: this represents the "integrated Sachs-Wolfe effect" and, differently from the Sachs-Wolfe term, it sums up all the contributions to $\delta T(\hat{n}^\alpha)$ by the Weyl potential, at all times until now *except* t_*.

Different combinations of these terms will matter at different scales of the CMB spectrum. In particular, at large scales ($\ell \lesssim 100$) $\delta_{\rm CMB}$ along with the Sachs-Wolfe term dominate, while the medium scales ($100 \lesssim \ell \lesssim 700$) are best captured by the Doppler term; these are also the scales of the "acoustic oscillations", which is where the CMB spectrum "wiggles" (a reflection of the acoustic waves travelling through the primordial plasma before recombination) are most evident. Finally, the small scales ($\ell \gtrsim 700$) tend to be quite suppressed. This mostly happens through the "Silk damping" [63], an effect that originates from recombination ending during a finite time interval rather than a fixed moment t_*, as assumed so far. This interval provides photons with the opportunity of diffusing from hotter to colder regions, reducing the intensity of the temperature perturbations and *damping* their power spectrum at high multipoles.

III.A.2 The polarization of the CMB

During the recombination epoch, $\sim 10\%$ of the CMB photons become polarised. This happens mostly because these photons undergo Thomson scatterings with the electrons that still have not recombined with protons during that time frame. This polarisation effect is best captured in terms of the so-called "Stokes parameters", two of which are important in the CMB scenario: $U(\hat{n}^\alpha)$ and $Q(\hat{n}^\alpha)$. Both encode the difference in intensity of the two orthogonal polarisations imparted to the photon, with the polarisation direction of $U(\hat{n}^\alpha)$ being shifted by an angle of $45^{\rm o}$ compared to $Q(\hat{n}^\alpha)$. These two parameters are, however, not invariant under rotation (i.e., they are not isotropic quantities), and we cannot use them to do cosmology. As it turns out, by taking the combination $(Q\pm iU)(\hat{n}^\alpha)$ and expanding it in spherical harmonics, it is possible to obtain a redefinition of the polarisation modes that is indeed invariant under rotation [61]:

$$(Q \pm iU)(\hat{n}^\alpha) = \sum_{\ell m}(E \mp iB)Y_{\ell m}(\hat{n}^\alpha). \tag{III.5}$$

Thus, the two newly defined polarisation modes, E and B, can be treated as random fields. We can then calculate their respective power spectra analogously to what was done for the temperature anisotropies and the lensing potential. In this way, polarisation modes can be used as a source of complementary information in combination with temperature anisotropies to improve cosmological constraints and break degeneracies. The spectra for the E modes and their cross-correlation with the temperature field, denoted as $\mathcal{D}_\ell^{EE}$ and $\mathcal{D}_\ell^{TE}$ respectively, are represented in the Fig. III.1. The B modes of polarisation and their correlation with temperature (and the E modes) are also interesting in their own respect, but they will

not be explored further in this Thesis. Here we just mention that the pattern that tensor perturbations produced during inflation would induce on the B modes is actually quite unique [64], as compared to scalar perturbations, and its detection would be considered as a decisive observational proof in favour of the inflationary theory. Interestingly, polarisation can also be induced by the "weak lensing" of the CMB, which we introduce in the next paragraph. Specifically, CMB lensing turns E modes into B modes, creating a spurious effect that needs to be subtracted to study polarisations properly.

III.A.3 Secondary anisotropies: CMB lensing

In their journey from recombination until the present era, the photons of the CMB have to deal with a universe that is inhabited by perturbations in the density of matter that gradually clump up to form the large-scale structures that we observe today. That means that δT will be subject to variations that are not really captured by Eq.(III.4), which only describes the physical mechanisms that shape the CMB spectrum up until t_*: these additional contributions are known as the *secondary* anisotropies of the CMB. One of the most important among these post-recombination anisotropies is the weak gravitational lensing of the CMB, here denoted simply as "CMB lensing". This is a deflection in the propagation direction of the CMB photons, $\hat{n}^\alpha$, that happens when they encounter a gravitational potential that pulls them inward, remapping or distorting their location in the CMB sky maps. The angle of deflection, θ^α, depends on the Weyl potential in Eq.(II.22), which is quite literally the equation that dictates how light responds to gravity in the standard model of cosmology. In particular, θ^α can be expressed as another integral taken along the line of sight [65]:

$$\theta^\alpha = -2\int_0^{\chi_*} d\chi \frac{\chi_* - \chi}{\chi\chi_*}\nabla^\alpha(\Phi+\Psi). \tag{III.6}$$

In the expression above, χ is the "comoving distance" that is traveled by photons in a perturbed universe; it is defined in terms of the conformal time as $\chi = \eta_0 - \eta + 2\int_\eta^{\eta_0}(\Phi+\Psi)d\eta'$. While Eq.(III.6) is only valid in a flat universe, it holds for any metric theory of gravity with a metric tensor of the same form as Eq.(II.15).

The deflection angle can be conveniently recast in terms of a perturbation field called "lensing potential" - $\psi(\hat{n}^\alpha)$, which is related to θ^α as $\theta^\alpha = \nabla^\alpha\psi$. As in the case of $\delta T(\hat{n}^\alpha)$, we can take $\psi(\hat{n}^\alpha)$ as a random Gaussian field, expand it in spherical harmonics and calculate its two-point function:

$$\langle\psi(\hat{n}^\alpha)\psi(\hat{n}'^\alpha)\rangle = \sum_{\ell m}\sum_{\ell' m'}\delta_{\ell m}\delta_{\ell' m'}C_\ell^{\psi\psi}. \tag{III.7}$$

We again find that the power spectrum, $C_\ell^{\psi\psi}$, is the only statistics that we need to describe

the statistical properties of the field in question, in this case the lensing potential. Its reconstruction, from the combination of the latest temperature and polarisation measurements by ACT, SPT and Planck, is shown in Fig. III.2.
There is now only one remaining step to explain how $C_\ell^{\psi\psi}$ impacts on the primary anistropies on the CMB, C_ℓ^{TT}. To show this, we first define $\delta\widetilde{T}$ as the temperature perturbation of the CMB *including* the lensing contribution and expand it:

$$\delta\widetilde{T}(\hat{n}^\alpha) = \delta T(\hat{n}^\alpha + \nabla\psi) = \delta T(\hat{n}^\alpha) + \theta^\alpha \nabla_\alpha \delta T + ... \tag{III.8}$$

Then, the spectrum of the temperature anisotropies including lensing, $\widetilde{C}_\ell^{TT}$, can be derived by computing the two-point function of Eq.(III.8). As one could expect by looking at the expansion, the final spectrum will inevitably depend on $C_\ell^{\psi\psi}$ as well. Here, we report just the small-scale limit of this calculation. For the full result we refer the reader to the excellent review on CMB lensing in [65]. That said, at small-scales one gets:

$$\widetilde{C}_\ell^{TT} = \ell^2 C_\ell^{\psi\psi} \frac{1}{4\pi} \int \frac{d\ell}{\ell} \ell^4 C_\ell^{TT}. \tag{III.9}$$

Then, mathematically speaking, the effect of $C_\ell^{\psi\psi}$ on the primary CMB anisotropies is that of a convolution, which transforms the temperature spectrum generated during recombination into the spectrum that we observe today. In a more qualitative way, the effect of the weak lensing on the CMB is that of "smoothing out" the peaks of C_ℓ^{TT} and redistributing the power lost at low/medium multipoles to the small scales. The weak lensing of light can also induce non-Gaussianities in the temperature spectrum of the CMB, an effect that can be computed by taking the four-point function or "trispectrum" of the temperature perturbations. From the trispectrum we can reconstruct the lensing potential spectrum and compare it to the $C_\ell^{\psi\psi}$ that we can compute from the calculation outlined above. This is a crucial consistency test that Planck, up until its 2018 data release, seemed to fail, finding instead a mismatch between the two estimates that has become known as the "lensing anomaly" [23], a problem of the ΛCDM model that will be treated at length by the papers in chapters IV-VI.

III.A.4 Secondary anisotropies: the Sunyaev-Zel'dovich effect

Another major late-time distortion on the CMB is the "Sunyaev-Zel'dovich effect" [69]. It refers to the inverse Compton scattering through which the electrons contained in the very hot gas of a galaxy cluster inject energy in the bypassing CMB photons, making them hotter. In particular, this scattering increases the energy $\mathcal{E}$ of a CMB photon by a shift of around $\Delta\mathcal{E}/\mathcal{E} \sim 10^{-2}$ [70]. The overall effect on the CMB is a then a frequency-dependent one, with

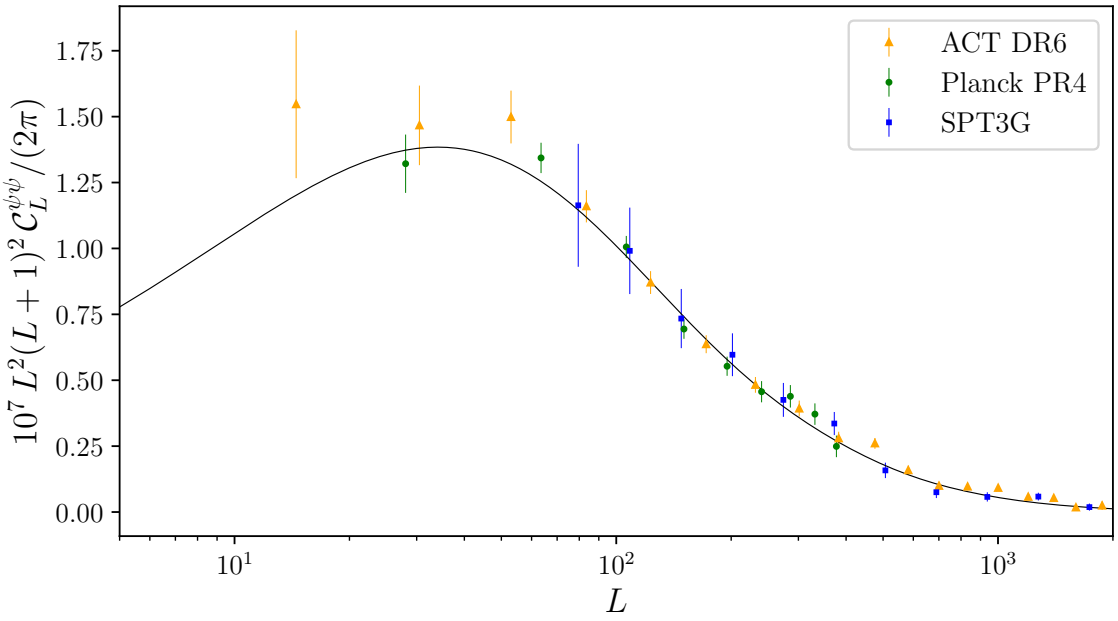


FIG. III.2. CMB lensing spectrum assuming the best-fit ΛCDM cosmology from ACT DR6 [66], PR4 [67] and SPT 3G [68] combined (black continuous line) and its reconstruction (data points). L is a rescaling of ℓ resulting from binning the lensing reconstruction from temperature and polarisation.

photons below the $\sim 217\,\mathrm{GHz}$ threshold being pushed to higher energies, thus increasing the intensity of the blackbody spectrum at $\nu \gtrsim 217\,\mathrm{GHz}$ [70]. More qualitatively, this secondary contribution to the *primary* temperature perturbations of the CMB can be roughly described as generating "shadows" in the maps of the CMB sky.

III.A.5 Estimating cosmology with the CMB: H_0

The CMB is an incredibly powerful source of information about the universe. With it, we can virtually constrain any free parameter of the ΛCDM model. An example is τ_{reio}, the optical depth at reionization, an integrated parameter that quantifies the "opacity" of the universe from the epoch of reionization until today. The former is a phase in the history of the universe where n_e, the number density of free electrons, grew again for the first time since recombination, scattering the CMB photons and making the universe a bit more opaque than it is now.

The optical depth, while being one of the worst constrained parameters by Planck [23], it is a good example of how we can use the power of temperature and especially polarisation anisotropies to constrain the same parameter. In fact, the reionisation process suppresses the temperature power spectrum by a factor of $e^{-2\tau_{\mathrm{reio}}}$ at $\ell \gtrsim 10$ [23, 71], while producing a

"bump" in the polarisation spectrum, C_ℓ^{EE} at $\ell \lesssim 30$ that is proportional to $\tau^2_{\rm reio}$ [71, 72].

H_0 is another parameter that the CMB can constrain quite well. Since it is the main protagonist of the Hubble tension, as explained in chapter VII, here we briefly review how CMB measurements can constrain it. We start from θ_*, the angular scale of the sound horizon at recombination, yet another parameter that Planck is able to measure to sub-percent precision. It can be found by measuring the position of the first peak of the temperature spectrum in Fig. III.1 and we can define it as:

$$\theta_* = \frac{r_*}{D_{A,*}}. \tag{III.10}$$

Here, r_* and $D_{A,*}$ are the comoving sound horizon and the angular diameter distance, both evaluated at recombination, $z_* \approx 1100$. They are defined as:

$$r_* = \int_{z_*}^{\infty} \frac{c_s(z)}{H(z)} dz, \tag{III.11}$$

$$D_{A,*} = \frac{H_0}{1+z} \int_0^{z_*} \frac{1}{H(z)} dz. \tag{III.12}$$

In Eq.(III.11), c_s is the sound speed of the waves travelling through the pre-recombination plasma; it is computed as $c_s = 3\Omega_{b,0}/(4(1+z)\Omega_{\rm CMB,0})$.
Now, $\Omega_{b,0}$ can be measured from ratio of the heights of the first and second acoustic peaks of the CMB (which is sensitive to this parameter specifically [73]), while $\Omega_{\rm CMB,0}$ is fixed by the measurement of the blackbody temperature of the CMB, using the fact that $\rho_{\rm CMB} \sim T^4$ and that $T \sim a^{-1}$. In addition, $H(z)$ also depends on Ω_m, which can be constrained through a characteristic increase in the power of the CMB modes that entered the horizon before $a_{\rm eq}$ known as the "potential envelope" effect [74]. With that, we now have all the parameters that we need to evaluate the Friedmann equation, Eq.(II.7), at present, and thus find H_0. The effect of changing H_0 on the CMB temperature spectrum can be visualised in Fig. III.3.

Notably, as it was just shown, our CMB estimate of H_0 depends heavily on the cosmological model that we assume. For this reason, a possible way to solve the Hubble tension can be sought in new models that could, for example, modify both the top and the bottom of the integrand in Eq.(III.10) while keeping θ_* unchanged compared to the nearly model-independent constraint found by Planck on this parameter: $\theta_* = 0.010411 \pm 0.000003$, including temperature, polarisation and lensing data [23].

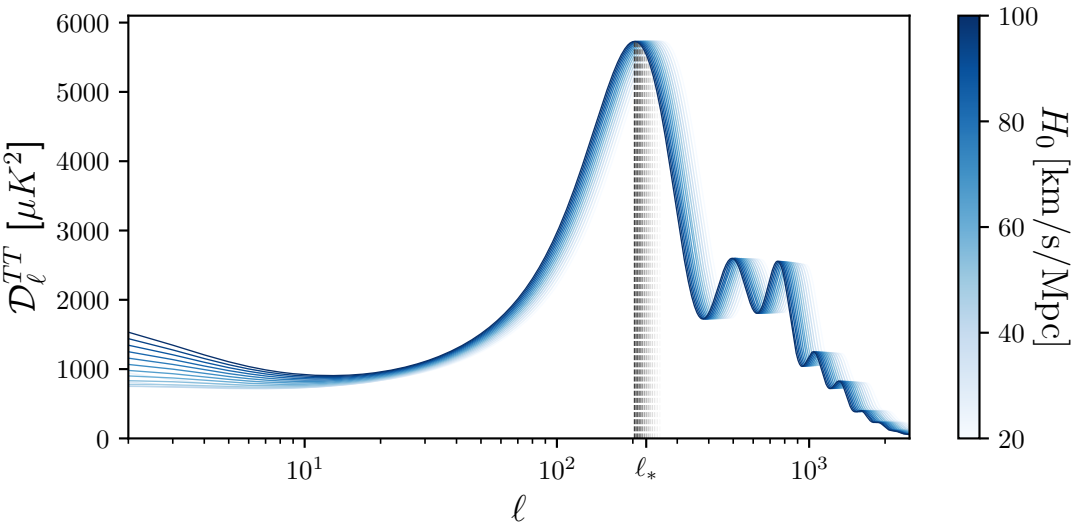


FIG. III.3. Varying H_0 clearly shifts the position of the first acoustic peak, ℓ_* (and the others too). Given Planck's extremely stringent constraint on ℓ_* [23], any change must be balanced by changing parameters that correlate with H_0 or assuming a different model.

III.B Baryon Acoustic Oscillations

In the previous section, we took a snapshot of the universe during its recombination era and we derived some of the most fundamental properties and uses of the CMB as a tool to test the cosmological paradigm. However, light is not the sole protagonist of this story of combining and decoupling. Baryons, from which the CMB photons start decoupling as protons and electrons combine into hydrogen, provide us with another important method to constrain cosmological models. In fact, both δT and δ_b, the perturbations of CMB temperature and baryons respectively, evolve as oscillations of the same photo-baryon fluid and, once recombination happens, they freeze with a characteristic oscillation "scale". The only difference is that these two types of perturbation become fixed at different times: $z_* \sim 1100$ for the CMB and $z_d \sim 1060$ for the baryons. The scale of the CMB is the same angle that was introduced by Eq.(III.10): θ_*. The scale of the baryonic oscillations is the comoving sound horizon evaluated by taking the integral in Eq.(III.11) at z_d rather than z_*. This scale is denoted as "r_d" and it is known as the "baryonic acoustic oscillations" (BAO) scale. As we saw in the previous section, calculating c_s is, essentially, just a matter of knowing Ω_b. Then, the recipe to calculate r_d only requires us to add Ω_m to the mix, at least for cosmological models where the physics of recombination works in the same way as qualitatively outlined in paragraph III.A.5 [75].

The baryon perturbations that decouple from photons after the end of recombination go on to become the large-scale structure of the universe, which includes astronomical objects like galaxies, of which we can measure the distribution with redshift surveys like DESI [14, 15]. Then, the observed distribution can be used to extract two different quantities that are related to the BAO scale, one along the line of sight and one perpendicular to it. These are, respectively, Δz, the redshift separation between pairs of galaxies, and $\Delta\theta$, their angular separation. We can define the latter as follows [14, 15, 76]:

$$\Delta\theta = \frac{r_d}{D_M(z)}, \tag{III.13}$$

where $D_M = (1+z)D_A$ is the transverse comoving distance. Compared to the definition of angular diameter distance given in Eq.(III.12), here we replace z_* with an arbitrary z. Δz is instead defined as:

$$\Delta z = \frac{r_d}{D_H(z)}, \tag{III.14}$$

where $D_H(z) = 1/H(z)$.

Galaxies are not the only tracer of the underlying distribution of dark matter and the BAO scale can be found with other objects or strategies. These include, for instance, quasars, used in the same way as galaxies, and of the "Ly-α forest" technique, which traces matter perturbations through the variations in the density of neutral hydrogen detected through the absorption spectra of quasars [77]. When combined, these tracers provide us with BAO measurements that can be simply summarised as pairs of redshifts and angle/redshift intervals: $\{z, \Delta\theta\}$ or $\{z, \Delta z\}$. An example of these measurements is given by table III of [76], which outlines the BAO measurements found by the eBOSS mission using galaxies, quasars and the Ly-α forest technique.

To conclude, we underline that BAO data cannot constrain H_0 alone, as BAO measure the $r_d H_0$ combination rather than either of those two parameters alone [78]. One solution is to use BAO data in combination with a complementary probe like the CMB. In fact, the CMB can fix r_d, which breaks the $r_d H_0$ degeneracy and provides us with a BAO value for H_0.

In this Thesis, we will make use of two BAO compilations: SDSS [76] and the newer DESI mission [14, 15], shown in Fig. III.4.

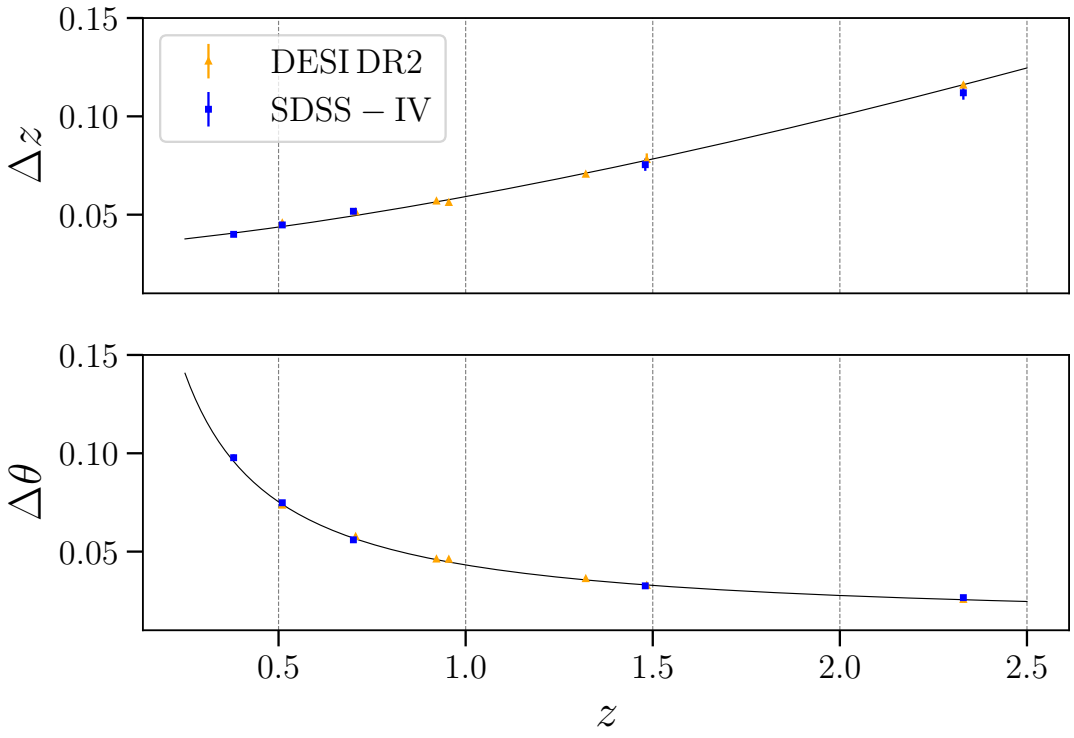


FIG. III.4. Transverse and radial measurements of the BAO scale at different redshifts, $\Delta\theta$ and Δz respectively (as defined in Eqs.(III.13-III.14)). The data points are the complete SDSS BAO catalogue [76] and the DESI DR2 measurements [15], while the continuous black line is found according to Planck PR3's best-fit ΛCDM parameters [23].

III.C Type-Ia Supernovae

The final observable that we consider in this Thesis are type-Ia supernovae (SNIa). Supernovae are the thermonuclear explosions of white dwarfs that, by accreting with dust or another star in their close proximity, reach and overtake the Chandrasekhar mass limit. Supernovae of this type in particular are characterised by an absorption spectrum that contains no hydrogen or helium lines at any point of their evolution. When such explosions happen, we can measure their lightcurves, namely the time variation of their brightness. It turns out that, while the lightcurve evolution of different SN will not look exactly the same, there is very little dispersion in the peak of their brightness, allowing lightcurve shapes to be corrected or *standardised* to follow the same pattern. For this reason, SNIa are often referred to as "standard candles". The "distance modulus" μ of a supernova, which measures its relative brightness and is a quantity directly comparable to the theory, can be found through

the following formula [79]:

$$\mu = m_B - M + \alpha x_1 - \beta c - \delta_{\text{bias}}. \tag{III.15}$$

Here, m_B, x_1 and c are all parameters that can be found by fitting the `SALT` standardisation model to the measured lightcurves [80]. In particular, m_B is the apparent magnitude of a supernova, while x_1 and c account for the diversity in stretch and colour of different lightcurves. Of the other parameters, α and β are fixed quantities whose value depends on the type of analysis [81], while δ_{bias} is a correction for selection-induced biases that can be computed through the set of simulations introduced in [82].

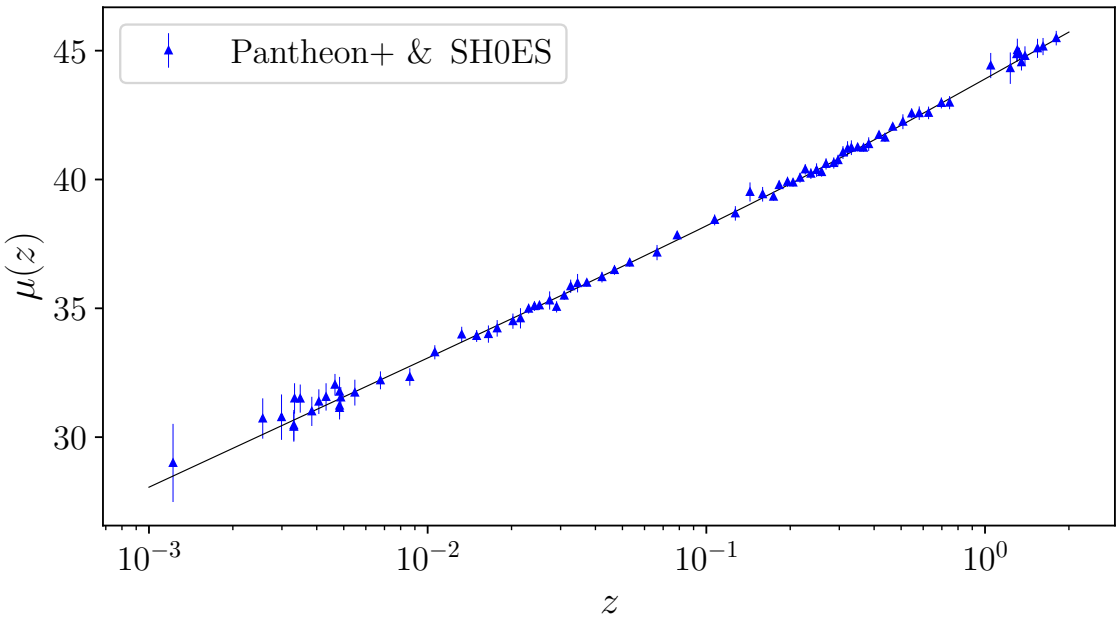


FIG. III.5. SNIa measurements of the distance modulus $\mu(z)$ from the SH0ES calibration of the Pantheon+ supernova catalogue (the blue triangles, reduced in number compared to the data from the original 1701 Pantheon+ lightcurves for visualisation purposes) [83]. The continuous black line is found according to the best-fit values for Ω_m and H_0 from the same calibration.

Notably, SNIa can be used as standalone objects to constrain H_0 directly in the so-called "Hubble flow", the region of the universe at $z \gtrsim 0.01$, where the cosmological expansion starts dominating over the peculiar motion induced by local gravitational potential wells on the supernovae themselves. However, the measurement of H_0 at these distances requires us to also know M, the absolute magnitude of SNIa. M can be obtained at smaller redshifts, at around $z \lesssim 0.01$, thanks to another kind of standard candle known as "cepheid variables", which can be used to calibrate M in those galaxies where we observe both SNIa and cepheids

[84]. In turn, cepheids need to be calibrated with techniques that can only be employed at even lower redshifts, at around $z \approx 0$, like parallaxes and eclipsing binaries. This type of "cascade" strategy that we adopt to calibrate the Hubble flow supernovae is known as "cosmic distance ladder" [84], owing to the fact that each calibration step that we take on this "ladder" needs to be informed by the step preceding it. These steps are also called "rungs", and these rungs can be roughly split according to the redshift and the objects that characterise each. In the first rung, at $z \approx 0$, we have both binary systems and cepheids, while in the "second rung", at $0 \lesssim z \lesssim 0.01$, one has both cepheids and supernovae. In the third and final rung, we only have SNIa, which, at this point of the ladder, are enough to constrain H_0.

Specifically, we can obtain H_0 through the following expression [78, 84]:

$$\log H_0 = -0.2\,\mu + \log cz + 5, \tag{III.16}$$

which is valid at $z \ll 1$. It must be stressed that cepheids are not the only supernova calibrator. Another example is the "tip of the red giant" method, which provides cosmological distances using the ascent of the red giant branch in the color-magnitude diagram compiled with the stars of a specific galaxy. It has been shown to be in good agreement with cepheids when both are utilised to calibrate SNIa [85].

In this Thesis, particularly in chapters VI-VIII, we will make use of the SNIa data from the "Pantheon+" catalogue [81, 86], shown in Fig. III.5.

III.D Bayesian Inference and the MCMC Algorithms

The theoretical framework of the ΛCDM model given in chapter II is a remarkably precise description of the universe, as we have seen from this model's ability to predict a plethora of phenomena that we have actually observed, the CMB *in primis*. However, as for many things in life, the devil's in the details. That is to say that, if we really want to precisely pin down the ΛCDM model, we also need to measure the free parameters that are left by the theory to be constrained by the observations. Remarkably, these parameters are just six in number[III.1]: two to fix the inflationary era (A_s and n_s, the amplitude and spectral index of the primordial perturbations spectrum), two to fix the energy contents of the universe ($\Omega_b h^2$ and $\Omega_c h^2$, the densities of baryons and CDM combined with the dimensionless Hubble constant $h = H_0/(100\,\mathrm{km\,s^{-1}\,Mpc^{-1}})$) and, finally, two for the road (θ_* and τ_{reio}, respectively

[III.1] Technically, they would be seven, as T_0, the temperature of the CMB is also one of them. However, it is measured from the CMB equilibrium spectrum with such precision [10, 87] that we assume it to be an essentially fixed number.

the sound horizon at recombination and the optical depth). In this chapter we have seen some of the observables that are available to us to measure these parameters, which do not represent an exhaustive list of observables though. *Gravitational waves* and *galaxy clustering* are just a few examples that we could add on, which, while interesting, will not be touched upon in this Thesis, as none of the papers presented here will make use of them.

The last thing we require to connect theory to data and constrain the parameters of the standard paradigm is a statistical tool. In this Thesis and, broadly speaking, in cosmology, this role is often taken by "Bayesian statistics", a statistical framework that revolves around one fundamental mathematical relation, the "Bayes theorem":

$$\mathcal{P}(\Theta|D) = \frac{\mathcal{P}(D|\Theta)\mathcal{P}(\Theta)}{\mathcal{P}(D)}. \tag{III.17}$$

Here, what we are interested in is $\mathcal{P}(\Theta|D)$, the "posterior distribution" of a set of parameters Θ given the observation of a set of data points D. To find it, as we see from the equation above, we need $\mathcal{P}(D|\Theta)$, the "likelihood" of observing a dataset D given a fixed sample of parameters Θ, and $\mathcal{P}(\Theta)$, the "prior distribution" of Θ, which quantifies our "prior knowledge" of what values Θ should take. The factor at the denominator is a normalisation constant that, as we will see in a moment, is quite useful to compare different cosmological models with each other.

Now, while the prior can be set to a constant (uniform) quantity, if we do not know much about the parameters, the likelihood stands at the heart of the connection between theory and data. Often, the likelihood is chosen to take a Gaussian profile, so that:

$$\mathcal{P}(D|\Theta) \sim \exp\left(-\frac{\chi^2}{2}\right), \tag{III.18}$$

where $\chi^2 = \sum(D_i - y_i(\Theta))C_{ij}(D_j - y_j(\Theta))$ is the variance of $D_i - y_i(\Theta)$, the difference between an observable (or data point) D_i and $y_i(\Theta)$, the same observable calculated from the assumed cosmological model. An example for these two quantities can be readily found in the temperature spectrum of the CMB, C_ℓ^{TT}, which we can both measure (D_i) and compute ($y_i(\Theta)$) from the theory outlined in Sec. III.A. Then, if we want to find the parameters of our model that "best fit" the data, we will need to minimize the χ^2.

In order to find $\mathcal{P}(\Theta|D)$ then, by virtue of Eq.(III.17), one would seemingly need to calculate $\mathcal{P}(D|\Theta)$ at *every* point Θ of the parameter space of our model. However, for models like ΛCDM with six parameters, a number that often tends to increase for its extensions, this would be computationally unfeasible. Instead, we can *simulate* the posterior [88], by

randomly choosing or *sampling* the values of Θ in the parameter space of our model. This is what algorithms known as MonteCarlo Markov Chain (MCMC) methods do. A widely used sampling algorithm from this class is the Metropolis-Hastings (MH) algorithm; the most important property of MH is that, eventually, the samples that are randomly generated from the likelihood will converge to the posterior distribution [88–90]. This is the algorithm that is employed by both `Cobaya` [91] and `CosmoMC` [92], the two MCMC samplers used for the data analysis of the models presented in chapters IV-VIII. It is with these codes that we can find the posterior for each parameter of our models.

Finally, a word about $\mathcal{P}(\mathcal{D})$, the "Bayesian evidence" factor at the bottom of Eq.(III.17). Its significance can be better understood by making its dependence on a specific model $\mathcal{M}$ explicit: $\mathcal{P}(\mathcal{D}) \equiv \mathcal{P}(\mathcal{D}|\mathcal{M})$. The Bayesian evidence can be thought of as the "average likelihood" calculated by assuming a specific model [90]. Then, by taking the ratio of the Bayesian evidence calculated on the same data $\mathcal{D}$ for two different models $\mathcal{M}_1$ and $\mathcal{M}_2$, we can infer which of the two models is preferred by the data:

$$\mathcal{B} = \frac{\mathcal{P}(\mathcal{D}|\mathcal{M}_1)}{\mathcal{P}(\mathcal{D}|\mathcal{M}_2)}, \tag{III.19}$$

where $\mathcal{B}$ is known as the "Bayes factor". According to "Jeffreys' scale" [93], a qualitative method to classify the Bayes factor values, $\mathcal{M}_1$ is favoured over $\mathcal{M}_2$ when $\mathcal{B} > 1$.

IV Exploring the Growth Index γ_L: Insights from Different CMB Dataset Combinations and Approaches

Preamble to the Paper

This is the first of the three chapters in this Thesis (along with chapters V and VI) that include papers on the investigation of MG parametrisations.

Here, and throughout all of the papers on this topic, we define MG as a parametric modification to the ΛCDM model that manifests itself in the perturbative equations of non-relativistic matter that were outlined in Sec. II.B, while leaving the background sector unchanged with respect to the standard model. Such definition is, of course, not exact, as we know that, in general, MG theories like $f(R)$ cosmologies modify both background and perturbations [94]. However, we will retain the MG definition in all of these papers, as a way to convey the idea that we aim at isolating the observable effects induced purely by a modification in the perturbative sector. In other words, our object of interest is the *phenomenology* of the deviations from the standard perturbative picture, which we look for in things like CMB lensing and large-scale structure growth.

In the following paper, we present an analysis of the constraints that we can obtain from the combination of different CMB datasets on the phenomenological model of MG known as the "γ parametrisation", introduced in [95]. The BAO distance measurements used in this paper are needed to fix the background of the model, which is described by the same ΛCDM model equations outlined in Sec.II.A. In particular, this model assumes a parametric form for $\delta_m(a)$ rather than using a modified version of Eq.(II.23). For the γ parametrisation, δ_m is found by integrating the following equation:

$$\frac{d\ln g}{d\ln a} = \Omega_m^{\gamma},$$

where $g \propto \delta_m$ and Ω_m is the density parameter of non-relativistic matter.

The parameter "γ" (indicated as "γ_L" within the paper itself), which gives the name to this model, is also its key ingredient. Its value depends sensibly on whether the data prefer a DE or a MG model and, for this reason, γ serves as an excellent diagnostic parameter to detect deviations from GR. In fact, while the ΛCDM model and its extensions like $w_{\rm DE}$CDM

(i.e., a model where the equation of state of DE is allowed to take a constant value other than $w_{\rm DE} = -1$) tend to agree quite well with $\gamma \sim 0.55$, fitting the growth index to the evolution of matter perturbations in a MG model like DGP gravity results in $\gamma \sim 0.68$ [95]. As shown in the paper below, the CMB constraints on γ are precise enough to distinguish between these two possibilities. However, the same cannot be said for *any* other MG model. For instance, for a scalar-tensor theory where a scalar degree of freedom ϕ is coupled to gravity, the value for the growth index turns out to be quite close to $\gamma \sim 0.55$ in general [96], making it hardly distinguishable from the standard theory with the current data, at least provided that the coupling to the scalar is not too strong. For these reasons, we should not regard the γ parametrisation as a specific cosmological model, but rather as a tool to detect departures from GR at the level of the late-time cosmological perturbations. In other words, and consistently with the other papers in this Thesis, we should not expect to gain a fundamental understanding of gravity from γ or any other parametrisation alone.

The motivation behind the choice to consider a MG parametrisation for this work was the fact that the Planck PR3 data (excluding the lensing reconstruction), as seen in chapter III, allow for a deviation from the standard model that can be interpreted as a gravity modification. This is shown in Figs.(9, 10) of [97], where the authors employ the "$\mu - \Sigma$" parametrisation of MG, the same framework used and presented in the paper of chapter V. The original intent of the paper presented below was to show whether the same results hold for the γ parametrisation as well. However, a paper with the same analysis we wanted to perform came out just before we could finalise ours [38]. As our results differed, we instead set out to understand the origin of this discrepancy and turned this analysis into a comparison between the two codes that were used to constrain γ: `MGCAMB` [33–37] and `CAMB_GammaPrime_Growth` [38, 39], concluding that, because of a problem with the implementation of γ in `MGCAMB`, the codes could not be reconciled.

The γ parametrisation affects the calculation of the CMB spectra by changing the lensing potential spectrum defined in Sec. III.A. In order to qualitatively clarify how this happens, we remind the reader that ψ, the lensing potential, is just a redefinition of the Weyl potential, $\Psi + \Phi$. Now, the variance of the non-relativistic matter perturbations δ_m, also known as the "matter power spectrum" and denoted in the paper as $P(k, a)$, can be shown to be related to the Weyl potential spectrum in the following way [65]:

$$C_\ell^{\Psi+\Phi}(k, a) = \frac{9\Omega_m^2 H^4}{8\pi^2 k} P(k, a), \tag{IV.1}$$

at least for a matter dominated universe. The γ parametrisation will then change the profile of $P(k, a)$, which, thanks to the equation above, also changes the spectrum of the Weyl

potential and, ultimately, $C_\ell^{\psi\psi}$ (denoted in the paper as $C_\ell^{\phi\phi}$).

One final note about notation: the letter Γ in this paper indicates the parameter space of the model and should not be confused with the Compton scattering rate defined in Sec. III.A.

Exploring the growth index γ_L: Insights from different cmb dataset combinations and approaches

Abstract: In this study we investigate the growth index γ_L, which characterizes the growth of linear matter perturbations, while analysing different cosmological datasets. We compare the approaches implemented by two different patches of the cosmological solver `CAMB`: `MGCAMB` [33–37] and `CAMB_GammaPrime_Growth` [38, 39]. In our analysis we uncover a deviation of the growth index from its expected ΛCDM value of 0.55 when utilizing the Planck dataset, both in the `MGCAMB` case and in the `CAMB_GammaPrime_Growth` case, but in opposite directions. This deviation is accompanied by a change in the direction of correlations with derived cosmological parameters. However, the incorporation of CMB lensing data helps reconcile γ_L with its ΛCDM value in both cases. Conversely, the alternative ground-based telescopes ACT and SPT consistently yield growth index values in agreement with $\gamma_L = 0.55$. We conclude that the presence of the $A_{\rm lens}$ problem in the Planck dataset contributes to the observed deviations, underscoring the importance of additional datasets in resolving these discrepancies.

IV.A Introduction

The standard model of cosmology embodies the most universally accepted concordance model for both astrophysical and cosmological regimes within an isotropic and homogeneous Universe [98, 99]. In this model, cold dark matter (CDM) acts as a stabilizing agent for galaxies and their clusters [100–102], while the late-time accelerating expansion of the Universe is sourced by a cosmological constant Λ [103, 104]. In this scenario, initial cosmic inflation drove the early Universe towards flatness that observes the cosmological principle [105, 106]. However, challenges persist within this framework. The cosmological constant continues to pose theoretical difficulties [107, 108], while the direct detection of CDM remains problematic [101, 102], and the UV completeness of the theory remains an open question [109]. In recent years, additional challenges to ΛCDM cosmology have emerged in the form of cosmic tensions. These tensions arise from discrepancies between direct measurements of the cosmic expansion rate and the growth of large scale structure (LSS), and those inferred indirectly from early Universe measurements [110–119].

The presence of cosmic tensions has become evident across multiple surveys, primarily manifested in the measurement of the Hubble constant, H_0, which has now exceeded 5σ [120–

123]. The indirect measurements of H_0 mainly rely on observations of the Cosmic Microwave Background radiation (CMB) with the latest reported value by the Planck collaboration giving $H_0 = 67.4 \pm 0.5\,\mathrm{km\,s^{-1}Mpc^{-1}}$ [23], while the last release from ACT puts $H_0 = 67.9 \pm 1.5\,\mathrm{km\,s^{-1}Mpc^{-1}}$ [55]. Conversely, late time probes offer several alternatives for the direct measurement of the Hubble expansion of the Universe. Among these, the most precise measurements are based on Type Ia Supernovae (SNIa) by the SH0ES Team, calibrated by Cepheids, yielding $H_0 = 73.04 \pm 1.04\,\mathrm{km\,s^{-1}Mpc^{-1}}$ [84]. Numerous other measurements also consistently favor higher values for the Hubble constant [124–131]. Finally, the latest measurements employing the Tip of the Red Giant Branch as a calibration method for SNIa continue to indicate elevated values for H_0 [132–135].

Another cosmological tension that is gaining significance relates to the growth of large-scale structures in the Universe. Several parameters capture these characteristics, with $S_8 = \sigma_{8,0}\sqrt{\Omega_{\mathrm{m},0}/0.3}$ being a key quantity that incorporates the matter density parameter at present $\Omega_{\mathrm{m},0}$ and is commonly used to quantify it, as it is directly measured by Weak Lensing (WL) experiments. The measurement of S_8 is more challenging, with discrepancies between early- and late-time probes ranging from $2-3.5\sigma$, but it still plays a crucial role in testing the validity of ΛCDM cosmology. Recent measurements from the Kilo-Degree Survey (KiDS-1000) report a lower value of $S_8 = 0.766^{+0.020}_{-0.014}$ [136], which is consistent with other WL measurements such as DES-Y3 [137] and HSC-Y3 [138]. On the other hand, Planck (TT,TE,EE+lowE) gives $S_8 = 0.834 \pm 0.016$ [23] which agrees with other CMB based measurements of this parameter [55, 56].

The presence of cosmic tensions has spurred numerous re-evaluations in the scientific community, leading to more rigorous investigations of potential systematic errors [115, 117, 139]. However, the persistence of these tensions across various direct and indirect measurements suggests that such explanations may be losing credibility. Consequently, alternative modifications to the standard model of cosmology have been proposed, encompassing a range of theoretical frameworks (see for example [109, 110, 114, 115, 140–147] and the references therein). This plethora of models that go beyond ΛCDM physics can be parametrized in numerous ways. By examining the phenomenological parameterization for the growth of linear matter perturbations $\delta_m = \delta\rho_m/\rho_m$ described in [95], the growth rate $G(a)$ can be approximately reformulated as $G(a) = f(a, \gamma_L, \Omega_{m,0})$, a time-dependent function f where the growth index γ_L can be seen as a fitting constant [148, 149] (discussed further in Sec. IV.B). This empirical formula gives a value of $\gamma_L \simeq 0.55$ for ΛCDM [95, 150].

This theoretical prediction for γ_L allows us to use this parameter as a testing tool for possible deviations from the concordance model of cosmology. In this work, we analyze this parameterization through the prism of the linear matter perturbation evolution Eqs.(IV.4-IV.5) defined in Sec. IV.B. In Sec. IV.C we include a discussion on the main differences in the implementation of γ_L in the two cosmological solvers considered in our study: `MGCAMB`

and `CAMB_GammaPrime_Growth`. In Sec. IV.D we discuss the data sets under investigation, along with the strategy that we followed to obtain the constraints on the $\Lambda\text{CDM} + \gamma_L$ model considered here, which are outlined in Sec. IV.E, where the outcomes of both approaches are compared. In particular, the results for `MGCAMB`'s scale-dependent approach is shown in paragraph IV.E.1, along with `CAMB_GammaPrime_Growth`'s scale-independent one in paragraph IV.E.2. Finally, the main results are summarized and discussed in Sec. IV.F.

IV.B Structure Formation and the Growth Index

The dynamics of the expansion of the Universe can be determined through the Friedmann equation:

$$\left(\frac{H}{H_0}\right)^2 = \sum_i \Omega_i \,, \tag{IV.2}$$

where $\Omega_i = \rho_i/\rho_c$ represents the relative density of each component with energy density ρ_i in a flat Universe where $\rho_c = 3H_0^2/(8\pi G_{GR})$, with G_{GR} being Newton's constant of gravitation in General Relativity (GR). Indeed we can use Eq.(IV.2) to constrain the observed accelerated expansion, but it has to reflect our ignorance of the fundamental nature of such acceleration. Since we do not know whether we are dealing with a physical energy density or rather a modification of the Friedmann equation with respect to the ΛCDM model, we can treat the accelerated expansion as stemming from an effective component with equation of state $w(a)$, rewriting Eq.(IV.2) as follows [148, 151]:

$$\left(\frac{H}{H_0}\right)^2 = \Omega_{\mathrm{m},0} a^{-3} + (1-\Omega_{\mathrm{m},0}) e^{3\int_0^{a'}[1+w(a')]d\ln a'} \,. \tag{IV.3}$$

However, background expansion alone cannot easily tell different cosmological theories apart, as functions like $w(a)$ can be tuned in different cosmologies to obtain the same time evolution for expansion history quantities such as $a(t)$ [95]. For this reason, in this paper we will assume a ΛCDM background; namely, $w(a) = -1$ in Eq.(IV.3).

Instead, we consider modifications to the growth of structure *only*. The evolution of the expansion rate feeds into the inhomogeneities that arise in the LSS due to early Universe gravitational instabilities and frictional terms. By investigating perturbations away from homogeneity and isotropy in both the gravitational and matter sectors, we can describe the

matter perturbation evolution equation as

$$\ddot{\delta}_m + 2H\dot{\delta}_m - 4\pi G_{\rm GR}\,\rho_m\delta_m = 0\,, \tag{IV.4}$$

where δ_m represents the gauge invariant fractional matter density, dots denote derivatives with respect to cosmic time, and where linear and subhorizon scales ($k \lesssim 0.1h\mathrm{Mpc}^{-1}$ and $k \gtrsim 0.0003h\mathrm{Mpc}^{-1}$ respectively, $h = H_0/100\,\mathrm{kms}^{-1}\mathrm{Mpc}^{-1}$) are being considered. A natural definition of the linear growth fraction for matter perturbations is $g(a) = \delta_m(a)/\delta_{m,0}$, where $\delta_{m,0}$ is the current value of δ_m. By taking a reparameterization of the matter perturbation evolution equation through the growth rate $G(a) = d\ln g(a)/d\ln a$, Eq. (IV.4) can be rewritten as [152]

$$\frac{dG}{d\ln a} + G^2 + \left(2 + \frac{1}{2}\frac{d\ln H^2}{d\ln a}\right)G - \frac{3}{2}G_{\rm eff}\Omega_{\rm m}(a) = 0\,, \tag{IV.5}$$

where $G_{\rm eff}$ is $G_{\rm MG}/G_{\rm GR}$, and $G_{\rm MG}$ is Newton's constant of gravitation for a generic deviation from GR. It was proposed in [95] that

$$G(a) = \Omega_{\rm m}^{\gamma_L}(a)\,, \tag{IV.6}$$

where $\gamma_L = \ln G/\ln\Omega_{\rm m}(a)$ is the *growth index*. A major advantage of this parameterization is its accuracy in replicating the numerical solution of Eq.(IV.5). For instance, in the framework of ΛCDM, the value $\gamma_L^{\Lambda\rm CDM} = 0.55$ can be as accurate as 0.05% [95].

An interesting approach considered in the literature has been to take the background Friedmann equations to be those of ΛCDM and to probe potential modifications away from the standard model at the level of γ_L [153–155]. In fact, for theories other than GR such as $f(R)$ and DGP braneworld cosmologies we get remarkably different values: $\gamma_L^{f(R)} = 0.42$ and $\gamma_L^{\rm DGP} = 0.68$ respectively [154]. A departure of γ_L from 0.55 would then represent a possible hint at new physics, offering us an opportunity to shed new light on the tensions afflicting the standard model of cosmology.

IV.C Mapping the growth index into observables: `MGCAMB` and `CAMB_GammaPrime_Growth`

To constrain the growth index γ_L, we first need a mean to map it into the CMB and LSS observables, where the latter are specifically probed by CMB lensing potentials in this work. Here, we adopt two different modifications of the standard Boltzmann solver `CAMB` [31, 32], namely `MGCAMB` [33–37] and `CAMB_GammaPrime_Growth` [38, 39]. Below, we briefly review the

main differences between the two approaches.

In the first approach, `MGCAMB` introduces the two scale- and redshift-dependent parameters $\mu(a,k)$ and $\eta(a,k)$, which fully describe the relations between the Ψ - Φ metric perturbations and the energy-momentum tensor of GR, as can be observed from Eqs. (5-9) in [34] (with $\eta = \mu = 1$ corresponding to GR and ΛCDM). Separating sub- and super-horizon evolutions of perturbations, `MGCAMB` then solves the two regimes separately [34]. `MGCAMB` maps γ_L into the function $\mu(a,k)$ through the following relation, valid for subhorizon perturbations [34, 35]:

$$\mu = \frac{2}{3}\Omega_{\rm m}^{\gamma_L - 1}\left[\Omega_{\rm m}^{\gamma_L} + 2 + \frac{H'}{H} + \gamma_L \frac{\Omega'_{\rm m}}{\Omega_{\rm m}} + \gamma'_L \ln(\Omega_{\rm m})\right]. \tag{IV.7}$$

Therefore, within `MGCAMB`, any change in γ_L is effectively a change in $\mu(a,k)$, where the latter appears in the evolution of both sub- and super-horizon perturbations, as described by Eqs. (16,17) and Eq. (21) of [34]. This choice implies that varying γ_L introduces a *scale-dependent* effect on observables such as the primary CMB angular power spectrum and the linear matter power spectrum. Ref. [34] demonstrated that, for a simple toy model where $\mu(a,k) = \mu(a)$, super-horizon changes in the linear matter power spectrum introduced by a varying $\mu(a)$ are within the cosmic variance. They thereby argued that Eq.(IV.7) and their approach to γ_L should be consistent with the (implicit) assumptions of scale-independence and subhorizon evolution by Eq.(IV.6). In practice, we however find that this is not necessarily the case for the (primary) CMB angular power spectrum. In Appendix A, we further show why this particular choice might explain the constraint on γ_L obtained by `MGCAMB` in paragraph IV.E.1.[IV.1]

The second code, `CAMB_GammaPrime_Growth` [38, 39, 158], adopts a phenomenological approach by rescaling the linear matter power spectrum $P(k)$, i.e.

$$P(\gamma_L, k, a) = P(k, a = 1)\, D^2(\gamma_L, a), \tag{IV.8}$$

by the (square of) the modified growth factor $D(\gamma_L, a)$ given by the numerical integral

$$D(\gamma_L, a) = \exp\left[-\int_a^1 da\, \frac{\Omega_{\rm m}^{\gamma_L}(a)}{a}\right]. \tag{IV.9}$$

For the CMB observables and data considered in this work, Eqs.(IV.8,IV.9) only affect the CMB lensing potential through the matter transfer function (see, e.g. Eqs. (9)-(14) in [159]). We will return to this point in Appendix A where we compare this approach by `CAMB_GammaPrime_Growth` versus that by `MGCAMB`, and their respective constraints on γ_L using Planck(+lensing) data.

[IV.1] See also Ref. [156, 157] for previous analyses with Planck data.

IV.D Datasets and Methodology

Together with the growth index γ_L defined in Sec. IV.B, we constrained the six parameters of the base ΛCDM model. The parameter space constrained here is therefore $\Gamma \equiv \{\Omega_{\rm b}h^2, \Omega_{\rm c}h^2, 100\theta_{\rm MC}, \tau_{\rm reio}, n_{\rm s}, \log(10^{10}A_{\rm s}), \gamma_L\}$, where $\Omega_b h^2$, the baryon density Ω_b combined with the dimensionless Hubble constant h, $\Omega_c h^2$, the density of cold dark matter combined with h, $100\theta_{MC}$, where θ_{MC} is an approximation of the observed angular size of the sound horizon at recombination, $\tau_{\rm reio}$, the reionization optical depth, n_s and $\log(10^{10}A_{\rm s})$, respectively the spectral index and amplitude $A_{\rm s}$ of the power spectrum of the scalar primordial perturbations.

We constrained the ΛCDM+γ_L model considered here with two different methods:

- Firstly, we used `MGCosmoMC` [33–37], a publicly available modification of the popular MCMC code `CosmoMC` [92, 160] that samples γ_L through the fast-slow dragging algorithm developed in [161]. The Einstein-Boltzmann solver implemented in `MGCosmoMC` to calculate CMB anisotropies and lensing power spectra is `MGCAMB` [33–37], a patch of the `CAMB` code [31] that includes several phenomenological modifications to the growth of matter perturbations, including the γ_L parameterization in Eq.(IV.6).

- Additionally, we implemented the modified version of `CAMB`, namely `CAMB_GammaPrime_Growth`, introduced in [38, 39, 158] into `CosmoMC`. While [38, 39, 158] also modify linear growth through the parameterization shown in Eq.(IV.6), they take γ_L to be scale-independent compared to `MGCAMB`.

The data considered in our analysis have been taken from the following datasets:

- the final release of the Planck mission [23, 51, 162], specifically the likelihoods and data for the CMB temperature and polarization anisotropies: TT, EE and TE (referred to, here, as *Planck*), along with the lensing reconstruction power spectrum (referred to as *lensing*);

- the likelihoods and data from the 9-years release (DR9) of the Wilkinson Microwave Anisotropy Probe (*WMAP*) [50];

- the likelihoods for the polarization and temperature anisotropies spectra from Atacama Cosmology Telescope's DR4 (*ACT*) [54];

- the EE and TE anisotropies measurements and likelihoods from the SPT-3G instrument of the South Pole Telescope (*SPT*) [57];

Parameter	**Prior**
$\Omega_{\rm b}h^2$	$[0.005, 0.1]$
$\Omega_{\rm c}h^2$	$[0.001, 0.99]$
$100\theta_{\rm MC}$	$[0.5, 10]$
$\tau_{\rm reio}$	0.065 ± 0.015
$n_{\rm s}$	$[0.8, 1.2]$
$\log(10^{10}A_{\rm s})$	$[1.61, 3.91]$
γ_L	$[0, 1]$

TABLE IV.1. A summary of the priors imposed on the parameters for the ΛCDM+γ_L model considered in our analysis.

- the final measurements from the SDSS survey by the eBOSS collaboration, of which we include Baryonic Acoustic Oscillations (BAO) data [76].

In particular, we constrained Γ with the following combinations:

- Planck, Planck+BAO, Planck+lensing, and Planck+BAO+lensing;
- ACT, ACT+WMAP, ACT+BAO and ACT+WMAP+BAO;
- SPT, SPT+WMAP, SPT+BAO and SPT+WMAP+BAO.

We note that all the constraints obtained using either the ACT or SPT data employed a Gaussian prior on $\tau_{reio} = 0.065 \pm 0.015$, as done by the ACT collaboration [54]; the other six parameters making up the ΛCDM+γ_L model considered here were all assumed to have flat priors, as summarised in Tab. IV.1 .

The convergence of the chains produced from the exploration of Γ by `MGCosmoMC/CosmoMC` for this analysis was evaluated through the Gelman-Rubin criterion [163], and we took $R \leq 0.02$ as a satisfactory limit at which to present the results outlined in Sec. IV.E.

Finally, to demonstrate that a Planck-like CMB only experiment is able to recover $\gamma_L = 0.55$ without bias, we constrained Γ using a mock Planck-like dataset generated according to a ΛCDM model defined by the parameter choices given in Tab. IV.2. The results are shown in Tab. IV.3, and we can see that CMB only data are able to recover $\gamma_L = 0.55$ with good accuracy with either `MGCAMB` or `CAMB_GammaPrime_Growth`.

Parameter	Fiducial Values
$\Omega_{\rm b}h^2$	0.02236
$\Omega_{\rm c}h^2$	0.1202
$100\theta_{\rm MC}$	1.04090
$\tau_{\rm reio}$	0.0544
$n_{\rm s}$	0.9649
$\log(10^{10}A_{\rm s})$	3.044

TABLE IV.2. The ΛCDM baseline values chosen to simulate mock Planck-like dataset used for the results of Tab. IV.3.

Parameter	`MGCAMB`	`CAMB_GammaPrime_Growth`
$\Omega_{\rm b}h^2$	0.02237 ± 0.00015	0.02236 ± 0.00016
$\Omega_{\rm c}h^2$	0.1201 ± 0.0016	0.1202 ± 0.0017
$100\theta_{\rm MC}$	1.04091 ± 0.00036	1.04089 ± 0.00036
$\tau_{\rm reio}$	0.0538 ± 0.0097	0.053 ± 0.010
$n_{\rm s}$	0.9650 ± 0.0041	0.9649 ± 0.0043
$\log(10^{10}A_{\rm s})$	3.044 ± 0.019	3.043 ± 0.021
γ_L	$0.544^{+0.035}_{-0.021}$	0.56 ± 0.10

TABLE IV.3. Results for the Planck-like dataset.

IV.E Results

In this section we are discussing the constraints we obtained for the dataset combinations listed in Sec. IV.D and the two different approaches explained in Sec. IV.C. In particular we will discuss in paragraph IV.E.1 the scale-dependent case as implemented in `MGCAMB`, and in paragraph IV.E.2 the scale-independent linear growth as implemented in `CAMB_GammaPrime_Growth`.

IV.E.1 `MGCAMB` Results

We show in Tab. IV.4 the constraints at 68% CL for the scale-dependent case as implemented in `MGCAMB` for the different combinations involving the Planck data, and we repeat the same for ACT in Tab. IV.5 and SPT in Tab. IV.6. We display instead the 1D posterior distributions and the 2D contour plots for all these cases in Tab. IV.1 and Tab. IV.2.

The analysis presented in Tab. IV.4 reveals a notable deviation from the expected value of $\gamma_L = 0.55$ considering the measurement obtained solely from Planck observations. Specifically, Planck indicates a value of $\gamma_L = 0.467^{+0.018}_{-0.029}$, deviating from the expected value by more than 3 standard deviations. However, it is important to note that this parameter does not contribute significantly to resolving the cosmological tensions. While it exhibits a slight

Parameter	**Planck**	**Planck+BAO**	**Planck+lensing**	**Planck+BAO+lensing**
$\Omega_{\rm b}h^2$	0.02253 ± 0.00016	0.02250 ± 0.00016	0.02249 ± 0.00016	0.02246 ± 0.00015
$\Omega_{\rm c}h^2$	0.1187 ± 0.0015	0.1190 ± 0.0013	0.1186 ± 0.0014	0.1189 ± 0.0012
$100\theta_{\rm MC}$	1.04110 ± 0.00032	1.04106 ± 0.00032	1.04107 ± 0.00032	1.04103 ± 0.00030
τ_{reio}	0.0510 ± 0.0085	0.0507 ± 0.0082	$0.0496^{+0.0087}_{-0.0073}$	$0.0490^{+0.0083}_{-0.0073}$
$n_{\rm s}$	0.9688 ± 0.0047	0.9681 ± 0.0045	0.9684 ± 0.0046	0.9675 ± 0.0042
$\log(10^{10}A_{\rm s})$	3.034 ± 0.018	3.034 ± 0.017	$3.030^{+0.018}_{-0.015}$	3.030 ± 0.017
γ_L	$0.467^{+0.018}_{-0.029}$	$0.469^{+0.017}_{-0.029}$	0.506 ± 0.022	$0.509^{+0.022}_{-0.020}$
H_0	68.02 ± 0.66	67.86 ± 0.60	68.00 ± 0.64	67.84 ± 0.57
S_8	0.839 ± 0.015	0.842 ± 0.015	0.824 ± 0.013	0.827 ± 0.012

TABLE IV.4. Constraints at 68% CL for the scale-dependent case as implemented in `MGCAMB`, considering the dataset combinations with Planck.

Parameter	**ACT**	**ACT+BAO**	**ACT+WMAP**	**ACT+WMAP+BAO**
$\Omega_{\rm b}h^2$	0.02153 ± 0.00032	0.02148 ± 0.00030	0.02239 ± 0.00021	0.02237 ± 0.00019
$\Omega_{\rm c}h^2$	0.1177 ± 0.0049	0.1200 ± 0.0025	0.1198 ± 0.0027	0.1203 ± 0.0020
$100\theta_{\rm MC}$	1.04229 ± 0.00078	1.04210 ± 0.00065	1.04174 ± 0.00066	1.04171 ± 0.00062
τ_{reio}	0.064 ± 0.015	0.065 ± 0.015	0.060 ± 0.012	0.060 ± 0.012
$n_{\rm s}$	1.008 ± 0.017	1.003 ± 0.014	0.9729 ± 0.0062	0.9722 ± 0.0052
$\log(10^{10}A_{\rm s})$	3.049 ± 0.034	3.056 ± 0.033	$3.062^{+0.025}_{-0.022}$	$3.064^{+0.025}_{-0.022}$
γ_L	$0.552^{+0.063}_{-0.087}$	$0.580^{+0.062}_{-0.078}$	$0.533^{+0.044}_{-0.018}$	$0.536^{+0.040}_{-0.018}$
H_0	68.0 ± 2.0	67.0 ± 1.0	67.7 ± 1.1	67.50 ± 0.83
S_8	0.829 ± 0.045	0.847 ± 0.028	0.843 ± 0.031	0.848 ± 0.025

TABLE IV.5. Constraints at 68% CL for the scale-dependent case as implemented in `MGCAMB`, considering the dataset combinations with ACT.

correlation with H_0, resulting in a modest increase of only 1σ in its value ($H_0 = 68.02 \pm 0.66$ km/s/Mpc), it does not exhibit any correlation with S_8 (see Fig. IV.1). Notably, the disagreement between WL measurements (which assume a ΛCDM model) and S_8 persists, further emphasizing the unresolved tensions in the current cosmological framework. Even when incorporating BAO data, the same conclusion holds true. The inclusion of BAO data does not alter the constraints on γ_L and S_8, but it does lead to a slight decrease in the estimated

Parameter	**SPT**	**SPT+BAO**	**SPT+WMAP**	**SPT+WMAP+BAO**
$\Omega_{\rm b}h^2$	0.02238 ± 0.00033	0.02237 ± 0.00032	0.02264 ± 0.00023	0.02259 ± 0.00021
$\Omega_{\rm c}h^2$	0.1175 ± 0.0057	0.1186 ± 0.0026	0.1153 ± 0.0028	0.1171 ± 0.0020
$100\theta_{\rm MC}$	1.03945 ± 0.00081	1.03933 ± 0.00069	1.03973 ± 0.00066	1.03954 ± 0.00064
τ_{reio}	0.065 ± 0.015	0.066 ± 0.015	0.060 ± 0.013	0.058 ± 0.013
$n_{\rm s}$	0.991 ± 0.025	0.987 ± 0.019	0.9733 ± 0.0075	0.9709 ± 0.0067
$\log(10^{10}A_{\rm s})$	3.040 ± 0.039	3.043 ± 0.038	3.041 ± 0.025	3.042 ± 0.026
γ_L	$0.622^{+0.075}_{-0.11}$	$0.635^{+0.063}_{-0.084}$	$0.556^{+0.023}_{-0.018}$	$0.558^{+0.024}_{-0.018}$
H_0	67.8 ± 2.3	67.3 ± 1.0	68.9 ± 1.2	68.11 ± 0.83
S_8	0.796 ± 0.048	0.804 ± 0.028	0.782 ± 0.032	0.801 ± 0.025

TABLE IV.6. Constraints at 68% CL for the scale-dependent case as implemented in `MGCAMB`, considering the dataset combinations with SPT.

value of H_0. However, a more significant impact is observed when including the lensing dataset. Specifically, with Planck+lensing the constraint on γ_L becomes $\gamma_L = 0.506 \pm 0.022$, reducing the tension with the expected value to 2σ. Furthermore, a mild correlation emerges between the γ_L parameter and the S_8 parameter (see Fig. IV.1). This correlation causes the mean value of S_8 to shift downward by 1 standard deviation, albeit not sufficiently enough to alleviate the existing S_8 tension. Once again, the inclusion of BAO data does not change the results, so that Planck+BAO+lensing gives similar constraints to the Planck+lensing combination.

A different picture emerges when the ground based CMB telescope ACT is taken into account in Tab. IV.5. In this case, the value of γ_L remains consistently within 1 standard deviation of the expected value across all dataset combinations, including also BAO and WMAP data. Furthermore, by referring to Fig. IV.1 and Fig. IV.2, we observe a change: the correlation between γ_L and other cosmological parameters disappears upon inclusion of the ACT data.

Similarly, when the SPT data are analyzed in Tab. IV.6 we observe that across all combinations of datasets γ_L is always in agreement within 1σ with $\gamma_L = 0.55$. In particular, when considering SPT data alone, or in combination with BAO data, higher values of γ_L are favored with larger error bars. However, upon including the WMAP dataset, the mean value of γ_L returns to $\gamma_L = 0.55$. Similar to the previous analysis, no correlation is observed between γ_L and the derived parameters depicted in Fig. IV.1 and Fig. IV.2 when examining this dataset.

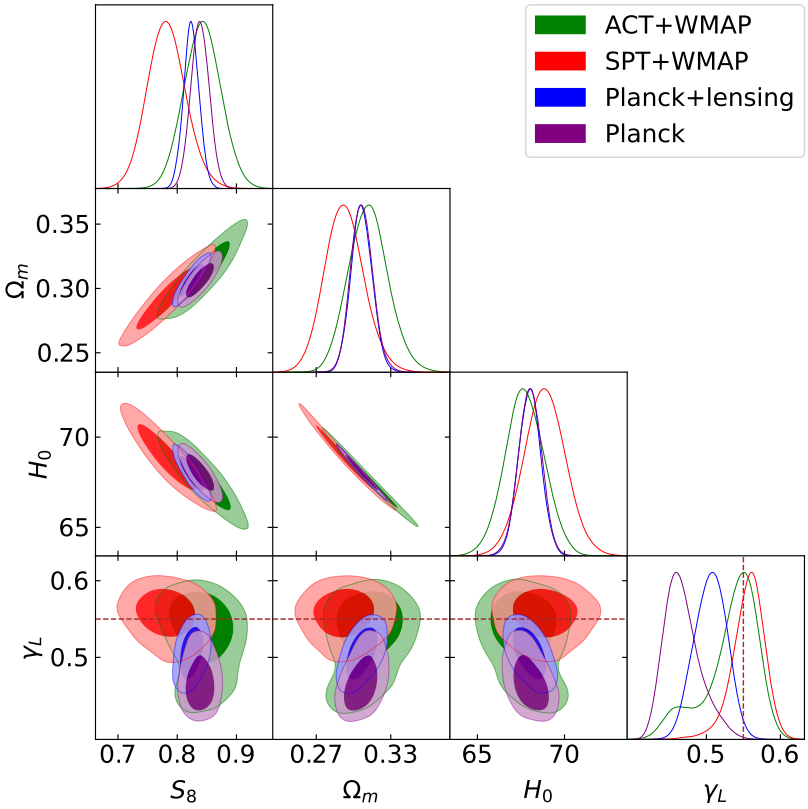


FIG. IV.1. 1D marginalized posterior distributions and 2D contour plots for the different CMB data combinations explored in this work, without the inclusion of the BAO data, for the scale-dependent case as implemented in `MGCAMB`. The dashed brown line in the plot is the value of the growth index in ΛCDM, $\gamma_L = 0.55$.

IV.E.2 `CAMB_GammaPrime_Growth` Results

The constraints at a confidence level of 68% CL for the `CAMB_GammaPrime_Growth` case as implemented in [38, 39, 158], are presented in Tab. IV.7, for the various combinations involving Planck data. Similarly, we provide the corresponding constraints for ACT in Tab. IV.8 and for SPT in Tab. IV.9. To further illustrate these cases, we present the 1D posterior distributions and the 2D contour plots in Fig. IV.3 and Fig. IV.4.

The examination of Tab. IV.7 reveals a significant deviation from the expected value of $\gamma_L = 0.55$ when considering the measurement based solely on Planck observations. Specifically, Planck indicates a value of $\gamma_L = 0.841^{+0.11}_{-0.074}$, surpassing the expected value by more than 3σ. However, it is worth noting that while this parameter does not contribute significantly to resolving the H_0 tension, it can substantially decrease the value of the S_8 parameter in the right direction to agree with the WL measurements (which assume a ΛCDM model). In fact, contrarily to the `MGCAMB` case, γ_L exhibits a slight correlation with both H_0 and S_8 (see

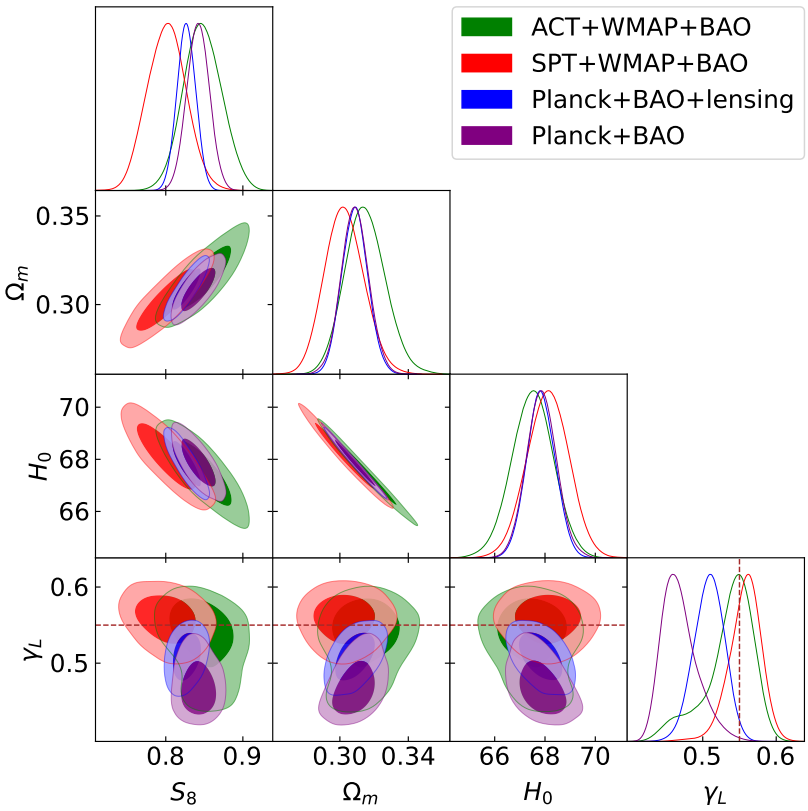


FIG. IV.2. 1D marginalized posterior distributions and 2D contour plots for the different CMB+BAO data combinations explored in this work, for the scale-dependent case as implemented in `MGCAMB`. The dashed brown line in the plot is the value of the growth index in ΛCDM, $\gamma_L = 0.55$.

Parameter	**Planck**	**Planck+BAO**	**Planck+lensing**	**Planck+BAO+lensing**
$\Omega_{\rm b}h^2$	0.02258 ± 0.00016	0.02255 ± 0.00016	0.02251 ± 0.00017	0.02248 ± 0.00016
$\Omega_{\rm c}h^2$	0.1181 ± 0.0015	0.1186 ± 0.0013	0.1183 ± 0.0015	0.1188 ± 0.0013
$100\theta_{\rm MC}$	1.04113 ± 0.00032	1.04108 ± 0.00031	1.04109 ± 0.00032	1.04103 ± 0.00032
$\tau_{\rm reio}$	$0.0496^{+0.0087}_{-0.0074}$	0.0495 ± 0.0084	$0.0493^{+0.0087}_{-0.0074}$	$0.0488^{+0.0086}_{-0.0075}$
$n_{\rm s}$	0.9709 ± 0.0047	0.9696 ± 0.0045	0.9696 ± 0.0048	0.9683 ± 0.0044
$\log(10^{10}A_{\rm s})$	3.030 ± 0.017	3.031 ± 0.018	$3.029^{+0.018}_{-0.016}$	$3.029^{+0.018}_{-0.016}$
γ_L	$0.841^{+0.11}_{-0.074}$	$0.831^{+0.11}_{-0.080}$	0.669 ± 0.069	0.658 ± 0.063
H_0	68.27 ± 0.69	68.06 ± 0.61	68.14 ± 0.70	67.92 ± 0.61
S_8	0.805 ± 0.018	0.810 ± 0.017	0.807 ± 0.019	0.812 ± 0.017

TABLE IV.7. Constraints at 68% CL for the `CAMB_GammaPrime_Growth` case as implemented in [38, 39, 158], considering the dataset combinations with Planck.

Parameter	**ACT**	**ACT+BAO**	**ACT+WMAP**	**ACT+WMAP+BAO**
$\Omega_{\rm b}h^2$	0.02151 ± 0.00031	0.02149 ± 0.00031	0.02236 ± 0.00021	0.02235 ± 0.00020
$\Omega_{\rm c}h^2$	0.1185 ± 0.0050	0.1199 ± 0.0026	0.1205 ± 0.0030	0.1206 ± 0.0022
$100\theta_{\rm MC}$	1.04221 ± 0.00077	1.04205 ± 0.00065	1.04168 ± 0.00066	1.04164 ± 0.00060
τ_{reio}	0.065 ± 0.015	0.065 ± 0.015	0.062 ± 0.013	0.061 ± 0.013
$n_{\rm s}$	1.007 ± 0.017	1.003 ± 0.014	0.9722 ± 0.0066	0.9720 ± 0.0055
$\log(10^{10}A_{\rm s})$	3.053 ± 0.034	3.057 ± 0.032	3.067 ± 0.026	3.067 ± 0.026
γ_L	0.52 ± 0.18	0.49 ± 0.15	0.50 ± 0.16	0.50 ± 0.14
H_0	67.7 ± 2.0	67.1 ± 1.0	67.4 ± 1.3	67.39 ± 0.89
S_8	0.839 ± 0.059	0.855 ± 0.032	0.847 ± 0.036	0.848 ± 0.027

TABLE IV.8. Constraints at 68% CL for the `CAMB_GammaPrime_Growth` case as implemented in [38, 39, 158], considering the dataset combinations with ACT.

Parameter	**SPT**	**SPT+BAO**	**SPT+WMAP**	**SPT+WMAP+BAO**
$\Omega_{\rm b}h^2$	0.02241 ± 0.00033	0.02238 ± 0.00031	0.02259 ± 0.00024	0.02253 ± 0.00022
$\Omega_{\rm c}h^2$	0.1164 ± 0.0056	0.1183 ± 0.0026	0.1167 ± 0.0032	0.1178 ± 0.0021
$100\theta_{\rm MC}$	1.03953 ± 0.00081	1.03935 ± 0.00067	1.03955 ± 0.00071	1.03942 ± 0.00064
τ_{reio}	0.065 ± 0.015	0.065 ± 0.015	0.062 ± 0.013	0.061 ± 0.013
$n_{\rm s}$	0.994 ± 0.024	0.989 ± 0.019	0.9709 ± 0.0080	0.9687 ± 0.0068
$\log(10^{10}A_{\rm s})$	3.035 ± 0.039	3.040 ± 0.035	3.049 ± 0.027	3.051 ± 0.027
γ_L	0.46 ± 0.19	0.41 ± 0.15	0.43 ± 0.14	0.41 ± 0.13
H_0	$68.3^{+2.1}_{-2.4}$	67.4 ± 1.0	68.3 ± 1.4	67.77 ± 0.89
S_8	0.803 ± 0.064	0.824 ± 0.032	0.802 ± 0.039	0.815 ± 0.027

TABLE IV.9. Constraints at 68% CL for the `CAMB_GammaPrime_Growth` case as implemented in [38, 39, 158], considering the dataset combinations with SPT.

Fig. IV.3), giving $H_0 = 68.27 \pm 0.69$ km/s/Mpc and $S_8 = 0.805 \pm 0.018$. It is important to emphasize that in the `CAMB_GammaPrime_Growth` case, there are two notable distinctions. Firstly, the preferred value of γ_L deviates from the expected value in the opposite direction compared to the `MGCAMB` case. Secondly, the correlations between γ_L, H_0, and S_8 exhibit a change in sign. However, as we noted in the previous section as well, the inclusion of the CMB

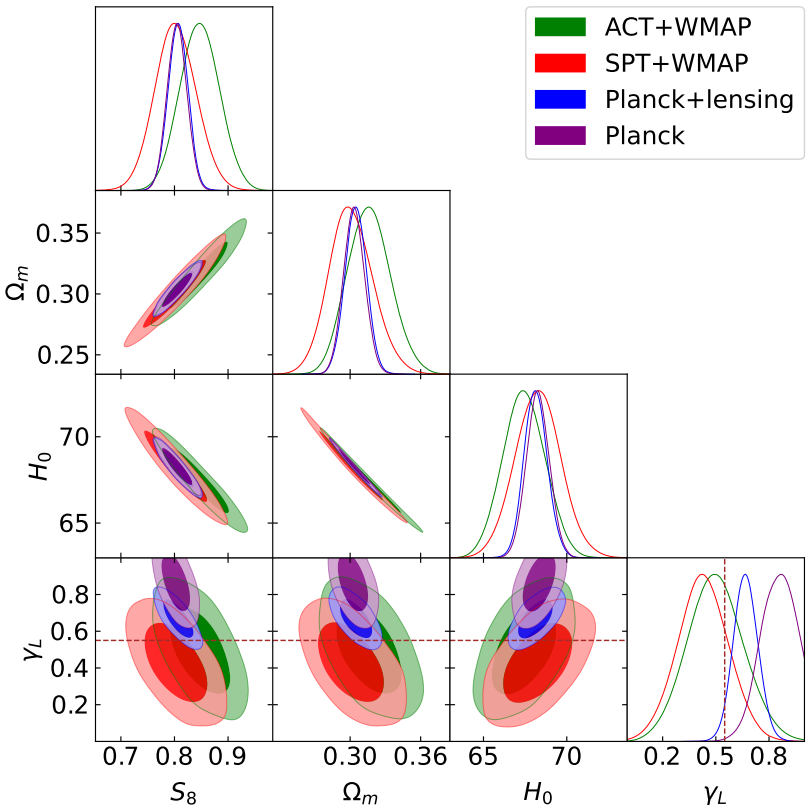


FIG. IV.3. 1D marginalized posterior distributions and 2D contour plots for the different CMB data combinations explored in this work, without the inclusion of the BAO data, for the `CAMB_GammaPrime_Growth` case as implemented in [38, 39, 158]. The dashed brown line in the plot is the value of the growth index in ΛCDM, $\gamma_L = 0.55$.

lensing dataset is crucial to shift the value of γ_L towards the expected $\gamma_L = 0.55$, reducing the disagreement at the level of 1.7σ. In particular we obtain $\gamma_L = 0.669 \pm 0.069$, in perfect agreement with [38], while leaving both H_0 and S_8 unaffected. Finally, the addition of the BAO data does not have a significant impact on either the Planck+BAO combination or the Planck+BAO+lensing combination.

If we now consider the independent CMB measurements obtained from ACT displayed in Tab. IV.8 we observe a similar pattern as in the previous section. Notably, γ_L returns to agree within 1σ with the expected value $\gamma_L = 0.55$. In this case the addition of BAO and WMAP data does not alter these conclusions. In this particular dataset combination, γ_L exhibits a negative correlation with S_8 and a positive degeneracy with H_0. However, their mean values remain robust and align with the values expected in a ΛCDM model, in absence of deviations in γ_L from 0.55. The same conclusions about constraints and parameter degeneracies remain valid when replacing ACT with SPT, as demonstrated in Tab. IV.9.

In conclusion, the observed deviation of γ_L when analyzing the Planck data can be attributed

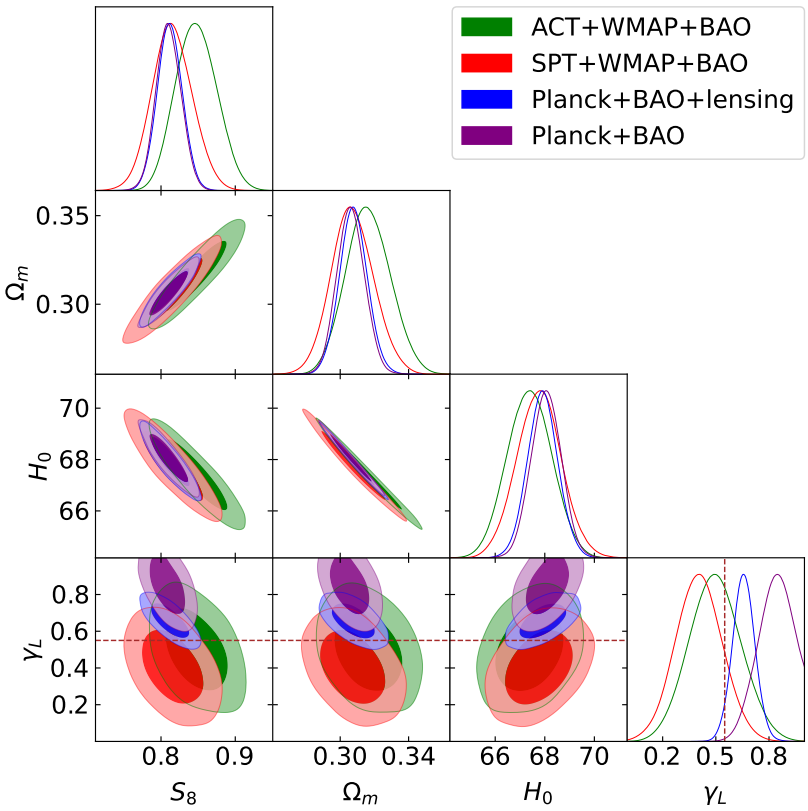


FIG. IV.4. 1D marginalized posterior distributions and 2D contour plots for the different CMB+BAO data combinations explored in this work, for the `CAMB_GammaPrime_Growth` case as implemented in [38, 39, 158]. The dashed brown line in the plot is the value of the growth index in ΛCDM, $\gamma_L = 0.55$.

to the presence of the $A_{\rm lens}$ problem [23, 164, 165], as highlighted in [38]. This problem refers to the excess of lensing detected in the temperature power spectrum, which is also associated with indications of a closed Universe [23, 166, 167]. The mitigation of the γ_L deviation from 0.55 upon incorporating the CMB lensing data serves as direct evidence supporting this interpretation.

IV.F Conclusions

We investigated the growth index γ_L, which characterizes the growth of linear matter perturbations in the form shown in Eq.(IV.6), by using different cosmological datasets, and comparing two approaches for the implementation of γ_L into `CAMB`: the `MGCAMB` and `CAMB_GammaPrime_Growth` codes.

Our analysis in the `MGCAMB` case revealed a γ_L that deviates from its ΛCDM value of 0.55,

preferring instead lower values and indicating a discrepancy of more than 3 standard deviations. However, incorporating the CMB lensing dataset helps reduce this disagreement to approximately 2 standard deviations.
In the `CAMB_GammaPrime_Growth` case instead, the preferred value of γ_L differs from the `MGCAMB` case, and exceeds the expected value in the opposite direction, producing a change of sign of the correlations with H_0 and S_8. Similarly to `MGCAMB`, for the `CAMB_GammaPrime_Growth` case the CMB lensing dataset helps in reconciling γ_L with the expected 0.55 value.
Moreover, the analysis of the ACT and SPT datasets shows consistent agreement of γ_L with the expected value within 1 standard deviation across various dataset combinations, and the addition of BAO data has minimal impact on the constraints and parameter correlations in both the `MGCAMB` and `CAMB_GammaPrime_Growth` cases.
Given these facts, we can attribute the deviation of γ_L observed in the Planck dataset to the $A_{\rm lens}$ problem (as already noticed in [38]) characterized by excess lensing in the temperature power spectrum.
Overall, these findings highlight the importance of considering additional datasets, such as CMB lensing, and other experiments, such as ACT and SPT, when tackling apparent discrepancies with the standard model, such as the deviations of γ_L encountered in this work.

IV.G Acknowledgments

This article is based upon work from COST Action CA21136 Addressing observational tensions in cosmology with systematics and fundamental physics (CosmoVerse) supported by COST (European Cooperation in Science and Technology). We would like to thank the referee for their constructive feedback and helpful comments. We acknowledge IT Services at The University of Sheffield for the provision of services for High Performance Computing. The `MGCAMB-CAMB_GammaPrime_Growth` code verification and comparison was performed on the Great Lakes HPC cluster, maintained by the Advanced Research Computing division, UofM Information and Technology Service. We further thank Dragan Huterer, Levon Pogosian, Alessandra Silvestri and Zhuangfei (Xavier) Wang for helpful discussions related to `MGCAMB` and their implementation of γ_L. EDV is supported by a Royal Society Dorothy Hodgkin Research Fellowship. MN acknowledges support from the Leinweber Center for Theoretical Physics, the NASA grant under contract 19-ATP19-0058, and the DOE under contract DE-FG02-95ER40899. JLS would also like to acknowledge funding from "The Malta Council for Science and Technology" as part of the REP-2023-019 (CosmoLearn) Project.

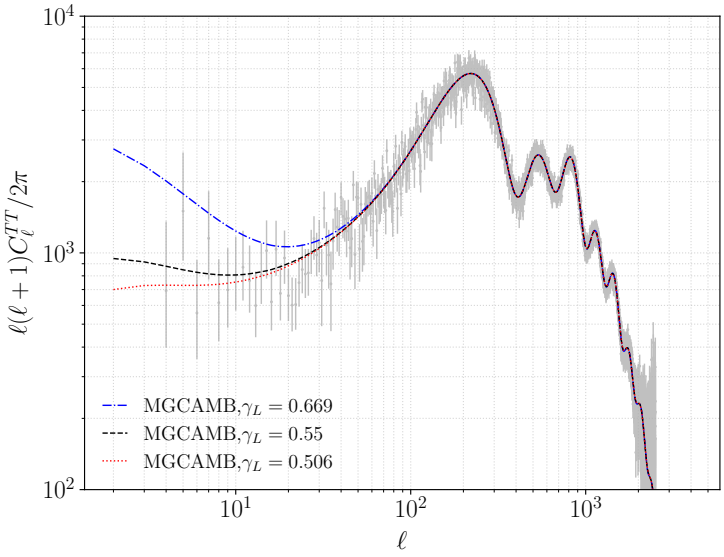


FIG. IV.5. The *unlensed* CMB TT angular power spectrum as predicted by `MGCAMB` at the same best-fit Planck 2018 cosmology, but for different values of γ_L. Blue and red lines correspond to the cases of $\gamma_L = 0.669$ and $\gamma_L = 0.506$ – the mean of γ_L constraints reported in the "Planck+lensing" columns in Tab. IV.4 and Tab. IV.7 – respectively. The black line denotes the GR case of $\gamma_L = 0.550$. The Planck 2018 measurements and their associated uncertainties are shown as grey points with error bars.

Appendix A: CMB observables in `MGCAMB` and `CAMB_GammaPrime_Growth`

In this appendix, we provide a direct comparison between the CMB observables as produced by the two codes: `MGCAMB` and `CAMB_GammaPrime_Growth`. Our aim is to understand the difference between their CMB predictions, which in turn drives the difference in their constraints on γ_L. We therefore examine a) the primary, i.e. unlensed, CMB temperature-temperature (TT) angular power spectrum $C_\ell^{\rm TT}$ and b) the CMB lensing potential angular power spectrum $C_\ell^{\phi\phi}$. We focus on the Planck(+lensing) dataset(s) and likelihood(s) as our case study. Unless explicitly stated otherwise, we adopt the best-fit base-ΛCDM cosmology in [23], specifically the "`Plik` best fit" column in their Table 1, for the following comparison.

Let us first investigate the *unlensed* CMB TT angular power spectrum as an example of primary CMB observables in the two codes. As discussed in Sec.IV.C, with `MGCAMB`, changes in γ_L do imply changes in primary CMB observables. Specifically, the variation is significant in the low-ℓ regime, as shown in Fig.IV.5. On the other hand, with `CAMB_GammaPrime_Growth`, no change in γ_L would alter the primary CMB observables, including the TT angular power spectrum. This is illustrated in Fig.IV.6.

Next, we look at the CMB lensing potentials, which should be sensitive to variations of

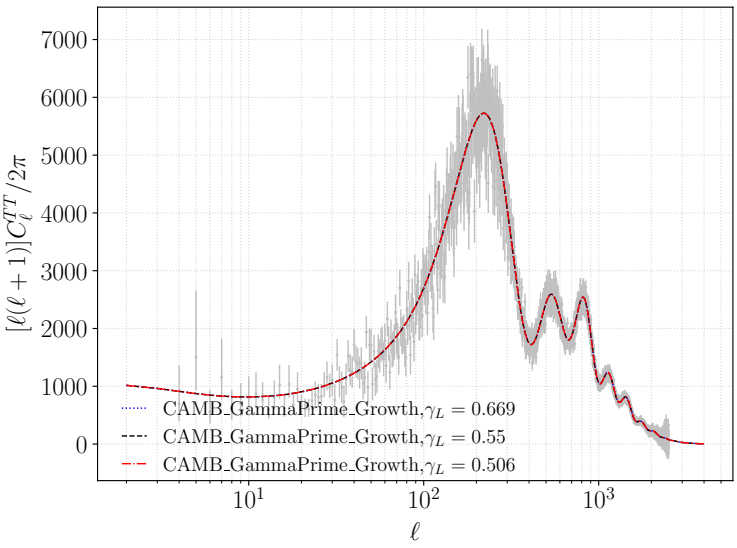


FIG. IV.6. Same as Fig.IV.5, but using `CAMB_GammaPrime_Growth`.

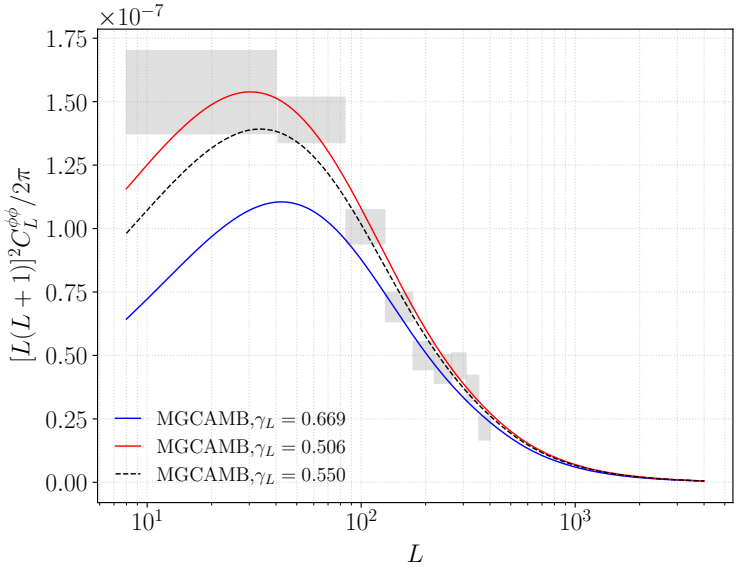


FIG. IV.7. The CMB lensing potential angular power spectrum as predicted by `MGCAMB` at the same best-fit Planck 2018 cosmology, for the same values of γ_L in Figs.IV.5,IV.6 (following the same color notation). The Planck 2018 minimum-variance (conservative) estimates of the CMB lensing potential bandpowers and their associated uncertainties are shown as grey boxes.

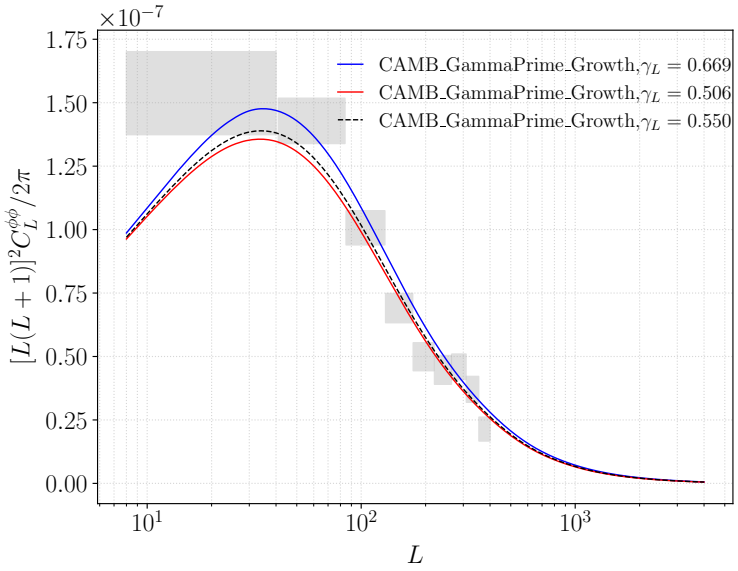


FIG. IV.8. Same as Fig.IV.7, but using `CAMB_GammaPrime_Growth`. As explained in Sec.IV.C, with `CAMB_GammaPrime_Growth`, no change in γ_L would alter the primary CMB observables, including the TT angular power spectrum.

γ_L in both codes. Comparing Figs.IV.7,IV.8 and the Planck 2018 CMB lensing potential angular power spectrum [52], it is evident why `MGCAMB` prefers $\gamma_L = 0.506$ while `CAMB_GammaPrime_Growth` prefers $\gamma_L = 0.669$. Both preferences are driven by the fit to the estimated $C_\ell^{\phi\phi}$. Upon further investigation with `MGCAMB` authors[IV.2], we have isolated and attributed the anomalous low-ℓ behavior in $C_\ell^{\phi\phi}$ from `MGCAMB` to a spurious early integrated Sachs-Wolfe (ISW) contribution from a term that contains a time-derivative instance of the modified-gravity parameter μ, i.e. $\dot{\mu}$. As pointed out and discussed in the main text, around Eq.(IV.7), and in this appendix, this early ISW contribution significantly alters the CMB power spectra on super-horizon scales. That, in turn, shifts the data preference for γ_L. As this feature was only discovered recently, we caution the community to use `MGCAMB` with the γ_L parameterization until a fix is released. We note that other modified-gravity parameterizations in `MGCAMB`, which in fact are what `MGCAMB` was originally intended for and recommended by `MGCAMB` authors themselves[IV.3], are still self-consistent and should be employed instead.

Finally, we have verified that adopting either best-fit cosmologies obtained by `MGCAMB` or `CAMB_GammaPrime_Growth` with "Planck+lensing" data sets (instead of "Plik best fit") does not affect our conclusions from this comparison.

[IV.2] Private communication.
[IV.3] Private communication.

Afterword

As this might have gone understated in the paper just presented, we stress here that a rather important technical rather than physical conclusion from this work is that the two codes analysed, `CAMB_GammaPrime_Growth` and `MGCAMB`, are essentially incompatible as far as the γ parametrisation is concerned, and that the difference in their predictions for the CMB spectrum at low ℓs is likely to be the main driver of the different constraints obtained with the two codes for γ. This is evident in Figs. IV.5-IV.8, which show that the impact of γ is only large in the low multipole region in the case of `MGCAMB`, which explains why the estimates of γ differ when we employ Planck data (which include low-ℓ data) but do not when ACT and SPT are used instead (which only include data above $\ell \sim 400$).

V Planck-PR4 Anisotropy Spectra Show Better Consistency with General Relativity

Preamble to the Paper

In Sec. III it was said that, in their journey from the last scattering surface to our detectors, the CMB photons have to interact with the large-scale structure of the universe, which in turn leads to a number of *secondary* effects that change the shape of the temperature and polarisation anisotropies that formed during the recombination era. The weak lensing of light is one of the main secondary sources of anisotropy affecting the CMB and it is also the object of study of the paper presented in this chapter. In particular, in this chapter we look at an excess in the amount of lensing that characterises the temperature and polarisation spectra of Planck since its 2013 data release [23, 73, 168, 169]: this is the well-known "lensing anomaly" of Planck. This anomalous lensing signal is quantified through the phenomenological "lensing parameter" - A_L - introduced in [164]. This parameter directly impacts the lensing spectrum of the CMB, $C_\ell^{\psi\psi}$ (denoted in the paper as $C_\ell^{\varphi\varphi}$), rescaling it as: $C_\ell^{\psi\psi} \longrightarrow A_L C_\ell^{\psi\psi}$.

A_L can be used as a tool to test the consistency between the amount of CMB lensing that we can measure from the anisotropy spectra and the amplitude of the lensing signal that we can reconstruct from the trispectra, which encode the non-Gaussian signals induced in the temperature anisotropies by the weak lensing of light. Interestingly, as mentioned above, up until its 2018 data release (PR3) Planck seemed to find that A_L should be greater than unity. This is not, however, what other CMB probes like ACT [44] and SPT [25] seem to measure, which instead show consistency with $A_L = 1$. The same consistency can even be found in the final data release by Planck (PR4 [53]).

In this paper we then set out to understand whether the lensing anomaly from the 2018 data release by Planck can be recast as a deviation of Planck's data from GR. In fact, while showing a lensing excess, the 2018 data by Planck also showed evidence for a mild deviation from GR in terms of the μ, Σ parametrisation [23], which is presented in Sec. V.B of the paper presented here. The reason to do this is that Σ, the parameter that PR3 finds to be at odds with GR, affects the Weyl potential in Eq.(V.3) and, as a consequence, the coupling of light to gravity. It is then presumable that, if the excess in the lensing signal disappears, so should any evidence for a modification of Eq.(V.3). In this paper we prove this.

On the metric shown in Eq.(V.1): while it differs from the metric for the same gauge (i.e., conformal Newtonian) in Eq.(II.15) just for the opposite sign in front of Φ, it was presented

here because it is the same metric employed by `MGCAMB`, the cosmology code used in this paper. In practice, Eqs.(II.19-II.22) can be easily changed according to the perturbed metric defined in the following paragraphs. For example, Eq.(II.21) can be easily turned into Eq.(V.2) by enforcing $\Phi \to -\Phi$ (i.e., the difference between the two metric definitions) and $\Phi = \Psi$ (i.e., consistency with GR).

Planck-PR4 Anisotropy Spectra Show Better Consistency with General Relativity

Abstract: We present the results from a series of analyses on two parametric tests of gravity that modify the growth of linear, sub-horizon matter perturbations in the ΛCDM model. The first test, known as the (μ, Σ) framework, modifies the Poisson and lensing equations from General Relativity (GR). The second test introduces the growth index γ, which directly affects the time evolution of matter density perturbations. Our study is motivated by results from the analysis of the Planck-PR3 2018 spectra, which indicate a preference for $\Sigma_0 \neq 0$ and $\gamma_0 > 0.55$, both of which deviate from the ΛCDM predictions at a significance level of $\sim 2.5\sigma$. To clarify the nature of these anomalous results and understand how the lensing anomaly fits into the picture, we analyze the most recent Planck-PR4 spectra extracted from the updated `NPIPE` maps. Overall, the Planck-PR4 data show better consistency with GR. The updated likelihood `Camspec` provides constraints on Σ_0 and γ_0 that are consistent with GR within 1.5σ and 2σ, respectively. The updated likelihoods `HiLLiPoP` and `LoLLiPoP` show even closer agreement, with all parameter values consistent with a ΛCDM cosmology within 1σ. This enhanced consistency is closely correlated with the lensing anomaly. Across the different likelihoods, the tendency of Σ_0 and γ_0 to drift towards non-standard values matches the observed preference for $A_L > 1$, both of which are significantly reduced or disappear within the Planck-PR4 data.

V.A Introduction

At the time of writing, our best understanding of the Universe is summarized by the standard ΛCDM model of cosmology. This model stands on two pillars of well-established physics: General Relativity (GR), which governs gravitational interactions, and the Standard Model of particle physics (SM), which describes all other fundamental interactions in nature. However, it also relies on three essential components — Inflation, Dark Matter, and Dark Energy — that are crucial for explaining numerous observations ranging from the Cosmic Microwave Background (CMB) radiation to the Large Scale Structure (LSS) of the Universe [20, 21, 23, 50, 54, 55, 57, 76, 86, 97, 137, 162, 170–219]. Nevertheless, a comprehensive physical interpretation of these three components remains elusive, both theoretically and experimentally.

Together with these longstanding foundational problems, in the last ten years a few statis-

tically significant tensions and anomalies have challenged the standard cosmological picture. The most puzzling issue is the so-called Hubble tension [110, 114, 115, 117, 120, 143, 147, 220–226]: at its core, the value of the Hubble constant (H_0) derived from CMB measurements within the ΛCDM framework [23] differs by more than 5σ from direct local measurements reported by the SH0ES team [84, 227, 228]. Additionally, other less significant problems have come to light, such as a well-known 2-3σ disagreement between the values of $S_8 = \sigma_8\sqrt{\Omega_m/0.3}$ derived from CMB measurements by Planck [23] and those inferred from large-scale structure observations [112, 119, 138, 210, 214, 229–236].

Foundational problems and longstanding tensions raise the question of whether the ΛCDM model accurately represents the true paradigm of the Universe or merely serves as a phenomenological, data-driven approximation to a more fundamental scenario that has yet to be fully understood. In other words, could it be that as our data becomes increasingly precise, our parameterization of more than 95% of the energy density of the Universe — primarily based on simplicity, which, after all, highlights our ignorance regarding these phenomena — becomes inadequate?

Taking a step back and (re)considering the big picture, we cannot help but note that the need to introduce the three unknown components underpinning ΛCDM cosmology is intricately rooted in the challenge of explaining observations based on the predictions of GR when assuming a SM particle content in the Universe. For instance, the current accelerated expansion of the Universe sharply contrasts with GR's predictions when only the matter content expected from the SM is considered, leading to the introduction of a cosmological constant term in the Einstein field equations, which is not free from conceptual problems [98, 107, 108, 237–259] and has recently been challenged by observations [14, 260].[V.1] Similarly, the CMB and LSS observations contrast with what is expected in GR when only the matter content predicted by the SM is taken into account, providing indirect evidence for cold dark matter. Finally, historically, inflation was introduced to avoid extremely fine-tuned initial conditions in the early Universe [105, 106, 299, 300] that were necessary to achieve a present-day Universe consistent with observations as it evolved over time — an evolution largely shaped by gravity.

Consequently, when it comes to *hazard* a physical interpretation for these three ingredients, we can follow two main approaches. One option is to work on the right-hand side of the Einstein equations, adding new forms of energy-momentum content to the stress-energy tensor $T_{\mu\nu}$ beyond what the SM predicts (such as introducing scalar fields to drive acceleration in the early or late Universe or a perfect fluid of cold dark matter particles to account for the observed structures). The second option is to work on the left-hand side of the Einstein equations, modifying the Einstein tensor $G_{\mu\nu}$, thereby altering the underlying theory of gravity. In fact, some benchmark scenarios of inflation (such as Starobinsky inflation [301]), along

[V.1] Readers interested in the latest developments regarding the Dark Energy interpretation of the first-year data release from the DESI collaboration [14] can refer to Refs. [261–266] for discussions on potential systematic effects in the data. For physical interpretations of these results, see, e.g., Refs. [216, 260, 267–298].

with many models attempting to interpret dark matter and dark energy, are fundamentally rooted in modified gravity (MG) theories.

With this premise, it goes without saying that testing whether gravity follows the predictions of GR on cosmological scales is of paramount importance. In the epoch of precision cosmology, CMB observations are a powerful tool for identifying any signatures of MG on such scales. As a matter of fact, the shape of the CMB angular spectra of temperature and polarization anisotropies arises from the dynamics of primordial density fluctuations and is largely determined by the gravitational forces experienced by the coupled photon-baryon fluid before decoupling. Unlike the evolution of late-time structures, such as galaxies or clusters, where nonlinear effects complicate the picture, the CMB primarily involves linear perturbation theory, governed by a system of linearized Einstein-Boltzmann equations. This makes CMB observations largely free from complications introduced by astrophysical processes (aside from modeling foreground contamination). Moreover, the wide range of angular scales covered by the CMB — from the largest observable scales (such as the quadrupole and dipole) to the smallest scales measured by current and forthcoming ground-based telescopes, such as the Atacama Cosmology Telescope [55, 66, 213] (ACT) and the South Pole Telescope [56, 57] (SPT) — allows gravity to be tested across an extensive range of scales through a multitude of different tests.

A particularly interesting test we can perform using CMB data involves assessing whether the gravitational deflection, or lensing, experienced by CMB photons along their paths [65] follows the predictions of GR within a standard cosmological model. At arcminute scales, lensing deflections distort the observed image of the CMB fluctuations, imprinting a distinctive non-Gaussian four-point correlation function (or trispectrum) in both the temperature and polarization anisotropies [65]. Additionally, although gravitational lensing does not alter the overall distribution of primary CMB anisotropies, it leaves distinctive signatures in the spectra of temperature and polarization anisotropies through a convolution between the latter and the CMB lensing potential spectrum [65]. To test whether these effects align with the theoretical predictions, one can introduce a phenomenological parameter A_L [164] which must be $A_L = 1$ as predicted by GR within a ΛCDM cosmology. This parameter can be used to arbitrarily tune the extent to which $C_\ell^{\varphi\varphi}$ (the spectrum of the lensing potential φ, a redefinition of the Weyl potential that allows for $\vec{\alpha} = \nabla\varphi$, where $\vec{\alpha}$ is the deflection angle of light [65]) affects the spectrum of primary CMB anisotropies [164]: $C_\ell^{\varphi\varphi} \longrightarrow A_L C_\ell^{\varphi\varphi}$.

Interestingly, since the 2013 data release [23, 73, 166, 168, 169, 302–306], the temperature and polarization power spectra of Planck have shown A_L to be greater than unity.[V.2] To be more quantitative, in the Planck-PR3 2018 data release a 2.8σ deviation from $A_L = 1$ is

[V.2] The presence of the lensing anomaly may hold significant implications when constraining scenarios beyond ΛCDM, as we argue in this paper in relation to MG scenarios. However, another well-documented example pertains to the curvature density parameter, Ω_k. Since an excess of lensing is naively expected with a higher abundance of cold dark matter, the observed lensing anomaly can be recast into a preference for a closed Universe, as discussed in several recent (and not so recent) works [165–167, 307–325].

found ($A_L = 1.180 \pm 0.065$), see Ref. [23].[V.3]

To address the lensing anomaly, a significant range of physical interpretations involving extensions to GR has been explored. In the spirit of hitting multiple targets with the same arrow, many of these approaches are also proposed as promising alternatives for explaining the Universe's late-time accelerated expansion while alleviating other persistent tensions observed across various cosmological and astrophysical datasets [110, 114, 326–329].

However, when it comes to drawing general conclusions about this plethora of extended theories of gravity, a concrete difficulty arises from the fact that in many MG models, the equations describing the evolution of cosmological perturbations deviate significantly from those of GR, and these deviations can vary among different models. Therefore, parametric tests have been proposed to recast these varying behaviors and model effects in both the dynamics of cosmological perturbations and the growth of cosmic structures. Of particular relevance is the so-called (μ, Σ) framework [33, 330, 331], where $\mu(k, a)$ and $\Sigma(k, a)$ are two arbitrary functions (both null in GR) of the wavenumber k and the scale factor a that alter the predictions for the Poisson and lensing equations. Yet another parametric test of gravity consists in considering the growth index γ, predicted to be $\gamma = 0.55$ in GR, which captures any potential deviations in the growth of perturbations [1, 38, 95, 96].

Interestingly, Planck-PR3 data measure Σ_0 (i.e., the current value of Σ when it is assumed constant in k) to be $\Sigma_0 = 0.27^{+0.15}_{-0.13}$ — over 2σ away from the null value expected within GR [23]. Regarding the γ parameter, the Planck-PR3 data, in combination with Redshift Space Distortions data, yield $\gamma_0 = 0.639^{+0.024}_{-0.025}$ [38]. If taken at face value, these results would provide additional hints for deviations from GR and, more broadly, from a canonical model of structure formation. However, several caveats are in order:

- Firstly, CMB data show a strong correlation between $A_{\rm L}$ and the (μ, Σ) or γ parameters – see, e.g., Fig. 2 of Ref. [332]. This correlation recasts the lensing anomaly as an approximate 2σ preference for $\Sigma_0 \neq 0$ in the Planck data [23, 332, 333], or equivalently (part of) the 4σ preference for $\gamma \neq 0.55$.

- Secondly, no indication of a lensing excess has been found in CMB experiments other than Planck, such as ACT and SPT. The value of A_L inferred from these experiments consistently aligns with $A_L = 1$ well within 2 standard deviations [55, 56]. Somewhat unsurprisingly, no significant indications of MG dynamics or suppression of structure growth (i.e., $\Sigma_0 \neq 0$ or $\gamma > 0.55$) have been found in the analysis of these ground-based telescope data either, see Refs. [1, 334].

- Since 2018, the Planck data has undergone extensive reanalyses. The updated Planck-PR4 (`NPIPE`) CMB maps feature significant advancements, such as enhanced sky coverage at high frequencies, improved processing of time-ordered data, and an approximate

[V.3] All the constraints reported in the paper will be at 68% CL, unless otherwise specified.

8% increase in the data used for lensing trispectrum reconstruction [53, 67]. Recent releases of new likelihoods from both `Camspec` [45] and `HiLLiPoP` [24] have shown that A_L can be measured to be near unity within the Planck-PR4 (`NPIPE`) data.[V.4] This lends support to the hypothesis that the lensing anomaly observed in the Planck-PR3 data may simply result from observational systematics, as already argued by ACT and SPT.

Fitting all the pieces into place, it seems natural to question whether, and to what extent, the new Planck-PR4 likelihoods can support or relax the indications of MG related to a non-vanishing Σ or the suppression of structure growth captured by the parameter γ. More broadly, this study aims to derive up-to-date constraints on parametric tests of gravity within these two frameworks, using the updated Planck-PR4 likelihoods [V.5], and to clarify their strict connection with the lensing anomaly.

The paper is structured as follows. In Sec. V.B, we introduce the two parametrizations of gravity under study. In Sec. V.C, we present the data and the methodology used. In Sec. V.D, we interpret our results, and in Sec. V.E, we derive our conclusions.

V.B Parametric Modified Gravity and Perturbation Theory

In first-order cosmological perturbation theory, and in the Newtonian gauge, the two scalar potentials Ψ and Φ perturb the time and spatial components of the zeroth-order flat FLRW metric as follows [40]:

$$\mathrm{d}s^2 = a^2[-(1+2\Psi)\mathrm{d}\tau^2 + (1-2\Phi)\mathrm{d}\mathbf{x}^2], \tag{V.1}$$

where $\mathrm{d}\tau = \mathrm{d}t/a$ is the conformal time. To fully study the perturbations of non-relativistic matter, we need to introduce two further scalars: the density contrast of the matter fluid, δ, and the divergence of its velocity, v. In particular, the relations between the metric potentials and δ are set by the specific theory of gravity considered. In Fourier space, GR gives us the following equalities, representing the Poisson and lensing equations, respectively:

$$k^2\Psi = -4\pi G a^2 \rho \Delta, \tag{V.2}$$

$$k^2(\Psi+\Phi) = -8\pi G a^2 \rho \Delta, \tag{V.3}$$

[V.4] See, e.g., recent Refs. [335–338] for updated constraints derived from Planck-PR4 based likelihoods on different extended cosmological scenarios.

[V.5] After our work presented here was shared with the community on `arXiv`, the DESI collaboration also released a series of updated constraints on the μ, Σ parametrization of modified gravity using the `HiLLiPoP, LoLLiPoP` likelihoods [339, 340], and a different modified gravity software (`ISiTGR` in [339, 340] instead of `MGCAMB + Cobaya`).

where $\Delta \equiv \rho\delta + 3\frac{\mathcal{H}}{k}(\rho + P)v$ is the comoving density contrast, which depends on the conformal Hubble function $\mathcal{H}$, the fluid's average density ρ, and its pressure P.

V.B.1 The (μ, Σ) Framework

In MG theories, we often see that Eqs. (V.2, V.3) are modified in different ways, usually by the presence of some additional dependence on the scale factor a or the wavenumber k [35]. We can capture such differences in the Poisson and lensing equations within a single, model-independent parametrization, the (μ, Σ) framework [331, 341, 342]:

$$k^2\Psi = -4\pi G a^2(\mu + 1)\rho\Delta, \tag{V.4}$$

$$k^2(\Psi + \Phi) = -8\pi G a^2(\Sigma + 1)\rho\Delta, \tag{V.5}$$

where μ and Σ are two arbitrary functions of a and k.

As long as we treat linear ($\delta \ll 1$) and sub-horizon ($k \gtrsim \mathcal{H}$) perturbations, Eq. (V.4) represents an adequate description of those models where, for instance, Newton's constant of gravity gains a dependence on time and/or scale that can be introduced through μ: $G \longrightarrow G_{\rm eff} \equiv (\mu + 1)G$. Similarly, because the Weyl potential $\Psi + \Phi$ directly affects weak lensing [97, 330], Eq. (V.5) encompasses any deviations in the way gravity deflects light as predicted in GR. However, in models like MOND, which entail extra scalar and tensor perturbations and therefore require more equations than just Eqs. (V.2) and (V.3) and the conservation equations for matter perturbations in GR, this parametrization is not sufficient to describe the theory's growth of structure [330].

More concretely, but not exhaustively, a few examples of what μ and Σ look like in theories of MG can be found in DGP gravity [343], $f(R)$ theories (where $G_{\rm eff} \sim (1 + \frac{df}{dR})^{-1}$ [344]), or the Brans-Dicke theory [345].

In this work, however, we do not consider any scale factor or wavenumber dependence of the (μ, Σ) functions, restraining ourselves to measuring their current, fixed values: μ_0, Σ_0. A detection of either $\mu_0 \neq 0$ or $\Sigma_0 \neq 0$ will indicate a deviation from the ΛCDM model.

V.B.2 The growth index γ

The (μ, Σ) framework is just one example of the MG parametrizations existing in the literature. If we still consider the linear, sub-horizon regime of perturbations, we can also look for deviations away from GR through the so-called *growth factor* γ [95, 150]. We write the

growth rate $f(a)$ to be:

$$f(a) = \frac{d\ln\delta}{d\ln a}. \tag{V.6}$$

Then, γ can be defined through the following ansatz, which one can choose to solve Eq. (V.6):

$$f(a) = \Omega_m^{\gamma}, \tag{V.7}$$

where Ω_m is the density fraction of non-relativistic matter.
According to this definition, since MG models often seem to predict the same expansion history (i.e., they are degenerate in the time evolution of Ω_m), any difference in the growth rate of matter perturbations predicted by alternative theories of gravity has to manifest itself through γ, which should deviate away from its ΛCDM model prediction: $\gamma \approx 0.55$ to 0.1% accuracy [95, 96]. Once again, we can list a few concrete examples for the values taken by γ in models other than ΛCDM. For instance, $\gamma \approx 0.68$ in DGP gravity [95, 96], with no more than 2% variation if assumed constant in time. For $f(R)$ theories where γ does not suffer excessive dispersion (i.e., dependence on k), $\gamma \approx 0.4$ [346], even though it can still show a non-negligible time dependence, up to $\gamma_0' = -0.2$ today [347].
As done with the (μ, Σ) parametrization described above, we choose not to assume any time or scale dependence for γ, opting instead to measure its fixed, current value γ_0. [V.6]

V.C Likelihoods and Sampling Methodology

Since we are primarily interested in re-evaluating the various hints for MG and their connection to the lensing anomaly — all originally identified in the 2018 Planck-PR3 data release [23] — our analysis focuses on Planck CMB measurements of temperature and polarization anisotropies, covering both the PR3 likelihoods and the more recently updated Planck likelihood codes. Specifically, the Planck likelihoods we use are named as follows.

- **Plik;** to reproduce the baseline results documented in the literature (and summarized in the introduction), we begin by considering the `Plik` likelihood for high-ℓ TT, TE, EE PR3 spectra, along with the `Commander` and `SimAll` likelihoods for the low-ℓ temperature and polarization spectra from the same data release [23]. Specifically, we use:

[V.6] Before going any further, we intend to clarify the nomenclature adopted throughout this article further. We refer to the (μ, Σ) framework or the γ model to denote the two generic frameworks introduced in this section. However, as explained, we focus on the case where Σ and γ do not have any explicit time or scale dependence. Therefore, these functions in our paper are just constants (in time and scale). We refer to them with the subscript 0, which not only denotes their present-day value but also indicates their value at any epoch as they do not change over time.

  - the high-ℓ `Plik` likelihood [23] for the TT spectrum in the multipole range $30 \leq \ell \leq 2508$, as well as for the TE and EE spectra at $30 \leq \ell \leq 1996$;
  - the low-ℓ `Commander` likelihood [23] for the TT spectrum in the multipole range $2 \leq \ell \leq 29$;
  - the low-ℓ `SimAll` likelihood [23] for the EE spectrum at $2 \leq \ell \leq 29$.

  For simplicity, we refer to this combination as **Plik**.

- **Camspec;** we replace the Planck-PR3 `Plik` high-ℓ TTTEEE likelihood with the more recent `Camspec` likelihood [45], based on the Planck-PR4 `NPIPE` data release [53, 67]. However, we retain the same low-ℓ likelihoods from the **Plik** combination. Therefore, we use:

  - the high-ℓ `Camspec` likelihood [45] for the TT, TE, and EE spectra in the multipole range $30 \leq \ell \lesssim 2500$;
  - the low-ℓ `Commander` likelihood [23] for the TT spectrum in the multipole range $2 \leq \ell \leq 29$;
  - the low-ℓ `SimAll` likelihood [23] for the EE spectrum at $2 \leq \ell \leq 29$.

  We refer to this combination as **Camspec**.

- **Camspec (TT-only);** we use the recent `Camspec` likelihood [45], based on the Planck-PR4 `NPIPE` data release [53, 67], for the high-ℓ temperature anisotropy spectrum, excluding TE and EE information at $\ell > 30$. However, we retain the same low-ℓ likelihoods from the **Plik** combination. Therefore, we use:

  - the high-ℓ `Camspec` likelihood [45] for the TT spectrum in the multipole range $30 \leq \ell \lesssim 2500$;
  - the low-ℓ `Commander` likelihood [23] for the TT spectrum in the multipole range $2 \leq \ell \leq 29$;
  - the low-ℓ `SimAll` likelihood [23] for the EE spectrum at $2 \leq \ell \leq 29$.

  We refer to this combination as **Camspec (TT-only)**.

- **HiLLiPoP;** we replace the Planck-PR3 `Plik` high-ℓ TTTEEE likelihood with the more recent `HiLLiPoP` likelihood [24], based on the Planck-PR4 `NPIPE` data release [53, 67]. Additionally, we replace the Planck-PR3 `SimAll` likelihood for E-mode polarization measurements at $\ell < 30$ with the Planck-PR4 `LoLLiPoP` likelihood [24], while keeping the low-ℓ `Commander` likelihood for the TT spectrum. Therefore, we use:

Parameter	Prior
$\Omega_{\rm b}h^2$	$[0.005, 0.1]$
$\Omega_{\rm c}h^2$	$[0.001, 0.99]$
$100\theta_{\rm MC}$	$[0.5, 10]$
$\tau_{\rm reio}$	$[0.01, 0.8]$
$n_{\rm s}$	$[0.8, 1.2]$
$\log(10^{10}A_{\rm s})$	$[1.61, 3.91]$
μ_0	$[-1.5, 1.5]$
Σ_0	$[-1.5, 1.5]$
γ_0	$[0, 1]$
A_L	$[0, 10]$

TABLE V.1. Flat priors imposed on the free parameters considered in this analysis.

  - the high-ℓ `HiLLiPoP` likelihood [24] for the TT, TE, and EE spectra in the multipole range $\ell \lesssim 2500$;
  - the low-ℓ `Commander` likelihood [23] for the TT spectrum in the multipole range $2 \leq \ell \leq 29$;
  - the low-ℓ `LoLLiPoP` likelihood [24] for the EE spectrum at $2 \leq \ell \leq 29$.

  We refer to this combination as **HiLLiPoP**.

- **HiLLiPoP (TT-only);** we use the recent `HiLLiPoP` likelihood [24], based on the Planck-PR4 `NPIPE` data release [53, 67], for the temperature anisotropy spectrum, excluding any information on TE and EE at $\ell > 30$. Additionally, we replace the Planck-PR3 `SimAll` likelihood for E-mode polarization measurements at $\ell < 30$ with the Planck-PR4 `LoLLiPoP` likelihood [24], while keeping the low-ℓ `Commander` likelihood for the TT spectrum. Therefore, we use:

  - the high-ℓ `HiLLiPoP` likelihood [24] for the TT spectrum in the multipole range $30 \leq \ell \lesssim 2500$;
  - the low-ℓ `Commander` likelihood [23] for the TT spectrum in the multipole range $2 \leq \ell \leq 29$;
  - the low-ℓ `LoLLiPoP` likelihood [24] for the EE spectrum at $2 \leq \ell \leq 29$.

  We refer to this combination as **HiLLiPoP (TT-only)**.

The six standard model parameters considered in this analysis are: the baryon density ($\Omega_{\rm b}h^2$); the density of cold dark matter ($\Omega_{\rm c}h^2$); the observed angular size of the sound horizon at recombination ($100\theta_{\rm MC}$); the reionization optical depth ($\tau_{\rm reio}$); the amplitude of the primordial spectrum of scalar perturbations ($\log(10^{10}A_{\rm s})$), and its spectral index ($n_{\rm s}$). Along with the

parameters of the two MG models introduced in Sec. V.B, μ_0, Σ_0 for the (μ, Σ) framework, and γ_0 for the γ model. In order to clarify the correlation with the lensing anomaly, for each of these models, we consider two cases: one where A_L is fixed to the GR value ($A_L = 1$), and another where A_L is left free to vary. We sampled the parameter space by using the MCMC engine `Cobaya` [91]. The Einstein-Boltzmann solver implemented in `Cobaya` to calculate and evolve perturbations within the (μ, Σ) model is `MGCAMB` [33, 35–37], while for the γ parametrisation of MG, we employed `CAMB_GammaPrime_Growth` [38]. All the parameters characterising the two MG models considered here have been assumed to have flat priors as listed in Tab. V.1. To assess the convergence of the chains obtained using this approach, we apply the Gelman-Rubin criterion [348], setting a threshold for chain convergence at $R - 1 < 0.01$. The results are derived from analyzing the MCMC chains using the `GetDist` code [349], after discarding a 30% burn-in fraction of samples from each chain.

V.D Results

	Plik	**Camspec**	**Camspec (TT-only)**	**HiLLiPoP**	**HiLLiPoP (TT-only)**
$\boldsymbol{\Omega_b h^2}$	0.02258 ± 0.00017	0.02231 ± 0.00015	0.02253 ± 0.00027	0.02232 ± 0.00014	0.02233 ± 0.00024
$\boldsymbol{\Omega_c h^2}$	0.1182 ± 0.0015	0.1187 ± 0.0013	0.1162 ± 0.0024	0.1183 ± 0.0012	0.1179 ± 0.0022
$\boldsymbol{100\theta_{MC}}$	1.04112 ± 0.00032	1.04086 ± 0.00026	1.04133 ± 0.00048	1.04091 ± 0.00026	1.04110 ± 0.00046
$\boldsymbol{\tau}$	0.0507 ± 0.0081	0.0493 ± 0.0083	0.0512 ± 0.0082	0.0570 ± 0.0060	0.0573 ± 0.0064
$\boldsymbol{\ln(10^{10} A_s)}$	3.033 ± 0.017	3.028 ± 0.017	3.027 ± 0.017	3.037 ± 0.014	3.036 ± 0.015
$\boldsymbol{n_s}$	0.9701 ± 0.0050	0.9663 ± 0.0044	0.9730 ± 0.0072	0.9695 ± 0.0041	0.9679 ± 0.0062
$\boldsymbol{\mu_0}$	$0.08^{+0.45}_{-0.91}$	$0.08^{+0.48}_{-0.87}$	$0.06^{+0.48}_{-0.84}$	$0.02^{+0.38}_{-0.95}$	$0.06^{+0.47}_{-0.92}$
$\boldsymbol{\Sigma_0}$	0.35 ± 0.14	$0.20^{+0.12}_{-0.14}$	0.38 ± 0.17	$0.12^{+0.11}_{-0.13}$	$0.20^{+0.13}_{-0.18}$
$\boldsymbol{H_0}$ [km/s/Mpc]	68.23 ± 0.70	67.74 ± 0.59	69.0 ± 1.2	67.91 ± 0.57	$68.13^{+0.94}_{-1.1}$
$\boldsymbol{S_8}$	$0.816^{+0.056}_{-0.083}$	$0.823^{+0.055}_{-0.082}$	$0.792^{+0.058}_{-0.082}$	$0.817^{+0.050}_{-0.087}$	$0.814^{+0.059}_{-0.083}$

TABLE V.2. 1σ constraints on the (μ, Σ) model when the lensing amplitude A_L is kept fixed to its reference value $A_L = 1$. As the likelihood combination employed changes from **Plik**, through to **Camspec** and finally to **HiLLiPoP**, the apparent MG evidence signal in Planck's data disappears, and consistency with $\Sigma_0 = 0$ is re-established. Counting polarization anisotropies out of the analysis (i.e., the TT-only columns) indicates that this signal is predominantly affecting the temperature data.

Constraints on the free and derived cosmological parameters characterizing the (μ, Σ) scenario are provided in Tables V.2 and V.3, corresponding to the cases where the A_L parameter is fixed and varied, respectively. The most significant findings for this model are discussed in detail in paragraph V.D.1. However, for a quicker overview, the reader may refer directly to Fig. V.1 and the left panel of V.2, which visually summarize the main results for this model. Similarly, the extended γ model is examined in paragraph V.D.2, with numerical constraints listed in Tables V.4 and V.5 for the fixed and varied A_L cases, respectively. Key aspects of this discussion are visually captured in Fig. V.4 and the right panel of Fig. V.2.

	Plik	**Camspec**	**Camspec (TT-only)**	**HiLLiPoP**	**HiLLiPoP (TT-only)**
$\boldsymbol{\Omega_b h^2}$	0.02260 ± 0.00017	0.02231 ± 0.00016	0.02256 ± 0.00029	$0.02232^{+0.00014}_{-0.00015}$	0.02230 ± 0.00026
$\boldsymbol{\Omega_c h^2}$	0.1181 ± 0.0016	0.1186 ± 0.0013	0.1160 ± 0.0025	0.1183 ± 0.0014	0.1181 ± 0.0024
$\boldsymbol{100\theta_{MC}}$	1.04115 ± 0.00033	1.04087 ± 0.00027	1.04136 ± 0.00048	1.04092 ± 0.00027	1.04108 ± 0.00050
$\boldsymbol{\tau}$	0.0499 ± 0.0084	0.0493 ± 0.0083	$0.0506^{+0.0088}_{-0.0077}$	0.0577 ± 0.0060	0.0579 ± 0.0062
$\boldsymbol{\ln(10^{10} A_s)}$	3.031 ± 0.018	3.028 ± 0.017	$3.025^{+0.019}_{-0.016}$	3.038 ± 0.015	3.038 ± 0.015
$\boldsymbol{n_s}$	0.9707 ± 0.0050	0.9667 ± 0.0047	0.9737 ± 0.0074	0.9695 ± 0.0045	0.9674 ± 0.0068
$\boldsymbol{\mu_0}$	$0.04^{+0.42}_{-0.92}$	$0.04^{+0.43}_{-0.90}$	$0.07^{+0.49}_{-0.86}$	$0.01^{+0.42}_{-0.88}$	$-0.01^{+0.41}_{-0.86}$
$\boldsymbol{\Sigma_0}$	$0.24^{+0.18}_{-0.23}$	$0.23^{+0.17}_{-0.22}$	$0.26^{+0.19}_{-0.26}$	$0.25^{+0.18}_{-0.24}$	$0.27^{+0.19}_{-0.23}$
$\boldsymbol{H_0}$ [km/s/Mpc]	68.32 ± 0.72	67.78 ± 0.61	69.1 ± 1.2	$67.91^{+0.59}_{-0.65}$	$68.0^{+1.0}_{-1.2}$
$\boldsymbol{S_8}$	$0.809^{+0.052}_{-0.083}$	$0.817^{+0.052}_{-0.083}$	$0.789^{+0.063}_{-0.077}$	$0.815^{+0.051}_{-0.083}$	$0.810^{+0.054}_{-0.083}$
$\boldsymbol{A_L}$	$1.069^{+0.083}_{-0.11}$	$0.992^{+0.081}_{-0.097}$	$1.076^{+0.093}_{-0.14}$	$0.942^{+0.077}_{-0.098}$	$0.963^{+0.079}_{-0.11}$

TABLE V.3. 1σ constraints on the (μ, Σ) model when the lensing amplitude A_L is left free to vary in the model.

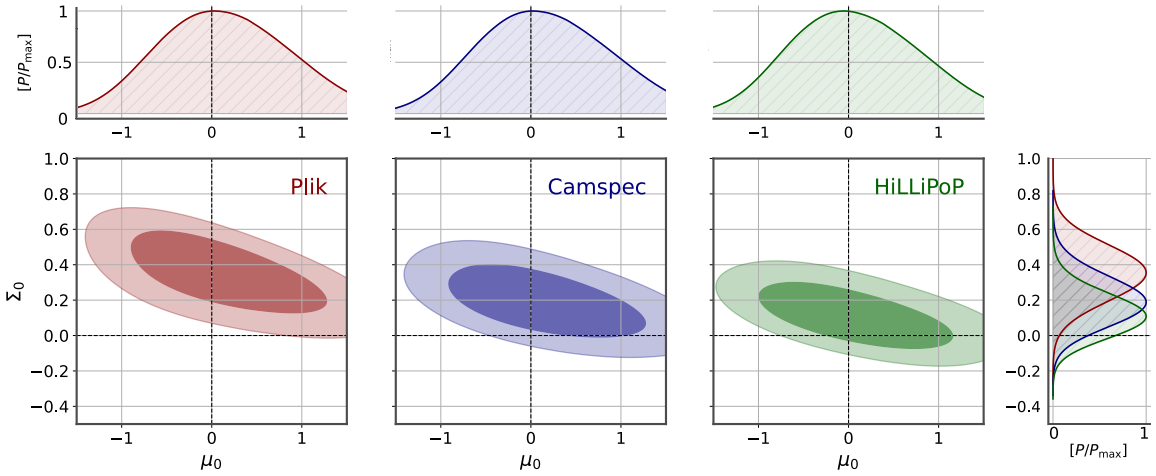


FIG. V.1. One-dimensional probability distribution functions and two-dimensional marginalized constraints in the (μ_0,Σ_0) plane for the different datasets listed in Sec. V.C. The lensing amplitude A_L is kept fixed at its reference value $A_L = 1$. The vertical and horizontal dashed lines represent the baseline values $\mu_0 = \Sigma_0 = 0$.

V.D.1 Constraints on the (μ, Σ) framework

We start with the constraints obtained from the combinations of likelihoods labeled as **Plik**. This combination of data is entirely based on the Planck-PR3 anisotropy spectra. Therefore, it is not surprising that we observe (nearly[V.7]) the same preference towards MG documented by the Planck Collaboration [23, 169]. Specifically, when constraining the parameter Σ_0, we find $\Sigma_0 = 0.35 \pm 0.14$, which is 2.5σ away from the value expected within GR. Additionally, referring to the leftmost panel of Fig. V.1 – where we show the 2D marginalized constraints in the (μ_0, Σ_0) plane along with the one-dimensional probability distribution functions of the two parameters – we observe that the point (0, 0), which corresponds to a baseline ΛCDM

[V.7] This is slightly different from the value measured by the Planck collaboration and reported in the introduction due to a different parametrization and implementation of the model in the Boltzmann code.

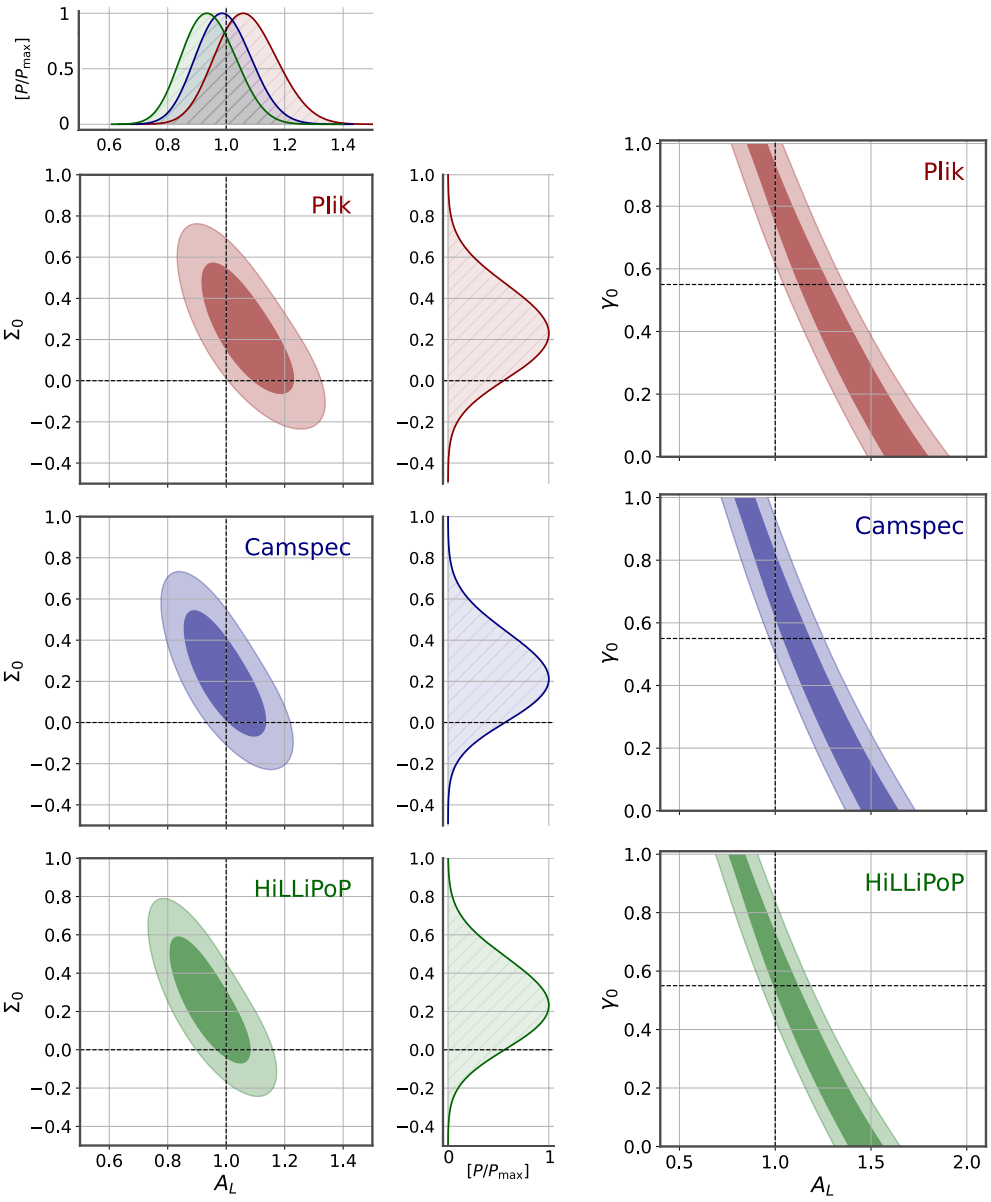


FIG. V.2. Left panel: one-dimensional probability distribution functions and two-dimensional marginalized contours in the (A_L,Σ_0) plane for the different datasets listed in Sec. V.C. The horizontal and vertical dashed lines represent the baseline values $\Sigma_0 = 0$ and $A_L = 1$, respectively. Right panel: two-dimensional marginalized constraints in the (A_L, γ_0) plane for the different datasets listed in Sec. V.C. The horizontal and vertical dashed lines represent the baseline values $\gamma_0 = 0.55$ and $A_L = 1$, respectively.

cosmology, falls well outside the 95% contours.

As already pointed out in Refs. [23, 332–334, 350], this apparent evidence for MG in Planck's PR3 data is closely linked to the lensing anomaly. This can be understood by the effect of Σ_0 in Eq. (V.5), which alters the strength of CMB lensing. **Values of $\Sigma_0 > 0$ produce**

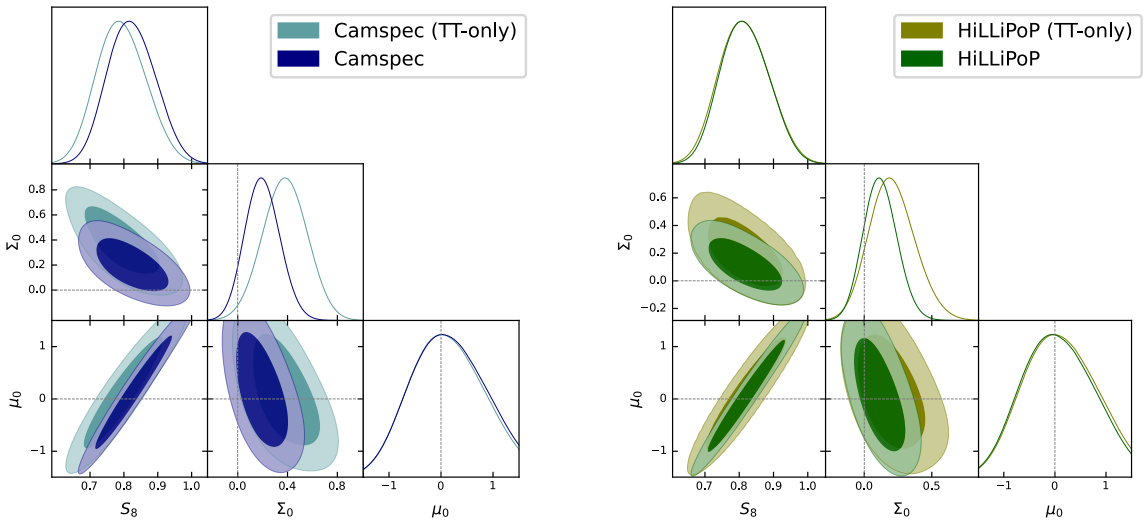


FIG. V.3. One-dimensional probability distribution functions and two-dimensional marginalized contours for the parameters γ_0, Ω_m, and S_8. The lensing amplitude A_L is kept fixed at its reference value $A_L = 1$. In the left side panel, we show the constraints involving the combinations of likelihood **Camspec** and **Camspec (TT-only)**, whereas in the right side panel, we show the constraints for the combination of likelihood **HiLLiPoP** and **HiLLiPoP (TT-Only)** – all likelihoods are defined in Sec. V.C. The vertical dashed lines in both panels correspond to the baseline values $\mu_0 = \Sigma_0 = 0$.

effects similar to those associated with $A_L > 1$, and the two can be recast into one another. As a result, CMB data are sensitive to both of these changes in much the same way. Unsurprisingly, when A_L is allowed to vary within the (μ,Σ) framework, a strong negative correlation emerges between Σ_0 and A_L. In this joint analysis, the combined effect of this correlation and the larger uncertainties translates into the $\Sigma_0 \to 0$ and $A_L \to 1$ shifts we find with **Camspec** and **HiLLiPoP**, diluting both the lensing anomaly and the preference for MG. This is also clearly reflected in the numerical constraints given in Tab. V.3. Taken at face value, the results for A_L and Σ_0 are both consistent with their GR predictions within 2 standard deviations. Nevertheless, referring to the left panel of Fig. V.2 – where we show the 2D marginalized constraints in the (A_L, Σ_0) plane along with the one-dimensional probability distribution functions of these parameters – we observe that, due to the strong correlations, the point corresponding to GR ($A_L = 1$, $\Sigma_0 = 0$) still falls outside the 95% confidence level contours.

When analyzing the new Planck-PR4-based likelihoods, we find that the contours in the (μ_0, Σ_0) plane shown in Fig. V.1 shift closer to GR as we move from the **Plik** to **Camspec**, and finally to the **HiLLiPoP** likelihood combinations. Overall, moving from the leftmost to the rightmost panel of the figure, we observe that the point ($\mu_0 = 0$, $\Sigma_0 = 0$) falls within the 3σ, 2σ, and 1σ confidence limits for the **Plik**, **Camspec**, and **HiLLiPoP** likelihoods, respectively. At its core, this improved consistency with GR is primarily driven by a shift

in the value of $\Sigma_0 \to 0$, as seen by comparing the one-dimensional probability distribution functions in Fig. V.1 for this parameter across the three datasets and confirmed by the numerical results: **Camspec** yields $\Sigma_0 = 0.20^{+0.12}_{-0.14}$ (1.4σ away from GR), while **HiLLiPoP** gives $\Sigma_0 = 0.12^{+0.11}_{-0.13}$ (consistent with GR within 0.9σ).

We again want to point out to the reader that these results are closely related to the behavior of the lensing anomaly in these new likelihoods. Firstly, the strength of the preference for $A_L > 1$ follows the same decreasing trend as the preference for $\Sigma_0 \neq 0$. Specifically, using **Camspec** temperature and polarization data reduces the preference for $A_L > 1$ to less than $\sim 1.6\sigma$ (see Tab. 6 of Ref. [45]), matching the extent of the shift in Σ_0. Using the **HiLLiPoP** likelihood, the results are consistent with $A_L = 1$ within 1 standard deviation (see Tab. 6 of Ref. [24]) — similar to what happens for Σ_0.

Pushing this comparison further, similarly to the A_L anomaly, the MG signal appears to be largely driven by the temperature anisotropy data in both the PR3 and PR4 based likelihoods. As shown by the numerical constraints in Tab. V.2 and the posteriors in Fig. V.3, for the data combinations **Camspec (TT-only)** and **HiLLiPoP (TT-only)** (i.e., those involving only TT measurements at $\ell > 30$), the deviation of Σ_0 from zero can be more pronounced compared to the full TTTEEE likelihood. Specifically, in **Camspec**, the preference for $\Sigma_0 \neq 0$ increases from 1.4σ to 2.2σ when polarization is excluded; see also the light-blue contours in the left-side panel of Fig. V.3. Conversely, with **HiLLiPoP (TT-only)**, no significant deviation from GR is found, as illustrated by the olive contours in the right-side panel of Fig. V.3. This trend closely follows the behavior observed for the lensing anomaly: as reported in Table 6 of Ref. [45], focusing solely on TT spectrum data in **Camspec** increases the lensing anomaly up to 2.3σ. However, no significant deviation from $A_L = 1$ is found when considering only the TT spectrum data in **HiLLiPoP**.

Given the close and expected relationship between Σ_0 and A_L, it is worth examining the impact of varying A_L within the μ, Σ framework using the new PR4-based data combinations. The results are summarized in Tab. V.3. Across all Planck-PR4 anisotropy spectrum datasets, the numerical results for both A_L and Σ_0 remain consistent with the GR values within one standard deviation. Additionally, referring to the left panel of Fig. V.2, we see that GR comfortably falls within the 95% CL contours. This contrasts with the results from **Plik**, shown in the same figure, reinforcing the interpretation that the earlier signals observed in Planck-PR3 spectra were likely due to systematic effects that have since been mitigated (if not erased) in the new data release.

We conclude this section with a final important remark: for **Plik**, **Camspec**, and **HiLLiPoP**, we find μ_0 to be well within the GR limit (see both Fig. V.1 and Fig. V.3), albeit with much wider error bars compared to Σ_0. This can be attributed to the limited impact of this parameter on the CMB spectra, reflecting the physical interpretation of the μ function as $G_{\rm eff}$. Fundamentally, the μ parameter influences the growth of structure; for instance, a higher μ

corresponds to larger values of σ_8. This strong correlation with the growth parameter S_8 is illustrated by the $\mu_0 - S_8$ contour in Fig. V.3. However, since the CMB constrains modified gravity (MG) primarily through the integrated Sachs-Wolfe effect and CMB lensing, it is unable to tightly constrain μ_0.

V.D.2 Constraints on the growth index γ

We anticipate that modifying the growth of perturbations using the γ parametrization will not significantly alter the conclusions drawn in the previous subsection with the (μ, Σ) framework. As usual, to establish a reference case, we first derive results from the Planck-PR3 based spectra using the data combination **Plik**. In this instance, we obtain $\gamma = 0.840^{+0.11}_{-0.074}$ – approximately 3.9σ away from what one might naively expect within GR. This finding aligns with the recently debated claims of deviations from a baseline structure growth history, as reviewed in the introduction.

However, as seen in Tab. V.4 and Fig. V.4, where we display the one-dimensional probability distribution function for the parameter γ_0 as obtained from the three different datasets[V.8], the indication of beyond-GR phenomenology is found to be reduced to the 2σ level in the Planck-PR4-based combination of likelihoods **Camspec** (which gives $\gamma_0 = 0.72 \pm 0.10$) and disappears entirely with **HiLLiPoP**, which shows consistency with GR well within one standard deviation, yielding $\gamma_0 = 0.621 \pm 0.090$.

	Plik	**Camspec**	**Camspec (TT-only)**	**HiLLiPoP**	**HiLLiPoP (TT-only)**
$\boldsymbol{\Omega_b h^2}$	0.02258 ± 0.00017	0.02232 ± 0.00016	$0.02249^{+0.00028}_{-0.00025}$	0.02230 ± 0.00015	0.02228 ± 0.00026
$\boldsymbol{\Omega_c h^2}$	0.1182 ± 0.0015	0.1186 ± 0.0013	0.1165 ± 0.0023	0.1184 ± 0.0013	0.1182 ± 0.0023
$\boldsymbol{100\theta_{MC}}$	1.04112 ± 0.00032	1.04088 ± 0.00027	1.04128 ± 0.00046	1.04091 ± 0.00027	1.04104 ± 0.00048
$\boldsymbol{\tau}$	0.0499 ± 0.0082	0.0487 ± 0.0083	0.0506 ± 0.0085	0.0572 ± 0.0063	0.0572 ± 0.0064
$\boldsymbol{\ln(10^{10} A_s)}$	3.031 ± 0.017	$3.027^{+0.018}_{-0.016}$	3.026 ± 0.017	3.036 ± 0.015	3.036 ± 0.015
$\boldsymbol{n_s}$	0.9704 ± 0.0048	0.9672 ± 0.0045	$0.9722^{+0.0071}_{-0.0063}$	0.9691 ± 0.0044	0.9670 ± 0.0068
$\boldsymbol{\gamma_0}$	$0.840^{+0.11}_{-0.074}$	0.72 ± 0.10	$0.827^{+0.16}_{-0.051}$	0.621 ± 0.090	0.66 ± 0.13
$\boldsymbol{H_0}$ [km/s/Mpc]	68.24 ± 0.69	67.81 ± 0.61	68.8 ± 1.1	67.87 ± 0.61	68.0 ± 1.1
$\boldsymbol{S_8}$	0.806 ± 0.018	0.811 ± 0.017	$0.787^{+0.024}_{-0.028}$	0.813 ± 0.016	0.811 ± 0.027

TABLE V.4. 1σ constraints on the γ model when the lensing amplitude A_L is kept fixed to its reference value $A_L = 1$. As the likelihood combination employed changes from **Plik**, through to **Camspec** and finally to **HiLLiPoP**, the apparent MG evidence signal in Planck-PR3 data disappears, and consistency with $\gamma_0 = 0.55$ is re-established. Counting polarization anisotropies out of the analysis (i.e., the TT-only columns) indicates that this signal is predominantly affecting the temperature data.

[V.8] An interesting difference between the two theoretical setups concerns the correlation with other matter clustering quantities. For instance, as shown in Fig. V.5, we find a weaker degeneracy between the MG parameter γ_0 and quantities such as S_8, compared to what we observed for μ_0, which also impacts the growth of cosmic structures.

	Plik	**Camspec**	**Camspec (TT-only)**	**HiLLiPoP**	**HiLLiPoP (TT-only)**
$\boldsymbol{\Omega_b h^2}$	0.02260 ± 0.00017	0.02257 ± 0.00028	0.02232 ± 0.00016	0.02229 ± 0.00025	0.02230 ± 0.00015
$\boldsymbol{\Omega_c h^2}$	0.1180 ± 0.0015	0.1159 ± 0.0023	0.1186 ± 0.0014	0.1181 ± 0.0024	0.1183 ± 0.0013
$\boldsymbol{100\theta_{MC}}$	1.04115 ± 0.00032	1.04138 ± 0.00047	1.04088 ± 0.00027	1.04107 ± 0.00047	1.04091 ± 0.00027
$\boldsymbol{\tau}$	$0.0494^{+0.0087}_{-0.0075}$	0.0505 ± 0.0085	$0.0487^{+0.0086}_{-0.0072}$	0.0572 ± 0.0063	0.0571 ± 0.0062
$\boldsymbol{\ln(10^{10} A_s)}$	$3.029^{+0.018}_{-0.016}$	$3.025^{+0.018}_{-0.016}$	$3.027^{+0.018}_{-0.015}$	3.036 ± 0.015	3.036 ± 0.015
$\boldsymbol{n_s}$	0.9708 ± 0.0048	0.9739 ± 0.0070	0.9670 ± 0.0046	0.9674 ± 0.0068	0.9692 ± 0.0044
$\boldsymbol{\gamma_0}$	< 0.597	< 0.610	< 0.621	< 0.603	< 0.605
$\boldsymbol{H_0}$ [km/s/Mpc]	68.34 ± 0.71	69.2 ± 1.1	67.81 ± 0.62	68.0 ± 1.1	67.89 ± 0.62
$\boldsymbol{S_8}$	0.803 ± 0.019	0.780 ± 0.028	0.811 ± 0.017	$0.809^{+0.026}_{-0.029}$	0.813 ± 0.017
$\boldsymbol{A_L}$	$1.31^{+0.19}_{-0.33}$	$1.32^{+0.20}_{-0.35}$	$1.20^{+0.17}_{-0.30}$	$1.18^{+0.17}_{-0.30}$	$1.14^{+0.16}_{-0.28}$

TABLE V.5. 1σ constraints on the γ model when the lensing amplitude A_L is left free to vary.

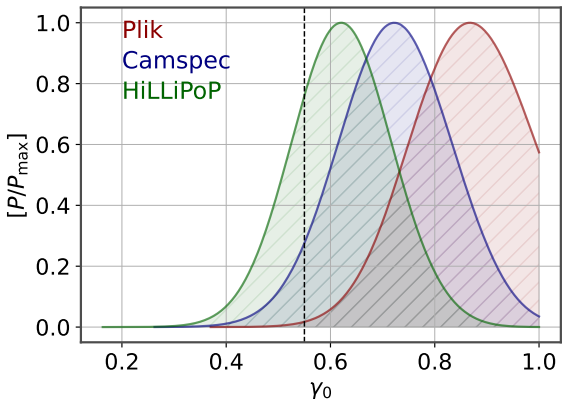


FIG. V.4. One-dimensional marginalized posterior distributions for γ_0 are presented for the three different datasets listed in Sec. V.C. The lensing amplitude A_L is kept fixed at its reference value $A_L = 1$. The vertical dashed line represents the baseline value $\gamma_0 = 0.55$.

As shown in Table V.4 and Fig. V.5, when using a TT-only likelihood instead of the full TTTEEE high-ℓ combination, we observe a shift in **Camspec (TT-only)** towards values of $\gamma_0 > 0.55$. Specifically, we find $\gamma_0 = 0.827^{+0.16}_{-0.051}$, which shifts further away from the GR expectation, as can be seen by comparing the dark blue contours with the light blue contours in the left-side panel of Fig. V.5. In contrast, the value of γ_0 inferred from the **HiLLiPoP (TT-only)** data combination remains consistent with ΛCDM within 1σ. Aside from a significant increase in the uncertainty of parameter value inference, no notable discrepancies are observed between the constraints inferred from the full TT, TE, EE combinations of spectra (dark green contours in the right panel of Fig. V.5) and those obtained by retaining only TT data (olive green contours in the right panel of Fig. V.5).

As discussed in the previous subsection, this trend mirrors the behavior of the lensing anomaly across the two different combinations of TT-only data, suggesting that the results for γ_0 can be significantly influenced by the excess lensing smoothing observed in the acoustic peaks of temperature anisotropy spectra. Therefore, following the same approach as in the (μ-Σ) framework, it is worthwhile to investigate the relationship between γ_0 and A_L when the latter

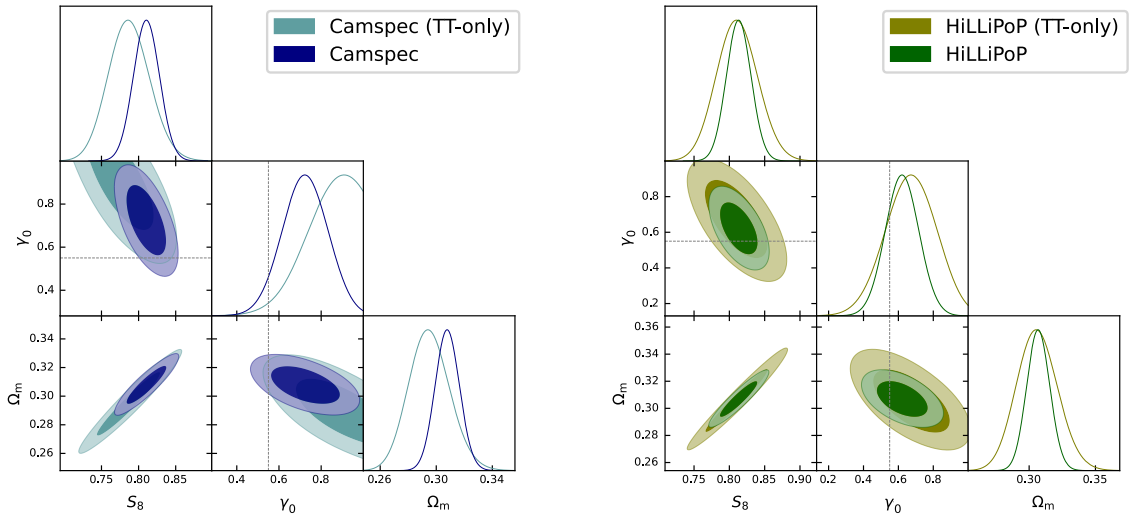


FIG. V.5. One-dimensional probability distribution functions and two-dimensional marginalized contours for the parameters γ_0, Ω_m, and S_8. The lensing amplitude A_L is kept fixed at its reference value $A_L = 1$. In the left-side panel, we show the constraints involving the combinations of likelihood **Camspec** and **Camspec (TT-only)**, whereas in the right-side panel, we show the constraints for the combination of likelihood **HiLLiPoP** and **HiLLiPoP (TT-only)** – all likelihoods are defined in Sec. V.C. The vertical dashed lines in both panels correspond to the baseline value $\gamma_0 = 0.55$.

is allowed to vary freely in the model. The main conclusions from previous sections largely hold: γ_0 exhibits a strong correlation with A_L, which is illustrated for the three datasets in the right panel of Fig. V.2.

Interestingly, allowing A_L to vary precludes achieving a two-tail constraint on γ_0. From **Plik**, we obtain joint constraints of $A_L = 1.31^{+0.19}_{-0.33}$ and $\gamma_0 < 0.597$. Taken at face value, both parameters remain consistent with GR within two standard deviations. However, as shown in the right panel of Fig. V.2, the point $A_L = 1$ and $\gamma_0 = 0.55$ still lies outside the 2D marginalized probability contours in the (A_L, γ_0) plane. Turning to the Planck-PR4-based likelihoods, **Camspec** yields $A_L = 1.32^{+0.20}_{-0.35}$ and $\gamma_0 < 0.610$, while **HiLLiPoP** gives $\gamma_0 < 0.603$ and $A_L = 1.18^{+0.17}_{-0.30}$. When interpreted at face value, these results indicate that both A_L and γ_0 are consistent with their ΛCDM values. The key difference between the results inferred from the Planck-PR4 spectra and those based on **Plik** is that both **Camspec** and **HiLLiPoP** produce contours such that the standard cosmological model now falls within the 95% confidence region in the (A_L,γ_0) plane. In other words, we can recover the standard ΛCDM model without reducing one anomaly at the expense of exacerbating another.

V.E Discussion And Conclusion

Precise CMB observations are a powerful tool for testing whether gravity follows GR on cosmic scales. On the brighter side, CMB physics primarily relies on linear perturbation theory, governed by a system of linearized Einstein-Boltzmann equations, which makes it largely immune to complications from astrophysical processes (beyond foreground contamination) or nonlinear dynamics that can complicate the analysis of late-time structures. Consequently, over the past two decades, numerous extended theories of gravity have been tested against CMB observations.

However, on the downside, in extended theories of gravity, the equations describing the evolution of cosmological perturbations (and the growth of cosmic structures) can deviate significantly from GR in ways that differ from model to model. To face this complexity, various parametric tests have been developed to recast these behaviors and establish broader frameworks for testing GR predictions. Within these frameworks, analyses of the Planck-PR3 2018 spectra have revealed multiple hints of potential deviations from the baseline predictions of a ΛCDM cosmology.

The first longstanding issue concerns the amplitude of the lensing spectrum as inferred from the smoothing of acoustic peaks in the temperature and polarization spectra. Since the 2013 data release, the temperature and polarization power spectra from Planck have shown an excess of lensing, leading to a value of the phenomenological parameter A_L greater than unity. In the Planck-PR3 2018 data release, A_L is measured to be $A_L = 1.180 \pm 0.065$ – i.e., 2.8σ away from the ΛCDM predictions.

Another interesting hint of deviation from GR appears when altering the predictions for the Poisson and lensing equations within the so-called (μ, Σ) framework, where $\mu(k, a)$ and $\Sigma(k, a)$ are two arbitrary functions of the wavenumber k and the scale factor a, both null in GR. Assuming them to be constant both in a and k, Planck-PR3 data measure $\Sigma_0 = 0.35 \pm 0.14$, which is 2.5σ away from the expected value.

Finally, yet another test that produces a non-null result involves measuring the growth index γ that captures potential deviations in the growth of perturbations. This parameter is predicted to be $\gamma = 0.55$ in GR and measured to be $\gamma = 0.840^{+0.011}_{-0.074}$ with Planck-PR3 data.

Although these results are certainly interesting, possibly suggesting departures from a ΛCDM model of structure formation, they come with a good number of caveats and warnings that we already pointed out in the introduction and further stress here: firstly, no indication of a lensing excess, $\Sigma_0 > 0$, or $\gamma \neq 0.55$ has been found in CMB experiments other than Planck, such as ACT and SPT. Secondly, within the Planck-PR3 spectra, a strong correlation between $A_{\rm L}$ and the Σ_0 or γ_0 parameters is observed, suggesting that these three problems may have a common root – most probably the excess smoothing in the TT Planck-PR3 spectrum, which is the main driver of the lensing anomaly. Finally, the latest versions of `CamSpec` [45]

and `HiLLiPoP` [24] (both based on Planck-PR4 `NPIPE` maps) show a much better agreement with $A_{\rm L} = 1$, pointing at an observational systematic issue in the Planck-PR3 spectra and immediately calling into question all the other hints for modified gravity discussed thus far. In an attempt to clarify once and for all whether these anomalous results should be considered genuine indicators of new physics beyond GR or whether they simply arise from observational systematics (while understanding how *exactly* the lensing anomaly fits into the picture), we present in this paper a re-evaluation of the modified gravity constraints inferred from the most recent Planck-PR4 spectra, derived from the new `NPIPE` data release. We stated the main conclusion of our analysis right in the title of this paper: *Planck-PR4 spectra show (better) agreement with GR*. Specifically:

- For the combination of likelihoods labeled as **Camspec** (which is primarily based on the `Camspec` likelihoods for the high-ℓ TT, TE, and EE spectra), we find that the constraint $\Sigma_0 = 0.20^{+0.12}_{-0.14}$ lies within 1.5σ of GR, see also Fig. V.1. Similarly, the indication of beyond-GR phenomenology in terms of non-canonical values of the growth index is reduced to approximately 2σ, with the numerical constraint reading $\gamma_0 = 0.72 \pm 0.10$, see also Fig. V.4.

- For the combination of likelihoods labeled as **HiLLiPoP** (which relies mainly on the `HiLLiPoP` likelihoods for the high-ℓ TT, TE, and EE spectra, along with the `LoLLiPoP` low-ℓ likelihood for E-mode polarization measurements), we find *close* agreement with GR. Within the (μ, Σ) framework, we obtain $\Sigma_0 = 0.12^{+0.11}_{-0.13}$, while for the growth index, we find $\gamma_0 = 0.621 \pm 0.090$ – both consistent with the baseline values within one standard deviation (see Fig. V.1 and Fig. V.4, again).

The better consistency with the predictions of GR found is closely correlated to the lensing anomaly. Indeed, across the different likelihoods, the shift towards values of $\Sigma_0 \neq 0$ and $\gamma_0 > 0.55$ follows the same trend as the reduced preference for $A_L > 1$. Specifically:

- Using **Camspec** for temperature and polarization data shifts the lensing anomaly to less than 1.6σ (see Tab. 6 of Ref. [45]), which roughly corresponds to the shifts observed both in Σ_0 and γ_0 – see Tab. V.2 and Tab. V.4, respectively.

- Using the **HiLLiPoP** combination, the results regarding the lensing amplitude are consistent with $A_L = 1$ within one standard deviation (see, e.g., Tab. 6 of Ref. [24]). Similarly, Σ_0 and γ_0 align with their respective baseline values within one standard deviation.

Pushing this comparison further, we find that, similar to the lensing anomaly, the shifts in the values of Σ_0 and γ_0 observed in **Plik** and, to some extent, in **Camspec** are largely driven by the temperature anisotropy data. Specifically:

- Focusing on **Camspec (TT-only)** (i.e., a combination of data involving only the TT spectrum at $\ell > 30$ from the `Camspec` likelihood), the deviation of Σ_0 from zero is more pronounced compared to the full `Camspec` TTTEEE likelihood, increasing from 1.4σ to 2.2σ, see also Tab. V.2 and Fig. V.3. Notably, in this case, a significant shift in $\gamma_0 = 0.827^{+0.16}_{-0.051}$ is also observed, pulling this parameter away from the GR expectations, see also Tab. V.4 and Fig. V.5.

- Focusing on **HiLLiPoP (TT-only)** (i.e., a combination of data involving only the TT spectrum at $\ell > 30$ from the `HiLLiPoP` likelihood), no significant deviation from GR is observed in either Σ_0 or γ_0 – see also Fig. V.3 and Fig. V.5. This is easily explained by noting that, for the same dataset, A_L remains consistent with unity.

Digging deeper into the correlation with the lensing anomaly, we vary the parameter A_L within both the (μ, Σ) framework and the extended model involving the growth index γ. In these extended parameter spaces, the correlations among parameters are such that the numerical constraints on all modified gravity indicators (i.e., A_L, Σ_0, and γ_0) remain consistent within two standard deviations of GR. This holds true even for the Planck-PR3-based data combination **Plik**. However, the joint marginalized constraints in the (A_L, Σ_0) plane shown in the left panel of Fig. V.2 and in the (A_L, γ_0) plane presented in the right panel of the same figure reveal that, for **Plik**, the point corresponding to ΛCDM consistently falls outside the 95% CL contours in both cases. In contrast, ΛCDM comfortably falls within the 95% CL contours for both **Camspec** and **HiLLiPoP**, underscoring that in these latter cases, Planck-PR4 data agree with the standard ΛCDM model without needing one anomaly to be resolved at the expense of another.

Wrapping everything up, there is a strong basis to conclude that a significant portion of the hints for modified theories of gravity identified and debated over the past few years might stem from observational systematics in the Planck-PR3 data, likely rooted in the well-documented excess smoothing in the high-ℓ peaks of the TT spectrum. To further validate this interpretation, it would be interesting to adapt the `Plik` high-ℓ likelihood to the Planck-PR4 data and reassess Planck's 2018 conclusions in their entirety.

V.F Acknowledgments

W.G. is supported by the Lancaster–Sheffield Consortium for Fundamental Physics under STFC grant: ST/X000621/1. E.D.V. is supported by a Royal Society Dorothy Hodgkin Research Fellowship. This article is based upon work from the COST Action CA21136 - "Addressing observational tensions in cosmology with systematics and fundamental physics (CosmoVerse)", supported by COST - "European Cooperation in Science and Technology".

We acknowledge the IT Services at The University of Sheffield for the provision of services for High Performance Computing.

Afterword

In the paper just presented, the constraints on μ and Σ were obtained by always using the PR3 temperature spectra as the baseline for the analysis, while polarisation data were added selectively. The reason for doing so was simply to show that the deviation of Σ from a null value is mainly driven by the anomalous lensing signal in the TT spectrum measurements of Planck (i.e., through the smoothing of the acoustic peaks).

We reiterate once again that the lack of any anomalous lensing signal of relevance in the PR4 reanalysis of the Planck data stems entirely from their treatment. In particular, and as opposed PR3, the PR4 analysis includes a larger sky fraction [24], while implementing a likelihood that does not take care of most of the foreground emission, which is removed at the map level for a PR4 realisation like Camspec [351]. In conclusion, this work corroborates the idea that the lensing anomaly in the PR3 analysis of Planck's data is a systematic issue rather than a true signal of deviation from the ΛCDM model, given that the PR4 results are closer to the measurements of A_L and Σ by ACT and SPT than they are to PR3.

VI Neutrino Mass Tension or Suppressed Growth Rate of Matter Perturbations?

Preamble to the Paper

In this final chapter on the topic of MG parametrisations, we explore possible connections between the effect that massive neutrinos might have on the large-scale structure and the growth of matter perturbations. In particular, we employ the γ parametrisation once again and treat $\sum m_\nu$, the total neutrino mass, as a free parameter. In the cosmological paradigm, we generally assume $\sum m_\nu = 0.06\,\mathrm{eV}$.

In order to understand how the effects of MG can be compared to those of massive neutrinos at cosmological scales, we briefly introduce how neutrinos affect the large-scale structure growth. A more thorough elucidation of this matter is given in Sec. VI.B of the paper presented here. On large scales, neutrinos cluster just like dark matter: $\delta_m = \delta_c + \delta_b + \delta_\nu$ [352]. As we zoom in closer to the free-streaming scale of neutrinos, k_{fs}, the neutrinos' contribution to the matter clustering starts to drop. Below k_{fs}, the main contribution of neutrinos to the growth of structure happens through their mean energy density Ω_ν, and so through the Hubble friction term (i.e., the second term) in Eq.(II.23): at these scales, the growth of matter perturbations ($\delta_m = \delta_c + \delta_b$) is *suppressed* [352]. As Ω_ν is directly proportional to Σm_ν, an increase in the value of Σm_ν corresponds to a suppression of the standard model's matter power spectrum, denoted in this paper as $P_m(k, a)$, by a factor that can be approximately calculated as [353]:

$$P_m(k, a, \Sigma m_\nu) \approx P_m(k, a) \times \left(1 - 8\frac{\Omega_\nu}{\Omega_m}\right). \tag{VI.1}$$

Any observable that depends on $P_m(k, a)$, such as the lensing potential of the CMB, will also be modified as a consequence.

As done in the papers presented in the last two chapters, the goal here is to take advantage of Planck's lensing anomaly as a way to search for a mechanism that could similarly cause the power loss observed in the temperature spectrum measured by Planck, like MG or, in this case, a non-zero $\sum m_\nu$. What is more, this study is also motivated by DESI's constraint on $\sum m_\nu$ [14], which has been found to exclude almost both of the neutrinos mass orderings allowed by neutrino oscillation experiments. A number of works found that, with the DESI BAO data, we can even extrapolate $\sum m_\nu$ to a negative effective value [354, 355]. Some papers also showed that the dynamical dark energy evidence found, again, by DESI [14] can

be explained in terms of a non-minimally coupled Horndeski model [281, 356]. With these facts in mind, it is then natural to ask whether MG can explain the unexpected constraint on the total neutrino mass in the same way it accounts for DESI's dynamical dark energy evidence and Planck's lensing anomaly. We ask this question in the paper presented below.

Neutrino Mass Tension or Suppressed Growth Rate of Matter Perturbations?

Abstract: Assuming a minimal ΛCDM cosmology with three massive neutrinos, the joint analysis of Planck cosmic microwave background data, DESI baryon acoustic oscillations, and distance moduli measurements of Type Ia supernovae from the Pantheon+ sample sets an upper bound on the total neutrino mass, $\sum m_\nu \lesssim 0.06$–0.07 eV, that lies barely above the lower limit from oscillation experiments. These constraints are mainly driven by mild differences in the inferred values of the matter density parameter across different probes that can be alleviated by introducing additional background-level degrees of freedom (e.g., by dynamical dark energy models). However, in this work we explore an alternative possibility. Since both $\Omega_{\rm m}$ and massive neutrinos critically influence the growth of cosmic structures, we test whether the neutrino mass tension may originate from the way matter clusters, rather than from a breakdown of the ΛCDM expansion history. To this end, we introduce the growth index γ, which characterizes the rate at which matter perturbations grow. Deviations from the standard ΛCDM value ($\gamma \simeq 0.55$) can capture a broad class of models, including non-minimal dark sector physics and modified gravity. We show that allowing γ to vary significantly relaxes the neutrino mass bounds to $\sum m_\nu \lesssim 0.13$–0.2 eV, removing any tension with terrestrial constraints without altering the inferred value of $\Omega_{\rm m}$. However, this comes at the cost of departing from standard growth predictions: to have $\sum m_\nu \gtrsim 0.06$ eV one needs $\gamma > 0.55$, and we find a consistent preference for $\gamma > 0.55$ at the level of $\sim 2\sigma$. This preference increases to ~ 2.5–3σ when a physically motivated prior $\sum m_\nu \geq 0.06$ eV from oscillation experiments is imposed.

VI.A Introduction

What began as Pauli's desperate remedy to preserve energy conservation in beta decay – the postulation of light, electrically neutral, and almost undetectable particles, soon to be called neutrinos – has since grown into one of the most remarkable success stories in modern physics. Despite Pauli's own skepticism about the testability of his hypothesis, not only have three distinct families of neutrinos been experimentally confirmed, but neutrino oscillation experiments have also precisely measured two independent mass-squared differences: $|\Delta m^2_{31}| \equiv |m^2_3 - m^2_1| \simeq 2.5 \times 10^{-3}\,\mathrm{eV}^2$ and $\Delta m^2_{21} \equiv m^2_2 - m^2_1 \simeq 7.5 \times 10^{-5}\,\mathrm{eV}^2$ [357–359]. On the one hand, these measurements imply that at least two neutrino species have nonzero

mass, providing concrete evidence for physics beyond the Standard Model, where neutrinos are originally treated as massless particles. Explaining neutrino masses – either through the effective dimension-five Weinberg operator [360], which induces small Majorana masses by violating lepton number, or via more elaborate seesaw mechanisms that introduce heavy right-handed neutrinos [361–364] – remains an open challenge that attracts significant research interest.

On the other hand, since the sign of Δm^2_{31} remains unknown, two possible mass orderings are still allowed: the *normal ordering* (NO) $\Delta m^2_{31} > 0$ and the *inverted ordering* (IO) $\Delta m^2_{31} < 0$. In both orderings, assuming the lightest neutrino mass is zero, neutrino oscillation experiments provide a lower limit on the total neutrino mass, $\sum m_\nu \equiv m_1 + m_2 + m_3$. This reads $\sum m_\nu > 0.06$ eV for the NO and $\sum m_\nu > 0.1$ eV for the IO [358].

Given their intrinsic importance, determining the neutrino mass ordering and precisely measuring the total neutrino mass $\sum m_\nu$ remain key objectives of neutrino physics. To this end, a number of ongoing and future neutrino oscillation experiments have been designed to resolve the mass ordering while simultaneously improving constraints on $\sum m_\nu$ [365–369]; see also Ref. [370]. Complementing these efforts, direct searches such as the KATRIN experiment provide competitive upper bounds on the total neutrino mass, currently $\sum m_\nu < 1.35$ eV [371].

On the cosmological side, in the simplest scenario – that is, within the standard Λ Cold Dark Matter (ΛCDM) model and three degenerate neutrino states – the DESI collaboration has recently reported that when DESI-2025 Baryon Acoustic Oscillation (BAO) measurements are combined with Planck-PR4 Cosmic Microwave Background (CMB) likelihoods, the cosmological upper limit on the total neutrino mass reads $\sum m_\nu \lesssim 0.064$ eV [372] at 95% Confidence Level (CL). This is worryingly close to the lower limits set by oscillation experiments within the NO and in strong tension with the IO. Furthermore, when extending the analysis to other sources of cosmological and astrophysical data, the cosmological bound on the total neutrino mass can be pushed even below the minimum scale predicted by terrestrial oscillation experiments, i.e., around $\sum m_\nu \lesssim 0.05$ eV [373], leading to an overall tension between oscillation results and cosmological observations [374]. Although part of this tension may reflect differences or inconsistencies across datasets, an even more striking feature emerges when the well-motivated physical prior $\sum m_\nu > 0$ (used in the DESI analyses) is relaxed, and the unphysical region $\sum m_\nu < 0$ is allowed. In this case, negative neutrino masses are found to be favored by the data, as reported by several independent groups [354, 355, 375–377].

It now appears well established that, within the minimal ΛCDM framework, the extremely small values inferred for the total neutrino mass largely originate from a mismatch in the preferred value of Ω_m [372, 375, 378–381]. In particular, BAO distance measurements from DESI favor a lower matter density, which lies in moderate (2-3σ) tension with values inferred from CMB observations. This tension often manifests as a preference for unnaturally small values of $\sum m_\nu$.

Interestingly, when considering extended cosmological scenarios – most notably those allowing for dynamical dark energy – the discrepancy is somewhat alleviated. As originally shown by the DESI collaboration [14, 15, 382] and subsequently corroborated by multiple re-analyses [3, 216, 260, 266–268, 270, 271, 273, 275–278, 280, 281, 285, 289, 291–293, 297, 338, 383–409], adopting a Chevallier Polarski Linder (CPL) parametrization [149, 410], in which the dark energy equation of state varies linearly with the expansion history of the Universe, leads to a significantly improved consistency between DESI BAO and Planck CMB data. In this extended scenario, a preference for dynamical dark energy emerges at the 2.8–4.2σ level, depending on the specific dataset combination. At the same time, the neutrino mass bounds are relaxed up to $\sum m_\nu < 0.16$ eV, restoring agreement with oscillation experiments [15, 359]. Given the mounting evidence for dynamical dark energy and its resilience across diverse independent probes, the predominant – though far from unanimous – narrative surrounding the neutrino mass problem is that the unphysically small cosmological upper limits on $\sum m_\nu$ may themselves reflect the inability of the minimal ΛCDM model to accurately describe the late-time expansion of the Universe. In other terms, within the minimal ΛCDM model, the late-time behavior of $H(z)$ is tightly governed by only two parameters: the present-day Hubble constant H_0 and the matter density parameter Ω_m. Stringent constraints from DESI BAO data on the transverse comoving distance $D_M(z)$, the Hubble parameter $H(z)$, and their combination $D_V(z)$ (all expressed relative to the sound horizon at the drag epoch r_d) translate directly into stringent bounds on Ω_m, driving the mismatch between cosmological upper limits and terrestrial lower limits on the total neutrino mass. Conversely, an evolving dark energy equation of state introduces additional freedom into $H(z)$, allowing more flexibility in fitting BAO measurements at different redshift while accommodating values of Ω_m that are in line with CMB-derived estimates. As a result, the differences in the inferred value of the matter density, combined with the enlarged parameter space, weaken the degeneracy between Ω_m and $\sum m_\nu$, relaxing the upper bounds on the neutrino mass.[VI.1] In this sense, one could argue that dynamical dark energy can be regarded as a solution that operates almost entirely at the level of *background* dynamics, leaving minimal effects at the level of perturbations in the CMB spectra.

Although this interpretation has gained significant traction, in this work we wish to propose and explore a complementary perspective on the neutrino mass discrepancy by shifting the focus from the expansion history to the growth of cosmic structures. The key observation motivating this shift is that both Ω_m and $\sum m_\nu$ not only affect the background expansion but also critically influence the growth of cosmic structures, driving gravitational clustering of over-densities and suppressing structure formation at small scales, respectively. Consequently, a mismatch between cosmological and terrestrial bounds on the total neutrino mass may point

[VI.1] We note that yet another key assumption underlying cosmological limits on the total neutrino mass is the standard neutrino physics. Many alternative models of new physics in the neutrino sector have been proposed and remain viable and actively explored alternatives, often leading to weaker cosmological bounds on $\sum m_\nu$. Without any claim of completeness, see, e.g., Refs. [375, 411–443].

to new physics impacting not only the background expansion but also the dynamics of the growth rate of matter perturbations over time, and structure formation more broadly – either alongside or instead of modifications to the expansion history.

To test this possibility, we consider a non-standard growth of structure by introducing a free growth index parameter, γ [95, 96]. This index effectively captures the physics of structure growth across a wide range of alternative scenarios, from dark energy models to beyond-Einstein gravity. Crucially, γ does not alter the background expansion. Instead, it directly impacts observables sensitive to matter perturbations, such as the CMB spectra and the matter power spectrum. This makes it possible to disentangle different models based on their perturbation-level effects, even when their expansion histories are identical. In this sense, it offers a clean framework to test whether new physics affecting the growth of structure can provide an alternative and complementary route to reconcile cosmological and terrestrial bounds on the neutrino mass. To this end, we perform a comprehensive analysis combining the latest DESI BAO data, Planck CMB likelihoods, and Type Ia supernova distance moduli measurements, explicitly allowing for departures from ΛCDM at the *perturbation* level while keeping the background fixed to the baseline model.

The structure of the manuscript is as follows. We start in Sec. VI.B by describing the linear growth factor and the growth index parameter, illustrating the degeneracy between the former and the neutrino mass. Section VI.C presents the different datasets employed in the analyses and the methodology followed to derive the results presented in Sec. VI.D. We draw our conclusions in Sec. VI.E.

VI.B Growth index and neutrinos

As emphasized in the introduction, our goal is to assess whether the unphysically tight bounds on the total neutrino mass, arising from the mild tension between the values of Ω_m preferred by geometric probes like BAO and those inferred from perturbation-sensitive observables such as the CMB in ΛCDM, may be driven, at least in part, by the assumption of standard structure growth, without necessarily indicating a failure of the standard background expansion, as in dynamical dark energy models. In this regard, many well-motivated extensions of the standard cosmological model predict a background evolution virtually identical to that of ΛCDM. Consequently, these models exhibit degeneracy in $\Omega_m(a)$ and cannot be distinguished based on background-level predictions alone. This happens, for instance, in those ΛCDM extensions where the effective equation of state of the accelerating component in the Hubble equation (whether this is dark energy or a modification of gravity) is free to vary slightly around -1 [444]. Similarly, in the DGP model [445] one can reproduce the same expansion history predicted by fixing $w_0 = -0.78$ and $w_a = 0.32$ in the CPL parametrization [95], making it hard to distinguish different models by means of background quantities only. However,

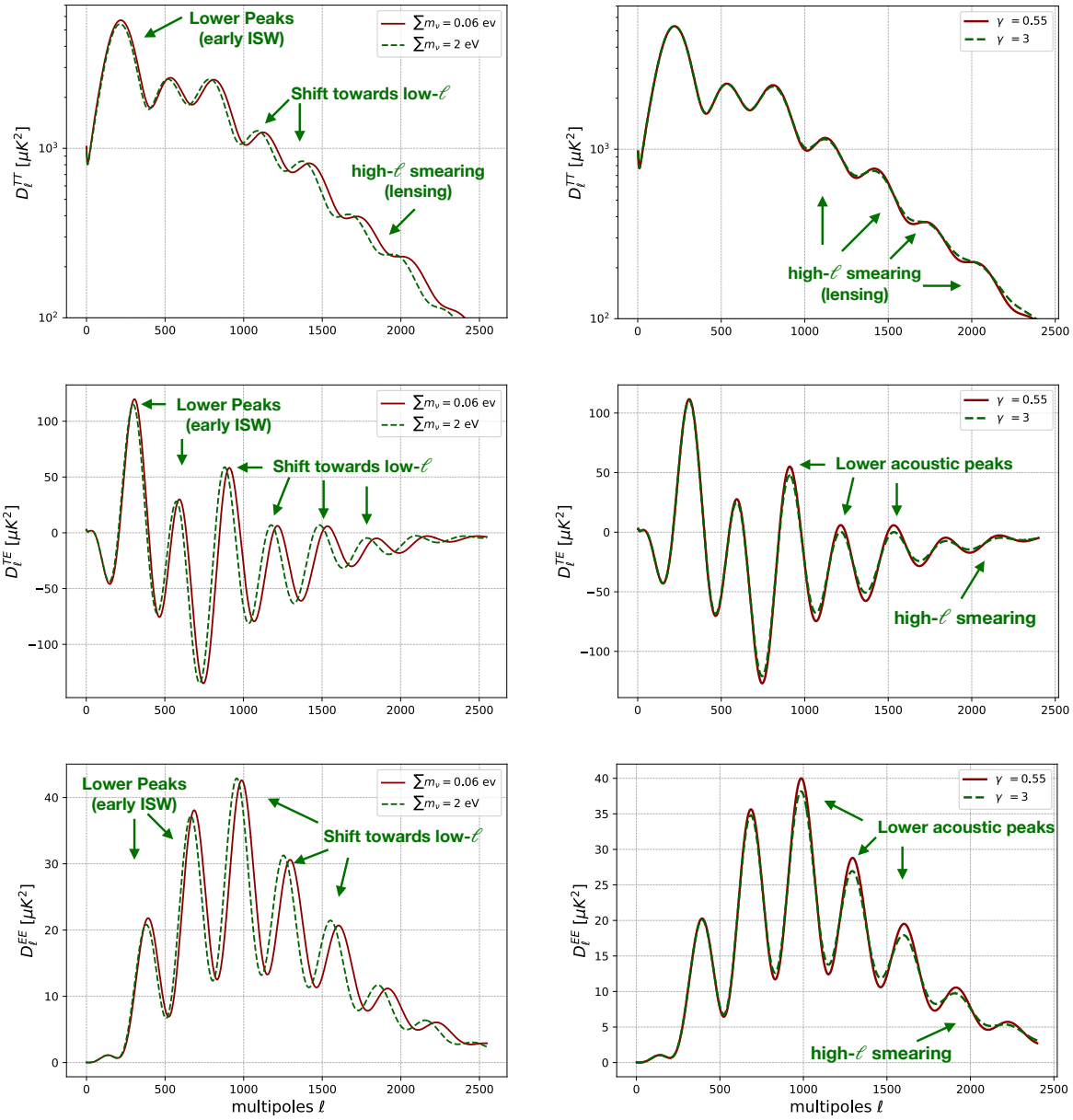


FIG. VI.1. CMB temperature, polarization and cross-correlation power spectra for different values of the total neutrino mass (left panels), and for different values of the growth index γ (right panels), see text for details.

such models can still produce distinct signatures in structure formation. If the actual growth of structures deviates from the ΛCDM expectation, these deviations could partially mimic or offset the effects usually attributed to massive neutrinos. Hence, the evolution of matter perturbations offers a powerful probe of alternative scenarios, ranging from modified gravity theories to non-minimal dark sector physics.

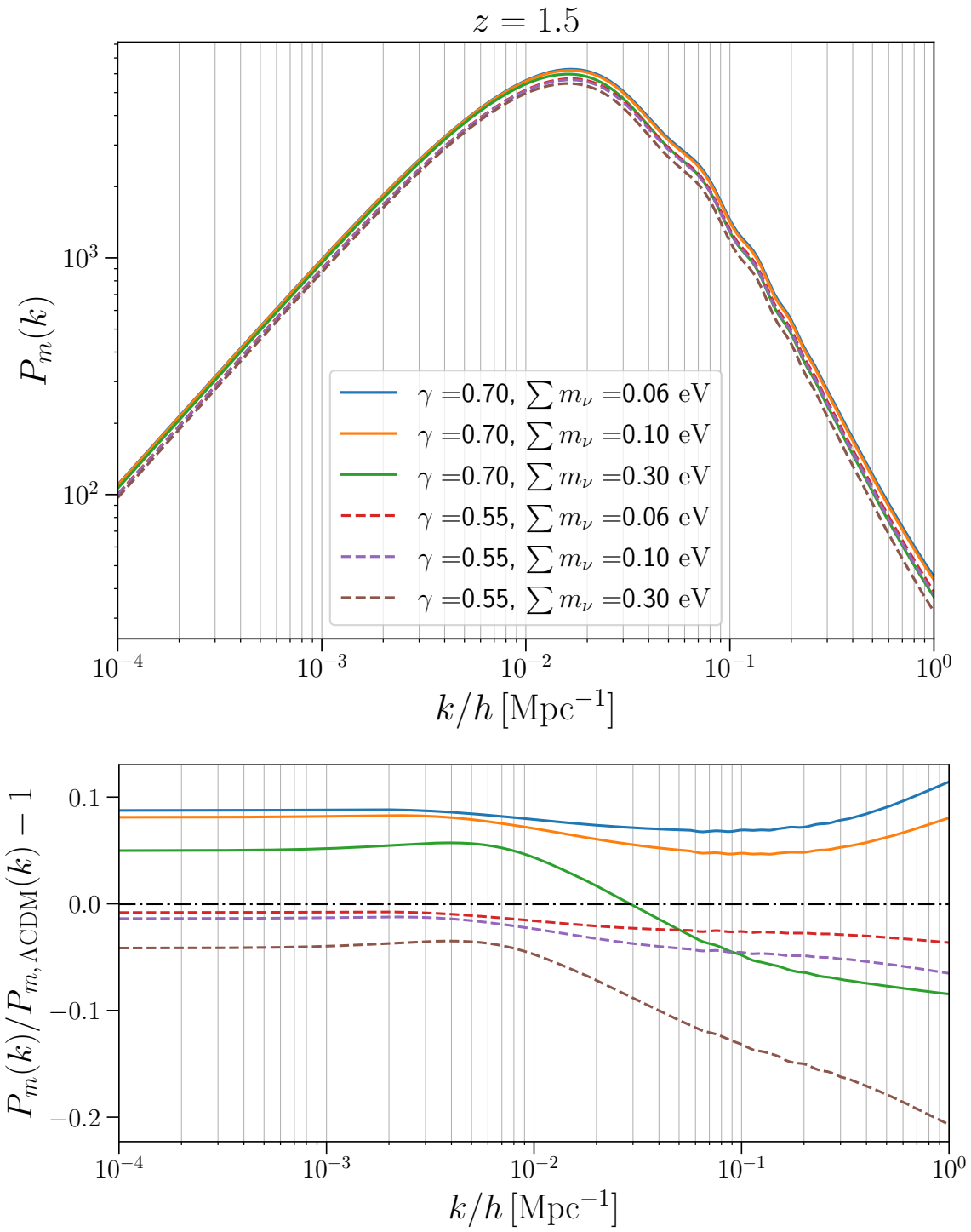


FIG. VI.2. Matter power spectrum at redshift $z = 1.5$ for a standard growth scenario ($\gamma = 0.55$, dashed lines) and a modified one with $\gamma = 0.7$ (solid lines). The different colors depict different values of the total neutrino mass, namely $\sum m_\nu = 0.06$, 0.1, and 0.3 eV. In the bottom panel, we show the ratios of the power spectra for the different parameter cases relative to the ΛCDM model.

The growth of density perturbations can be studied using the perturbed equations of motion derived from the underlying gravitational theory. In the sub-horizon, linear regime, the physical interpretation is straightforward: the growth is driven by a source term proportional to the amount of matter that can cluster, and suppressed by a friction term – often referred to as Hubble drag – associated with the expansion of the Universe [40, 446].

A key observable in this regime is the growth rate of structure, defined as

$$f = \frac{d\ln\delta_{\rm m}}{d\ln a} = \frac{\delta'_{\rm m}}{\delta_{\rm m}}a \ , \tag{VI.2}$$

where $\delta_{\rm m}$ is the matter density contrast and $'$ denotes the derivative with respect to the scale factor. The growth rate captures how efficiently matter overdensities grow over time, from their primordial seeds to the observed large-scale structure.

A commonly used approach to capture deviations from standard structure formation history is to introduce the so-called growth index γ [95, 150], defined as the exponent that yields a power-law solution to the growth rate equation in terms of the matter density parameter:

$$f(a) \simeq \Omega_m(a)^\gamma \simeq \left[\frac{\Omega_{\rm m}a^{-3}}{\Omega_{\rm de}(a)+\Omega_{\rm m}a^{-3}}\right]^\gamma \ . \tag{VI.3}$$

Note that, in this expression, $\Omega_m(a)$ denotes the matter density fraction at scale factor a.

Although γ can, in general, acquire a time and/or scale dependence according to the underlying theory of gravity or dark energy, in many relevant cases it can be accurately approximated as a constant. For a dark energy fluid with constant equation of state w, one finds $\gamma \simeq 3(w-1)/(6w-5)$ [96], which gives the canonical value $\gamma = 6/11 \simeq 0.55$ in the ΛCDM case ($w=-1$) [95]. In many alternative scenarios, however, γ can differ substantially. Just to mention a few concrete examples: in DGP braneworld gravity, one finds $\gamma \approx 0.68$, with less than 2% variation when treated as constant [95, 96], while in $f(R)$ gravity models with mild scale dependence, $\gamma \approx 0.4$ [346], though a significant time dependence may still arise, with present-day slopes as large as $\gamma' \simeq -0.2$ [347].

Overall, the growth index plays a central role in linking theory to observations concerning the clustering of matter perturbations. Specifically, in linear perturbation theory, the evolution of matter inhomogeneities is governed by the linear growth function, defined as $D(a) \equiv \delta_{\rm m}(a)/\delta_{\rm m}(a_0)$, and satisfying $f(a) \equiv d\ln D(a)/d\ln a$. Assuming the parametrization in Eq. (VI.3) with constant γ, we obtain [1, 38]

$$D(\gamma, a) = \exp\left[-\int_a^1 \frac{\Omega_{\rm m}(a)^\gamma}{a}\,da\right], \tag{VI.4}$$

where the growth function is normalized such that $D(\gamma, a=1) = 1$ for all values of γ. This

introduces an important subtlety that will be crucial for interpreting the following results in the context of massive neutrino cosmologies. Namely, models predicting a larger growth index, i.e. $\gamma > 0.55$, imply a *slower* growth rate at any given epoch. Indeed, since $\Omega_{\rm m}(a) < 1$ by construction, Eq. (VI.3) implies $f(\gamma > 0.55, a) < f(\gamma = 0.55, a)$, corresponding to a lower formation rate. However, due to the normalization $D(a = 1) = 1$, a slower growth rate today implies that the linear growth function must have been *larger* in the past to reach the same amplitude at present. In other words, we find that $D(\gamma > 0.55, a) > D(\gamma = 0.55, a)$ for $a < 1$. As a result, models with larger γ predict an enhanced growth function in the past, despite a systematically reduced growth rate throughout cosmic history.

Keeping this result in mind, when it comes to massive neutrinos, many important observations are in order to clarify their impact on structure formation and their connection with the growth index γ.

First and foremost, once neutrinos become non-relativistic particles, they contribute to the total non-relativistic matter density – a contribution that depends ultimately on the value of the total neutrino mass. It is therefore unsurprising that different values of $\sum m_\nu$ would inherently affect the theoretical value of the growth index γ, even within the standard ΛCDM framework. An analytical expression for the growth rate f in the presence of massive neutrinos was derived in Ref. [447]. However, we have numerically confirmed that, even for total neutrino masses well above the current observational limits, the theoretical variations in γ remain negligible compared to the uncertainties in its inferred value. Consequently, having established that the theoretical impact of treating neutrinos as massive particles on γ is effectively negligible for the purpose of this study, we will use $\gamma = 0.55$ as our reference value in the following analysis to test deviations from the ΛCDM model.

A second, more subtle but important point – partially noted in the introduction – is that both massive neutrinos and deviations from the canonical growth index value impact cosmological observables related to perturbations (such as the CMB angular power spectra and the matter power spectrum) in distinct yet qualitatively similar ways.

Massive neutrinos affect the angular power spectra of CMB temperature and polarization anisotropies through several mechanisms: by contributing to the late-time non-relativistic energy density, they alter the angular scale relation at the last scattering surface and modify the late Integrated Sachs-Wolfe (ISW) effect. Moreover, the exact value of $\sum m_\nu$ influences the neutrino transition to the non-relativistic regime by changing their pressure-to-density ratio, inducing metric fluctuations visible in the early ISW effect. Most significantly, massive neutrinos suppress the growth of structure, reducing the amplitude of the matter power spectrum. This suppression also affects the weak lensing of the CMB, damping power on small angular scales.[VI.2] The overall impact on the CMB power spectra includes a reduction in the amplitude of the first acoustic peak (mainly due to the ISW effect) and also a shifting

[VI.2] For constraints on the neutrino mass based on CMB lensing or damping tail effects, see Refs. [448, 449].

of higher acoustic peaks toward lower multipoles. These effects are illustrated in the left panel of Fig. VI.1, which compares two reference total neutrino mass values: $\sum m_\nu = 0.06$ eV (the minimum mass consistent with oscillation experiments and commonly assumed in ΛCDM) and an unphysically large mass of $\sum m_\nu = 2$ eV, chosen to clearly highlight the effects described above.

Similarly, non-canonical values of the growth index γ directly modify the rate at which matter perturbations grow over time, affecting the amplitude and evolution of matter density fluctuations, which in turn influence secondary anisotropies in the CMB through gravitational lensing. Roughly speaking, since the lensing potential is highly sensitive to the distribution and amplitude of matter fluctuations along the line of sight, a growth index different from the canonical $\gamma \approx 0.55$ will alter the clustering strength of matter, changing the gravitational potential wells that CMB photons traverse on their journey toward us. This modification of the gravitational potentials affects the lensing of the CMB by smoothing the acoustic peaks in the temperature and polarization power spectra. This smoothing occurs because lensing deflects the paths of CMB photons, mixing power between different multipoles and reducing the sharpness of the acoustic peaks. As shown in the right panel of Fig. VI.1, increasingly large values of $\gamma > 0.55$ produce more pronounced smoothing at small angular scales (high multipoles) – exactly where the temperature anisotropy spectrum becomes approximately linearly dependent on the lensing power spectrum [65]. This effect can be easily compensated by increasing the neutrino mass, since neutrinos, which are hot dark matter particles, reduce CMB lensing as they suppress clustering at small scales [450, 451], leading to a less pronounced smoothing at low multipoles. Consequently, a large, positive degeneracy is expected among these two parameters, as we will precisely see in the results of our numerical analyses when both γ and $\sum m_\nu$ are free parameters of the model.

Another way to understand the similar effects of γ and $\sum m_\nu$ is by examining their impact on the matter power spectrum. This key complementary observable (which is ultimately linked to the CMB power spectra, especially at high multipoles) provides a direct way to quantify how deviations in γ and the total neutrino mass impact the amplitude and shape of matter fluctuations. Fig. VI.2 depicts the matter power spectrum at $z = 1.5$ for the standard structure formation scenario with $\gamma = 0.55$ and a modified one with $\gamma = 0.7$. Three different possible values for $\sum m_\nu$ have been considered, namely the smallest total neutrino mass consistent with particle physics experiments ($\sum m_\nu = 0.06$ eV) and two other possible cases, $\sum m_\nu = 0.1$ eV and $\sum m_\nu = 0.3$ eV. As expected, larger neutrino masses suppress the matter power spectrum. Neutrinos are hot dark matter relics with very large velocity dispersions, suppressing the growth of structure at scales smaller than their free-streaming scale when they turn non-relativistic. The amount of suppression depends on the precise value of the total neutrino mass.

On the other hand, in cosmologies with a non-standard growth rate, the linear matter power

spectrum can be expressed as [1, 38]:

$$P_{\rm m}(\gamma, k, a) = P_{\rm m}^{\Lambda{\rm CDM}}(k, a = 1)\, D^2(\gamma, a), \tag{VI.5}$$

where $P_{\rm m}^{\Lambda{\rm CDM}}(k, a = 1)$ is the fiducial linear matter power spectrum evaluated today, while $D(\gamma, a)$ is the growth function defined in Eq. (VI.4). As previously pointed out, a larger value of the growth index γ suppresses the growth rate f, while enhancing the growth function $D(\gamma, a)$ at earlier times. According to Eq. (VI.5), this translates into an enhanced matter power spectrum in the past (as seen in Fig. VI.2 at $z = 1.5$). As a result, a positive degeneracy between $\sum m_\nu$ and γ is expected: the suppression of structure formation due to larger neutrino masses can be partially compensated by a larger value of γ, which boosts the amplitude of $D(\gamma, a)$ and hence of the matter power spectrum. This is the case illustrated in Fig. VI.2, where the matter power spectrum obtained for $\sum m_\nu = 0.1$ eV and $\gamma = 0.55$, is nearly indistinguishable from the case of $\sum m_\nu = 0.3$ eV and $\gamma = 0.7$, at least for $k/h > 0.1\,{\rm Mpc}^{-1}$. It is therefore expected that modified growth scenarios with $\gamma > 0.55$ can easily accommodate larger neutrino masses, and this very interesting possibility should be carefully analyzed with the most recent cosmological observations, as we shall present in the following sections.

VI.C Methodology and datasets

The considerations outlined in Sec. VI.B motivate us to analyze extensions of the ΛCDM parameter space – hereafter referred to as λ – by including γ and $\sum m_\nu$ as additional free parameters.[VI.3] In particular, we consider the following extended parameter space combinations:

- $\lambda \cup \{\sum m_\nu\}$,
- $\lambda \cup \{\gamma\}$,
- $\lambda \cup \{\sum m_\nu, \gamma\}$.

The cosmology calculations have been performed with a patched version of the Boltzmann solver `CAMB` [31, 32], specifically adapted for the γ parameterization of modified gravity: `CAMB_GammaPrime_Growth` [38]. We stress that, while γ can, in general, be time-dependent, in this paper we take it to be constant at all redshifts.

To efficiently explore the extended parameter spaces, we perform Markov Chain Monte Carlo (MCMC) analyses using the `Cobaya` sampler [91], varying the cosmological parameters within

[VI.3] Note that λ includes the six standard model parameters, namely: the matter densities of baryons ($\Omega_{\rm b}h^2$) and dark matter ($\Omega_{\rm c}h^2$), the optical depth to reionization (τ), the amplitude (A_s) and spectral index (n_s) of the primordial scalar fluctuations, and the angular size of the sound horizon at last scattering ($\theta_{\rm MC}$).

the flat priors listed in Tab. VI.1. Note that, as explained in more detail in the next section, for the total neutrino mass we consider two relevant cases: one in which we impose a lower prior limit $\sum m_\nu > 0.06$ eV, based on oscillation experiment results assuming the NO, and another in which this lower limit is relaxed to $\sum m_\nu > 0$ eV. We ensure that all produced chains satisfy the Gelman Rubin convergence criterion, requiring a convergence threshold of $R < 0.01$. These chains are then analyzed using the `Getdist` package [349] to derive constraints on the parameter space and generate the plots presented in Sec. VI.D.

The dataset employed in our analysis includes two different combinations of likelihood releases for the CMB spectra measured by the Planck satellite. In particular:

- **Plik**: This includes the Planck-PR3 likelihood `plik` [51] for the temperature (TT), polarization (EE), and temperature polarization cross-correlation (TE) spectra at $\ell > 30$, the `simall` likelihood [23] for E-mode polarization measurements at $\ell < 30$, and the `Commander` likelihood [452] for temperature anisotropies at $\ell < 30$. The `plik` lensing likelihood [52] is also included in this combination.

- **Camspec**: This includes the `Camspec` [45] likelihood for the TT, TE, and EE spectra at $\ell > 30$, based on the Planck-PR4 `NPIPE` CMB maps [53], always in combination with the `simall` likelihood [23] for E-mode polarization and the `Commander` likelihood [452] for temperature anisotropies at $\ell < 30$. In this combination, for CMB lensing, we use the Planck-PR4 `NPIPE` lensing likelihood [53, 67].

Note that we consider these two independent combinations of likelihoods for very important reasons: over the years, several mild anomalies have been identified in the Planck-PR3 data, many of which can alter the constraints on the parameters of interest in this study. The most significant example is the excess smoothing of acoustic peaks observed in the Planck-PR3 spectra, which appears to be reduced in the PR4 likelihoods based on the `NPIPE` maps.[VI.4] Several groups have highlighted that these differences in excess smoothing between the PR3 and PR4 high-multipole likelihoods can significantly impact constraints on the total neutrino mass [302, 337, 355, 359, 374, 454–456]. Similarly, as first shown by some of us in Ref. [2] and subsequently confirmed by the DESI collaboration itself [340, 457], the overall differences in smoothing between the Planck-PR3 and Planck-PR4 spectra also have important consequences for constraints on the growth index γ. Depending on which high-multipole CMB likelihood is used, CMB constraints on γ can vary significantly, resulting in either better or worse agreement with the baseline ΛCDM prediction [2]. Given the significant impact of

[VI.4] This effect can be accurately quantified through the phenomenological parameter $A_{\rm lens}$ [164], which captures the amplitude of the lensing power spectrum inferred from the smoothing of acoustic peaks in the temperature and polarization spectra. Analyses based on the Plik PR3 spectra suggest that $A_{\rm lens}$ deviates from the expected baseline value ($A_{\rm lens} = 1$) at the level of about 2.8σ [23, 304, 332, 453]. In contrast, when using the temperature and polarization PR4 spectra from `Camspec`, the preference for $A_{\rm lens} > 1$ is reduced to below 1.7σ [45], even if this comes at the cost of a moderate internal disagreement between the value of the angular size of the sound horizon, θ, inferred from temperature and polarization data, as well as an overall worse global fit to the different spectra.

Parameter	Prior
$\Omega_{\rm b}h^2$	$[0.005,\ 0.1]$
$\Omega_{\rm c}h^2$	$[0.001,\ 0.99]$
τ	$[0.01,\ 0.8]$
n_s	$[0.8,\ 1.2]$
$\log(10^{10}A_s)$	$[1.61,\ 3.91]$
$100\,\theta_{\rm MC}$	$[0.5,\ 10]$
$\sum m_\nu$ [eV]	$[0,\ 5]$
$\sum m_\nu$ [eV] (NO)	$[0.06,\ 5]$
γ	$[0,\ 1]$

TABLE VI.1. Flat priors adopted for the parameters presented in Sec. VI.C. The label "NO" denotes an additional prior restriction on $\sum m_\nu$, accounting for the normal neutrino ordering constraints from particle physics experiments [358].

choosing either the Planck-PR3 or Planck-PR4 likelihoods on the constraints of both parameters of interest, it is not only important, but in fact essential, to consider both combinations in order to draw reliable conclusions.

In addition to the CMB data outlined above, we consider geometrical probes of the late Universe in the form of precise constraints on the transverse comoving distance, the Hubble rate, and their combination (all relative to the sound horizon at the drag epoch), derived from BAO data and distance modulus measurements from SNIa. In particular, we consider:

- **DESI**: This includes the isotropic and anisotropic BAO measurements from the second data release by the DESI collaboration, based on observations of over 14 million extragalactic objects such as galaxies and quasars [458], as well as Lyman-α tracers [459]. These measurements are summarized in Table IV of Ref. [15].

- **PP**: These are the distance moduli obtained from observations of 1550 SNIa up to $z = 2.26$ in the Pantheon+ sample, without the inclusion of Cepheid host distances [86].

In closing, we would like to spend a few words on the choice of the SNIa sample adopted in this analysis. At present, three independent compilations are available – Pantheon+ [86], DESy5 [217–219], and Union3 [460] – each constructed from different observational datasets and calibration strategies. Including all of them would considerably inflate the number of combinations under consideration, making the analysis unnecessarily cumbersome and less easy to interpret. For this reason, we restrict our analysis to Pantheon+, which is typically regarded as the more conservative catalogue, yielding constraints more consistent with Planck ΛCDM results. In contrast, DESy5 tends to favor deviations, especially in dynamical dark energy models. However, the nature of this shift remains debated. For instance, Ref. [262]

Parameter	Plik+DESI+PP	Plik+DESI+PP (NO)	Camspec+DESI+PP	Camspec+DESI+PP (NO)
$\Omega_b h^2$	0.02260 ± 0.00014	0.02264 ± 0.00014	0.02236 ± 0.00013	0.02240 ± 0.00013
$\Omega_c h^2$	$0.1171^{+0.0012}_{-0.00086}$	$0.1165^{+0.0010}_{-0.00079}$	$0.11740^{+0.00091}_{-0.00075}$	$0.11682^{+0.00081}_{-0.00073}$
$100\,\theta_{MC}$	1.04123 ± 0.00029	1.04129 ± 0.00029	1.04101 ± 0.00024	1.04106 ± 0.00023
τ	$0.0500^{+0.0085}_{-0.0074}$	$0.0502^{+0.0084}_{-0.0074}$	$0.0490^{+0.0086}_{-0.0074}$	$0.0494^{+0.0085}_{-0.0074}$
$\ln(10^{10} A_s)$	$3.027^{+0.018}_{-0.016}$	$3.026^{+0.018}_{-0.016}$	$3.024^{+0.018}_{-0.016}$	$3.023^{+0.018}_{-0.016}$
n_s	0.9726 ± 0.0038	0.9739 ± 0.0037	0.9696 ± 0.0037	0.9711 ± 0.0036
γ	0.707 ± 0.075	0.742 ± 0.069	0.660 ± 0.063	0.696 ± 0.060
$\sum m_\nu$ [eV]	< 0.188	< 0.208	< 0.134	< 0.164
Ω_m	0.2993 ± 0.0040	0.3000 ± 0.0040	0.3004 ± 0.0039	0.3016 ± 0.0038
H_0 [km/s/Mpc]	68.52 ± 0.35	68.42 ± 0.34	68.36 ± 0.32	68.21 ± 0.31
S_8	$0.791^{+0.021}_{-0.014}$	$0.780^{+0.017}_{-0.013}$	$0.798^{+0.016}_{-0.012}$	$0.787^{+0.014}_{-0.011}$

TABLE VI.2. Mean values and 68% CL errors on the most relevant cosmological parameters, including the growth index γ, together with the 95% CL upper limits on the total neutrino mass $\sum m_\nu$ arising from different combinations of cosmological datasets.

links the tension with Planck ΛCDM cosmology to a ∼0.04 mag calibration offset in low-redshift DESy5 SNIa. In response to these findings, the DES collaboration, in Ref. [461], argued that such an offset arises from improved modeling of intrinsic scatter and host galaxy properties, as well as differences in the selection functions used across different samples. While we do not take a stance on this issue, these considerations motivate our use of Pantheon+, as it offers a conservative, well-tested compilation, limits residual systematics, and avoids unnecessary complexity. Last but not least, Pantheon+ yields the tightest neutrino mass constraints across both ΛCDM and dynamical dark energy scenarios (see, e.g., Ref. [15] or Tab. 8 of Ref. [359]).[VI.5]

VI.D Results

We present our main findings in Tab. VI.2, which compares the results obtained by simultaneously varying the neutrino mass and the growth index γ using different CMB likelihoods in combination with DESI BAO and Pantheon+ SNIa measurements. For reference, results obtained by varying each of these parameters individually while keeping the other fixed are reported in Tab. VI.3, and discussed in Appendix A. As already noted in the previous section, we consider two distinct prior choices for $\sum m_\nu$, as listed in Tab. VI.1. Specifically, the label "NO" refers to the case where we impose the lower bound on $\sum m_\nu$ from particle physics experiments, i.e., enforcing a prior $\sum m_\nu > 0.06$ eV, consistent with current neutrino oscillation measurements [358].

[VI.5] For example, combining CMB and DESI with Pantheon+ gives $\sum m_\nu < 0.117$ eV in the dynamical dark energy model, while DESy5 leads to $\sum m_\nu < 0.129$ eV [15].

First and foremost, we confirm that the constraints on the neutrino mass are significantly relaxed compared to the minimal ΛCDM+$\sum m_\nu$ case with the growth index fixed to $\gamma = 0.55$. When both $\sum m_\nu$ and γ are allowed to vary simultaneously, the most constraining bound, $\sum m_\nu < 0.134$ eV at 95% CL, is obtained using the Camspec likelihood in combination with DESI and PP data. This limit remains substantially larger – by more than a factor of 2 – than the corresponding bound obtained for the same dataset combination when fixing $\gamma = 0.55$, which yields $\sum m_\nu < 0.0643$ eV at 95% CL, remarkably close to the lower bound expected from terrestrial measurements.

Secondly, we confirm a non-negligible dependence on the specific CMB likelihood adopted in the analysis. As shown in Tab. VI.2, when varying both parameters, the bound on the neutrino mass changes from the aforementioned $\sum m_\nu < 0.134$ eV to $\sum m_\nu < 0.188$ eV upon replacing the Planck-PR4 Camspec and lensing likelihoods with the older Plik PR3 counterparts, further relaxing the upper limit on the total neutrino mass.

Either way, however, the limits on $\sum m_\nu$ remain largely consistent with the lower bounds from oscillation experiments, both within the NO and the IO, thereby alleviating the emerging tension observed in ΛCDM. Therefore we can relatively safely apply the NO prior in the analysis and enforce $\sum m_\nu > 0.06$ eV. Doing so, the neutrino mass bound from Camspec+DESI+PP becomes further relaxed to $\sum m_\nu < 0.164$ eV, implying a shift of about 0.03 eV towards larger mass values. Similarly, when enforcing the NO prior, the bound obtained from Plik+DESI+PP becomes $\sum m_\nu < 0.208$ eV, corresponding to a shift of approximately 0.02 eV. For both cases, the size and magnitude of this shift can be seen in Fig. VI.3, which shows the 2D 68% and 95% probability contours in the (γ, $\sum m_\nu$) plane. Specifically, in the left panel, the solid green contours correspond to the results obtained from Plik+DESI+PP, while the empty dashed grey contours illustrate how these results shift when a NO prior is imposed. Similarly, the solid red contours in the right panel show the constraints from Camspec+DESI+PP, and the grey contours indicate how they change when enforcing $\sum m_\nu > 0.06$ eV. Clearly, the impact of the prior is more pronounced in the Camspec-based results.

Most importantly, as clearly seen from the two-dimensional allowed regions in Fig. VI.3, there is a strong positive correlation between γ and $\sum m_\nu$: larger values of the total neutrino mass imply a suppression of the growth of structure in the Universe, which can be compensated by a higher growth index. Therefore, when it comes to the growth index γ, several interesting observations are in order. Firstly, using the Camspec likelihood in combination with DESI and SNIa observations (without assuming a NO prior on the neutrino mass), we obtain $\gamma = 0.660 \pm 0.063$ at 68% CL, indicating a $\sim 1.8\sigma$ shift from the standard growth rate model. This shift increases to $\sim 2.1\sigma$ when replacing Camspec with Plik, which yields $\gamma = 0.707 \pm 0.075$ at 68% CL. Due to the strong positive correlation between γ and $\sum m_\nu$, this tendency towards a larger growth index becomes significantly more pronounced when

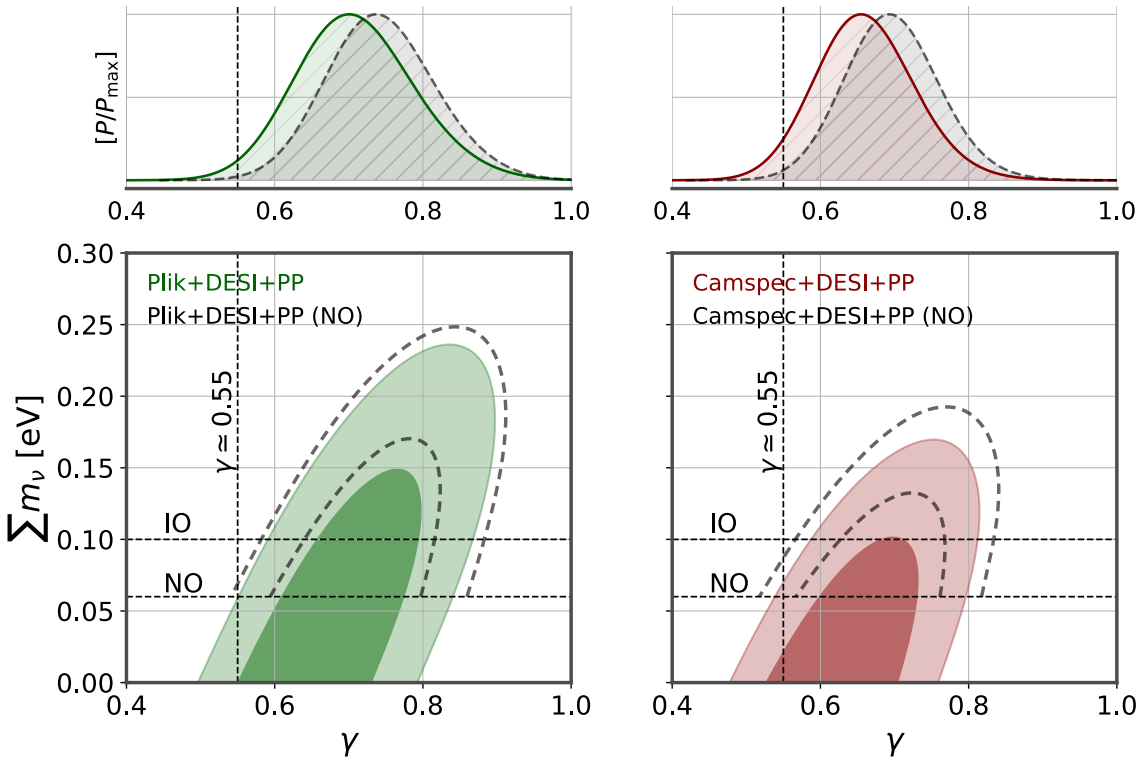


FIG. VI.3. One-dimensional marginalized posterior distributions and two-dimensional 68% and 95% CL contours in the (γ, $\sum m_\nu$) plane for different Planck CMB likelihoods combined with DESI and PP data. The horizontal black dashed line labeled "NO" marks the lower bound on the total neutrino mass set by oscillation experiments ($\sum m_\nu > 0.06$ eV). Values below this line are therefore in tension with oscillation data. Instead, the horizontal black dashed line labeled "IO" indicates the lowest value of the total neutrino mass compatible with the inverted ordering ($\sum m_\nu > 0.1$ eV). If the total neutrino mass lies between the NO and IO lines, only the normal ordering is allowed, whereas for values above the IO line both orderings remain viable. The vertical black dashed line corresponds to the standard prediction for the growth index ($\gamma \simeq 0.55$).

enforcing a NO prior on $\sum m_\nu$. For Camspec+DESI+PP we obtain $\gamma = 0.696 \pm 0.060$, while for Plik+DESI+PP we get $\gamma = 0.742 \pm 0.069$ – i.e., $\sim 2.4\sigma$ and $\sim 2.8\sigma$ away from the expected value of $\gamma = 0.55$, respectively. This further shift towards larger values of γ induced by the NO prior can be clearly seen in the 1D posterior distributions shown in the top histograms of Fig. VI.3. In both the left and right panels, the dashed grey curves (corresponding to the analysis with the NO prior) are visibly shifted towards higher values of γ compared to the distributions obtained when this prior is not applied.

The situation becomes even more intriguing when examining the 2D contours in Fig. VI.3 for the different cases. As already noted, allowing for a non-standard growth of structure can reconcile the current tension in the neutrino sector: even in the most constraining scenario, the cosmological bounds on neutrino masses remain fully compatible with laboratory results,

showing no conflict between cosmological and terrestrial constraints. However, this agreement comes at the cost of departing from the standard structure growth predicted in ΛCDM. As illustrated in the figure, the point defined by the intersection of $\gamma = 0.55$ (i.e., the baseline prediction for the growth index) and $\sum m_\nu = 0.06$ eV (i.e., the minimal mass allowed by oscillation experiments) lies literally at the boundary of the 95% confidence region for Plik+DESI+PP (i.e., the combination allowing the most freedom in the neutrino mass), and very close to the boundary for Camspec+DESI+PP. This means that any neutrino mass value larger than this lower limit would necessarily require a larger γ, thus moving away from ΛCDM predictions for structure formation. Conversely, if we wish to remain consistent with $\gamma = 0.55$ (i.e., following the vertical black dashed line in the figure), the only viable region lies below $\sum m_\nu = 0.06$ eV, thereby reintroducing the tension with oscillation experiments. Similarly, as far as the mass ordering is concerned, while the 95% CL upper bounds on $\sum m_\nu$ remain consistent with both NO and IO, crossing the lower limit set by oscillation experiments within the IO necessarily implies a departure from standard structure formation growth within this framework. Indeed, it is crucial to note that the point defined by $\gamma = 0.55$ and $\sum m_\nu = 0.1$ eV (i.e., the minimal mass allowed within the IO) always lies well outside the 95% probability contours and consistency with the IO (i.e., restricting attention to the region of the plane above the corresponding horizontal line in Fig. VI.3) necessarily implies values of γ significantly larger than those predicted by ΛCDM.

We now turn to a broader exploration of the implications of allowing departures from the standard structure growth history, focusing on additional parameters of interest for other outstanding cosmological tensions. We begin with the $S_8 \equiv \sigma_8(\Omega_{\rm m}/0.3)^{0.5}$ parameter that quantifies the amplitude of matter fluctuations on intermediate scales and which has played a central role in the longstanding discussions surrounding potential discrepancies between CMB-derived results and weak lensing survey estimates [112, 119, 136–138, 210, 214, 229, 231, 462–472]. As shown in Fig. VI.4, we observe a strong anti-correlation between γ and S_8. Larger values of the growth index tend to favour both larger values of the total neutrino mass (see Fig. VI.3) and smaller values of S_8. Quantitatively, for Plik+DESI+PP, we find $S_8 = 0.791^{+0.021}_{-0.014}$, which reduces to $S_8 = 0.780^{+0.017}_{-0.013}$ when assuming a NO prior. Similarly, for the Camspec likelihood, we obtain $S_8 = 0.798^{+0.016}_{-0.012}$ without prior assumptions, shifting to $S_8 = 0.787^{+0.014}_{-0.011}$ under the NO prior. In both cases, as seen in Fig. VI.4, the NO prior leads to a noticeable drift of the posteriors toward lower S_8 values and away from the canonical GR limit $\gamma = 0.55$, echoing the behaviour already discussed in previous sections. This interplay between γ, $\sum m_\nu$ and S_8 can be particularly relevant in light of ongoing discussions about the persistence of the weak lensing discrepancy, generalizing the discussion presented in Refs. [1, 38] to massive neutrino cosmologies. Despite recent claims suggesting this tension may have been alleviated or even resolved [27, 472], our results indicate that the inclusion of a flexible growth history introduces parameter shifts in a

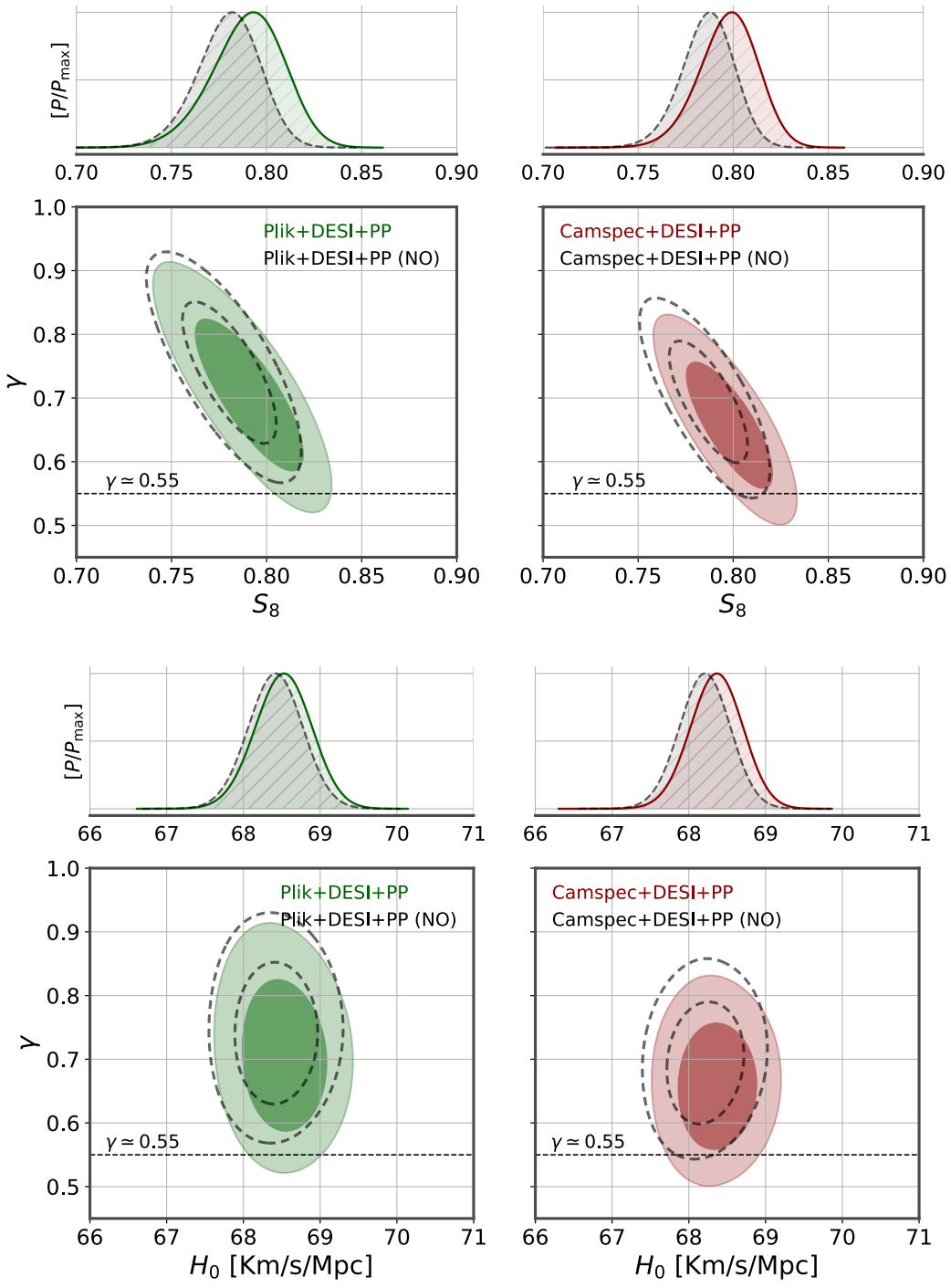


FIG. VI.4. One-dimensional marginalized posterior distributions and two-dimensional 68% and 95% CL probability contours for γ and S_8 (top panels) and γ and H_0 (bottom panels) for the different Planck CMB likelihoods combined with DESI and PP. The horizontal black dashed line corresponds to the standard prediction for the growth index, $\gamma \simeq 0.55$.

direction potentially capable of reconciling lensing data with CMB-derived inferences, should the discrepancy persist. If we aim to be more quantitative in assessing the extent to which varying γ alleviates the S_8 tension, we should first note that weak-lensing surveys report somewhat different determinations of S_8. To mention a few concrete examples, KiDS-1000 in combination with 2dFLenS and BOSS yields $S_8 = 0.766^{+0.020}_{-0.014}$ [136], the DES-Y3 3×2pt analysis gives $S_8 = 0.776 \pm 0.017$ [137], while the more recent KiDS-Legacy release finds $S_8 = 0.815^{+0.016}_{-0.021}$ [472], which, as mentioned above, shows no discrepancy with the ΛCDM Planck-only based inferences of $S_8 = 0.834 \pm 0.016$ [23].[VI.6] A direct quantification of the tension is therefore non-trivial, not only because of these differing estimates but also because S_8 is itself a model-dependent parameter. As such, a fully consistent comparison would require reanalyzing the weak-lensing data within the same theoretical framework adopted here, which lies well beyond the scope of this manuscript. Nevertheless, even accounting for these caveats, one can clearly see that the results presented in Appendix A, Tab. VI.3, obtained for fixed $\gamma = 0.55$, yield values scattered around $S_8 \simeq 0.816$ that, considering the uncertainties, remain in a ~ 2.1–2.3σ tension with KiDS-1000+2dFLenS+BOSS and DES-Y3, while being in good agreement with KiDS-Legacy. By contrast, when allowing the growth index γ to vary freely, the inferred values shift to $S_8 \simeq 0.79$–0.80, consistently lying within $\lesssim 1\sigma$ of all weak-lensing determinations. This heuristic argument shows that a flexible growth history can naturally drive the inferred clustering amplitude toward substantially improved consistency with lensing observations. More broadly, this drift underscores the relevance of neutrino physics assumptions in any interpretation of the weak lensing tension, and the model dependence of derived parameters such as S_8. Taken together, these findings suggest that S_8 remains sensitive to beyond-ΛCDM physics, particularly when degrees of freedom such as modified growth or non-canonical neutrino properties are considered.

In contrast to the behaviour observed for S_8, we do not find any significant correlation between γ and H_0 in our analysis. The values we obtain remain remarkably stable across datasets and assumptions. For Plik+DESI+PP we find $H_0 = 68.52 \pm 0.35$ Km/s/Mpc, shifting only slightly to $H_0 = 68.42 \pm 0.34$ Km/s/Mpc when a NO prior is imposed. Similarly, for Camspec+DESI+PP we obtain $H_0 = 68.36 \pm 0.32$ Km/s/Mpc (without prior assumptions), decreasing mildly to $H_0 = 68.21 \pm 0.31$ Km/s/Mpc under the NO prior. These minor shifts can be traced back to the known negative correlation between H_0 and $\sum m_\nu$, and are not driven by the growth index itself. As such, while an alternative structure growth model with a free γ can relax the neutrino mass bounds and might remain of interest in relation to the weak lensing discrepancy (should this issue persist rather than fade definitively) it does not provide a mechanism for addressing the Hubble tension. The path toward a coherent explanation capable of simultaneously accounting for all current anomalies remains, at present, largely

[VI.6] For a more comprehensive review of S_8 measurements from different weak-lensing surveys, see Ref. [78].

unfulfilled.

Last but not least, it is important to consider the matter density parameter $\Omega_{\rm m}$, as it plays a key role in the interpretation of our results and lies at the heart of the broader discussion on the neutrino mass tension. As seen by comparing the values given in Tab. VI.2 (as well as in Tab. VI.3 in Appendix A) across all the parameter spaces explored and for all combinations of datasets, we find values of $\Omega_{\rm m}$ that are consistent within one standard deviation. Specifically, when varying only the total neutrino mass, we find $\Omega_{\rm m} = 0.3009 \pm 0.0037$ for Plik+DESI+PP and $\Omega_{\rm m} = 0.3018 \pm 0.0036$ for Camspec+DESI+PP. When varying only the growth index γ, these values remain essentially unchanged: $\Omega_{\rm m} = 0.2990 \pm 0.0038$ (Plik+DESI+PP) and $\Omega_{\rm m} = 0.3006 \pm 0.0037$ (Camspec+DESI+PP).[VI.7] Finally, when both γ and $\sum m_\nu$ are varied simultaneously, we obtain consistent values such as $\Omega_{\rm m} = 0.2993 \pm 0.0040$ (Plik+DESI+PP) and $\Omega_{\rm m} = 0.3004 \pm 0.0039$ (Camspec+DESI+PP). Under the NO prior, these latter two values shift only mildly to $\Omega_{\rm m} = 0.3000 \pm 0.0040$ and $\Omega_{\rm m} = 0.3016 \pm 0.0038$, respectively. These results illustrate a crucial point: fixing or varying γ alongside the total neutrino mass does not significantly alter the inferred value of $\Omega_{\rm m}$. However, this consistency hides an important distinction. Fixing $\gamma = 0.55$ leads to neutrino mass bounds that are very close to lower limits from particle physics experiments, to the extent of raising a very concerning tension. Conversely, allowing γ to vary relaxes this problem *without* changing the value of $\Omega_{\rm m}$. This finding directly challenges the often-stated claim that the neutrino mass tension originates from constraints on $\Omega_{\rm m}$ inferred from different probes under the assumption of a ΛCDM background. We show that this is true if one also assumes a standard ΛCDM structure formation history. Once this assumption is relaxed, the tension in $\sum m_\nu$ can be alleviated without altering the background evolution. More broadly, our results demonstrate that it is possible to relax constraints on the total neutrino mass by modifying the structure growth history, without changing the inferred values of parameters describing the background dynamics and without invoking additional degrees of freedom at the background level, such as scenarios involving dynamical dark energy. This offers a complementary path to addressing the neutrino mass problem, shifting the attention to the important imprints of neutrinos on perturbation-level observables rather than on the background expansion itself. Exploring this interplay between perturbation-level and background-level modifications is crucial, as changes to the expansion history that help relax neutrino mass bounds often come at the cost of lowering H_0 further, thereby exacerbating the Hubble tension. If the goal is to retain enough freedom to simultaneously address multiple anomalies within a coherent framework, it becomes essential to introduce the necessary degrees of freedom and explore both aspects. In this sense, alternative structure formation histories may offer a viable and physically well-motivated possibility.

[VI.7] We note that the tendency toward larger values of the growth index γ is also present when fixing the total neutrino mass in the cosmological model, and that it persists regardless of the CMB likelihood employed; see the discussion in Appendix A.

VI.E Summary

Assuming the minimal ΛCDM framework with three degenerate massive neutrinos, the DESI collaboration recently reported an upper bound of $\sum m_\nu \lesssim 0.064$ eV at 95% CL when combining DESI-2025 BAO data with Planck-PR4 CMB observations. This bound is uncomfortably close to the lower limit set by oscillation experiments in the case of normal ordering and firmly excludes the inverted ordering, thus raising serious concerns. In particular, it has been argued that these tight limits mainly stem from a mild but persistent mismatch in the preferred matter density: BAO measurements from DESI favour lower values of $\Omega_{\rm m}$ than those inferred from the CMB, resulting in an indirect pressure toward smaller values of $\sum m_\nu$.

An appealing way to alleviate this issue is to consider extensions beyond the standard cosmological framework. Models featuring dynamical dark energy, which modify the late-time expansion history of the Universe, can significantly relax the neutrino mass bounds and reduce the tension. Therefore, the mainstream (but far from universally accepted) interpretation is that the unnaturally low bounds on $\sum m_\nu$ may themselves point to the failure of ΛCDM to accurately describe the expansion history at late times. However, matter density and massive neutrinos do not only affect the background evolution, but also play crucial roles in the growth of cosmic structure: matter density drives the gravitational clustering of overdensities, while massive neutrinos suppress the formation of structure at small scales due to their large thermal velocities. Therefore, new physics affecting the dynamics of primordial perturbations and structure formation can offer a complementary possibility to alleviate the neutrino mass tension.

In this paper, we explore this possibility by considering a flexible, phenomenological approach to structure growth by allowing the growth rate $f(a)$ to depart from its ΛCDM prediction. Specifically, we parametrize it using the growth index γ through $f(a) \simeq \Omega_{\rm m}(a)^\gamma$ and treat γ as a free parameter. A larger value of γ suppresses the growth rate, implying a larger growth function in the past and modifying the way matter perturbations cluster in the (early) Universe. This, in turn, affects both the high-multipole CMB lensing signal and the shape of the matter power spectrum. Such effects can be compensated by a larger neutrino mass. In this regard, it is important to emphasize the role of CMB lensing in driving the neutrino mass bounds, particularly when the growth index is fixed to its standard value. The lensing potential encodes the integrated matter distribution along the line of sight and is especially sensitive to the amplitude of clustering on intermediate and small scales. Since massive neutrinos suppress structure growth, their effect is clearly imprinted in the lensing signal at high multipoles. In the standard scenario with $\gamma = 0.55$, any deviation from the measured lensing power is necessarily attributed to a lower neutrino mass, thereby tightening the constraint on $\sum m_\nu$. However, when γ is allowed to vary, structure suppression can be partially absorbed by a larger growth index, weakening the need for extremely small neutrino masses.

This illustrates how perturbation-level flexibility, especially in structure growth, can mitigate tensions that appear under stricter assumptions.
Our main results can be summarized as follows:

- By jointly varying $\sum m_\nu$ and the growth index γ, we find that the cosmological bounds on the total neutrino mass are substantially relaxed compared to the standard case. Across all combinations of Planck-CMB, DESI-BAO, and Pantheon+ SNIa data, we find that allowing γ to vary broadens the allowed range for $\sum m_\nu$ from ~ 0.06–0.07 eV (assuming $\gamma = 0.55$) up to ~ 0.13–0.2 eV. These values are consistent with terrestrial constraints and demonstrate that new physics at the perturbation level offers a viable, complementary solution to the neutrino mass tension.

- This agreement, however, comes at the cost of deviating from the standard structure growth predictions of ΛCDM. As shown in Fig. VI.3, the point defined by $\gamma = 0.55$ (i.e., the baseline value of γ) and $\sum m_\nu = 0.06$ eV (i.e., the lowest total neutrino mass allowed by particle physics experiments) lies on the boundary of the 95% confidence region. This means that any neutrino mass value larger than this lower limit would necessarily require a larger γ, thus moving away from ΛCDM predictions for structure formation. Conversely, if we wish to remain consistent with $\gamma = 0.55$, the only viable region lies below $\sum m_\nu = 0.06$ eV, reintroducing the tension with oscillation experiments.

- Regarding the neutrino mass ordering, we find that the inverted ordering remains allowed within modified structure growth models. However, accommodating mass values consistent with the inverted ordering requires values of γ significantly larger than the ΛCDM prediction.

- Overall, we observe a consistent trend favouring larger-than-standard values of γ. This preference persists whether one varies only γ or both γ and $\sum m_\nu$ simultaneously. In the latter case, the preference reaches 1.8σ for Plik+DESI+PP and 2σ for Camspec+DESI+PP. Imposing a prior consistent with normal ordering ($\sum m_\nu > 0.06$ eV) strengthens the preference further, up to 2.4σ and 2.8σ, respectively.

- Importantly, we find that allowing γ to vary relaxes the neutrino mass bounds without altering the inferred value of $\Omega_{\rm m}$. This is clearly seen by comparing the values reported in Tab. VI.2 and Tab. VI.3. While previous studies attributed the tight neutrino mass bounds to the ability of ΛCDM to accurately describe the late-time background dynamics, we show that this interpretation only holds under the assumption of standard ΛCDM structure growth. Once this assumption is relaxed, the tension can be alleviated without modifying the ΛCDM background evolution.

- Last but not least, Fig. VI.4 reveals a strong anti-correlation between γ and S_8: larger growth indices lead to both larger allowed neutrino masses and smaller values of S_8. This interplay may be relevant for the ongoing debate about the weak lensing anomaly. While some recent analyses suggest that the S_8 tension may be subsiding, our results indicate that a flexible growth history can still shift parameters in a direction that could better reconcile lensing and CMB data, if the tension persists. On the other hand, we find no significant correlation between γ and H_0, implying that growth index freedom does not offer a mechanism for addressing the Hubble tension.

All in all, in the absence of a definitive cosmological detection of neutrino mass, our analysis provides a novel and complementary angle on the tension between cosmology and particle physics. It highlights the critical role of perturbations in constraining new physics and underscores the importance of testing both the background and structure formation histories when interpreting cosmological data. As future observations improve and our modelling of structure formation becomes more refined, non-canonical scenarios (e.g., modified theories of gravity or a non-minimal dark sector) may well emerge as essential components of a more complete cosmological paradigm that accurately accounts for massive neutrinos.

VI.F Acknowledgments

W.G. is supported by the Lancaster Sheffield Consortium for Fundamental Physics under STFC grant: ST/X000621/1. O.M. acknowledges the financial support from the MCIU with funding from the European Union NextGenerationEU (PRTR-C17.I01) and Generalitat Valenciana (ASFAE/2022/020). E.D.V. is supported by a Royal Society Dorothy Hodgkin Research Fellowship. This work has been supported also by the Spanish MCIN/AEI/10.13039/501100011033 grants PID2020-113644GB-I00, ID2023-148162NB-C21 and PID2023-148162NB-C22, and by the European ITN project HIDDeN (H2020-MSCA-ITN-2019/860881-HIDDeN) and SE project ASYMMETRY (HORIZON-MSCA-2021-SE-01/101086085-ASYMMETRY) and well as by the Generalitat Valenciana grants PROMETEO/2019/083, PROMETEO/2021/083, and CIPROM/2022/69. OM acknowledges the financial support from the MCIU with funding from the European Union NextGenerationEU (PRTR-C17.I01) and Generalitat Valenciana (ASFAE/2022/020) We acknowledge the IT Services at The University of Sheffield for the provision of services for High Performance Computing. This article is based upon work from the COST Action CA21136 - "Addressing observational tensions in cosmology with systematics and fundamental physics (CosmoVerse)", supported by COST - "European Cooperation in Science and Technology".

Appendix A: Full Analysis Results

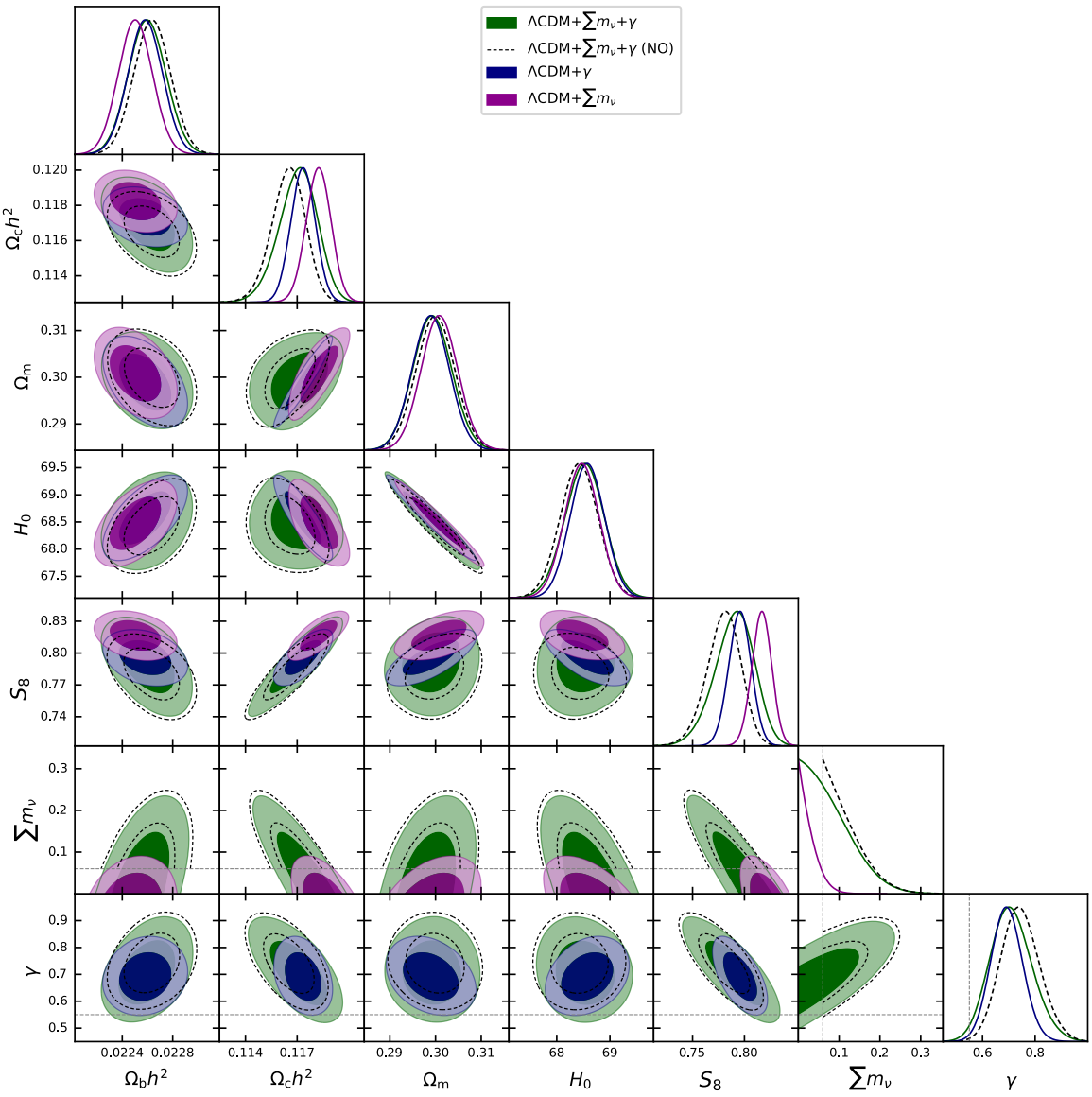


FIG. VI.5. One-dimensional marginalized posterior distributions and two-dimensional 68% and 95% CL contours for several cosmological parameters of interest, obtained from the analysis of Plik+DESI+PP under the different cosmological models and prior choices indicated in the figure legend. The dashed grey lines denote the lower bound on the total neutrino mass from oscillation experiments ($\sum m_\nu \simeq 0.06$ eV) and the standard ΛCDM prediction for the growth index ($\gamma = 0.55$).

In this Appendix, we briefly illustrate the cosmological constraints on the growth index γ and on the total neutrino mass $\sum m_\nu$ for cosmological scenarios in which only one between $\sum m_\nu$ and γ is allowed to vary freely while the other is kept fixed in the model.

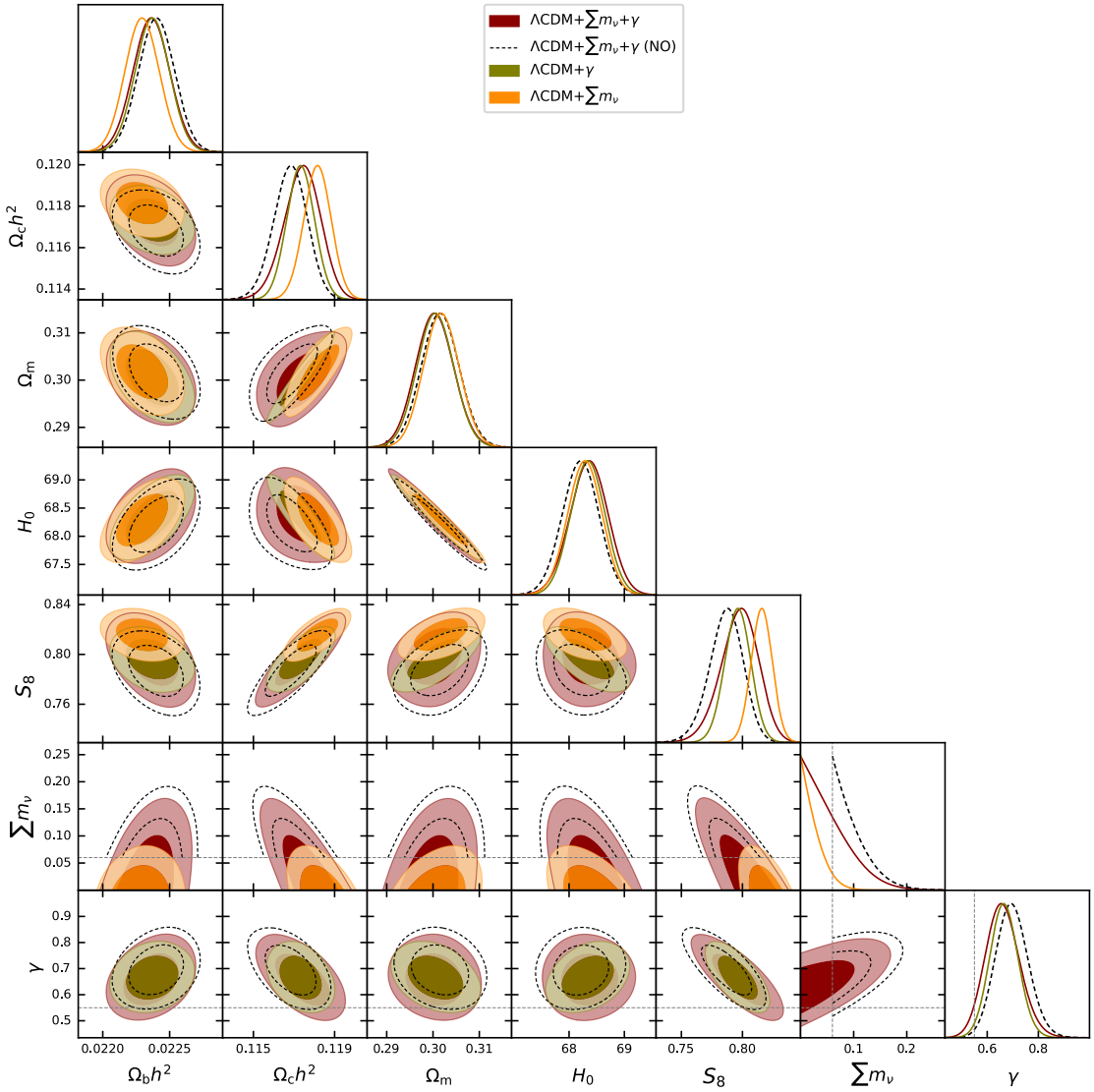


FIG. VI.6. One-dimensional marginalized posterior distributions and two-dimensional 68% and 95% CL contours for several cosmological parameters of interest, obtained from the analysis of Camspec+DESI+PP under the different cosmological models and prior choices indicated in the figure legend. The dashed grey lines denote the lower bound on the total neutrino mass from oscillation experiments ($\sum m_\nu \simeq 0.06$ eV) and the standard ΛCDM prediction for the growth index ($\gamma = 0.55$).

We show in Tab. VI.3 the main results obtained in this scenario, while Fig. VI.5 and Fig. VI.6 display the one-dimensional distribution functions and the two-dimensional probability contours obtained for the different models (including the case where both γ and $\sum m_\nu$ are varied simultaneously), for Plik+DESI+PP and Camspec+DESI+PP, respectively.

Focusing on the neutrino mass constraints within a universe with a standard growth index $\gamma = 0.55$, we find extremely tight bounds on $\sum m_\nu$ for both the Camspec and Plik CMB

Parameter	**ΛCDM+$\sum m_\nu$**		**ΛCDM+γ**	
	Plik+DESI+PP	**Camspec+DESI+PP**	**Plik+DESI+PP**	**Camspec+DESI+PP**
$\Omega_{\rm b}h^2$	0.02250 ± 0.00013	0.02229 ± 0.00012	0.02258 ± 0.00013	0.02237 ± 0.00012
$\Omega_{\rm c}h^2$	0.11824 ± 0.00067	0.11815 ± 0.00064	0.11734 ± 0.00066	0.11733 ± 0.00064
$100\,\theta_{\rm MC}$	1.04116 ± 0.00028	1.04096 ± 0.00023	1.04121 ± 0.00028	1.04101 ± 0.00023
τ	$0.0580^{+0.0066}_{-0.0075}$	0.0561 ± 0.0069	$0.0498^{+0.0085}_{-0.0075}$	$0.0488^{+0.0085}_{-0.0073}$
$\log(10^{10}A_{\rm s})$	3.048 ± 0.014	3.042 ± 0.014	$3.028^{+0.018}_{-0.016}$	$3.024^{+0.018}_{-0.015}$
$n_{\rm s}$	0.9694 ± 0.0033	0.9676 ± 0.0034	0.9719 ± 0.0033	0.9698 ± 0.0035
$\sum m_\nu$ [eV]	< 0.0710	< 0.0643	0.06	0.06
γ	0.55	0.55	0.692 ± 0.056	0.666 ± 0.052
$\Omega_{\rm m}$	0.3009 ± 0.0037	0.3018 ± 0.0036	0.2990 ± 0.0038	0.3006 ± 0.0037
H_0 [Km/s/Mpc]	68.47 ± 0.30	68.28 ± 0.29	68.57 ± 0.30	68.34 ± 0.29
S_8	0.8167 ± 0.0090	0.8157 ± 0.0082	0.796 ± 0.010	0.796 ± 0.010

TABLE VI.3. Mean values and 68% CL errors on the most relevant cosmological parameters, including the growth index γ, together with the 95% CL upper limits on the total neutrino mass $\sum m_\nu$ arising from different combinations of cosmological data sets.

likelihoods. These 95% CL upper limits are $\sum m_\nu < 0.0643$ eV for Camspec+DESI+PP, and slightly relaxed to $\sum m_\nu < 0.0710$ eV for Plik+DESI+PP. In either case, the limits are close to the minimum bound expected from neutrino oscillation experiments, $\sum m_\nu > 0.06$ eV, hinting at a mild tension.

In the complementary case where the total neutrino mass is fixed to $\sum m_\nu = 0.06$ eV and the growth index is allowed to vary, the tendency toward larger values of γ is confirmed. Indeed, we find $\gamma = 0.692 \pm 0.056$ for Plik+DESI+PP and $\gamma = 0.666 \pm 0.052$ for Camspec+DESI+PP, deviating from the expected value by $\sim 2.5\sigma$ and $\sim 2.2\sigma$, respectively.

As for the correlations between γ and the remaining cosmological parameters, they behave as expected: as seen both in Fig. VI.5 and Fig. VI.6 γ is negatively correlated with $\Omega_c h^2$, due to the growth rate being parameterized as $\Omega_m(a)^\gamma$.

Afterword

To conclude this chapter, we emphasise that the imposition of a prior on Σm_ν affects the constraints on γ, as can be seen in Fig. VI.3, by virtue of two distinct effects: a shift and a stretch. Firstly, the clear positive degeneracy existing between γ and Σm_ν is simply truncated at higher Σm_ν, naturally shifting γ to larger values. Secondly, we have a volume effect: by restricting the prior on the neutrino mass, our posterior ends up stretching onto an area of the parameter space where the values of Σm_ν have a smaller probability of being consistent with the data (at least according to DESI, which prefers lower values for the neutrino mass) but where the probability of other parameters, which correlate with Σm_ν, is instead higher (such as Ω_m, which is measured to be smaller by DESI as compared to the CMB constraints).

VII Updated Constraints on Omnipotent Dark Energy: a Comprehensive Analysis with CMB and BAO Data

Preamble to the Paper

This chapter is dedicated to the study of a modification of the ΛCDM model that is introduced not at the perturbative level, as it was the case for the papers on MG treated in the last three chapters, but at the level of the background expansion equations outlined in the first part of chapter III; the perturbations of other species are still impacted by this change though, as the Hubble function still enters perturbation equations like Eq.(II.23).

In particular, we turn Λ, the cosmological constant, into DE, that is to say a form of energy that still drives the accelerated expansion of the universe but whose energy density, $\rho_{\rm DE}$, varies in time. Consistently with the phenomenological approach adopted throughout this Thesis, we will consider a parametric model of DE rather than a specific model of DE, like quintessence [473]. The parametrisation studied in this chapter is "Omnipotent dark energy" - ODE - [474, 475], a model where the energy density of DE can switch its sign from de-Sitter to anti de-Sitter (or viceversa), at different cosmological epochs. If we take a Taylor expansion of $\rho_{\rm DE}$ around a value of the scale factor a_m and require a_m to be either at a maximum or at a minimum of $\rho_{\rm DE}$, we are guaranteed that the phantom divide line (i.e., where $w_{\rm DE} = -1$) is crossed at least once, at $a = a_m$. One of the main goals of this paper is to enquire about the possibility of explaining DESI's results on the time evolution of DE, which would seem to point at a form of DE that was recently in the phantom regime but is now crossing the phantom divide line into the quintessence region [14, 15, 284, 382], by using the ODE model.

Another important reason motivating our work is the model's potential to alleviate the Hubble tension. As it was mentioned in chapter I, the Hubble tension is an open issue in cosmology that deals with different estimates of H_0. In fact, measurements of H_0 provided by late-time indicators like SNIa differ sensibly from the early-time estimates by probes like the CMB. In the case of BAO the situation is perhaps more ambiguous, because, as we said in chapter III, the BAO measurement of H_0 is correlated to r_d. In any case, the discrepancy now reaches an astounding 7.1σ significance, prompting us to find a solution in the form of DE alternatives to the standard model. The ODE could potentially alleviate this problem, as it was shown in [6] that a combination of CMB, BAO and SN data favors a recent, brief period

in the phantom regime and a less recent phase of negative DE density, both contributing to an alleviation of the H_0 tension.

This paper represents an update to the analysis in [6] that integrates new data into the investigation of the ODE model, like the BAO distance measurements by DESI, which came out in between the publication of [6] and the work outlined in the next sections.

Updated Constraints on Omnipotent Dark Energy: a Comprehensive Analysis with CMB and BAO Data

Abstract: In this work, we present updated observational constraints on the parameter space of the DMS20 dark energy model, a member of the *omnipotent dark energy* (ODE) class. Our analysis combines multiple CMB datasets—including measurements from the Planck satellite (PL18), the South Pole Telescope (SPT), and the Wilkinson Microwave Anisotropy Probe (WMAP)—with Type Ia supernova data from the Pantheon+ catalog (PP), and baryon acoustic oscillation (BAO) measurements from the DESI and SDSS surveys. We find that certain data combinations, such as SPT+WMAP+BAO and PL18+BAO, can reduce the significance of the H_0 tension below 1σ, but with considerably large uncertainties. However, the inclusion of PP data restores the tension in H_0. To provide a comprehensive view of the ODE phenomenology, we also investigate the evolution of its energy density, emphasizing its dynamical behavior at low redshifts. Our results generically exhibit multiple phantom divide line crossings in a single expansion history; if confirmed, this points beyond the simplest minimally coupled canonical single-field quintessence/phantom descriptions and motivates more general dark-sector realizations.

VII.A Introduction

The ΛCDM model has emerged as the dominant and most widely accepted cosmological framework. Its success is largely attributed to its remarkable accuracy in explaining a broad range of astrophysical and cosmological observations without excessive model complexity. Despite these successes, however, the ΛCDM model faces some unresolved challenges, particularly in capturing a consistent expansion history when various combinations of mainstream cosmological observables, such as the cosmic microwave background (CMB), baryon acoustic oscillations (BAO), large-scale structure (LSS), and local distance ladder measurements of the Hubble constant are simultaneously considered [110, 115, 143, 476, 477].

With the increasing precision of modern observations [111], it is anticipated that deviations from the standard ΛCDM model will become more apparent. Indeed, various discrepancies in the estimation of key cosmological parameters have already emerged, some of which show statistically significant departures from the predictions of the model [110, 112, 115, 117, 477–479]. Among these issues, one of the most prominent and statistically significant is the ongoing discrepancy related to the Hubble constant, H_0 (for a detailed review, see [110, 114, 115, 117, 120, 143, 147, 221, 224–226, 477] and references therein). A notable conflict

exists between the values of H_0 inferred from the CMB measurements [23, 56, 480] assuming the ΛCDM model, and those derived from direct, independent measurements obtained through local astrophysical observations [126–130, 132–135, 227, 228, 481–496]. This tension, commonly referred to as the H_0 tension, has reached a statistical significance greater than 5σ [84, 227, 228], and is now considered one of the most pressing issues within the context of the ΛCDM model. To solve this tension, cosmologists have been exploring both possible systematic errors [84, 228, 485, 487, 488, 497–505] and alternative cosmological models [110, 114, 115, 140, 141, 147, 220, 222, 223, 225, 477, 506]. In addition to the H_0 tension, another point of discussion in cosmology is the S_8 tension [110, 112, 119, 462] (see also [145, 236]), which concerns discrepancies between the amplitude of matter fluctuations inferred from early-universe measurements, such as the Planck CMB data, and the S_8 values derived from late-time observations, including weak gravitational lensing and galaxy clustering, though it seems to have lost significance after the new KiDS-Legacy release [136–138, 210, 214, 229, 231, 463–469, 471, 472, 507]. Furthermore, recent results from the DESI collaboration analyzing the BAO feature have found evidence for dynamical dark energy (DDE) when their measurements are combined with other major observations [14, 15, 284, 508, 509]. This evidence for DDE is relevant only in the post-recombination era, with a statistical significance of 3.1σ when combined with the CMB. The significance ranges from 2.7σ to 4.2σ when different supernovae samples are included in the dataset combination. The indication persists even without the CMB; for example, only the DES supernovae sample [510] when combined with DESI BAO yields a 3.3σ significance. It is important to note that the evidence for DDE does not hinge on DESI BAO either, e.g., see Refs. [510, 511] that report preference of a DDE without this data set. A plethora of models have been proposed in the literature to address the existing cosmological tensions [477], a substantial portion of which incorporate a DDE component that is non-negligible in the late and/or early universe [14, 216, 260, 266–268, 271, 273, 275–278, 280, 285, 289, 291–293, 297, 298, 338, 383–400, 402, 512].

The simplest phenomenological DDE model replaces the cosmological constant, whose effective equation of state (EoS) parameter is $w = -1$, with a DE fluid that has a constant EoS parameter able to satisfy $w_{\rm DE} \neq -1$; this is often referred to as the wCDM model. Many models extend this approach by allowing a varying EoS parameter, with the most well-known example being the Chevallier-Polarski-Linder (CPL) parametrization [149, 410], in which $w_{\rm DE}$ is assumed to be a linear function of the scale factor in the Robertson–Walker (RW) metric. Notably, unless restricted to specific regions of parameter space, such extensions generically allow $w_{\rm DE}$ to cross the phantom divide line (PDL), $w_{\rm DE} = -1$. However, parameterizing DDE solely via its EoS parameter fails to capture the phenomenology of models in which DDE attains negative effective energy densities in the past, as such components

would exhibit a singular EoS parameter [513]. From both theoretical and phenomenological perspectives, models predicting negative energy densities in the dark sector have garnered increasing attention in recent years, particularly for their potential to resolve the H_0 tension [284, 477, 514–538]. DDE models capable of simultaneously incorporating all of these features were dubbed *omnipotent dark energy* (ODE) models in Ref. [475], where it was argued that such a flexible DDE component may be necessary for a satisfactory resolution of the prevailing cosmological tensions.

In Ref. [474], the DMS20 model was proposed as a promising solution to the cosmological tensions and was found to prefer a PDL crossing at $z \sim 0.1$. The recent analysis in Ref. [475] identified DMS20 as an ODE model and showed that its ability to reach negative energy densities for $z \gtrsim 2$—mimicking a negative cosmological constant at high redshifts—plays a crucial role in alleviating the tensions. This behavior is consistent with the predictions of the $\Lambda_{\rm s}$CDM model [520, 521, 525], which suggests a transition from an Anti-de Sitter (AdS) to a de Sitter (dS) phase. This transition can be interpreted either as an emergent effect from modified gravity or as the result of an actual field within the framework of general relativity (GR).

In this paper, we revisit and update the observational constraints on the DMS20 model using Type Ia supernova data from the Pantheon+ catalog, BAO measurements from the DESI and SDSS surveys, and CMB temperature and polarization data from Planck, the South Pole Telescope, and the Wilkinson Microwave Anisotropy Probe. Motivated by previous studies of the DMS20 model that reported posterior distributions leaning against the edges of the prior ranges for certain dataset combinations, we extend these prior ranges. This not only relaxes the constraints on the model parameters but also enables the model to exhibit richer phenomenology that is qualitatively different—for example, a crossing of the PDL, occurring either from the quintessence regime to the phantom regime or vice versa. Nevertheless, we also present our results after excluding the MCMC samples corresponding to the extended priors, to facilitate direct comparison with previous studies.

The structure of this paper is organized as follows. In Sec. VII.B, we review the key physical features of the omnipotent dark energy model, focusing on the aspects most relevant for cosmological tests. In Sec. VII.C, we describe the observational datasets used in our analysis and outline the methodology employed to constrain the model's free parameters. In Sec. VII.D, we present and discuss our main results, highlighting their implications for cosmological tensions and the broader landscape of dark energy models. Finally, in Sec. VII.E, we summarize our conclusions and offer some perspectives on future research directions.

VII.B Omnipotent Dark Energy: a review

In this section, we review the class of ODE models and the DMS20 model as a concrete member of this class. The term ODE describes a family of phenomenological proposals that allow energy densities to transition between positive and negative values, and to exhibit oscillatory or non-monotonic evolution histories. ODE models permit arbitrary EoS, including singularities and PDL crossings, unconstrained by standard energy conditions. As an effective source in the Friedmann equations, ODE provides a flexible framework to address the limitations of the cosmological constant. More precisely, a DE model is referred to as an ODE if, for any point in its parameter space, it can exhibit all six possible combinations of the conditions $\rho_{\rm DE} > 0$, $\rho_{\rm DE} < 0$, and $w_{\rm DE} > -1$, $w_{\rm DE} = -1$, $w_{\rm DE} < -1$ within a single expansion history. Here, $\rho_{\rm DE}$ denotes the energy density of the DE component [475].

Two distinctive features of ODE are its capacity to realize a non-monotonic energy density evolution and to reach negative energy densities, as suggested by various observational reconstructions [535, 539–544]. Such behavior has been shown to alleviate key cosmological tensions, including the H_0 and S_8 discrepancies [474, 514, 515, 517, 520, 521, 524, 540, 545–549]. Hereafter, we consider an ODE component, whether as an effective source from modified gravity or a fluid within GR, that satisfies the usual continuity equation that follows from the local conservation of the energy-momentum tensor for the RW metric. Given this weak assumption, unlike usual phantom DE [550], which maintains $w_{\rm DE} < -1$, the non-monotonicity feature of ODE models requires that its EoS parameter crosses the PDL. Moreover, since its energy density vanishes during the transition between negative and positive density regions at a scale factor $a_{\rm p}$, its EoS parameter exhibits a pole of the form $\lim_{a\to a_{\rm p}^{\pm}} w_{\rm DE}(a) = \mp\infty$; this also corresponds to a PDL crossing, but a discontinuous one [513].

The DMS20 model proposed in Ref. [474] serves as a concrete example of an ODE model. In this model, the DE density, $\rho_{\rm DE}$, is parameterized to ensure an extremum at a scale factor a_m, satisfying the condition $\left.\frac{{\rm d}\rho_{\rm DE}}{{\rm d}a}\right|_{a=a_m} = 0$. The DE density is then expressed by expanding $\rho_{\rm DE}$ around a_m:

$$\rho_{\rm DE}(a) = \rho_{\rm DE0}\frac{1+\alpha(a-a_m)^2+\beta(a-a_m)^3}{1+\alpha(1-a_m)^2+\beta(1-a_m)^3}, \tag{VII.1}$$

where α and β are constants defining the polynomial terms (for further details, see Refs. [474, 475]). The absence of a linear term in the expansion follows from the vanishing of the first derivative at $a = a_m$. The parameter a_m has significant physical implications: from the continuity equation, it follows that $w_{\rm DE}(a_m) = -1$, provided that $\rho_{\rm DE}$ is non-zero at the extremum. For $\alpha > 0$, this corresponds to a transition from $w_{\rm DE} > -1$ to $w_{\rm DE} < -1$ as the universe expands, while for $\alpha < 0$, the crossing occurs in the opposite direction. The EoS for

the ODE model is given by:

$$w_{\rm DE}(a) = -1 - \frac{a[2\alpha(a-a_m) + 3\beta(a-a_m)^2]}{3[1+\alpha(a-a_m)^2 + \beta(a-a_m)^3]}, \tag{VII.2}$$

which yields $w_{\rm DE}(a=0) = -1$ and $w_{\rm DE}(a\to\infty) = -2$.

This model introduces three extra parameters: $\{a_m, \alpha, \beta\}$. Depending on the values of these parameters, certain features of ODE may remain dormant. For instance, when $\alpha = \beta = 0$, the DE density reduces to the cosmological constant Λ, recovering the standard ΛCDM model. For a detailed discussion of the dynamical behavior of the model across different values of $\{a_m, \alpha, \beta\}$, see Ref. [475]. Here, we simply note that the EoS of DMS20 cannot, in general, be represented *exactly* by the CPL parametrization, $w_{\rm DE} = w_0 + w_a z/(1+z)$, where $z = (1-a)/a$ is the redshift. Here, $w_0 = w_{\rm DE}(z=0)$, and w_a controls the leading time-variation of $w_{\rm DE}$ within the CPL ansatz (equivalently, $w(a) = w_0 + w_a(1-a)$, so $\mathrm{d}w/\mathrm{d}a = -w_a$ is constant by construction). More generally, (w_0, w_a) are best regarded as a convenient two-parameter data-compression of the model predictions for a given set of observables and redshift sensitivities (see, e.g., [28, 551, 552]). These two parameters are essential for characterizing the behavior of dark energy across a wide range of models, as discussed in [553]. However, as shown in Fig. VII.1, for any choice of $\{a_m, \alpha, \beta\}$ we observe an oscillatory pattern in $w_{\rm DE}$, which cannot be described by the linear CPL form. In fact, w_a would need to acquire a redshift dependence to account for the behavior of the EoS in Eq.(VII.2). It is seen from Fig. VII.1 that variations in α significantly influence the present-day values of both w and w_a, while having a negligible effect at higher redshifts. Specifically, as α increases, w shifts further into the phantom regime, and w_a also increases. In the middle panel, we observe that β induces more pronounced oscillations in w, although its effect on w_a is relatively minor. Lastly, the parameter a_m shows a similar trend to α, highlighting its role in shaping the present-day dynamics of dark energy. It is evident that the linear CPL parametrization fails to capture the non-linear features of the ODE model, whose oscillatory behavior cannot be reproduced by such a simplified form. With only one additional parameter, our ODE parametrization is thus able to recover a complementary class of DE models with a richer phenomenology.

To understand the background evolution of this model, we begin with the expansion rate of the universe, governed by the modified Friedmann equation:

$$\frac{H^2(a)}{H_0^2} = \Omega_{\rm m0} a^{-3} + \Omega_{\rm r0} a^{-4} + \Omega_{\rm DE0} f(a), \tag{VII.3}$$

where

$$f(a) = \frac{1 + \alpha(a-a_m)^2 + \beta(a-a_m)^3}{1 + \alpha(1-a_m)^2 + \beta(1-a_m)^3}. \tag{VII.4}$$

In Eq. (VII.3), the subscript "m" refers to all forms of matter (including both baryonic and cold dark matter), while "r" denotes radiation (photons and other relativistic relics). The density parameters $\Omega_{i0} \equiv \rho_{i0}/(3H_0^2)$ represent the present-day values of the respective energy densities.

The DMS20 model does not introduce modifications to other sectors of the universe or its constituent species. Consequently, the background evolution remains unchanged for all components other than DE itself. The linear evolution of DE perturbations follows the standard prescription, where we impose synchronous gauge conditions for metric perturbations. The continuity and Euler equations governing the DE fluid are given by

$$\dot{\delta}_x = -(1+w)\left(\theta + \frac{\dot{h}}{2}\right) - 3(\hat{c}_s^2 - w)\mathcal{H}\delta_x - 9(1+w)(\hat{c}_s^2 - c_a^2)\mathcal{H}^2\frac{\theta_x}{k^2},$$

$$\dot{\theta}_x = -(1-3\hat{c}_s^2)\mathcal{H}\theta_x + \frac{\hat{c}_s^2 k^2}{1+w}\delta_x - k^2\sigma_x. \tag{VII.5}$$

These equations are quite general, as they assume only a non-interacting fluid and allow for the presence of shear stress σ_x, a non-adiabatic sound speed, and a time-dependent equation of state parameter w. Henceforth, we assume the fluid is shear-free and that w is given by Eq. (VII.2).

VII.C Data and Methodology

TABLE VII.1. Flat priors are adopted to test the ODE model against all of the likelihood combinations presented in Sec. VII.D, with the exception of those involving the `SPT+WMAP` dataset combination, where a Gaussian prior is imposed on the optical depth: $\mathcal{P}(\tau) = \mathcal{N}(0.0544,\ 0.0073^2)$.

Parameter	Prior
$\Omega_{\rm b}h^2$	$[0.017,\ 0.027]$
$\Omega_{\rm c}h^2$	$[0.09,\ 0.15]$
τ	$[0.01,\ 0.8]$
n_s	$[0.9,\ 1.1]$
$\log(10^{10}A_s)$	$[2.6,\ 3.5]$
$100\,\theta_{\rm MC}$	$[1.03,\ 1.05]$
α	$[-8,\ 8]$
β	$[-8,\ 8]$
a_m	$[0,\ 1.4]$

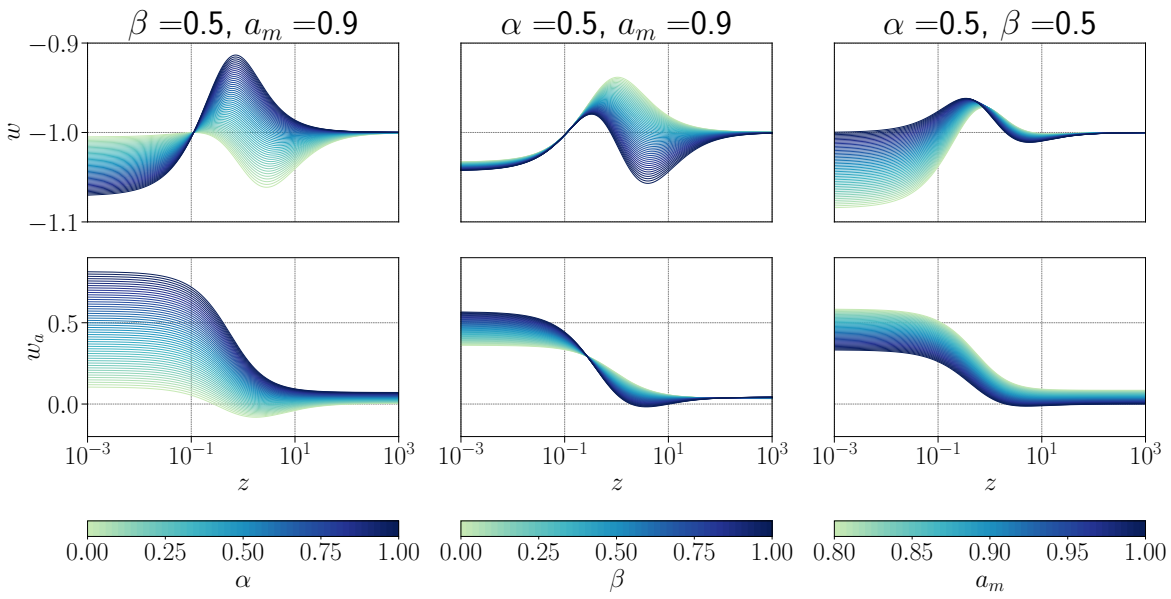


FIG. VII.1. The redshift evolution of $w_{\rm DE}$ and the CPL parameter w_a are shown for different values of $\{a_m, \alpha, \beta\}$. Clearly w_a cannot remain constant in this model, so the linear CPL parametrization of $w_{\rm DE}$ fails to capture the oscillatory behavior characteristic of ODE.

We generate theoretical predictions for the ODE model using a modified version of the Boltzmann solver `CAMB` [31, 32], while parameter estimation is performed with the publicly available sampler `Cobaya` [91]. The sampling of the posterior distributions is carried out using the Monte Carlo Markov Chain (MCMC) method, originally developed for `CosmoMC` [92]. This implementation incorporates the "fast dragging" technique [160, 554], which improves efficiency in exploring parameter spaces with varying computational complexity.
In varying combinations, the likelihoods employed in this analysis use data from the following cosmological surveys:

- **Planck 2018 (`PL18`):** We include the full Planck 2018 temperature and polarization likelihoods (TT, TE, EE), along with the Planck 2018 lensing likelihood [23], reconstructed from the four-point correlation function of temperature fluctuations.

- **South Pole Telescope (`SPT`):** We incorporate CMB temperature and polarization anisotropy measurements (TT, TE, EE) from the SPT collaboration [56, 57].

- **Wilkinson Microwave Anisotropy Probe (`WMAP`):** We utilize the CMB temperature and polarization data from the WMAP 9-year release [555]. To mitigate dust contamination, we exclude WMAP low-ℓ polarization data by setting the minimum multipole for TE and EE to $\ell = 24$. For this reason, whenever we use the WMAP spectra we consistently apply a Gaussian prior on the optical depth to reionization,

$\tau = 0.0544 \pm 0.0073$, which is the baseline choice used by the SPT–3G collaboration when they include the WMAP data in their analysis [57]. We also assume that there is no correlation between the SPT and WMAP datasets, as they probe largely different regions of the sky [57].

- **Dark Energy Spectroscopic Instrument (`DESI`):** We include baryon acoustic oscillation (BAO) measurements from the DESI collaboration, based on galaxy and quasar observations [556], as well as Lyman-α tracers [557], compiled in Table I of Ref. [14]. These measurements span the redshift range $0.1 < z < 4.2$, divided into seven bins, and include both isotropic and anisotropic BAO constraints. The isotropic BAO measurements are expressed as $D_V(z)/r_d$, where D_V is the volume-averaged distance normalized to the comoving sound horizon at the drag epoch, r_d. The anisotropic constraints include $D_M(z)/r_d$ and $D_H(z)/r_d$, where D_M is the comoving angular diameter distance and D_H the Hubble horizon. Correlations between D_M/r_d and D_V/r_d are accounted for.

- **Sloan Digital Sky Survey (`eBOSS`):** We incorporate the galaxy, quasar and Lyman-α measurements of D_M/r_d and D_H/r_d from the eBOSS experiment, as presented in Table 3 of Ref. [558].

- **Pantheon+ (`PP`):** We include distance modulus measurements of Type Ia supernovae from the Pantheon+ sample [86], consisting of 1,550 supernovae over the redshift range $0.001 \leq z \leq 2.26$.

For the DMS20 model parameters, we adopt the agnostic, flat priors outlined in Tab. VII.1, except, as noted above, for an informative Gaussian prior on τ whenever the `SPT+WMAP` dataset combination is considered. Specifically, the parameter space of the DMS20 model extends the standard ΛCDM framework by introducing the three parameters defined in Eq. (VII.1), namely α, β, and a_m, in addition to the six baseline ΛCDM parameters: the physical baryon and cold dark matter densities ($\Omega_{\rm b}h^2$, $\Omega_{\rm c}h^2$), the optical depth to reionization (τ), the amplitude and spectral index of the primordial scalar fluctuations ($\log(10^{10}A_s)$, n_s), and the angular size of the sound horizon at last scattering ($\theta_{\rm MC}$). Compared to Refs. [474, 475], the priors on α and β are extended to include negative values, and a_m is allowed to exceed 1, thereby enabling the possibility of PDL crossings occurring in the future (i.e., for $a > 1$). These choices are discussed in more detail in the next section.

All of the 1D and 2D posteriors were calculated and visualized using the `Getdist` code [349], while the functional posteriors for $w_{\rm DE}(z)$ and $\rho_{\rm DE}(z)$ shown in the next section were produced using the `fgivenx` plotting package [559].

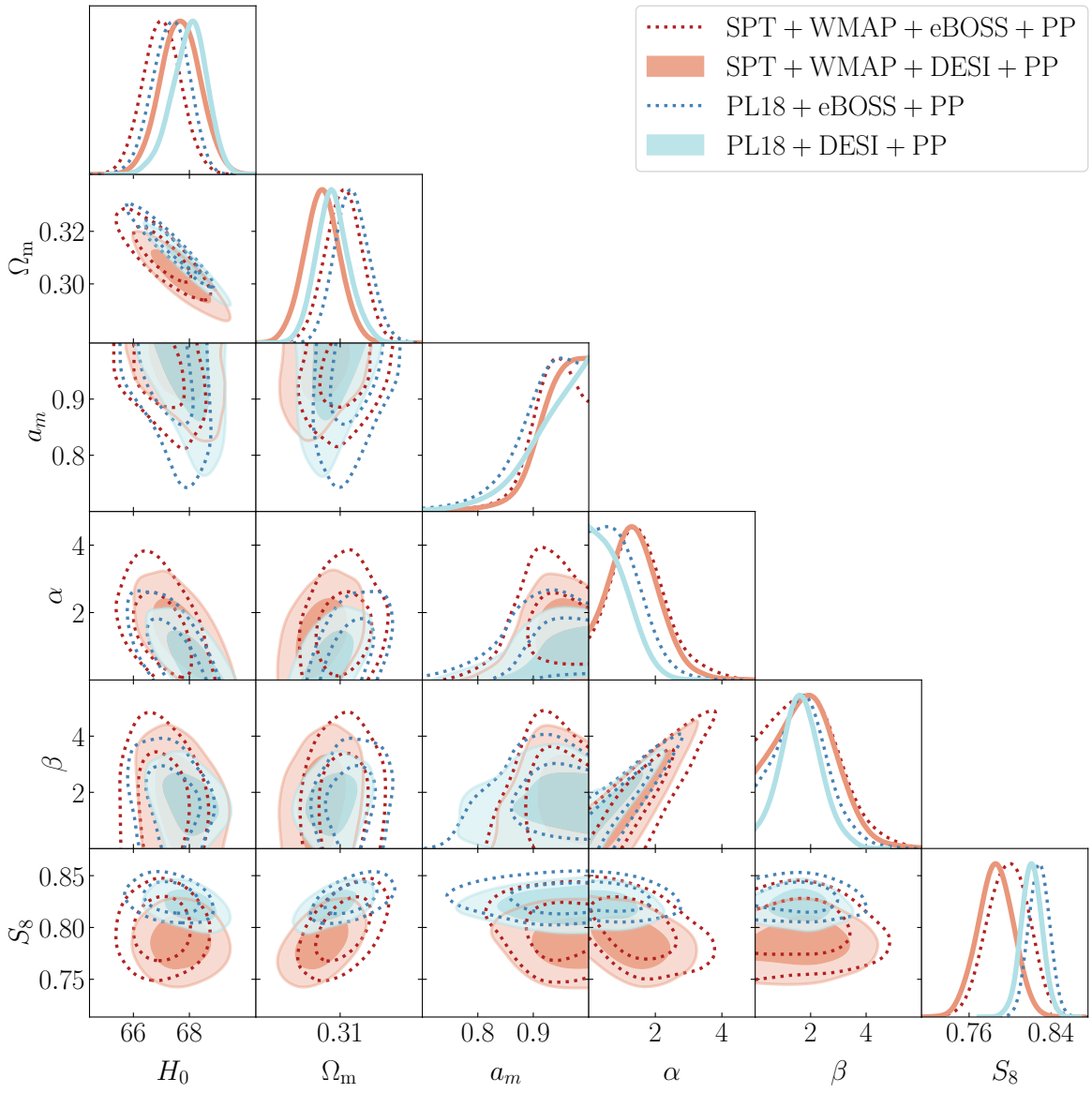


FIG. VII.2. 1D and 2D marginalized constraints on the ODE parameter space, derived from the post-filtered chains that include only samples with $\alpha > 0$, $\beta > 0$, and $a_m \in [0, 1]$.

VII.D Results and Discussion

We begin our discussion by justifying our choice of priors for the extra parameters of DMS20, namely, $\{a_m, \alpha, \beta\}$. In contrast to Refs. [474, 475], the prior ranges for $\{\alpha, \beta\}$ are chosen to include negative values, and the prior range for a_m is extended to include values greater than 1. In Refs. [474, 475], the choice of priors enforces $\alpha > 0$, $\beta > 0$, and $a_m \in [0, 1]$. This restricts $\rho_{\rm DE}$ to an evolution history with certain properties, the most important being

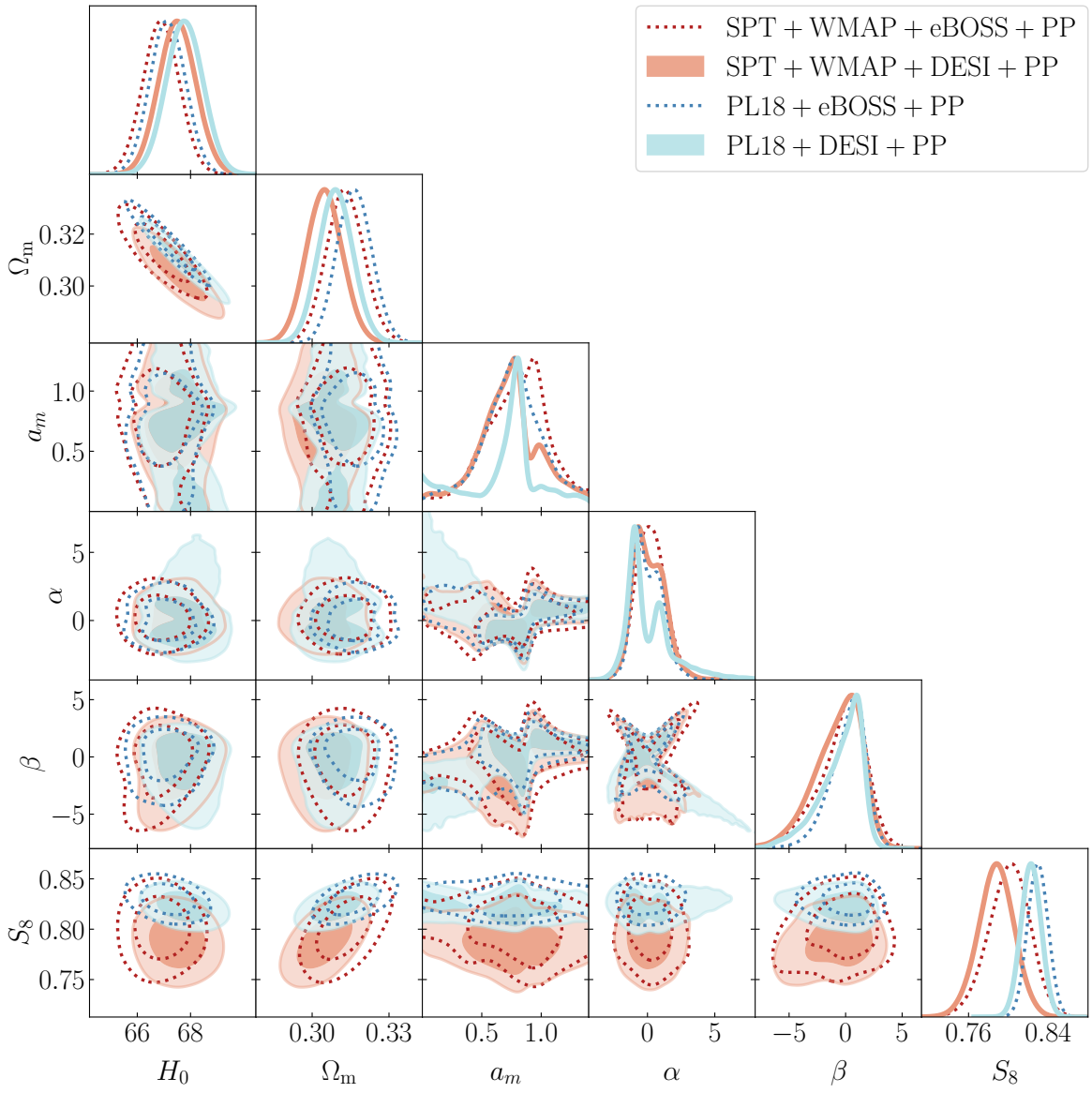


FIG. VII.3. 1D and 2D marginalized constraints on the ODE parameter space, obtained from the chains sampled with the full-prior ranges listed in Table VII.1, without any post-processing cuts (full-prior results).

the guaranteed existence of a PDL crossing at $a = a_m$, where the EoS parameter transitions from quintessence ($w_{\rm DE} > -1$) to phantom ($w_{\rm DE} < -1$) as the universe expands. However, in both of the previous studies, the reported posteriors for these parameters do not exclude the prior bounds for many of the dataset combinations, particularly those that do not include the SH0ES H_0 measurement. Moreover, recent indications of a dynamical dark energy component

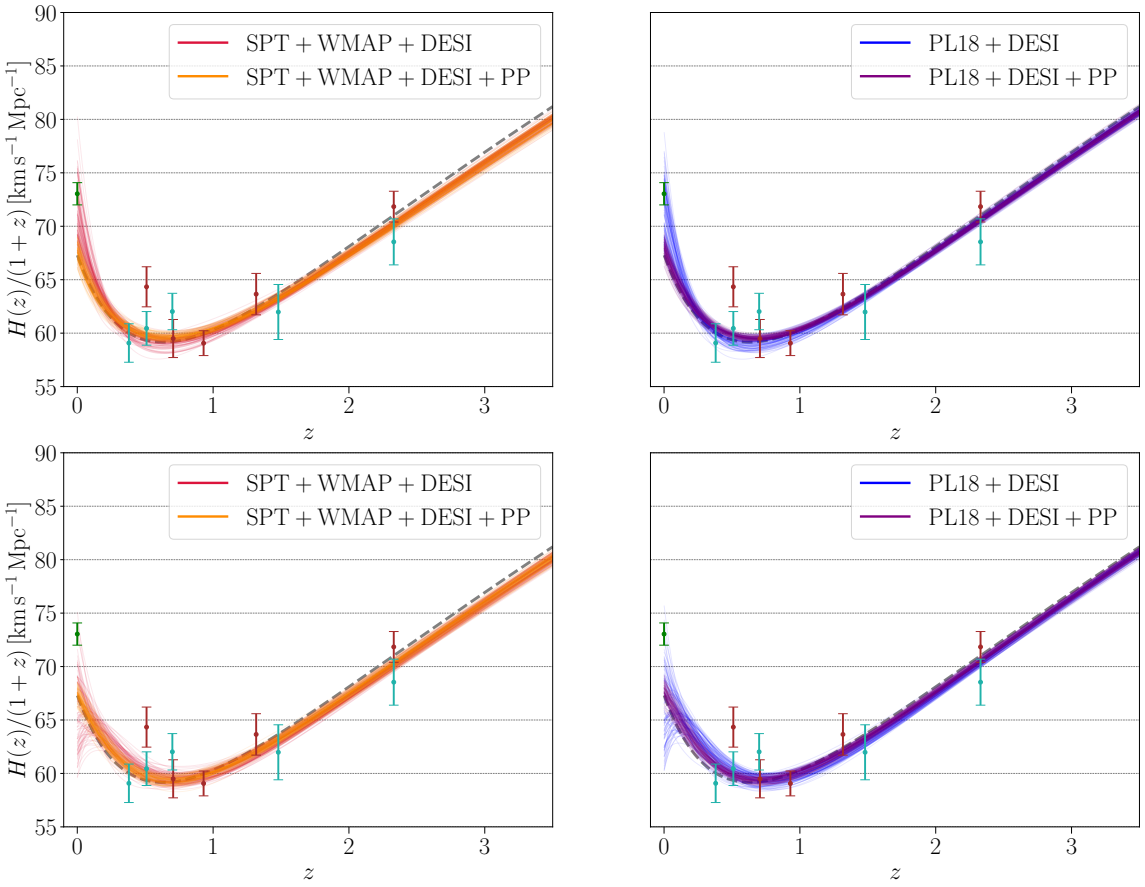


FIG. VII.4. ODE constraints (top panels post-filtered results, bottom panels full-prior results) on the redshift evolution of the $H(z)/(1+z)$ function, derived from the `SPT+WMAP+DESI` and `PL18+DESI` data combinations, with and without supernovae. Also shown are D_H/r_d measurements from `eBOSS` [76] (green) and `DESI YR1` [14] (red), obtained using luminous red galaxies, emission line galaxies, and quasars as tracers; the point at $z = 0$ is the SH0ES constraint $H_0 = 73.04 \pm 1.04\,\mathrm{km\,s^{-1}\,Mpc^{-1}}$ [84]. These measurements are converted into $H(z)$ using the Planck constraint $r_d = 147.09 \pm 0.26$ Mpc. The grey dashed line represents the ΛCDM best-fit curve from `TTTEEE+lowE+lensing` [23].

suggest evidence for a preference of a PDL crossing in the opposite direction,[VII.1] i.e., where the EoS parameter transitions from phantom ($w_{\rm DE} < -1$) to quintessence ($w_{\rm DE} > -1$) as the universe expands [14, 15]. In fact, the PDL crossing at $a = a_m$ occurs in this opposite direction when $\alpha < 0$. More generally, various qualitatively different DE density evolution histories become available in the DMS20 model when the parameters are allowed to explore this extended parameter space; see Table II and Fig. 1 of Ref. [475] and the discussions therein.

In this work, we chose the extended priors in Tab. VII.1 to take a more conservative approach

[VII.1] It is important to note that the prior ranges chosen in Refs. [474, 475] allow (but do not guarantee) for a second PDL crossing in this opposite direction in addition to the one at $a = a_m$, and even a third crossing may occur in a discontinuous way if the DE density attains negative values in the past. In fact, when the model is constrained with data, all three of these crossings were found to play an important role in the evolution of the DE density.

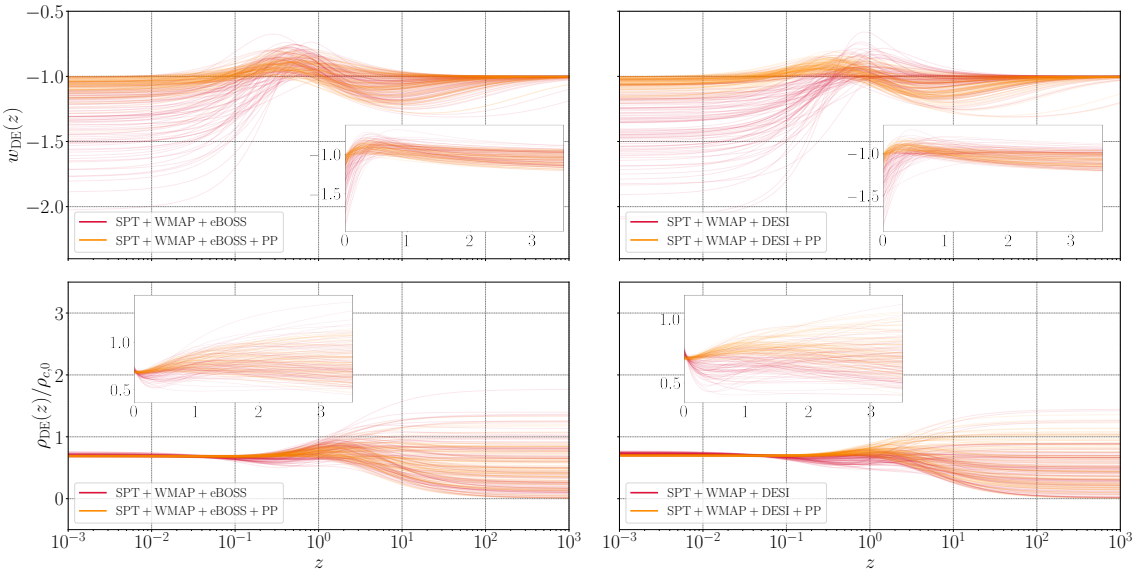


FIG. VII.5. Redshift evolution of $w_{\rm DE}(z)$ (top panels) and $\rho_{\rm DE}(z)/\rho_{c,0}$ (bottom panels) obtained from the post-filtered results using `SPT` as the baseline CMB dataset. In each panel the reader can find the same plot contained in the panel itself, re-expressed through a linear but shorter redshift range.

that does not guarantee the existence of a_m within the expansion history, and allowed the MCMC analysis to explore the parameter space of the model more freely. Indeed, the results we report suggest that these extended regions of parameter space are always consistent with our dataset combinations, and are sometimes even preferred. To better compare our results with previous works, we also report results obtained after filtering the MCMC chains by dropping any samples with $\alpha < 0$, $\beta < 0$, or $a_m > 1$. We ensured that all of the filtered chains satisfied the Gelman–Rubin convergence criterion with $R - 1 < 0.07$; this approach is equivalent to performing the analysis with the corresponding restricted priors. We refer to the results from the full chain as the "full-prior results," and to those from the post-processed chains as the "post-filtered results."

In this section, we present the main results of our analysis using different combinations of datasets. We analyze constraints on our dynamical dark energy model ODE, characterized by the parameters α, β, and a_m, using various combinations of the CMB and BAO measurements described in the previous section, with and without supernovae distance moduli.

In Figs.VII.2 and VII.3, we present the parameter constraints derived from both the full-prior and post-filtered analyses. We find that using full priors results in multimodal posterior distributions for certain parameters, while the post-filtered analysis yields unimodal distributions. The multimodality in the full results arises from the phenomenological degeneracies in the parameter space, i.e., different regions of the parameter space correspond to similar expansion histories; see Tab.II in [475]. The ΛCDM model is nested in DMS20 and corresponds

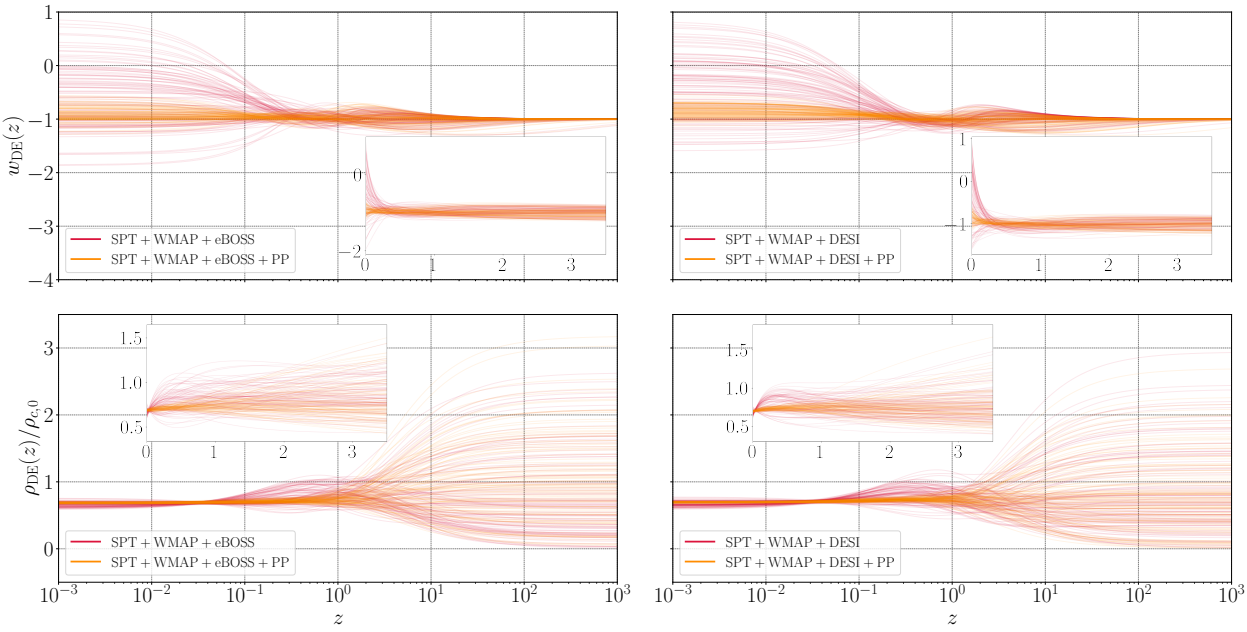


FIG. VII.6. Same as Fig. VII.5 but for the full-prior results.

to the $\alpha = \beta = 0$ section of the parameter space. It is seen from Fig. VII.3 that there is always consistency, in all of the data set combinations shown in the triangular plot, with the part of the parameter space corresponding to ΛCDM, and there is no evidence for dynamics in the DE density evolution. Overall, despite the different prior choices (to be discussed in detail later), the results remain statistically consistent across all analyses. A comparative analysis of the `SPT+WMAP+DESI+PP` and `PL18+DESI+PP` combinations shows that the latter yields tighter parameter constraints, as illustrated by the red and blue contour plots. Moreover, the inferred value of S_8 is systematically lower when using the `SPT+WMAP+DESI+PP` combination compared to `PL18+DESI+PP`. Substituting `DESI` with `eBOSS` leads to additional shifts in the best-fit values of several parameters (see the following discussions for the respective σ deviations), highlighting the sensitivity of the results to the choice of BAO dataset.

We present the complete set of parameter estimates from our analysis in Tabs. VII.2, VII.4, VII.3 and VII.5. Post-filtered results show significantly tighter constraints on cosmological parameters compared to the full-prior setup. In both the `SPT` and `PL18` cases, the parameters α, β, and a_m are more precisely determined when the prior ranges on model parameters are restricted. This is expected as the post-filtering removes a significant portion that is within 68% CL of the mean values of the full-prior marginalized posteriors. The inclusion of `PP` data further enhances the precision of these constraints. For instance, the `SPT+WMAP+DESI+PP` combination with post-filtered priors (see Tab. VII.2) yields, at 68% CL, $\alpha = 1.40^{+0.65}_{-0.84}$,

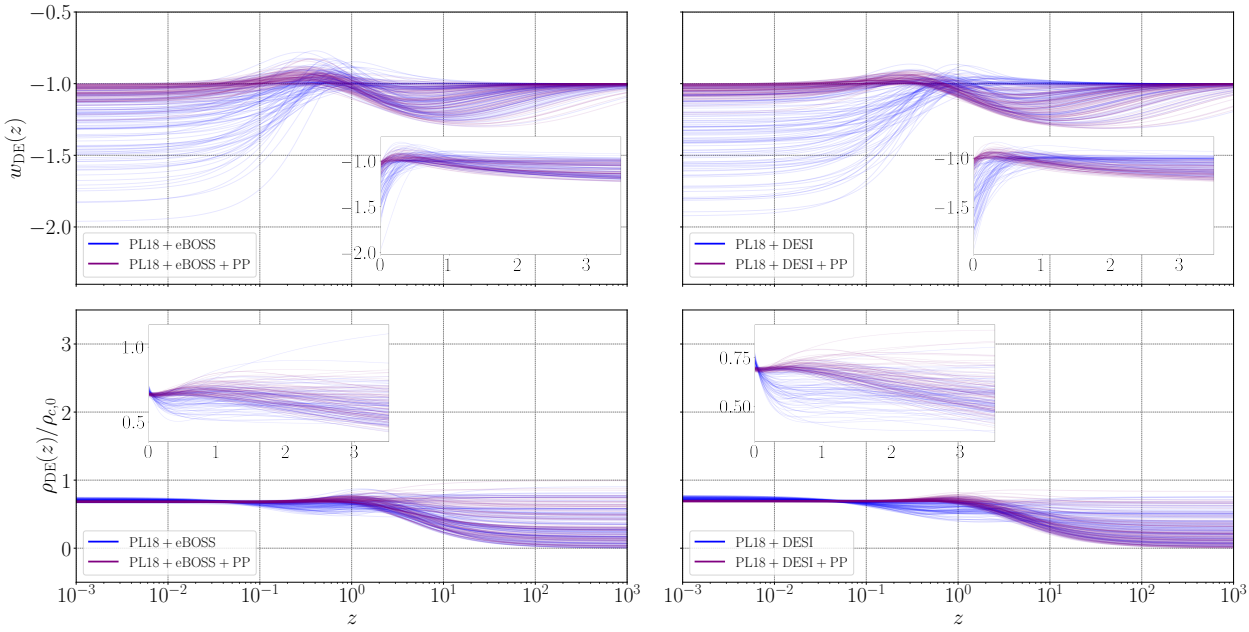


FIG. VII.7. Redshift evolution of $w_{\rm DE}(z)$ (top panels) and $\rho_{\rm DE}(z)/\rho_{c,0}$ (bottom panels) obtained from the post-filtered results using `PL18` as the baseline CMB dataset. In each panel the reader can find the same plot contained in the panel itself, re-expressed through a linear but shorter redshift range.

$\beta = 1.88^{+0.95}_{-1.2}$, and $a_m > 0.930$. In contrast, the same dataset under the full-prior setup gives $\alpha = 0.1^{+1.0}_{-1.3}$, $\beta = -0.7^{+2.5}_{-1.5}$, and $a_m = 0.73 \pm 0.28$ at 68% CL (see Tab. VII.3). This corresponds to deviations of 1.06σ, 0.93σ, and 0.71σ for α, β, and a_m, respectively, when comparing the prior cut-off case with the full-prior analysis for the same dataset combinations.

While the full-prior results are better for interpreting the true phenomena that our data sets prefer, the post-filtered results are easier to interpret and match the previous studies [474, 475]. The post-filtered results enforce the existence of a DE EoS parameter that crosses from a quintessence regime to phantom regime at $a = a_m$. For instance, we see in Tab. VII.4 that `PL18+eBOSS` yields a clear peak for the scale of the PDL crossing at $a_m = 0.76^{+0.17}_{-0.11}$ and the addition of `PP` yields $a_m > 0.904$. This is accompanied by a reduction in the uncertainty of H_0, which changes from $H_0 = 69.4^{+1.4}_{-2.4}$ km/s/Mpc to $H_0 = 67.33^{+0.69}_{-0.62}$ km/s/Mpc with 0.83σ deviations, closer to Planck's ΛCDM value.

Interestingly, replacing the eBOSS data with the newer DESI dataset further tightens the constraints on the ODE parameters (α, β) and H_0. The Hubble constant shifts slightly toward higher values, reflecting the preference of DESI for a lower matter density relative to eBOSS, and the well-known anti-correlation between H_0 and Ω_m. We note that a PDL

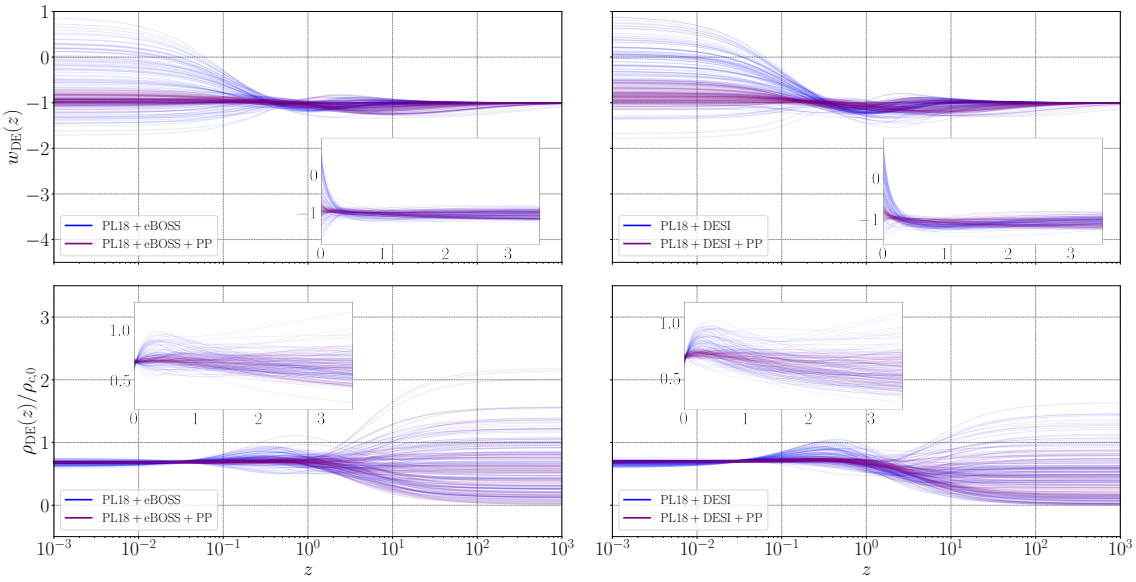


FIG. VII.8. Same as Fig. VII.7 but for the full-prior results.

TABLE VII.2. 68% CL constraints on the free parameters (above the line) and derived parameters (below the line), obtained from the post-filtered results using `SPT` as the baseline CMB dataset. *BE* is the Bayesian Evidence.

	SPT+WMAP +eBOSS	SPT+WMAP +eBOSS+PP	SPT+WMAP +DESI	SPT+WMAP +DESI+PP
$\boldsymbol{\Omega_b h^2}$	0.02242 ± 0.00021	0.02241 ± 0.00020	0.02244 ± 0.00020	0.02244 ± 0.00019
$\boldsymbol{\Omega_c h^2}$	$0.1163^{+0.0021}_{-0.0019}$	0.1167 ± 0.0019	$0.1157^{+0.0016}_{-0.0014}$	0.1157 ± 0.0016
$\boldsymbol{100\theta_{MC}}$	1.04018 ± 0.00065	1.04015 ± 0.00063	1.04028 ± 0.00062	1.04029 ± 0.00064
$\boldsymbol{\tau}$	0.0532 ± 0.0072	0.0532 ± 0.0072	0.0538 ± 0.0070	0.0537 ± 0.0070
$\boldsymbol{\ln(10^{10} A_s)}$	3.031 ± 0.015	3.032 ± 0.015	3.030 ± 0.015	3.030 ± 0.015
$\boldsymbol{n_s}$	0.9679 ± 0.0061	0.9673 ± 0.0057	0.9690 ± 0.0055	0.9691 ± 0.0055
α	< 3.12	$1.54^{+0.66}_{-0.94}$	< 1.80	$1.40^{+0.65}_{-0.84}$
β	< 3.94	$1.88^{+0.81}_{-1.5}$	< 2.98	$1.88^{+0.95}_{-1.2}$
a_m	$0.826^{+0.13}_{-0.069}$	$0.934^{+0.056}_{-0.023}$	$0.74^{+0.16}_{-0.12}$	> 0.930
Ω_m	$0.296^{+0.022}_{-0.016}$	0.3113 ± 0.0070	$0.276^{+0.025}_{-0.016}$	0.3030 ± 0.0069
H_0 [km/s/Mpc]	$68.8^{+1.7}_{-2.7}$	67.02 ± 0.68	$71.0^{+1.8}_{-3.2}$	67.68 ± 0.71
S_8	$0.787^{+0.024}_{-0.021}$	0.798 ± 0.020	$0.775^{+0.020}_{-0.017}$	0.786 ± 0.018
r_d [Mpc]	148.03 ± 0.53	147.93 ± 0.50	148.16 ± 0.44	148.18 ± 0.45
BE	-0.31	1.04	-0.95	0.84

crossing from $w_{\rm DE} < -1$ to $w_{\rm DE} > -1$ always seems to occur in our post-filtered results, and it is then followed by a second PDL crossing at $a = a_m$ (see Figs. VII.5 and VII.7), which is well constrained in most cases.

TABLE VII.3. 68% CL constraints on the free parameters (above the line) and derived parameters (below the line), obtained from the full-prior results using `SPT` as the baseline CMB dataset. *BE* is the Bayesian Evidence.

	SPT+WMAP +eBOSS	SPT+WMAP +eBOSS+PP	SPT+WMAP +DESI	SPT+WMAP +DESI+PP
$\boldsymbol{\Omega_b h^2}$	0.02242 ± 0.00021	0.02241 ± 0.00020	0.02243 ± 0.00020	0.02244 ± 0.00020
$\boldsymbol{\Omega_c h^2}$	0.1167 ± 0.0020	$0.1169^{+0.0020}_{-0.0017}$	0.1159 ± 0.0017	0.1158 ± 0.0016
$\boldsymbol{100\theta_{MC}}$	1.04014 ± 0.00065	1.04012 ± 0.00065	1.04026 ± 0.00064	1.04029 ± 0.00064
$\boldsymbol{\tau}$	0.0531 ± 0.0071	0.0531 ± 0.0072	0.0535 ± 0.0072	0.0536 ± 0.0072
$\boldsymbol{\ln(10^{10} A_s)}$	3.032 ± 0.015	3.032 ± 0.015	3.030 ± 0.015	3.030 ± 0.015
$\boldsymbol{n_s}$	0.9674 ± 0.0059	0.9670 ± 0.0058	0.9686 ± 0.0056	0.9689 ± 0.0055
α	$0.6^{+1.9}_{-2.6}$	$0.2^{+1.0}_{-1.2}$	$0.6^{+2.3}_{-3.1}$	$0.1^{+1.0}_{-1.3}$
β	$-0.7^{+3.9}_{-3.5}$	$-0.3^{+2.5}_{-1.5}$	$-2.6^{+2.3}_{-4.6}$	$-0.7^{+2.5}_{-1.5}$
a_m	$0.66^{+0.26}_{-0.32}$	0.79 ± 0.27	0.58 ± 0.28	0.73 ± 0.28
Ω_m	$0.330^{+0.029}_{-0.038}$	0.3129 ± 0.0073	$0.323^{+0.036}_{-0.041}$	0.3048 ± 0.0071
H_0 [km/s/Mpc]	65.4 ± 3.3	66.90 ± 0.68	$65.9^{+3.6}_{-4.2}$	67.50 ± 0.70
S_8	0.804 ± 0.025	$0.801^{+0.022}_{-0.019}$	0.796 ± 0.024	0.788 ± 0.018
r_d [Mpc]	147.94 ± 0.53	147.88 ± 0.51	148.12 ± 0.47	148.16 ± 0.46
BE	0.43	0.67	0.25	1.62

TABLE VII.4. 68% CL constraints on the free parameters (above the line) and derived parameters (below the line), obtained from the post-filtered results using `PL18` as the baseline CMB dataset. *BE* is the Bayesian Evidence.

	PL18+eBOSS	PL18+eBOSS+PP	PL18+DESI	PL18+DESI+PP
$\boldsymbol{\Omega_b h^2}$	0.02242 ± 0.00013	0.02241 ± 0.00014	0.02248 ± 0.00014	0.02247 ± 0.00014
$\boldsymbol{\Omega_c h^2}$	0.1195 ± 0.0010	0.1195 ± 0.0010	0.11860 ± 0.00093	0.11883 ± 0.00098
$\boldsymbol{100\theta_{MC}}$	1.04099 ± 0.00030	1.04097 ± 0.00031	1.04113 ± 0.00028	$1.04107^{+0.00030}_{-0.00026}$
$\boldsymbol{\tau}$	0.0553 ± 0.0072	0.0554 ± 0.0072	0.0574 ± 0.0076	0.0571 ± 0.0077
$\boldsymbol{\ln(10^{10} A_s)}$	3.046 ± 0.014	3.046 ± 0.014	3.048 ± 0.015	3.048 ± 0.015
$\boldsymbol{n_s}$	0.9664 ± 0.0038	0.9665 ± 0.0038	0.9688 ± 0.0038	0.9683 ± 0.0038
α	< 1.50	< 1.25	< 1.02	< 1.01
β	$2.44^{+0.91}_{-2.1}$	$1.71^{+0.84}_{-1.0}$	< 2.84	1.66 ± 0.72
a_m	$0.76^{+0.17}_{-0.11}$	> 0.904	$0.66^{+0.26}_{-0.13}$	> 0.913
Ω_m	$0.297^{+0.020}_{-0.013}$	0.3146 ± 0.0066	$0.277^{+0.030}_{-0.019}$	$0.3071^{+0.0058}_{-0.0067}$
H_0 [km/s/Mpc]	$69.4^{+1.4}_{-2.4}$	$67.33^{+0.69}_{-0.62}$	$71.7^{+2.3}_{-3.9}$	$67.99^{+0.68}_{-0.56}$
S_8	0.821 ± 0.012	0.828 ± 0.010	$0.806^{+0.015}_{-0.013}$	0.821 ± 0.010
r_d [Mpc]	147.17 ± 0.24	147.19 ± 0.24	147.35 ± 0.23	147.31 ± 0.24
BE	7.02	7.59	7.55	9.28

We observe that for the `SPT+WMAP+eBOSS` combination, the mean value of H_0 is noticeably lower compared to the corresponding result with `PL18`. However, replacing eBOSS with DESI leads to a significant shift of the Hubble constant towards higher values, with $H_0 = 71.0^{+1.8}_{-3.2}$ km/s/Mpc, in agreement with local measurements with 1.56σ deviations as compared to

TABLE VII.5. 68% CL constraints on the free parameters (above the line) and derived parameters (below the line), obtained from the full-prior results using `PL18` as the baseline CMB dataset. BE is the Bayesian Evidence.

	PL18+eBOSS	PL18+eBOSS+PP	PL18+DESI	PL18+DESI+PP
$\boldsymbol{\Omega_b h^2}$	0.02241 ± 0.00014	0.02241 ± 0.00014	0.02245 ± 0.00014	0.02246 ± 0.00014
$\boldsymbol{\Omega_c h^2}$	0.1196 ± 0.0010	0.11959 ± 0.00099	0.11904 ± 0.00098	0.11889 ± 0.00097
$\boldsymbol{100\theta_{MC}}$	1.04096 ± 0.00030	1.04097 ± 0.00030	1.04105 ± 0.00029	1.04107 ± 0.00029
$\boldsymbol{\tau}$	0.0549 ± 0.0073	0.0551 ± 0.0073	0.0560 ± 0.0075	0.0566 ± 0.0075
$\boldsymbol{\ln(10^{10} A_s)}$	3.045 ± 0.014	3.045 ± 0.014	3.046 ± 0.015	3.047 ± 0.015
$\boldsymbol{n_s}$	0.9662 ± 0.0038	0.9663 ± 0.0038	0.9677 ± 0.0038	0.9681 ± 0.0038
α	$0.6^{+1.9}_{-3.3}$	$0.02^{+0.91}_{-1.2}$	1.1 ± 3.9	$0.2^{+1.2}_{-1.9}$
β	$-1.5^{+3.9}_{-3.2}$	$0.1^{+1.8}_{-1.1}$	< -2.12	$-0.5^{+2.3}_{-1.0}$
a_m	$0.58^{+0.28}_{-0.54}$	$0.75^{+0.28}_{-0.24}$	< 0.743	< 0.824
Ω_m	$0.334^{+0.030}_{-0.039}$	0.3165 ± 0.0068	0.329 ± 0.036	0.3093 ± 0.0067
H_0 [km/s/Mpc]	65.6 ± 3.3	67.14 ± 0.66	$66.1^{+3.1}_{-4.2}$	67.77 ± 0.69
S_8	0.836 ± 0.016	0.830 ± 0.010	$0.831^{+0.018}_{-0.016}$	0.823 ± 0.010
r_d [Mpc]	147.15 ± 0.24	147.17 ± 0.24	147.27 ± 0.23	147.29 ± 0.23
BE	7.65	7.90	9.84	9.59

$\sim 5\sigma$ for the ΛCDM case, along with a correspondingly lower matter density. Moreover, as in the results with `PL18`, the addition of `PP` improves the constraints on α, β, slightly deviating from $\alpha, \beta = 0$ (ΛCDM). It also increases the preference for the ODE model over ΛCDM, in both the filtered and the full-prior cases, as one can see from the bayesian evidence values in Tabs. VII.2, VII.3, VII.4 and VII.5. However, such preference is not substantial when `SPT` is used instead of `Planck` as the CMB benchmark dataset, with the former case showing only slightly positive bayesian evidence values when `SPT` CMB data are used alongside the Pantheon+ supernovae measurements.

Different behaviors are observed when analyzing the model with the full priors. As shown in Tabs. VII.3 and VII.5, β consistently prefers a mean value in the negative region, with the 68% CL for the `SPT+WMAP+DESI` case being negative, and the `PL18+DESI` case having an upper bound of -2.12. Hence, we see that the post-filtering forces the β values to be larger. One could expect, in parallel, that post-filtering would shift the a_m constraints to lower values by dropping the $a_m > 1$ samples in the chain. However, in contrast, the favored values of a_m are smaller for the full-prior, resulting in an upper limit when DESI data are used with Planck. This is due to the correlations between $\{\alpha, \beta, a_m\}$. Finally, although α appears to have significantly larger uncertainties, Fig. VII.3 shows that its posterior is bimodal around zero for the any dataset combination including `PP` (except for the `SPT+WMAP+eBOSS+PP` case), with the peak for the negative values corresponding to a larger probability.

In our analysis, the inferred values of the Hubble constant H_0 remain consistently lower than

the SH0ES measurement ($H_0 = 73.04 \pm 1.04$ km/s/Mpc), though the extent of the discrepancy varies across datasets. For example, the `SPT+WMAP+eBOSS` combination yields $H_0 = 68.8^{+1.7}_{-2.7}$ km/s/Mpc with post-filtered priors (Tab. VII.2), and $H_0 = 65.4 \pm 3.3$ km/s/Mpc with full priors (Tab. VII.3) having the deviations of 2.13σ and 2.21σ respectively with the inferred SH0ES value. In contrast, the `PL18+DESI+PP` combination provides a more precise full-prior estimate of $H_0 = 67.77 \pm 0.69$ km/s/Mpc (Tab. VII.5) with the deviation of 4.12σ with SH0ES value and 0.43σ with Planck value. Although certain configurations formally yield a significantly reduced tension with the SH0ES measurement (e.g., the analyses without `PP`), these tension reductions are mainly due to increased uncertainties of the H_0 constraints, a direct consequence of the three extra parameters of the DMS20 model. Nevertheless, it is worth noting that both the `SPT+WMAP+DESI` and `PL18+DESI` post-filtered results reduce the discrepancy with SH0ES to roughly 1σ, due to both a genuine shift of the mean H_0 value toward higher values and the increased uncertainties.

Top panels of Fig. VII.4 illustrate the evolution of the Hubble parameter for the `PL18+DESI`, `PL18+DESI+PP`, `SPT+WMAP+DESI`, and `SPT+WMAP+DESI+PP` data set combinations of the post-filtered results, while the bottom panels present the corresponding results for the full-prior case. While all these scenarios, along with the baseline ΛCDM model, remain discrepant with the DESI LRG measurement at redshift $z = 0.510$, we can see some improvement in the full-prior results. These figures show, as it was also discussed in the previous paragraph, that the post-filtered results for `PL18+DESI` and `SPT+WMAP+DESI` reduce the H_0 tension relative to ΛCDM albeit with large uncertainties. As shown in the figures, the inclusion of `PP` data reduces the uncertainty and lowers the mean value of H_0, putting it in strong tension with the SH0ES measurement. Comparing the top panels with the bottom ones, it is evident that restricting the priors to satisfy $\alpha > 0$ and $\beta > 0$ significantly limits the flexibility of DMS20 to describe different expansion histories.

Next, we present the evolution of the dark energy density, $\rho_{\rm DE}(z)$, and the corresponding EoS parameter, $w_{\rm DE}(z)$, derived from the posterior chains of our analysis, as shown in Figs. VII.5 and VII.7 for the post-filtered results, and in Figs. VII.6 and VII.8 for the full-prior ones. While noticeable deviations from a cosmological constant ($w = -1$) are permitted across all results, such behavior is not necessarily favored, as discussed previously. A further striking feature shared by all results is the generic occurrence of a double PDL crossing, characterized by opposite crossing directions in each instance. However, the full-prior and post-filtered results differ noticeably, as the order of the PDL crossings may be reversed between them. Specifically, the post-filtered results show an initial crossing into the quintessence regime, followed by a second crossing into the phantom regime. This ordering is by construction, as the post-filtered results assume the existence of a PDL crossing from the quintessence to the

phantom regime, which must be the latest crossing if multiple ones occur. In contrast, the full-prior results may instead exhibit an initial crossing into the phantom regime, followed by a second one into the quintessence regime—although they can also display the same crossing pattern as the post-filtered results. However, note that, while the double PDL crossing is generic, it is not present in all the MCMC samples for either full or post-filtered results. A double crossing for the post-filtered results would correspond to a initially increasing DE density that goes through a decreasing phase before falling back to a decreasing regime; while this behavior describes the majority of the samples in Figs. VII.5 and VII.7, DE density evolutions that start with an initially increasing phase are also ubiquitous, especially when `DESI` is not present in the data set. Similar observations can be made for the full-prior results. As a corollary to these discussions, we see that the present day value of the EoS parameter is always in the phantom regime for the post-filtered results by construction, but it is mostly in the quintessence regime for the full-prior results especially when `DESI` is present in the data set combination. Addition of `PP` exacerbates this behavior further. This late-time preference for a quintessence EoS parameter obtained from combining CMB, `DESI` and `PP` data agrees with the findings of [14, 15]. To quantify this preference (it also serves as a measure to quantify deviations from ΛCDM), we report constraints on the present-day dark energy equation of state parameter w_0 in Tab. VII.6 for the full-prior results. The inferred values range from $w_0 = -0.93^{+0.11}_{-0.13}$ for the `SPT+WMAP+eBOSS+PP` combination to $w_0 = -0.34^{+0.53}_{-0.73}$ for `PL18+DESI`, indicating, depending on the specific case, a mild preference for quintessence-like behavior within the 2σ range. Although $w_0 = -1$ remains consistent with all datasets at the 95% CL, the central values point to slight deviations from a pure cosmological constant, in agreement with the evolving trends in $\rho_{\rm DE}(z)$ and $w_{\rm DE}(z)$ discussed earlier.

TABLE VII.6. Values of w_0 for different dataset combinations (full-prior results). Uncertainties correspond to 68% CL, with 95% CL shown in parentheses.

`Dataset`	w_0
PL18+eBOSS	$-0.55^{+0.50\ (+1.3)}_{-0.71\ (-0.99)}$
PL18+eBOSS+PP	$-0.92^{+0.087\ (+0.25)}_{-0.12\ (-0.20)}$
PL18+DESI	$-0.34^{+0.53\ (+1.2)}_{-0.73\ (-1.0)}$
PL18+DESI+PP	$-0.848^{+0.097\ (+0.27)}_{-0.16\ (-0.22)}$
SPT+WMAP+eBOSS	$-0.65^{+0.44\ (+1.3)}_{-0.71\ (-1.0)}$
SPT+WMAP+eBOSS+PP	$-0.93^{+0.11\ (+0.27)}_{-0.13\ (-0.23)}$
SPT+WMAP+DESI	$-0.44^{+0.58\ (+1.3)}_{-0.75\ (-1.0)}$
SPT+WMAP+DESI+PP	$-0.86^{+0.11\ (+0.27)}_{-0.15\ (-0.22)}$

VII.E Conclusion

In this work, we have carried out a comprehensive analysis of a dynamical dark energy model parameterized by the parameters $\{\alpha, \beta, a_m\}$, extending their prior ranges beyond those considered in previous studies, to enable a broader exploration of the parameter space of the model. This extended framework allows for qualitatively richer evolution histories of the dark energy density $\rho_{\rm DE}(z)$ and equation of state $w_{\rm DE}(z)$, including possible phantom divide line (PDL) crossings in both directions. By combining a variety of observational datasets—including CMB measurements from SPT, WMAP, and Planck; BAO data from eBOSS and DESI; and supernovae observations from Pantheon+ (PP)—we find mild deviations from a cosmological constant at intermediate redshifts, as our results are generally consistent with ΛCDM within 2σ or less. In particular, the EoS generically exhibits two PDL crossings in opposite directions within a single expansion history. These features are robust across different dataset combinations, suggesting that dynamical dark energy with physically nontrivial features might be present in a concordance model.

We also investigated the impact of prior choices by comparing the constraints obtained from full-prior and post-filtered MCMC chains. The post-filtered results assume the presence of a PDL crossing from quintessence to phantom regime, and are better comparable to Refs. [474, 475] that analyze the same DE model. The full priors reveal multimodal behavior highlighting the critical role of prior selection in capturing the full phenomenology of the model, as in this case the preferred present-day value of the EoS parameter is in the quintessence regime unlike the post-filtered results, which assume a present-day phantom value. Both cases are statistically consistent with -1. For some data set combinations the H_0 tension is ameliorated formally due to significantly enlarged uncertainties in comparison to the ΛCDM model, however the combinations of our CMB, BAO and supernovae data give tight constraints on H_0, in strong tension with the SH0ES measurements.

A robust qualitative feature that emerges across essentially all of our likelihood combinations is the frequent appearance of multiple (regular) crossings of the phantom divide line (PDL), $w_{\rm DE} = -1$, within a single dark-energy evolution history. If this phenomenology persists with future data, it would carry nontrivial implications for fundamental model building, but it is crucial to state precisely what is excluded. In particular, a minimally coupled single scalar field with a standard kinetic structure, $\mathcal{L}_\phi = \epsilon X - V(\phi)$ (with $\epsilon = +1$ for quintessence and $\epsilon = -1$ for a pure phantom), cannot realize a *stable* crossing of $w_{\rm DE} = -1$ while maintaining $\rho_{\rm DE} > 0$: such models satisfy $w_{\rm DE} \geq -1$ (quintessence) or $w_{\rm DE} \leq -1$ (phantom) as long as $\rho_{\rm DE} > 0$ (see, e.g., Ref. [538]). Therefore, even a single smooth PDL crossing with strictly positive $\rho_{\rm DE}$ already points beyond the vanilla quintessence/phantom paradigm. Multiple crossings—especially when accompanied by oscillatory behavior and, in parts of parameter space, sign changes in $\rho_{\rm DE}$—tighten these requirements further and naturally motivate multi-

degree-of-freedom dark-sector realizations (e.g. *quintom* or effective multi-fluid descriptions) and/or an effective origin from modified gravity. (We note, however, that if $\rho_{\rm DE}$ is allowed to cross zero, a single-field phantom setup can accommodate transitions from $\rho_{\rm DE} < 0$ with $w_{\rm DE} > -1$ to $\rho_{\rm DE} > 0$ with $w_{\rm DE} < -1$ at late times; see Ref. [538]. In this case the divergence of $w_{\rm DE} = p_{\rm DE}/\rho_{\rm DE}$ at $\rho_{\rm DE} = 0$ is a kinematic artifact of the ratio, rather than a singularity of the background expansion; see, e.g., Refs. [538, 560].) Importantly, this discussion should *not* be interpreted as excluding general single-field constructions: more elaborate frameworks—for instance non-minimally coupled scalars or single-field EFTs with non-trivial kinetic structure/braiding and broken shift symmetry—can yield an *effective* equation of state that crosses -1 and may fit current data well (see, e.g., Refs. [561, 562]). Our point is instead that the specific combination of features suggested by our constraints makes the simplest minimally coupled canonical realizations inadequate and provides concrete motivation to pursue fundamental ODE-like realizations, including non-canonical fields (e.g. [563, 564]), coupled systems, or emergent dark-sector phenomena. Additionally, as a complementary diagnostic, one may map the ODE phenomenology onto an effective CPL description in the (w_0, w_a) plane by treating (w_0, w_a) as a data-compression of the model predictions: for a range of ODE parameter choices, one can generate the corresponding observables and determine the best-fitting (w_0, w_a) while verifying that the residuals remain small (e.g. [551]). For a meaningful comparison with data-driven constraints in the (w_0, w_a) plane, the mapping should also account for the redshift sensitivity and error budget of the probes employed (e.g. [28, 552]). A dedicated implementation of this programme is beyond the scope of the present analysis and is left to future work.

VII.F Acknowledgments

SAA acknowledges the support of the DGAPA postdoctoral fellowship program at ICF-UNAM, Mexico. EDV is supported by a Royal Society Dorothy Hodgkin Research Fellowship. RCN thanks the financial support from the Conselho Nacional de Desenvolvimento Científico e Tecnologico (CNPq, National Council for Scientific and Technological Development) under the project No. 304306/2022-3, and the Fundação de Amparo à Pesquisa do Estado do RS (FAPERGS, Research Support Foundation of the State of RS) for partial financial support under the project No. 23/2551-0000848-3. Ö.A. acknowledges the support by the Turkish Academy of Sciences in the scheme of the Outstanding Young Scientist Award (TÜBA-GEBİP). AAS acknowledges the funding from ANRF, Govt. of India, under the research grant no. CRG/2023/003984. This article is based upon work from COST Action CA21136 Addressing observational tensions in cosmology with systematics and fundamental physics (CosmoVerse) supported by COST (European Cooperation in Science and Technology). The authors acknowledge the use of the HPC resources at the University of Sheffield.

Afterword

In the final part of this chapter, we spend a few words about the choice to carry out a background-only analysis. As mentioned both in the preamble of the paper just presented and throughout its sections, the deviation of ODE from the standard paradigm only happens at the level of Eqs.(VII.1,VII.2). The reason to do this is that the parametrisation presented here represents a purely phenomenological way of introducing dynamical dark energy, which does affect perturbations but only through the dependence of the equations presented in section II.B to the evolution of the density and equation of state of DE defined in Eqs.(VII.1,VII.2). The benefit of this analysis choice is that it spares us from having to implement changes on the perturbation equations directly, which would be required in the case of MG or interacting models.

VIII Slow-rolling Down the Curvature: a Re-assessment of the Planck Constraints on ϕ^2 Inflation in a Closed Universe

Preamble to the Paper

In this final paper-chapter, we present the data analysis of the scalar primordial perturbations in a universe with a closed geometry, for which $\Omega_{\mathcal{K}} < 0$. In particular, the next sections involve the implementation in `CAMB` of a generalised version of the parametric primordial spectrum introduced in Eq.(II.43) that includes the case where $\mathcal{K} = 1$. The derivation for the expression of the primordial spectrum used in this paper follows from [565, 566]. In these two papers, the authors re-derive $P_{\mathcal{R}}$ by introducing a new gauge-independent variable that, unlike $\mathcal{R}$, is conserved at super-horizon scales both in the flat *and* the closed universe limits of this model. This new variable is dubbed $\zeta_{\rm BST}$, and it is linked to $\mathcal{R}$ as follows:

$$\zeta_{\rm BST} = \mathcal{R} + \frac{1}{3}\frac{\Delta\Phi}{\mathcal{H}' - \mathcal{H}^2}.$$

Here, $\mathcal{H}$ is the "comoving Hubble function", defined as $\mathcal{H} = aH$, while Φ is the usual metric perturbation defined in the conformal Newtonian gauge. The result of this calculation is presented in Eq.(VIII.7); it is not repeated here to avoid complicating this Preamble with a fairly cumbersome expression for $P_{\mathcal{R}}$.

A major difference with respect to the flat case is that the perturbation modes for a closed universe are discrete rather than continuous. This follows from the fact that perturbations are treated according to the 3-sphere geometry of a closed universe, so that once we decompose perturbations like Φ or $\zeta_{\rm BST}$ into eigenmodes along a spherical space, the oscillation of each mode n will be described by spherical harmonics functions. This discretization is labeled here through n, an integer variable that takes values such that $n \geq 2$ and is related to k, the wavenumber that is a continuous variable in a flat universe, as $n^2 = k^2 + \mathcal{K}$. In a way, such discretization is analogous to the decomposition of the CMB temperature perturbations into modes ℓ with amplitude C_ℓ, done along the two-dimensional surface of a sphere.

The main goal of the paper presented in this chapter is to reassess the robustness of the constraints that Planck, specifically its PR3 data release, found on $\Omega_{\mathcal{K}}$ by employing the following parametrisation:

$$P_{\mathcal{R}} \propto \frac{(n^2 - 4\mathcal{K})^2}{n(n^2 - \mathcal{K})^2} A_s \left(\frac{k}{k_*}\right)^{n_s - 1}.$$

The factor that, in the equation above, precedes the standard power-law form for $P_{\mathcal{R}}$ as given in Eq.(II.43) is an ad-hoc addition aimed at accommodating the suppression of the primordial spectrum at large scales induced by models where $\Omega_{\mathcal{K}} < 0$. This expression for $P_{\mathcal{R}}$ was employed, for instance, to explain the suppression in the quadrupole of the CMB temperature spectrum of WMAP [567]. A similar suppression has also been observed in Planck's PR3 data in both the quadrupole and the octupole modes of the temperature spectrum [23], an observation that has been interpreted as evidence for a closed universe [166, 167]. The importance of these observations begs the question of whether the expression above, which is purely phenomenological and not justified on any theoretical grounds, can be considered as a reliable tool to test for fundamental departures from spatial flatness. The paper presented here is an attempt at tackling exactly this question, by taking into consideration the model for $P_{\mathcal{R}}$ briefly outlined above as an alternative method to constrain the spatial curvature of the universe.

Finally, this paper can be seen as a ramification of the MG analyses presented in chapters IV-VI in the sense that, here too, we seek to leverage some of the features in Planck's PR3 temperature spectrum that seem to point at possible departures from the ΛCDM model. While only valid for inflaton potentials satisfying $V(\phi) \sim \phi^2$, the model analysed in this paper can still be considered as a fairly general and, most importantly, theoretically robust parametrisation of the primordial spectrum in a closed universe.

Slow-rolling down the curvature: a reassessment of the Planck constraints on ϕ^2 inflation in a closed universe

Abstract: We revisit the Cosmic Microwave Background (CMB) constraints on the spatial curvature of the Universe, assessing how they change when the curvature parameter and the primordial inflationary scalar spectrum are treated consistently within theoretically motivated frameworks. Instead of relying on the phenomenological parametrisation commonly used to capture curvature effects at the largest scales, we present a case study based on closed quadratic inflation, where the primordial spectrum is derived in full generality and in a gauge-invariant manner. Within this framework, we analyze both the `plik` PR3 and `CamSpec` PR4 Planck CMB likelihoods and find that the constraints on $\Omega_{\mathcal{K}}$ shift towards spatial flatness. In `plik` the preference for $\Omega_{\mathcal{K}} < 0$ decreases from $\gtrsim 3.5\sigma$ to $\sim 2.5\sigma$, while in `CamSpec` it reduces further to $\sim 2\sigma$. At large angular scales ($\ell < 10$), our model explains the low-ℓ power suppression anomaly, notably improving the fit to the quadrupole. However, the reduced preference for highly negative values of $\Omega_{\mathcal{K}}$ only partially accounts for the lensing anomaly at high multipoles, worsening the fit to the `plik` spectrum at small scales. By contrast, in the `CamSpec` PR4 spectrum, where the lensing anomaly is less pronounced, the model yields an overall improvement. Our analysis highlights a key conceptual point: closed-inflation models tie the curvature parameter to the inflationary dynamics and the primordial spectrum, enforcing consistency conditions that do not necessarily allow for the large deviations from flatness seen in phenomenological parametrisations. In the case of quadratic inflation, these restrictions reduce the apparent evidence for negative curvature reported by earlier analyses, while allowing for a mildly closed geometry.

VIII.A Introduction

The spatially-flat ΛCDM model, built on the assumption of the validity of general relativity at cosmological scales and the existence of the two energy components contained in its name, Λ (the cosmological constant) and CDM (cold dark matter), is to date our best attempt at unifying all of the cosmological observations currently available to us under the flag of a single paradigm. Despite its successes, this model suffers from some yet unresolved problems that put its validity into question – see [78] and the references therein for the most up-to-date summary of these issues. A notable incosistency is the *Hubble tension* [110, 114, 115, 117,

120, 143, 147, 220–226], which refers to a non-trivial mismatch in the measurement of H_0, the present-day value of the Hubble parameter H, by different cosmological tracers. This tension is best exemplified by the astounding 6.2σ discrepancy between the measurement of H_0 obtained by the SH0ES team from Cepheid-calibrated type Ia supernovae [84, 227], a late-time probe, and that from the cosmic microwave background (CMB) temperature and polarisation anisotropy spectra, an early-time probe, which the South Pole Telescope (SPT) ground-based observatory reports to be $H_0 = 66.66 \pm 0.60\,\mathrm{km\,s^{-1}\,Mpc^{-1}}$ in their recent SPT-3G D1 release [25]. If measurement systematics are to be ruled out as the root of the problems plaguing the ΛCDM scenario, such as the Hubble tension mentioned above [84, 228, 485, 487, 488, 497–505], solutions need to be sought in alternative models of cosmology, by challenging the standard model's foundations.

An integral part of these foundations is the theory of *inflation* [105, 106], commonly described by a minimally coupled scalar field, ϕ, that slowly rolls down the slope of its potential, $\mathcal{V}(\phi)$. While providing a mechanism that explains the origin of the primordial density perturbations that went on to form the structures in the universe we now observe, inflation can also offer a solution to the so-called *flatness problem*. First pointed out by Robert Dicke in 1969, the flatness problem is, in essence, a fine-tuning problem related to the amount of spatial curvature that characterises the universe: $\Omega_\mathcal{K}$, where the subscript $\mathcal{K}$ denotes the curvature parameter and can take the values -1, 0, or 1, depending on whether the universe is open, flat, or closed, respectively. The total energy budget of the universe can be defined as $\Omega = 8\pi G\rho/3H^2$, with ρ including the densities of matter, radiation, and Λ; for a flat universe, $\Omega = 1$. Dicke observed that since (1) Ω strays away from unity as the universe expands and (2) we currently observe the universe to be very close to flatness, or equivalently $\Omega_0 \approx 1$, then at early times the value of Ω must have been even closer to 1 than it is today – an almost perfectly flat universe. To avoid such fine-tuning of the Universe's initial conditions, we resort to inflation, which postulates an early period of exponential expansion able to guarantee a nearly flat Universe today for a wide range of initial values of Ω.

State-of-the-art cosmological observations almost unanimously agree that the current universe, as far as we can tell, is spatially flat. The latest baryon acoustic oscillation (BAO) distance measurements from the Dark Energy Spectroscopic Instrument (DESI) yield $\Omega_\mathcal{K} = 0.025 \pm 0.041$ [15], in good agreement with previous SDSS BAO results, $\Omega_\mathcal{K} = 0.079^{+0.083}_{-0.10}$ [76]. Both measurements are consistent with spatial flatness within 1σ. The 3×2pt measurements of the weak lensing of galaxies, their clustering, and the cross-correlation of the two can also be shown to agree with $\Omega_\mathcal{K} = 0$: the Dark Energy Survey (DES), when combined with CMB and Type Ia supernovae (SNIa) data, reports $\Omega_\mathcal{K} = 0.001 \pm 0.002$ [97], while the KiDS-Legacy analysis finds $\Omega_\mathcal{K} = 0.011^{+0.054}_{-0.057}$ [211]. CMB data from the Atacama Cosmology Telescope (ACT) also indicate flatness to within $\sim 1.3\sigma$ (including Planck CMB and DESI BAO data) [44]. Similarly, the CMB spectra of SPT alone constrain $\Omega_\mathcal{K}$ to be less than 1σ

away from a null value [25].

Perhaps the only discordant result, though entangled with many caveats and technicalities, comes from the temperature and polarisation spectra released by the Planck satellite, which still remains the most precise CMB probe. The Planck Release 3 (PR3), without including lensing reconstruction data, suggests evidence for a closed universe, with $\Omega_\mathcal{K} = -0.044^{+0.018}_{-0.015}$ [23, 166, 167], deviating from flatness at more than 3σ. In the recent Planck Release 4 (PR4) this evidence is reduced, yet differences between likelihoods remain: `CamSpec` [45] yields $\Omega_\mathcal{K} = -0.025^{+0.013}_{-0.010}$, still over 2σ away from ΛCDM, while `HiLLiPoP` [24] finds consistency with flatness to within 1σ.

Inevitably, the presumed Planck preference for a curved Universe sparked (and continues to attract) a series of dedicated analyses, thereby [116, 165–167, 297, 307–325, 568–588]. This renewed interest in spatial curvature remains timely and relevant not primarily because of the aforementioned Planck preference for a closed Universe (an indication reduced in the PR4 release and, if taken at face value, not supported by most other early- and late-Universe probes), but because $\Omega_\mathcal{K}$ remains a parameter of central importance in many models extending beyond ΛCDM. These include, among others, proposed solutions to the Hubble tension [220, 589–591] and models of dynamical dark energy invoked to explain the present-day accelerated expansion of the Universe [297, 322, 592, 593].

In almost all studies characterizing spatial curvature, including the Planck analyses themselves, the primordial spectrum P_ζ in a non-flat universe is modeled using the following heuristic formula [307, 308, 567, 594–596]:

$$P_\zeta \propto \frac{(n^2-4\mathcal{K})^2}{n(n^2-\mathcal{K})^2} A_s \left(\frac{k}{k_*}\right)^{n_s-1}, \tag{VIII.1}$$

where

$$n^2 = k^2 + \mathcal{K} \tag{VIII.2}$$

takes discrete values such that $n \geq 3$ when $\mathcal{K} = 1$. The pivot scale is usually fixed at $k_* = 0.05\,\mathrm{Mpc}^{-1}$, which corresponds to the scale at which the amplitude A_s and the tilt n_s of the primordial spectrum are evaluated.

Eq. (VIII.1) is an adaptation of the power-law expression generally used to test flat models, which can be recovered by fixing $\mathcal{K} = 0$. The n-dependent prefactor is introduced to heuristically capture the modifications induced by curvature on the largest scales, where a closed geometry leads to discrete eigenmodes and non-trivial deviations from the flat case. While this construction is convenient, it lacks a direct derivation from a concrete inflationary model and should be interpreted with caution, as depending on the underlying model it may not adequately reproduce the imprints of the inflationary dynamics on the primordial spectrum

at those scales. This limitation has been discussed in several works that attempted to move beyond such a heuristic treatment [597–601].[VIII.1]

Yet another source of concern, besides the heuristic nature of Eq.(VIII.1), is that, as emphasised in Ref. [626] (see also [47, 602, 603]), predictions for a closed universe can vary significantly across different gauges, especially on large scales corresponding to wavelengths comparable to the curvature radius. Broadly speaking, this is due to the fact that, in a closed FRW geometry ($\mathcal{K} > 0$), scalar perturbations are expanded in hyperspherical harmonics on S^3 with discrete wavenumbers n. The physically propagating modes start at $n \geq 3$, while the $n = 1, 2$ sectors are non-dynamical or pure gauge. At the largest scales, corresponding to small n, the usual time slicings (e.g., Newtonian, synchronous, comoving) differ markedly, and the constraint equations introduce $\mathcal{O}(\mathcal{K}/n^2)$ terms that mix scalar-field and metric perturbations. As a consequence, spectra computed for gauge-fixed variables (such as $\delta\phi$ in comoving gauge or the Bardeen potentials in Newtonian gauge) can exhibit gauge-dependent amplitudes and tilts precisely where curvature effects are strongest.[VIII.2] Therefore, alternative formulations and analyses performed within a fixed gauge – even when aiming to go beyond this parametrisation and provide more precise calculations – may still carry residual ambiguities rooted in the gauge choice.

Although these issues may seem like technical subtleties of mainly academic interest, they can become highly relevant when deriving observational constraints on the spatial curvature parameter from Planck data. The apparent Planck preference for a closed universe arises not only from the well-known lensing anomaly – i.e., the preference for enhanced smoothing of the acoustic peaks at small scales [303, 304, 306, 332, 453, 627] – but also from small yet important differences in the fit to the CMB power spectra at the largest scales [567, 623]. Planck measurements of temperature and polarisation anisotropies indeed reveal a series of long-standing anomalies in this regime: the TT spectrum at the lowest multipoles $\ell \lesssim 10$ (notably the quadrupole and octopole) lies systematically below the best-fit ΛCDM prediction [23, 51]. It is precisely on these scales that the heuristic n-dependent corrections in Eq. (VIII.1) – and, more broadly, gauge-dependent treatments in alternative formulations – can mimic a preference for negative curvature, thereby potentially contributing to the apparent Planck signal for $\Omega_{\mathcal{K}} < 0$ and raising doubts about the robustness of curvature constraints derived from gauge-dependent approaches.

In this work, we reassess the implications of the above limitations by adopting the primordial power spectrum for a closed universe originally derived in Ref. [565]. Specifically, we employ a gauge-invariant variable, constructed in analogy with the Mukhanov–Sasaki variable, which combines scalar field and metric perturbations to yield a fully gauge-invariant expression for the primordial spectrum in a closed geometry. We use this theoretically motivated spectrum

[VIII.1] For discussions surrounding inflation in a closed Universe, see also Refs. [597, 602–625].

[VIII.2] This issue is further compounded by the choice of initial vacuum in a closed geometry, where there is no exact Minkowski sub-horizon limit and naive Bunch–Davies prescriptions can pick up gauge-specific normalisations on large scales.

as a case study to evaluate the impact on current constraints on $\Omega_{\mathcal{K}}$ from Planck data and to reassess the presumed preference for a closed universe within physically motivated models of closed inflation. The details of the derivation are summarised in Sec. VIII.B, the data used in our analysis are described in Sec. VIII.C, the results are presented in Sec. VIII.D, and our conclusions on the flatness of the present universe are drawn in Sec. VIII.E.

VIII.B The Gauge-invariant Primordial power Spectrum in a Closed Universe

In a closed Friedmann–Lemaître–Robertson–Walker (FLRW) universe, we consider an inflationary phase driven by a scalar field ϕ with a quadratic potential $\mathcal{V}(\phi) = \frac{1}{2}m^2\phi^2$. As one of the simplest and most widely used slow-roll potentials, it provides a standard benchmark for studying inflationary dynamics and for isolating the effects induced purely by the spatial curvature in a closed FLRW background.

The line element of the FLRW metric in conformal time η is given by

$$ds^2 = a^2(\eta)\left[-d\eta^2 + d\chi^2 + s_{\mathcal{K}}^2(\chi)\, d\Omega^2\right], \tag{VIII.3}$$

where $a(\eta)$ is the scale factor, χ is the comoving radial distance, and $d\Omega^2 = d\theta^2 + \sin^2\theta\, d\phi^2$ is the infinitesimal solid angle. For the closed model, the function $s_{\mathcal{K}}(\chi)$ takes the form

$$s_{\mathcal{K}}(\chi) = \frac{\sin\left(\sqrt{|\mathcal{K}|}\,\chi\right)}{\sqrt{|\mathcal{K}|}}, \tag{VIII.4}$$

with curvature parameter $\mathcal{K} = +1$.

In the slow-roll regime, the scalar field satisfies the following conditions:

$$\dot{\phi}^2 \ll \mathcal{V}(\phi), \quad |\ddot{\phi}| \ll 3H|\dot{\phi}|. \tag{VIII.5}$$

The slow-roll parameters are defined as

$$\epsilon = 1 - \frac{\mathcal{H}'}{\mathcal{H}^2}, \quad \delta = \epsilon - \frac{\epsilon'}{2\mathcal{H}\epsilon}, \tag{VIII.6}$$

where $\mathcal{H}$ denotes the comoving Hubble parameter, related to the Hubble parameter by $\mathcal{H} = aH$. The prime indicates a derivative with respect to conformal time η.

The power spectrum in the slow-roll approximation using a gauge-invariant variable, originally derived in Ref. [565], is summarised here together with the assumptions underlying its derivation. The calculation proceeds within the framework of canonical quantum gravity. Implementing canonical quantization for the perturbed inflationary universe model leads to the

corresponding Wheeler–DeWitt equation. Applying a semiclassical Born–Oppenheimer type of approximation to this equation allows one to recover Schrödinger equations for the perturbation modes (see Eq. (57) in Ref. [565]), together with the quantum-gravitationally corrected Schrödinger equation at the next order of approximation. From the resulting Schrödinger equation, the power spectrum for the gauge-invariant generalised Mukhanov-Sasaki variable is obtained (see Eq. (74) in Ref. [565]). The initial state of the perturbation modes is taken to be the adiabatic vacuum, the standard choice for quantum fluctuations in this framework. The quantum-gravitationally corrected Schrödinger equation and the corresponding corrected spectrum are derived in Ref. [566].

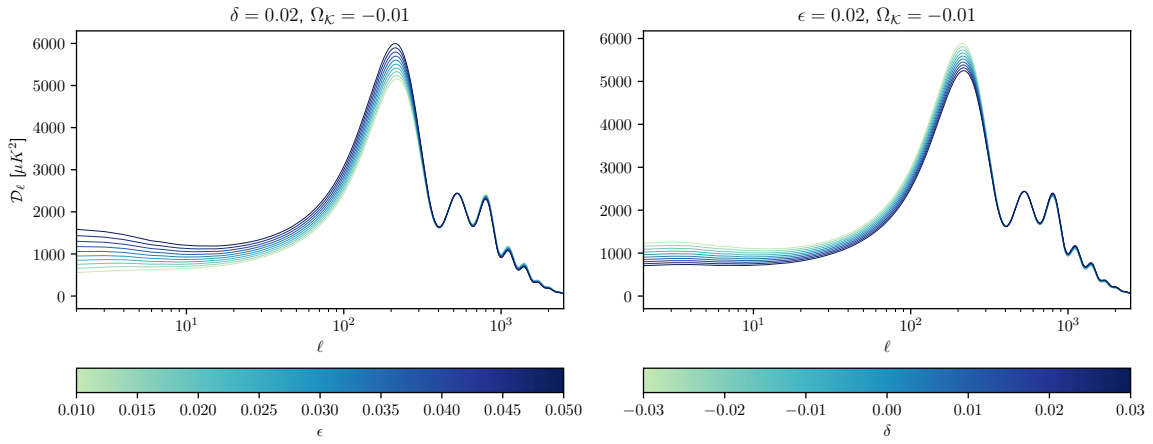


FIG. VIII.1. Left panel: Variations of C_ℓ^{TT} when the slow-roll parameter ϵ is varied in the range $\epsilon = [0.01, 0.05]$ with fixed $\delta = 0.02$ and $\Omega_{\mathcal{K}} = -0.01$. Right panel: Variations of C_ℓ^{TT} when the slow-roll parameter δ is varied in the range $\delta = [-0.03, 0.03]$ with fixed $\epsilon = 0.02$ and $\Omega_{\mathcal{K}} = -0.01$.

In addition to the power spectrum of the generalised Mukhanov–Sasaki variable, the power spectrum of the gauge-invariant variable $\zeta_{\rm BST}$ (named after Bardeen, Steinhardt, and Turner [628]) is also obtained in Ref. [565] (see Eq. (79) therein), where it is expressed in terms of the former. The variable $\zeta_{\rm BST}$ remains conserved during the evolution of super-Hubble modes in non-flat FLRW models [626]; hence, it is the natural quantity for relating the primordial scalar perturbations at the end of inflation to the temperature anisotropies of the CMB and the quantity that directly enters as input in our Boltzmann code computations.

In obtaining the power spectrum, the derivation was performed to first order in the slow-roll parameters ϵ and δ, with higher-order terms neglected. In addition, curvature corrections involving higher powers of $\mathcal{K}/\mathcal{H}^2$ were omitted, a justified approximation since during inflation the comoving Hubble horizon $\mathcal{H}^{-1}$ decreases rapidly.

The primordial power spectrum for $\zeta_{\rm BST}$ takes the following explicit form[VIII.3],[VIII.4]:

$$P_{\zeta_{\rm BST}} = \frac{1}{\pi}\frac{H^2}{M_P^2\left(\epsilon+\frac{\mathcal{K}}{\mathcal{H}^2}\right)}\frac{1-\mathcal{K}/n^2}{f_\epsilon^3(n)}\left[1+\frac{\mathcal{K}\left(\epsilon+\mathcal{K}/\mathcal{H}^2\right)}{n^2-4\mathcal{K}}\right] \times \tilde{C}_{\epsilon,\delta}\left(\frac{n}{aH}f_\epsilon(n)\right)^{-2(\gamma-3\lambda_{\epsilon,\delta}(n)/2)}, \tag{VIII.7}$$

with

$$\tilde{C}_{\epsilon,\delta} = 1-2\epsilon+\left(\gamma-\frac{3}{2}\lambda_{\epsilon,\delta}(n)\right)(4-2\gamma_E-2\ln(2)), \tag{VIII.8}$$

where $\gamma = 2\epsilon-\delta$, and $\gamma_E \simeq 0.5772$ is the Euler–Mascheroni constant. The functions $f_\epsilon(n)$ and $\lambda_{\epsilon,\delta}(n)$ are given by

$$f_\epsilon(n) = \left\{1-\frac{\mathcal{K}}{n^2}-\frac{\mathcal{K}}{n^2-4\mathcal{K}}\left(2+3\epsilon+\frac{(3\epsilon-1)\mathcal{K}}{n^2}\right) + \frac{3(3-2\epsilon)\mathcal{K}^2}{(n^2-4\mathcal{K})^2}\left(1-\frac{\mathcal{K}}{n^2}\right)\right\}^{\frac{1}{2}}, \tag{VIII.9}$$

and

$$\lambda_{\epsilon,\delta}(n) = 1-\left\{1-\frac{8\mathcal{K}}{n^2-4\mathcal{K}}\frac{1}{4\gamma+3} \times\left(3\gamma+12\delta+\frac{3\epsilon}{2}\frac{n^2-\mathcal{K}}{n^2-4\mathcal{K}}\right)\right\}^{\frac{1}{2}}. \tag{VIII.10}$$

These functions arise when solving the Schrödinger equation for the perturbation modes in a closed FLRW background: $f_\epsilon(n)$ appears in the argument of the Bessel functions, and $\lambda_{\epsilon,\delta}$ determines their order, encoding the corrections induced by spatial curvature in a closed FLRW geometry (see Eq. (63) in Ref. [565]).

Furthermore, let us recall the power spectrum in the flat case [629], which can be recovered from the power spectrum in Eq. (VIII.7) by taking the large-wavenumber limit:

$$P_\zeta^{\rm f}(k) = \frac{1}{\pi}\frac{H^2}{M_P^2\epsilon}C_{\epsilon,\delta}\left(\frac{k}{aH}\right)^{-2\gamma}, \tag{VIII.11}$$

[VIII.3] Here, the Planck mass is defined as $M_{\rm P} := \sqrt{1/G}$, and calculations are performed in natural units, $\hbar = c = 1$.

[VIII.4] For convenience and consistency with our numerical implementation, we write the spectrum in the compact, power-law-like form commonly used in standard slow-roll treatments (e.g. Eq. (8.226) of [626]). This expression is algebraically equivalent to the logarithmic form given in Eqs. (74) and (77) of Ref. [565] to first order in the slow-roll parameters which is the order to which the original derivation applies.

where

$$C_{\epsilon,\delta} = 1 - 2\epsilon + \gamma(4 - 2\gamma_E - 2\ln(2)). \tag{VIII.12}$$

Here, the power spectrum is expressed in terms of the conserved gauge-invariant variable ζ for the flat FLRW model. Its relation to $\zeta_{\rm BST}$ is discussed in [626].

We stress that this derivation of the primordial spectrum based on Ref. [565], is carried out for a quadratic inflationary background. The background equations are first solved explicitly for the potential $V(\phi) = m^2\phi^2/2$, and the resulting functions $H(t)$, $a(t)$, and $\phi(t)$ are then inserted into the perturbation equations. Therefore, although the final expressions are written in terms of slow-roll parameters, the resulting spectrum is not universal in a closed Universe: it is valid only for the quadratic potential used in the derivation. This model dependence is not merely a byproduct of methodology, but reflects an intrinsic obstruction specific to the closed case that has no analogue in flat inflation. When $\mathcal{K} > 0$, the Friedmann equation contains the additional contribution $\mathcal{K}/a^2$, whose evolution cannot be rewritten in terms of ϵ, δ, and their time derivatives. Unlike the slow-roll terms, the curvature contribution does not scale with the slow-roll hierarchy and depends explicitly on the full background solution through $a(t)$. The suppression of $\mathcal{K}/a^2$, the duration of the curvature-dominated regime, and the onset of the slow-roll phase all depend sensitively on the detailed form of $V(\phi)$. As a result, two different potentials with identical values of (ϵ, δ) can lead to different background evolutions in the closed case. This already prevents the Mukhanov–Sasaki frequency from being written solely in terms of slow-roll parameters, in contrast with the flat scenario. In addition, the curvature-modified Mukhanov–Sasaki equation contains contributions proportional to $\mathcal{K}$ and to the discrete Laplacian eigenvalues on S^3, $n(n+2)$. These terms involve a, a', and a'' in ways that cannot be encoded by the slow-roll hierarchy alone. This is a purely geometric effect of the closed spatial topology: the discrete spectrum of scalar harmonics and the curvature-dependent contributions couple directly to the background evolution, introducing an explicit dependence on $V(\phi)$.

We note that [565] demonstrated that the power spectrum in a closed FLRW model is suppressed at large scales and exhibits a cutoff at the largest scales, compared to the flat case, due to the finiteness of the spatial geometry. It should also be pointed out that the power spectrum in Eq. (VIII.7) exhibits an explicit and prominent scale dependence at large scales due to the curvature of the universe. Consequently, the usual power-law approximation, which assumes only weak scale dependence quantified by the spectral index, is not applicable in this case.

VIII.C Methodology and datasets

In this section, we describe the numerical implementation of the inflationary model (paragraph VIII.C.1) and discuss how we test its viability against CMB data (paragraph VIII.C.2).

VIII.C.1 Re-expressing P_ζ^c

We first expand on how Eq. (VIII.7) was implemented into the Boltzmann solver `CAMB` [31, 32] for the calculation of the observables used in this analysis, namely the temperature, polarisation, and CMB lensing potential spectra.

In the flat ΛCDM model, the mild scale dependence of the primordial power spectrum can be rewritten in the form of a power law:

$$P_\zeta^f(k) = A_s \left(\frac{k}{k_*}\right)^{n_s-1}, \tag{VIII.13}$$

which can be used as a parametric approximation of Eq. (VIII.11). Because Eq. (VIII.13) is the mathematical form employed by `CAMB` to evaluate P_ζ^f, it would be natural to also re-express Eq. (VIII.7) in terms of a power law, by calculating what A_s and n_s would look like in our model. However, as explained in Sec. VIII.B, this is not trivial due to the strong k-dependence of the primordial spectrum in this model. We therefore adopt the following strategy to implement Eq. (VIII.7).

First, due to the complexity of the full expression in Eq. (VIII.7), we introduce the following approximations to simplify its implementation in `CAMB` [31, 32]: we set the slow-roll parameters to zero within the functions $f_\epsilon(n)$ and $\lambda_{\epsilon,\delta}(n)$, where their contributions are verified to be negligible. Thus, for convenience, in the present analysis, we consider the power spectrum in Eq. (VIII.7) with

$$f(n) := \lim_{\epsilon\to 0} f_\epsilon(n) \quad \text{and} \quad \lim_{\epsilon,\delta\to 0} \lambda_{\epsilon,\delta}(n) = 0. \tag{VIII.14}$$

The function in Eq. (VIII.8) also simplifies to $\tilde{C}_{\epsilon,\delta}(n) \approx C_{\epsilon,\delta}$. We denote the resulting expression for the power spectrum in the closed FLRW universe by $P_\zeta^c(n)$:

$$\begin{aligned} P_\zeta^c(n) = \frac{1}{\pi}\frac{H^2\left(1-\mathcal{K}/n^2\right)}{M_P^2\left(\epsilon+\frac{\mathcal{K}}{\mathcal{H}^2}\right)f^3(n)}\left[1+\frac{\mathcal{K}}{n^2-4\mathcal{K}}\left(\epsilon+\frac{\mathcal{K}}{\mathcal{H}^2}\right)\right] \\ \times C_{\epsilon,\delta}\left(\frac{n}{aH}f(n)\right)^{-2\gamma}. \end{aligned} \tag{VIII.15}$$

The approximation introduced by Eq. (VIII.14) is not based on a strict order-by-order expansion of the parameters ϵ and $\mathcal{K}/n^2$ (the combination of which is neglected in $f_\epsilon(n)$ and

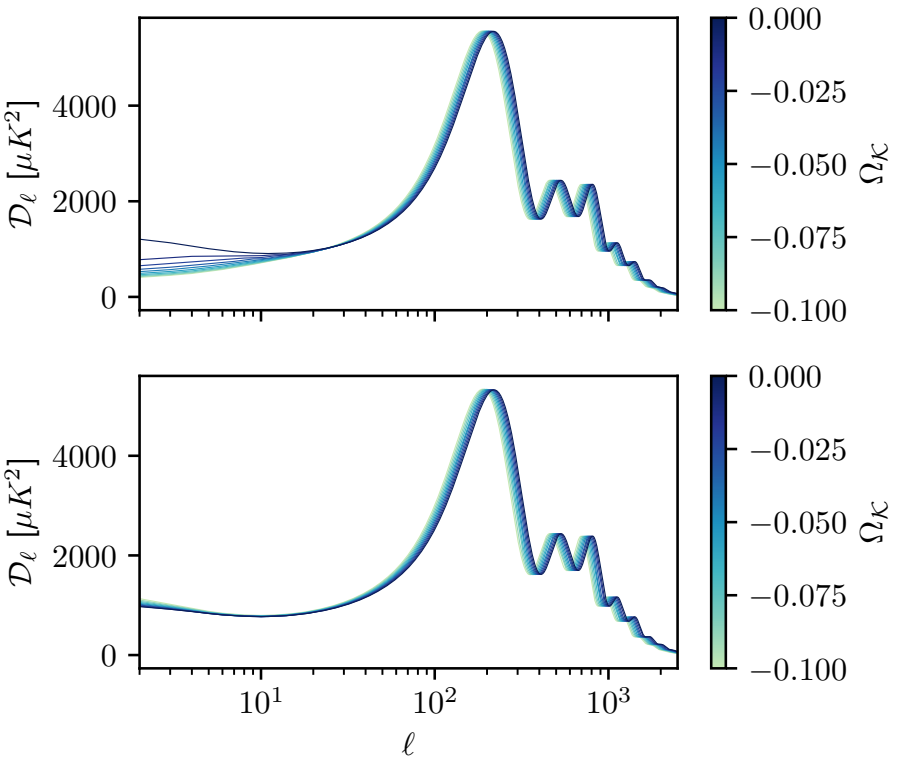


FIG. VIII.2. The CMB TT spectrum according to Eq.(VIII.16) (upper figure) and the one calculated with the standard `CAMB` implementation (lower figure). The lower $\Omega_\mathcal{K}$, the stronger the suppression of the low-ℓ spectrum.

$\lambda_{\epsilon,\delta}(n)$ but still appears in Eq. (VIII.15)), but rather on numerical relevance for the CMB observables. This simplification was designed so that the modified $P_\zeta^c(n)$ can be rewritten as a multiplicative correction to the standard power-law spectrum as explained in the following lines, avoiding numerical instabilities in `CAMB`. This choice aims to increase the speed of convergence of the MCMC scans while ensuring a negligible impact on the resulting cosmological constraints.

Second, we generalize the primordial spectrum to include our non-flat scenario by introducing a factor, $\Phi(n, \epsilon, \delta)$, that reduces to unity when $\Omega_\mathcal{K} = 0$:

$$P_\zeta^c(n) = P_\zeta^{\rm f}(n)\, \Phi(n, \epsilon, \delta), \tag{VIII.16}$$

where $P_\zeta^f(n)$ simply results from redefining the wavenumber in Eq. (VIII.13) according to Eq. (VIII.2). Here, $\Phi(n, \epsilon, \delta)$ is not just an arbitrary function that needs to be constrained or reconstructed by the data. As a matter of fact, it is precisely defined as the ratio between

Eq. (VIII.15) and its equivalent expression in the ΛCDM limit, Eq. (VIII.11):

$$\begin{aligned}\Phi(n,\epsilon,\delta) &= \frac{P_\zeta^{\rm c}(n)}{P_\zeta^{\rm f}(n)} \\ &= \frac{\epsilon}{\left(\epsilon+\frac{\mathcal{K}}{\mathcal{H}^2}\right)}\left(1-\frac{\mathcal{K}}{n^2}\right) \\ &\quad\times\left[1+\frac{\mathcal{K}}{n^2-4\mathcal{K}}\left(\epsilon+\frac{\mathcal{K}}{\mathcal{H}^2}\right)\right] f(n)^{-2\gamma-3}.\end{aligned} \tag{VIII.17}$$

Therefore, by construction, in the $\mathcal{K}\to 0$ limit $\Phi(n,\epsilon,\delta)$ reduces to unity, recovering the flat-universe case. Conversely, in a closed universe ($\mathcal{K}=1$), the flat contribution cancels out and the expression isolates the purely curvature-dependent corrections. In this way, the result can be interpreted as a "correction factor" to the familiar power law of Eq. (VIII.13), which makes its implementation into `CAMB` straightforward.

In order to check whether the approximations introduced by Eq. (VIII.14) are robust and can be safely used to constrain P_ζ with data, in Appendix B we carry out a comparison between the approximated (i.e., Eq. (VIII.15)) and the full (i.e., Eq. (VIII.7)) versions of P_ζ by implementing both in `CAMB`. The difference between the approximated and non-approximated spectra of the CMB temperature anisotropies is shown to be well within the uncertainties of Planck's 2018 measurements of the temperature spectrum [23], meaning that choosing Eq. (VIII.15) over Eq. (VIII.7) does not introduce any relevant systematic shift in the constraints for our model outlined in Sec. VIII.D.

Finally, the effect of varying the slow-roll parameters ϵ and δ in this setup is illustrated in Fig. VIII.1. Increasing ϵ leads to an overall enhancement of the CMB temperature power spectrum, particularly at low multipoles, while increasing δ produces the opposite effect, suppressing power across all scales. In Fig. VIII.2, instead, we compare the TT spectrum obtained from our model using Eq. (VIII.16) to the standard `CAMB` implementation of curvature. While both approaches yield similar results at high multipoles (the damping tail), the suppression of low-ℓ power, especially the quadrupole, is significantly stronger in our model. The standard implementation shows only a mild suppression at low-ℓ for the same values of $\Omega_{\mathcal{K}}$.

VIII.C.2 Planck Likelihoods and Data

The ΛCDM parameter space – hereafter referred to as λ – is expanded by the additional parameters introduced by our model: $\lambda \longrightarrow \lambda_c = \lambda \cup \{\epsilon, \delta, \Omega_\mathcal{K}\}$.[VIII.5]

To efficiently sample λ_c within the prior volume given by the flat priors[VIII.6] listed in Tab. VIII.1, we use the `Cobaya` Markov Chain Monte Carlo (MCMC) package [91]. The sample chains obtained in this fashion are then analyzed using the `Getdist` plotting code [349], so as to derive the constraints on λ_c and their graphical 1D and 2D representations, presented in Sec. VIII.D.

The viability of the inflationary model outlined in Sec. VIII.B is tested using exclusively CMB data: both the curvature and the slow-roll parameters ϵ and δ directly affect the primordial spectrum P_ζ, which in turn determines the temperature anisotropies of the CMB, as illustrated in Fig. VIII.1 and Fig. VIII.2. This makes the Planck CMB measurements a natural probe to constrain the model. The Planck CMB likelihoods employed in our analysis, along with their corresponding keys, are listed below.

Parameter	Prior
$\Omega_\mathrm{b}h^2$	$[0.017,\ 0.027]$
$\Omega_\mathrm{c}h^2$	$[0.09,\ 0.15]$
τ	$[0.01,\ 0.2]$
$\log(10^{10}A_s)$	$[2.6,\ 3.5]$
$100\,\theta_\mathrm{MC}$	$[1.03,\ 1.05]$
$\Omega_\mathcal{K}$	$[-0.05,\ 0]$
ϵ	$[0,\ 0.05]$
δ	$[-0.03,\ 0.03]$

TABLE VIII.1. Flat priors adopted to constrain the parameters of the inflationary model presented here, including $\epsilon, \delta, \Omega_\mathcal{K}$.

- **PL18**: this is a likelihood combination including `plik` [51] for the temperature (TT), polarization (EE), and temperature-polarization cross-correlation (TE) Planck 2018 spectra at $\ell > 30$, while in the $\ell < 30$ range we use the `simall` likelihood [23] for E-mode polarization measurements, and the `Commander` likelihood [452] for the TT anisotropies.

[VIII.5] λ includes the energy densities of baryonic ($\Omega_\mathrm{b}h^2$) and dark ($\Omega_\mathrm{c}h^2$) matter, the optical depth integrated to the reionization epoch (τ), the sound horizon-angular diameter distance ratio calculated at last scattering (θ_MC) as well as the amplitude (A_s) and tilt (n_s) of the flat primordial scalar spectrum Eq.(VIII.13) employed in Eq. (VIII.16). n_s is, in this case, a derived parameter, as it depends on ϵ and δ: $n_s = 2\delta - 4\epsilon$.

[VIII.6] Note that throughout this work we assume a prior $\epsilon > 0$. In canonical single-field inflation this follows from the null-energy condition, which fixes $\dot{H}$ to be negative in flat space. In closed geometries the curvature term can slightly modify its magnitude, but it cannot flip its sign without breaking the slow-roll dynamics: if curvature-dominated $\dot{H}$, the evolution would no longer be controlled by the inflaton field and the system would not describe a genuine slow-roll phase. Such configurations therefore lie outside the class of models considered here.

- **lensing**: this is the lensing spectrum, $C_\ell^{\phi\phi}$, from the 2018 data release of Planck's maps [52]; ϕ is the lensing potential that can be reconstructed through quadratic estimators of TT and EE.

- **CamSpec**: this combination includes the `CamSpec` [45] likelihood for the TT, TE, and EE spectra at $\ell > 30$, based on the Planck-PR4 `NPIPE` CMB maps [53]. As in the PL18 case, we combine it with the `simall` likelihood [23] for E-mode polarization and the `Commander` likelihood [452] for temperature anisotropies at $\ell < 30$.

	PL18	**PL18+lensing**	**CamSpec**	**CamSpec+lensing**
$\boldsymbol{\Omega_b h^2}$	0.02251 ± 0.00016	0.02248 ± 0.00015	0.02230 ± 0.00015	0.02227 ± 0.00014
$\boldsymbol{\Omega_c h^2}$	0.1191 ± 0.0014	0.1187 ± 0.0014	0.1189 ± 0.0012	0.1188 ± 0.0012
$\boldsymbol{100\theta_{MC}}$	1.04105 ± 0.00032	1.04105 ± 0.00031	1.04087 ± 0.00026	1.04084 ± 0.00026
$\boldsymbol{\tau}$	0.0539 ± 0.0081	0.0515 ± 0.0082	0.0511 ± 0.0083	0.0496 ± 0.0081
$\boldsymbol{\ln(10^{10} A_s)}$	3.041 ± 0.016	$3.035^{+0.016}_{-0.015}$	3.032 ± 0.017	3.029 ± 0.016
$\boldsymbol{\epsilon}$	$0.0170^{+0.0057}_{-0.0028}$	$0.0141^{+0.0074}_{-0.0045}$	$0.0159^{+0.0069}_{-0.0035}$	$0.0144^{+0.0076}_{-0.0046}$
$\boldsymbol{\delta}$	> 0.0142	> 0.00650	> 0.0101	> 0.00562
$\boldsymbol{\Omega_\mathcal{K}}$	$-0.026^{+0.012}_{-0.011}$	$-0.0084^{+0.0062}_{-0.0036}$	$-0.0160^{+0.011}_{-0.0063}$	$-0.0078^{+0.0060}_{-0.0032}$
n_s	0.9671 ± 0.0044	0.9680 ± 0.0044	0.9656 ± 0.0042	0.9656 ± 0.0042
Ω_m	0.418 ± 0.043	$0.344^{+0.015}_{-0.022}$	$0.379^{+0.026}_{-0.043}$	$0.344^{+0.014}_{-0.021}$
H_0 [km/s/Mpc]	$58.5^{+2.7}_{-3.5}$	$64.3^{+2.0}_{-1.5}$	$61.4^{+3.2}_{-2.6}$	$64.3^{+2.0}_{-1.4}$
S_8	$0.934^{+0.044}_{-0.038}$	$0.855^{+0.017}_{-0.020}$	$0.891^{+0.031}_{-0.039}$	$0.853^{+0.017}_{-0.019}$
$\Delta\chi^2$	-1.73	-1.18	0.49	0.20

TABLE VIII.2. Constraints at 68% CL from different Planck likelihood combinations (PL18, PL18+lensing, CamSpec, and CamSpec+lensing) on the extended parameter space including $\Omega_\mathcal{K}$, ϵ, δ, together with the usual ΛCDM parameters and derived quantities (Ω_m, H_0, S_8). The last row reports the difference in the best-fit χ^2, defined as $\Delta\chi^2 = \chi^2(\Omega_\mathcal{K}) - \chi^2(\epsilon, \delta, \Omega_\mathcal{K})$.

In closing this section, we stress that, although $\Omega_\mathcal{K}$ can also be constrained by complementary distance measurements such as BAO or SNIa, our main goal here is not to provide the tightest bounds from a combination of different probes. Rather, we aim to quantify to what extent phenomenological or gauge-dependent parametrisations of the primordial spectrum affect the curvature constraints extracted from the CMB. For this reason, in the main text we restrict our analysis to CMB temperature and polarisation anisotropy measurements alone, which makes it easier to isolate the role of both the lensing anomaly and the large-scale anomalies in shaping the inferred value of $\Omega_\mathcal{K}$. For completeness, results including low-redshift probes are presented in Appendix A.

	PL18	**PL18+lensing**	**CamSpec**	**CamSpec+lensing**
$\boldsymbol{\Omega_b h^2}$	0.02256 ± 0.00016	0.02250 ± 0.00016	0.02234 ± 0.00015	0.02229 ± 0.00014
$\boldsymbol{\Omega_c h^2}$	0.1184 ± 0.0014	0.1184 ± 0.0014	0.1184 ± 0.0012	0.1185 ± 0.0012
$\boldsymbol{100\theta_{MC}}$	1.04113 ± 0.00032	1.04109 ± 0.00031	1.04092 ± 0.00026	1.04088 ± 0.00027
$\boldsymbol{\tau}$	0.0499 ± 0.0078	0.0493 ± 0.0080	$0.0477^{+0.0083}_{-0.0074}$	$0.0475^{+0.0084}_{-0.0070}$
$\boldsymbol{\ln(10^{10} A_s)}$	3.032 ± 0.016	3.029 ± 0.016	$3.024^{+0.017}_{-0.015}$	$3.024^{+0.017}_{-0.015}$
$\boldsymbol{n_s}$	0.9695 ± 0.0045	0.9692 ± 0.0045	0.9676 ± 0.0043	0.9667 ± 0.0044
$\boldsymbol{\Omega_\mathcal{K}}$	< -0.0304	$-0.0107^{+0.0070}_{-0.0047}$	$-0.024^{+0.013}_{-0.010}$	$-0.0099^{+0.0071}_{-0.0043}$
Ω_m	$0.450^{+0.049}_{-0.028}$	$0.352^{+0.018}_{-0.024}$	$0.408^{+0.040}_{-0.047}$	$0.351^{+0.018}_{-0.024}$
H_0 [km/s/Mpc]	$56.3^{+1.3}_{-3.3}$	63.5 ± 2.0	$59.1^{+2.9}_{-3.5}$	$63.6^{+2.2}_{-1.8}$
S_8	$0.956^{+0.040}_{-0.026}$	0.860 ± 0.020	0.914 ± 0.038	$0.858^{+0.018}_{-0.021}$

TABLE VIII.3. Constraints at 68% CL on $\Omega_\mathcal{K}$ from different Planck likelihood combinations (PL18, PL18+lensing, CamSpec, and CamSpec+lensing), using the standard `CAMB` implementation of positive curvature. We also report the corresponding derived parameters (Ω_m, H_0, S_8).

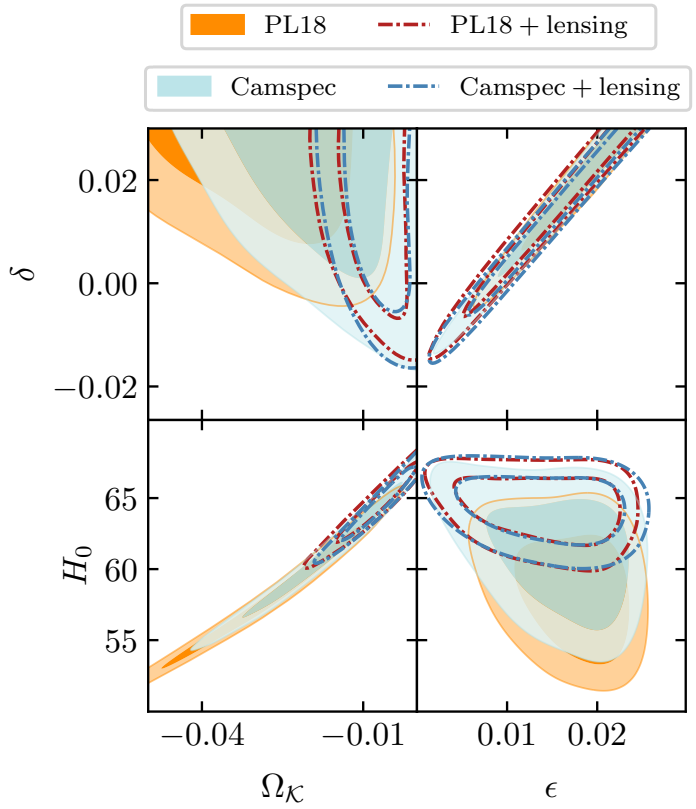


FIG. VIII.3. Two-dimensional marginalized constraints at 68% and 95% CL on $\Omega_\mathcal{K}$, ϵ, δ in the gauge-invariant closed-universe model, from different Planck likelihood combinations (PL18, PL18+lensing, CamSpec, and CamSpec+lensing).

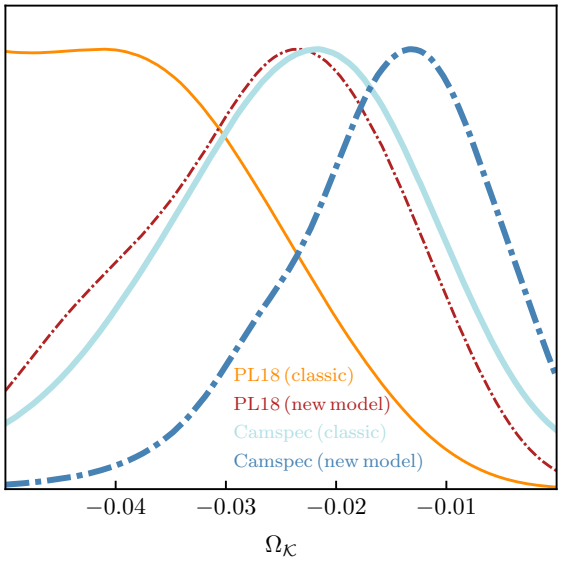


FIG. VIII.4. One-dimensional marginalized constraints at 68% CL on $\Omega_\mathcal{K}$ from PL18 and CamSpec likelihoods, comparing the standard `CAMB` implementation of curvature with our gauge-invariant closed-universe model.

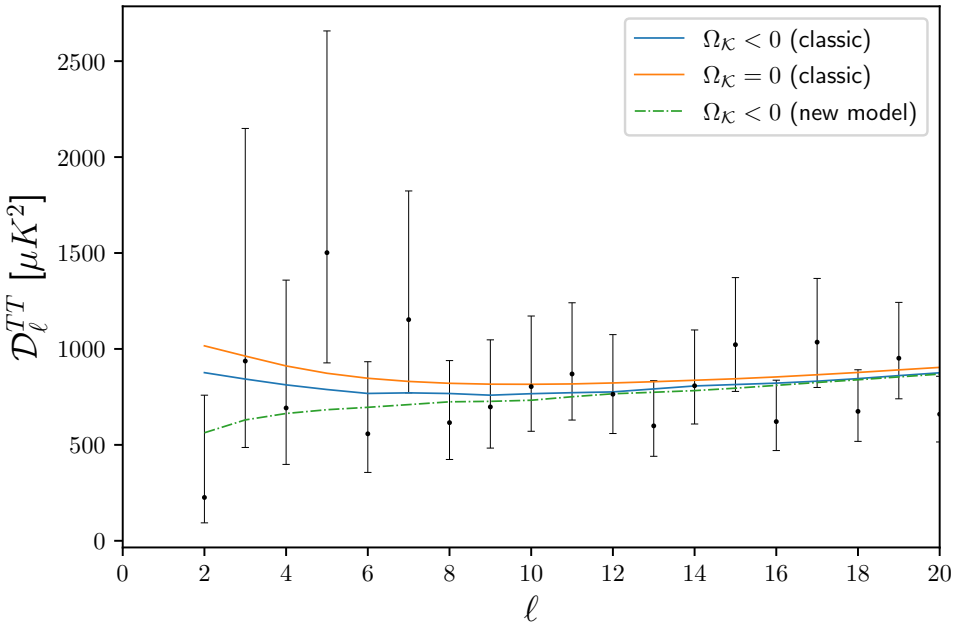


FIG. VIII.5. Comparison of the best-fit CMB temperature spectra at low multipoles: ΛCDM (orange, solid line), the standard curvature implementation (blue, solid line), and our gauge-invariant positive-curvature model (green, dash-dotted line). The data points are the Planck 2018 TT spectrum measurements.

VIII.D Results

In this section we present the cosmological constraints obtained with the methodology and datasets described in Sec. VIII.C. Unless otherwise stated, all quoted uncertainties correspond to 68% CL. We work within the extended parameter space of our gauge-invariant closed-universe model, in which the curvature parameter $\Omega_{\mathcal{K}}$ is sampled together with the slow-roll parameters ϵ and δ, in addition to the usual ΛCDM parameters.

We consider different combinations of Planck likelihoods, namely PL18, PL18+lensing, CamSpec, and CamSpec+lensing, in order to assess the impact of the lensing anomaly and of alternative high-ℓ likelihood choices. The CMB-only constraints on our parameterization are reported in Table VIII.2. For comparison, we show in Table VIII.3 the corresponding results obtained with the standard `CAMB` implementation of curvature. The two-dimensional marginalized posteriors for $\{\Omega_{\mathcal{K}}, \epsilon, \delta\}$ are displayed in Fig. VIII.3, while Fig. VIII.4 compares the one-dimensional marginalized constraints on $\Omega_{\mathcal{K}}$ between our implementation and the `CAMB` curvature treatment. Finally, Fig. VIII.5 compares the three best-fit temperature spectra at low multipoles ($\ell \lesssim 20$), corresponding to ΛCDM, the standard $\Omega_{\mathcal{K}}$ implementation, and our gauge-invariant parametrization, against the Planck 2018 data. Note that, for completeness, we also perform an extended analysis including geometric measurements from DESI and Pantheon+. The corresponding triangle plot is shown in Fig. VIII.6 and discussed in the Appendix A, together with Table VIII.F.

We begin by discussing the constraints from the PL18 likelihood. In the standard `CAMB` implementation, the data prefer a more negative value of the curvature parameter, with the posterior reaching the prior boundary and yielding only an upper limit, $\Omega_{\mathcal{K}} < -0.0304$ at 68% CL. This corresponds to a $\sim 3.4\sigma$ indication for a closed universe [166, 167]. In contrast, in our gauge-invariant parametrization we obtain a bounded constraint, $\Omega_{\mathcal{K}} = -0.026^{+0.012}_{-0.011}$ at 68% CL. As shown in Fig. VIII.4, this result is slightly more consistent with spatial flatness, corresponding to a $\sim 2.5\sigma$ preference for positive curvature. In our parametrization, the slow-roll parameters are constrained to $\epsilon = 0.0170^{+0.0057}_{-0.0028}$ and $\delta > 0.0142$ at 68% CL while for the other ΛCDM parameters, the differences between the two approaches are modest. τ shifts upward by about 0.5σ, in correlation with a higher amplitude A_s, while n_s shifts downward by 0.5σ. The remaining free parameters remain stable. As in the standard analysis, the derived parameters remain in tension with late-time measurements, with $H_0 < 60\,\mathrm{km\,s^{-1}\,Mpc^{-1}}$, $\Omega_m > 0.4$, and $S_8 > 0.93$. This behavior can be understood from the strong positive correlation between $\Omega_{\mathcal{K}}$ and H_0 visible in Fig. VIII.3: more negative curvature values imply a smaller Hubble constant. In contrast, ϵ and δ are positively correlated with each other but show no significant correlation with either $\Omega_{\mathcal{K}}$ or H_0. We quantify the relative goodness of fit by reporting $\Delta\chi^2 \equiv \chi^2(\Omega_{\mathcal{K}}) - \chi^2(\epsilon, \delta, \Omega_{\mathcal{K}})$, which highlights whether the inclusion of the slow-roll parameters ϵ and δ improves the description of the data. The comparison of the

best-fit values shows that the standard `CAMB` implementation provides a slightly better fit, with $\Delta\chi^2 = -1.73$. Nevertheless, as illustrated in Fig. VIII.5, while the standard curvature case already produces a suppression of power at large scales, our parametrization provides a better match to the observed low multipoles, particularly in reproducing the suppressed quadrupole. The fact that our parametrisation improves the fit to the lowest Planck multipoles (better capturing the large-scale power suppression anomaly) while still producing an overall worsening of the global fit implies that it slightly degrades the fit at high-ℓ relative to the standard phenomenological parametrisation. The reason is that, in closed quadratic inflation, the exact (gauge-invariant) spectrum ties curvature corrections to the background dynamics, and the posterior favours less negative values of $\Omega_\mathcal{K}$ (i.e. a geometry closer to flatness) than in the heuristic case. The very negative $\Omega_\mathcal{K}$ values that help explain the lensing anomaly at high-ℓ are therefore not allowed within our inflationary model, leading to a poorer fit to the high-ℓ `plik` PR3 spectra. Therefore this exercise teaches us an important lesson: when computing the primordial spectrum within physically motivated closed-inflation models, large- and small-scale anomalies in the Planck CMB data do not necessarily pull in the same direction. In our case, power-law inflation reproduces the low-ℓ suppression more faithfully, consistent with the theoretical spectrum derived in Ref. [565], but at the cost of a reduced ability to accommodate highly negative values of $\Omega_\mathcal{K}$ and hence a weaker fit to the lensing anomaly.

When adding the lensing likelihood to PL18, the posterior of the curvature parameter shifts towards zero in both the standard and our gauge-invariant parametrizations, as expected. The resulting constraints are very similar, with $\Omega_\mathcal{K} = -0.0107^{+0.0070}_{-0.0047}$ in the standard `CAMB` implementation and $\Omega_\mathcal{K} = -0.0084^{+0.0062}_{-0.0036}$ in our model. The derived parameters also shift slightly in the same direction as the curvature, but the effect is not sufficient to alleviate the tensions with late-time probes, since H_0 remains below the ΛCDM value while S_8 remains higher. In our parametrization, the slow-roll parameter ϵ is constrained to $\epsilon = 0.0141^{+0.0074}_{-0.0045}$, with a broader posterior than in the PL18-only case. As visible in the two-dimensional posteriors of Fig. VIII.3, this is mainly a projection effect due to correlations. The parameter δ remains bounded from below, with $\delta > 0.0065$ at 68% CL. The ΛCDM parameters remain essentially unchanged with respect to the PL18-only case. The comparison of best fits shows that the original `CAMB` curvature treatment still provides a slightly better fit, with $\Delta\chi^2 = -1.18$.

We next consider the CamSpec likelihood, which is known to provide a reduced indication for curvature compared to PL18. This behavior is confirmed in both the standard `CAMB` analysis and in our parametrization. As shown in the one-dimensional posteriors of Fig. VIII.4, our model shifts the curvature parameter further towards consistency with flatness, with a preference of about 2σ for positive curvature. The slow-roll parameters are constrained to $\epsilon = 0.0159^{+0.0069}_{-0.0035}$ and $\delta > 0.0101$ at 68% CL while the derived parameters lie between the values

obtained with PL18 alone and PL18+lensing, reflecting the intermediate behavior of the curvature constraint in this likelihood. The shifts (or stability) of the other ΛCDM parameters follow the same trends observed with PL18, with no major deviations. A noticeable difference however is that, in this case, the comparison of best fits slightly favors our parametrization, with $\Delta\chi^2 = +0.49$. While this difference is not statistically significant (especially given that our model includes two additional parameters), it can be understood in light of the behaviour of the CamSpec PR4 spectra, where the lensing anomaly is still present but strongly reduced compared to `Plik`. This residual preference for enhanced smoothing of the acoustic peaks at high-ℓ still translates into a mild preference for a closed universe, but with less negative values of $\Omega_\mathcal{K}$ than in Planck PR3. In this regime, the values of $\Omega_\mathcal{K}$ allowed by our model not only improve the fit to the lowest multipoles capturing the power suppression anomaly (note that the `Commander` likelihood encompassing temperature anisotropies at $\ell < 30$ remains common to both combinations) but also provide a satisfactory fit to the higher multipoles. As a result, the improvement at low-ℓ is no longer offset by a significant deterioration at high-ℓ, yielding a small net improvement and reinforcing the interpretation outlined above.

Finally, when the lensing likelihood is added to CamSpec, the differences between the two high-ℓ likelihoods are effectively washed out. The constraints from CamSpec+lensing and PL18+lensing are nearly identical, with $\Omega_\mathcal{K} = -0.0078^{+0.0060}_{-0.0032}$ in our parametrization, $\epsilon = 0.0144^{+0.0076}_{-0.0046}$, and $\delta > 0.00562$ at 68% CL. The comparison of best-fit values yields a slight preference for our model, with $\Delta\chi^2 = +0.20$, though this difference is not statistically significant given the two additional parameters. In fact this can also be regarded as an additional consistency test: once lensing is included, the residual preference for negative curvature in CamSpec is further reduced relative to PL18+lensing, and the constraints inevitably move towards the $\Omega_\mathcal{K} \to 0$ limit where all parametrisations become effectively indistinguishable, consistently recovering the flat primordial power spectrum.

VIII.E Discussion and Conclusion

In this work, we have revisited the Planck Cosmic Microwave Background constraints on spatial curvature within a quadratic model of closed inflation, where the primordial power spectrum of scalar modes is calculated in a theoretically well-motivated, gauge-invariant framework.

Our work aims to clarify two issues that might appear as technical subtleties but in fact can hold important consequences when inferring constraints on the curvature density parameter. The first is the phenomenological nature of the primordial spectrum for a closed universe usually adopted in standard analyses. The widely used parametrisation in Eq.(VIII.1) can heuristically capture the modifications induced by curvature on the largest scales, where a closed geometry leads to discrete eigenmodes and non-trivial deviations from the flat case.

However, while convenient, it does not guarantee that, within concrete inflationary models, the relation between the primordial spectrum and background quantities such as the present-day spatial curvature correctly reproduces the imprints of the inflationary dynamics at those scales. The second is the possible gauge dependence present in many alternative formulations of the primordial spectrum in closed geometries, which can lead to different predictions at large scales.

By focusing on quadratic inflation in a closed universe, the primordial spectrum can be calculated in a fully gauge-invariant manner [565]. We implemented this formulation in `CAMB`, extended the ΛCDM parameter space to include the curvature parameter $\Omega_{\mathcal{K}}$ and the two slow-roll parameters ϵ and δ, and constrained them using Planck CMB data.

We considered different combinations of Planck likelihoods (PL18, PL18+lensing, CamSpec, and CamSpec+lensing) to test the robustness of the apparent preference for positive curvature. Our main numerical findings can be summarized as follows:

- Analyzing the dataset combination referred to as PL18 (based on the `plik` PR3 high-ℓ spectra) within our quadratic model of closed inflation, we find a weaker $\sim 2.5\sigma$ preference for a closed universe compared to that obtained using the standard parametrisation Eq.(VIII.1) of the primordial power spectrum. This is clearly reflected in the shift towards spatial flatness (i.e. $\Omega_{\mathcal{K}} \to 0$) observed in the one-dimensional posterior distributions for $\Omega_{\mathcal{K}}$ shown in Fig. VIII.4. We also note that, for this dataset, our model yields a slightly worse fit compared to the standard parametrisation. This result highlights the importance of calculating and implementing primordial predictions consistently within predictive models of closed inflation, as this can modify both the statistical preference for a closed universe and the final constraints on $\Omega_{\mathcal{K}}$.

- Analyzing the dataset combination referred to as CamSpec (based on the `CamSpec` PR4 high-ℓ spectra) within our quadratic model of closed inflation, the preference for positive curvature is further reduced, to about 2σ, while the slow-roll parameters remain constrained at meaningful levels. This outcome is somewhat expected, since the indication for curvature is weaker in `CamSpec` than in `plik`. For this combination, our model also yields a slight improvement in the fitting of the Planck data compared to the standard parametrisation (although the difference is not statistically significant given the larger number of parameters).

- Adding Planck lensing data (to both PL18 and CamSpec), we observe a further shift of the posteriors in both models towards $\Omega_{\mathcal{K}} = 0$, as expected. In this regime, the two parametrisations become broadly consistent, since both primordial spectra converge to the standard flat case.

Beyond the numerical constraints, for both PL18 and CamSpec our parametrisation modifies the shape of the CMB temperature spectrum at large angular scales, yielding an im-

proved description of the low-ℓ power suppression anomaly observed at multipoles $\ell < 10$, see Fig. VIII.5. In particular, the low quadrupole is better reproduced compared to the standard `CAMB` curvature implementation, highlighting the physical impact of our gauge-invariant treatment of the primordial spectrum. However, as already noted, this improvement at large scales does not necessarily translate into an overall better fit compared to the standard closed parametrisation. While in CamSpec we observe a small improvement in the global fit, in PL18 we find a slight worsening. This behaviour can be traced back to the different constraints on spatial curvature. In closed quadratic inflation, the exact (gauge-invariant) spectrum ties curvature corrections to the background dynamics, and the posterior favours less negative values of $\Omega_{\mathcal{K}}$ (i.e. a geometry closer to flatness) than in the heuristic case. The very negative values of $\Omega_{\mathcal{K}}$ that help explain the lensing anomaly at high-ℓ are therefore not allowed within our inflationary model, leading to a poorer fit to the high-ℓ `plik` PR3 spectra. On the other hand, in the `CamSpec` high-ℓ PR4 spectra the preference for a smoothing excess of the acoustic peaks is reduced, and the less negative values of $\Omega_{\mathcal{K}}$ favored by our closed-inflation model are sufficient to yield an overall improvement.

As for the other parameters, we observe minimal to non-existent shift in their best-fit values, and all the derived parameters (H_0, Ω_m, S_8) remain in tension with late-time probes.

Overall, our case study demonstrates that deriving the primordial spectrum consistently within closed-inflation models – where the calculation is fully gauge-invariant and quantities such as the primordial spectrum, inflationary parameters, and geometric degrees of freedom are treated on equal footing – can lead to meaningful differences in the inferred constraints on $\Omega_{\mathcal{K}}$, with implications that extend well beyond the interpretation of the (apparent or spurious) Planck preference for a closed universe. Our broader message is that implementing physically motivated closed-universe models can substantially modify the results that would otherwise be inferred from purely phenomenological parametrisations of the primordial power spectrum.

There also remains considerable scope for theoretical progress. In this work we focused on quadratic inflation, a model that in the flat case is essentially excluded because of its predictions for the tensor-to-scalar ratio, which conflict with current BICEP/Keck limits [48, 630, 631]. That said, precise calculations for the tensor spectrum in a closed universe have not been derived for this model, preventing us from assessing the impact of spatial curvature on primordial gravitational waves. Building on existing discussions [622, 624, 632] extending the gauge-invariant treatment to tensor perturbations therefore represents a natural next step. More broadly, applying this framework to other benchmark inflationary scenarios that are successful in the flat case, such as Starobinsky inflation, will be essential for building a more comprehensive picture. These theoretical advances, together with the improved precision of forthcoming Stage-IV CMB experiments, will be crucial to establish with confidence the role of curvature in the cosmological model.

VIII.F Acknowledgments

W.G. is supported by the Lancaster–Sheffield Consortium for Fundamental Physics under STFC grant: ST/X000621/1. E.D.V. is supported by a Royal Society Dorothy Hodgkin Research Fellowship. This article is based upon work from the COST Action CA21136 - "Addressing observational tensions in cosmology with systematics and fundamental physics (CosmoVerse)", supported by COST - "European Cooperation in Science and Technology". We acknowledge the IT Services at The University of Sheffield for the provision of services for High Performance Computing.

Appendix A: Constraints including low-redshift data

	PL18+lensing	**PL18+lensing +DESI+P+**	**CamSpec+lensing**	**CamSpec+lensing +DESI+P+**
$\boldsymbol{\Omega_b h^2}$	0.02248 ± 0.00015	0.02257 ± 0.00013	0.02227 ± 0.00014	0.02234 ± 0.00012
$\boldsymbol{\Omega_c h^2}$	0.1187 ± 0.0014	$0.11744^{+0.00075}_{-0.00068}$	0.1188 ± 0.0012	$0.11743^{+0.00072}_{-0.00064}$
$\boldsymbol{100\theta_{MC}}$	1.04105 ± 0.00031	1.04126 ± 0.00028	1.04084 ± 0.00026	1.04104 ± 0.00023
$\boldsymbol{\tau}$	0.0515 ± 0.0082	$0.0612^{+0.0066}_{-0.0078}$	0.0496 ± 0.0081	$0.0595^{+0.0064}_{-0.0078}$
$\boldsymbol{\ln(10^{10} A_s)}$	$3.035^{+0.016}_{-0.015}$	$3.053^{+0.013}_{-0.015}$	3.029 ± 0.016	$3.048^{+0.013}_{-0.015}$
$\boldsymbol{\epsilon}$	$0.0141^{+0.0074}_{-0.0045}$	< 0.0145	$0.0144^{+0.0076}_{-0.0046}$	$0.0111^{+0.0070}_{-0.011}$
$\boldsymbol{\delta}$	> 0.00650	> -0.00172	> 0.00562	$0.007^{+0.015}_{-0.019}$
$\boldsymbol{\Omega_\mathcal{K}}$	$-0.0084^{+0.0062}_{-0.0036}$	> -0.000583	$-0.0078^{+0.0060}_{-0.0032}$	> -0.000511
n_s	0.9680 ± 0.0044	0.9713 ± 0.0034	0.9656 ± 0.0042	0.9691 ± 0.0034
Ω_m	$0.344^{+0.015}_{-0.022}$	0.3017 ± 0.0036	$0.344^{+0.014}_{-0.021}$	0.3032 ± 0.0035
H_0 [km/s/Mpc]	$64.3^{+2.0}_{-1.5}$	68.28 ± 0.28	$64.3^{+2.0}_{-1.4}$	68.06 ± 0.27
S_8	$0.855^{+0.017}_{-0.020}$	0.8096 ± 0.0083	$0.853^{+0.017}_{-0.019}$	0.8094 ± 0.0081

TABLE VIII.4. Constraints at 68% CL from different Planck likelihood combinations with the inclusion of geometric measurements (DESI and Pantheon+) on the extended parameter space including $\Omega_\mathcal{K}$, ϵ, δ, together with the usual ΛCDM parameters and derived quantities (Ω_m, H_0, S_8).

We investigate our parametrization when combining Planck CMB data with low-redshift geometric measurements from DESI and Pantheon+. The inclusion of late-time distance indicators removes the preference for a closed universe, and in this regime our model becomes not optimal to explain observations since it forces $\Omega_\mathcal{K} < 0$. Nevertheless, it is instructive to verify the consistency of the results. Using PL18+lensing together with DESI and Pantheon+, we find results fully consistent with flat ΛCDM, both for the primary and derived parameters. In particular, as one can see from Table VIII.F, we obtain $\Omega_\mathcal{K} > -0.000583$, $\epsilon < 0.0145$, and $\delta > -0.00172$ at 68% CL. Replacing PL18 with CamSpec leads to very similar constraints, $\Omega_\mathcal{K} > -0.000511$, $\epsilon = 0.0111 \pm 0.0034$, and $\delta = 0.007^{+0.015}_{-0.019}$. The corresponding triangular

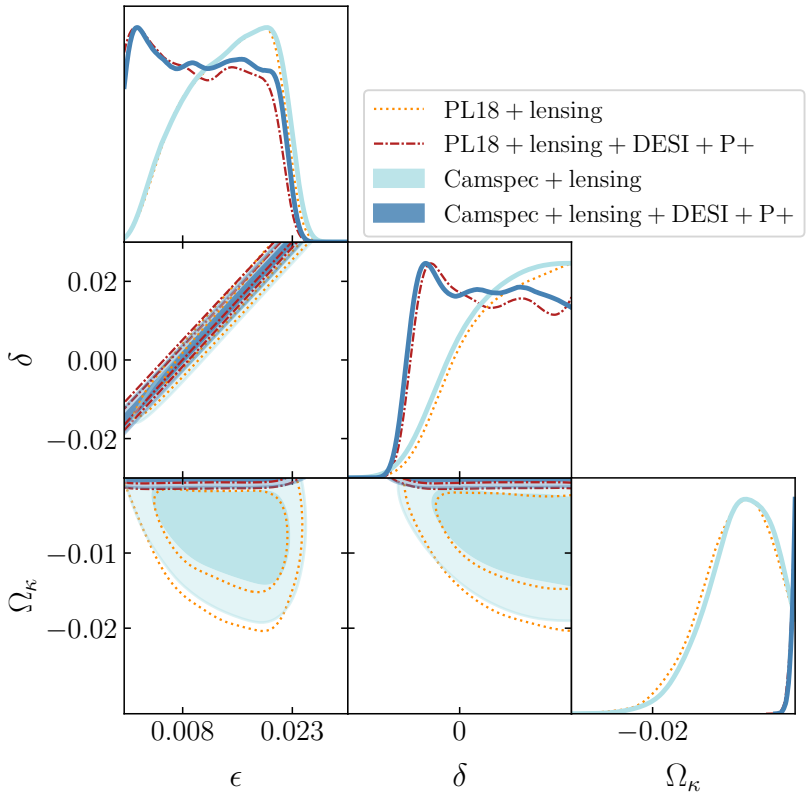


FIG. VIII.6. One- and two-dimensional marginalized constraints at 68% and 95% CL on $\Omega_\mathcal{K}$, ϵ, δ in the gauge-invariant closed-universe model, including geometric measurements from DESI and Pantheon+, combined with Planck likelihoods.

plots are displayed in Fig. VIII.6, showing that in these cases, fully consistent with a flat universe, the slow-roll parameters ϵ and δ are largely unconstrained.

Appendix B: On the validity of the approximation in Eq.(VIII.14)

To validate the robustness of the approximation introduced by Eq. (VIII.14), we have implemented both the approximated (i.e., Eq. (VIII.15)) and the full (i.e., Eq. (VIII.7)) expressions of P_ζ in `CAMB`, and explicitly compared their impact on the computation of the CMB temperature angular power spectra $\mathcal{D}_\ell$. The results are shown in Fig. VIII.7. For values of ϵ of order $\epsilon \sim 0.01$ and $\delta \sim 0.02$ (i.e., of the order of the best-fit values quoted in the manuscript), the relative difference between the approximate and full implementations is at most 0.05% on the largest scales, and becomes negligible at smaller scales. Altering the value of δ has only a minimal impact, see the right panel. Similarly, when increasing ϵ to values up to three times larger than those preferred by the MCMC analysis, the aforementioned difference between the two implementations remains below 0.5% at small scales.

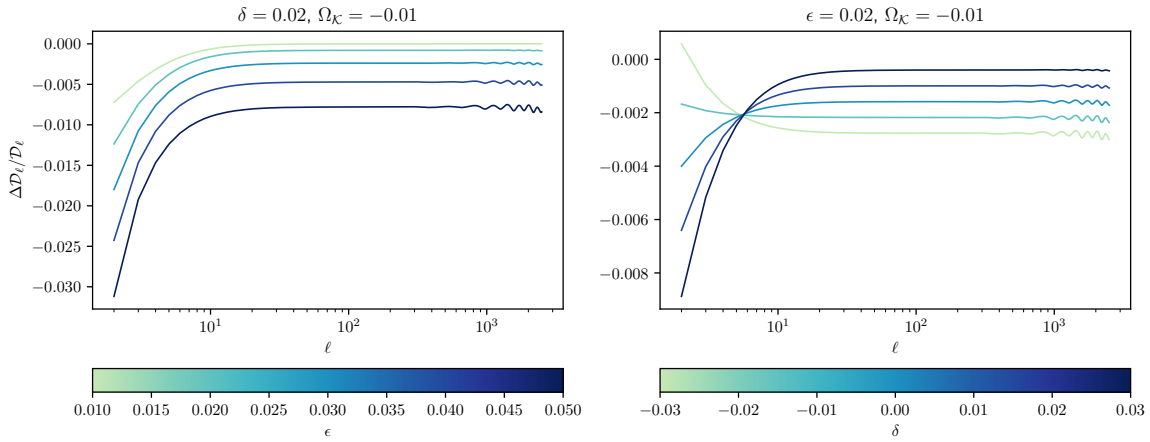


FIG. VIII.7. Fractional difference between the approximated and non-approximated theoretical predictions of the CMB TT power spectrum for our model. The difference becomes most pronounced as ϵ increases, but its magnitude does not exceed $\sim 3\%$ for multipoles below $\ell \approx 10$ (in the cosmic-variance-limited regime), and remains below $\sim 1\%$ for multipoles above $\ell \approx 10$.

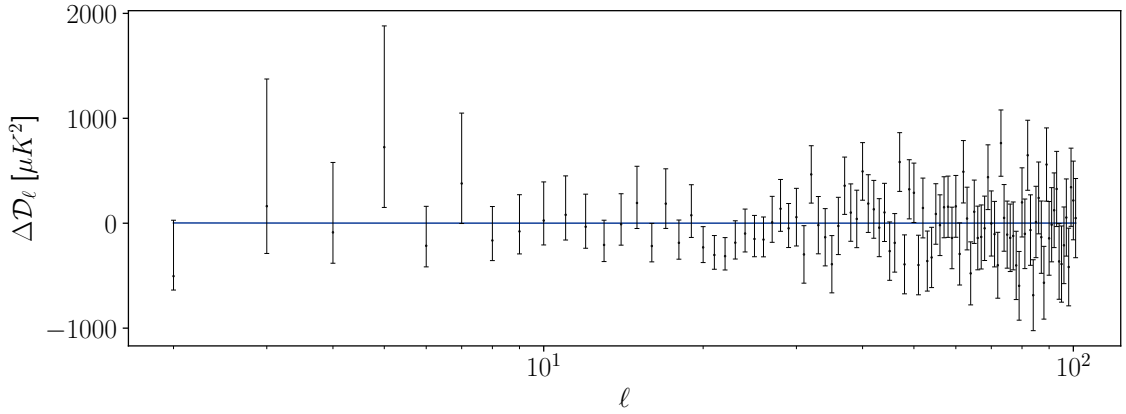


FIG. VIII.8. Difference between the theoretical predictions of the approximated and non-approximated forms of the CMB TT power spectrum for our model (the nearly horizontal blue line), compared with the Planck 2018 temperature data (points with error bars) [23]. Both versions of the spectrum are computed using the best-fit parameter values obtained for the approximate case with the Planck 2018 data. A difference between the two implementations is present, but it is not large enough to exceed the experimental uncertainties or to induce any tangible systematic offset in the inferred constraints.

However, given the tight uncertainties on ϵ reported in the manuscript, such values already lie well outside the region favoured by the analysis. Only for values of ϵ as large as five times the best-fit region does the discrepancy reach the percent level, still remaining $\sim 1\%$ at small scales. In this extreme regime, the largest deviations, reaching at most $\sim 3\%$, occur

at very low multipoles. However, on the one hand, these correspond to scales where Planck temperature data are dominated by cosmic variance and therefore have comparatively large error bars, as illustrated in Fig. VIII.8. On the other hand, these values of ϵ are strongly excluded by the data and are therefore never probed in our MCMC runs. As a result, across the entire parameter range explored by the present analysis, the uncertainty induced by our approximation is always negligible compared to the observational uncertainties and cannot lead to any appreciable effect on the final constraints. Additionally, the region where our approximations more faithfully reproduce the non-approximated spectrum is found to be exactly coincident with the region of parameter space favoured by the data. This is seen in Fig. VIII.8: when considering the best-fit parameter values (i.e., in the region of maximum likelihood), the difference between the approximate and full implementations is completely indistinguishable. We therefore conclude that, since the implementation differences are well within experimental errors, it is safe to neglect $\lambda_{\epsilon,\delta}(n)$ and the terms proportional to ϵ in $f_\epsilon(n)$.

Afterword

We conclude this chapter with a further note on the motivation to study this model. Again, here we deal with quadratic inflation, which in the flat case has been shown to be incompatible with the data by BICEP/Keck, as the model's predictions for the tensor-to-scalar ratio do not match the survey's bounds [48, 630, 631]. However, what is relevant here is that this model can better fit the low multipole region of Planck's temperature spectrum, thanks to the $\mathcal{D}_\ell$ suppression that is also observed by WMAP. While it is true that an inflaton potential such as $V(\phi) \sim \phi^2$ is observationally excluded, the same calculation for a closed universe could still be repeated for other viable, non-monomial models of the potential [633]. This, of course, would have to be shown in further work.

IX Conclusions

The cosmological paradigm, also known as the ΛCDM model, is currently our best picture of the universe at the largest scales. With the use of just a handful of ingredients, the standard theory of cosmology is able to predict extraordinary phenomena about the universe, from its hot and chaotic infancy all the way to its current, accelerating expansion.

This Thesis started out with a description of the pillars of this theory of the universe, including general relativity, the gravitational theory developed by Einstein, and its most abundant yet most elusive components: Λ, the cosmological constant, and cold dark matter. From this starting point, we briefly traced the life and growth of the universe, from its earliest moments: the epoch of inflation. This is when, a bit like today but at energy scales much larger, the universe expanded dramatically, losing any trace of the magnetic monopoles that inhabited it early on and "ironing out" any residue of spatial curvature left from the first split-second of its existence. We then used the tiny quantum fluctuations generated during the inflationary era as the initial conditions that went on to become the sea of relic radiation known as cosmic microwave background first and the large-scale structure of the universe later on.

While amazingly powerful in its predictions about the universe, the standard model recently started revealing a number of cracks that are getting wider the more precise the current and future cosmological experiments become. In this Thesis, we have explored some of these issues, by presenting a series of five papers that aimed at tackling three different issues: an excess of weak lensing measured in the photons of the cosmic microwave background (the lensing anomaly), a mismatch in the measured rate of expansion of the universe (the Hubble tension) and the possibility that the current universe might not be spatially flat after all.
We have reached the following conclusions.

- The lensing anomaly, measured in the Planck data, can be recast as an apparent signal of modified gravity, which, however, disappears once we analyse these data with different methods (i.e., different likelihoods). At the same time, a modification of gravity does not seem to be quite enough to explain the tight constraint on the neutrinos mass found by DESI, and more needs to be done to interpret this result.

- A type of dark energy that can behave both as non-phantom and phantom at different epochs can alleviate the Hubble tension, but it requires the use cepheid calibrators to reach a similar result.

- The universe can be consistently measured to be flat, even with the same Planck data

that suffer from the lensing anomaly and that, in some cases, can show evidence for spatial curvature too. It is a matter of using the right parametrisations.

There is however, and fortunately, still much that can be done to test the standard model further.

Firstly, it would be intriguing to investigate these modifications of gravity by leveraging, for instance, the currently available cosmic microwave background lensing datasets and their cross-correlations with complementary tracers of the large-scale structure. Galaxies are an example of such tracers, which, especially when cross-correlated with CMB lensing measurements (as done in e.g., [634]), can prove to be a powerful tool to measure structure growth and therefore test for modified gravity signals in the data. Analyses of this kind could be rather timely for a couple of reasons. Firstly, the combination of Planck's data with the latest releases by ACT and SPT, two ground-based CMB observatories, provided us with the most precise measurement of the CMB lensing spectrum to date [635]. Secondly, the first major release of weak lensing and clustering data by Euclid will likely be available before the end of this year (2026), allowing us to constrain the phenomenology of gravity at the cosmological level with unprecedented precision.

It would also be quite exciting to explore the neutrino mass-ordering problem further. This truly is one of the most compelling open research topics currently under investigation by cosmologists and particle physicists alike, for a number of reasons. Firstly, while a combination of reactor, atmospheric and solar neutrinos experiments does not seem able to unambiguously differentiate between the normal and inverted (IO) orderings of the neutrino masses quite yet [358], the future of oscillation experiments remains promising. For example, after just ~ 60 days of data collection, the JUNO experiment recently provided one of the most precise constraints of the $\Delta m^2_{2,1}$ splitting to date [636]. Similarly, the DUNE mission is set to definitively establish the correct neutrino mass-ordering [637]. At the same time though, the combination of the latest BAO measurements by DESI with CMB data excludes the plausibility of the IO for the neutrino masses [15], seemingly pointing at a discrepancy between the cosmology and the particle physics sectors. It would then be intriguing to keep investigating the robustness of the cosmological measurements of Σm_ν.

It is true, the cosmological paradigm is now at the peak of its crisis. A crisis that, to us cosmologists, represents an immense an opportunity that needs to be seized, if we are to uncover the fundamental truths about the universe.

Bibliography

[1] E. Specogna, E. Di Valentino, J. Levi Said, and N.-M. Nguyen, Exploring the growth index γL: Insights from different CMB dataset combinations and approaches, Phys. Rev. D **109**, 043528 (2024), arXiv:2305.16865 [astro-ph.CO].

[2] E. Specogna, W. Giarè, and E. Di Valentino, Planck-PR4 anisotropy spectra show better consistency with general relativity, Phys. Rev. D **111**, 103510 (2025), arXiv:2411.03896 [astro-ph.CO].

[3] E. Specogna, S. A. Adil, E. Ozulker, E. Di Valentino, R. C. Nunes, O. Akarsu, and A. A. Sen, Updated Constraints on Omnipotent Dark Energy: A Comprehensive Analysis with CMB and BAO Data, (2025), arXiv:2504.17859 [gr-qc].

[4] W. Giarè, O. Mena, E. Specogna, and E. Di Valentino, Neutrino mass tension or suppressed growth rate of matter perturbations?, Phys. Rev. D **112**, 103520 (2025), arXiv:2507.01848 [astro-ph.CO].

[5] E. Specogna, T. Vardanyan, W. Giarè, and E. Di Valentino, Slow-rolling down the curvature: a reassessment of the Planck constraints on ^{2} inflation in a closed universe, (2025), arXiv:2509.26263 [astro-ph.CO].

[6] S. A. Adil, O. Akarsu, E. Di Valentino, R. C. Nunes, E. Özülker, A. A. Sen, and E. Specogna, Omnipotent dark energy: A phenomenological answer to the hubble tension, Physical Review D **109**, 10.1103/physrevd.109.023527 (2024).

[7] B. Ryden, *Introduction to cosmology* (Cambridge University Press, 2016).

[8] R. H. Dicke, P. J. E. Peebles, P. G. Roll, and D. T. Wilkinson, Cosmic Black-Body Radiation, Astrophys. J. **142**, 414 (1965).

[9] G. F. Smoot, COBE observations and results, AIP Conf. Proc. **476**, 1 (1999), arXiv:astro-ph/9902027.

[10] D. J. Fixsen, E. S. Cheng, J. M. Gales, J. C. Mather, R. A. Shafer, and E. L. Wright, The Cosmic Microwave Background spectrum from the full COBE FIRAS data set, Astrophys. J. **473**, 576 (1996), arXiv:astro-ph/9605054.

[11] B. Maffei *et al.*, BISOU: A balloon project to measure the CMB spectral distortions, in *16th Marcel Grossmann Meeting on Recent Developments in Theoretical and Experimental General Relativity, Astrophysics and Relativistic Field Theories* (2021) arXiv:2111.00246 [astro-ph.IM].

[12] A. Kogut *et al.*, The Primordial Inflation Explorer (PIXIE): mission design and science goals, JCAP **04**, 020, arXiv:2405.20403 [astro-ph.CO].

[13] https://www.ias.u-psud.fr/sites/default/files/FOSSIL-web$_0$.*pdf* .

[14] A. G. Adame *et al.* (DESI), DESI 2024 VI: cosmological constraints from the measurements of baryon acoustic oscillations, JCAP **02**, 021, arXiv:2404.03002 [astro-ph.CO].

[15] M. Abdul Karim *et al.* (DESI), DESI DR2 results. II. Measurements of baryon acoustic oscillations and cosmological constraints, Phys. Rev. D **112**, 083515 (2025), arXiv:2503.14738 [astro-ph.CO].

[16] A. Guth, *The Inflationary Universe* (Addison-Wesley, 1997).

[17] P. J. E. Peebles, Large-scale background temperature and mass fluctuations due to scale-invariant primeval perturbations, Astrophys. J. **263**, L1 (1982).

[18] P. J. E. Peebles, Tests of Cosmological Models Constrained by Inflation, Astrophys. J. **284**, 439

(1984).

[19] P. J. E. Peebles, The mean mass density of the Universe, Nature **321**, 27 (1986).

[20] A. G. Riess *et al.* (Supernova Search Team), Observational evidence from supernovae for an accelerating universe and a cosmological constant, Astron. J. **116**, 1009 (1998), arXiv:astro-ph/9805201.

[21] S. Perlmutter *et al.* (Supernova Cosmology Project), Measurements of Ω and Λ from 42 High Redshift Supernovae, Astrophys. J. **517**, 565 (1999), arXiv:astro-ph/9812133.

[22] S. Casertano *et al.* (H0DN), The Local Distance Network: a community consensus report on the measurement of the Hubble constant at 1% precision, (2025), arXiv:2510.23823 [astro-ph.CO].

[23] N. Aghanim *et al.* (Planck), Planck 2018 results. VI. Cosmological parameters, Astron. Astrophys. **641**, A6 (2020), [Erratum: Astron.Astrophys. 652, C4 (2021)], arXiv:1807.06209 [astro-ph.CO].

[24] M. Tristram *et al.*, Cosmological parameters derived from the final Planck data release (PR4), Astron. Astrophys. **682**, A37 (2024), arXiv:2309.10034 [astro-ph.CO].

[25] E. Camphuis *et al.* (SPT-3G), SPT-3G D1: CMB temperature and polarization power spectra and cosmology from 2019 and 2020 observations of the SPT-3G Main field, (2025), arXiv:2506.20707 [astro-ph.CO].

[26] E. Di Valentino, J. Levi Said, and E. N. Saridakis, Cosmological tensions in the era of precision cosmology: Insights from Tensions in Cosmology 2025, Nature Astron. **10**, 180 (2026), arXiv:2509.25288 [astro-ph.CO].

[27] B. Stölzner *et al.*, KiDS-Legacy: Consistency of cosmic shear measurements and joint cosmological constraints with external probes, Astron. Astrophys. **702**, A169 (2025), arXiv:2503.19442 [astro-ph.CO].

[28] W. J. Wolf and P. G. Ferreira, Underdetermination of dark energy, Phys. Rev. D **108**, 103519 (2023), arXiv:2310.07482 [astro-ph.CO].

[29] W. J. Wolf, M. Sanchioni, and J. Read, Underdetermination in classic and modern tests of general relativity, Eur. J. Phil. Sci. **14**, 57 (2024), arXiv:2307.10074 [physics.hist-ph].

[30] P. G. Ferreira, W. J. Wolf, and J. Read, The Spectre of Underdetermination in Modern Cosmology, Phil. Phys. **3**, 1 (2025), arXiv:2501.06095 [physics.hist-ph].

[31] A. Lewis, A. Challinor, and A. Lasenby, Efficient computation of CMB anisotropies in closed FRW models, Astrophys. J. **538**, 473 (2000), arXiv:astro-ph/9911177.

[32] C. Howlett, A. Lewis, A. Hall, and A. Challinor, CMB power spectrum parameter degeneracies in the era of precision cosmology, JCAP **04**, 027, arXiv:1201.3654 [astro-ph.CO].

[33] G.-B. Zhao, L. Pogosian, A. Silvestri, and J. Zylberberg, Searching for modified growth patterns with tomographic surveys, Phys. Rev. D **79**, 083513 (2009), arXiv:0809.3791 [astro-ph].

[34] L. Pogosian, A. Silvestri, K. Koyama, and G.-B. Zhao, How to optimally parametrize deviations from General Relativity in the evolution of cosmological perturbations?, Phys. Rev. D **81**, 104023 (2010), arXiv:1002.2382 [astro-ph.CO].

[35] A. Hojjati, L. Pogosian, and G.-B. Zhao, Testing gravity with CAMB and CosmoMC, JCAP **08**, 005, arXiv:1106.4543 [astro-ph.CO].

[36] A. Zucca, L. Pogosian, A. Silvestri, and G.-B. Zhao, MGCAMB with massive neutrinos and dynamical dark energy, JCAP **05**, 001, arXiv:1901.05956 [astro-ph.CO].

[37] Z. Wang, S. H. Mirpoorian, L. Pogosian, A. Silvestri, and G.-B. Zhao, New MGCAMB tests of

gravity with CosmoMC and Cobaya, (2023), arXiv:2305.05667 [astro-ph.CO].

[38] N.-M. Nguyen, D. Huterer, and Y. Wen, Evidence for suppression of structure growth in the concordance cosmological model, (2023), arXiv:2302.01331 [astro-ph.CO].

[39] Y. Wen, N.-M. Nguyen, and D. Huterer, Sweeping Horndeski Canvas: New Growth-Rate Parameterization for Modified-Gravity Theories, (2023), arXiv:2304.07281 [astro-ph.CO].

[40] C.-P. Ma and E. Bertschinger, Cosmological perturbation theory in the synchronous and conformal Newtonian gauges, Astrophys. J. **455**, 7 (1995), arXiv:astro-ph/9506072.

[41] https://noirlab.edu/public/images/noirlab2512a/ .

[42] S. Dodelson, *Modern Cosmology*, 3rd ed. (Academic Press, 2025).

[43] D. Baumann, Inflation, in *Theoretical Advanced Study Institute in Elementary Particle Physics: Physics of the Large and the Small* (2011) pp. 523–686, arXiv:0907.5424 [hep-th].

[44] E. Calabrese *et al.* (ACT), The Atacama Cosmology Telescope: DR6 Constraints on Extended Cosmological Models, (2025), arXiv:2503.14454 [astro-ph.CO].

[45] E. Rosenberg, S. Gratton, and G. Efstathiou, CMB power spectra and cosmological parameters from Planck PR4 with CamSpec, Mon. Not. Roy. Astron. Soc. **517**, 4620 (2022), arXiv:2205.10869 [astro-ph.CO].

[46] V. F. Mukhanov and G. V. Chibisov, Quantum Fluctuations and a Nonsingular Universe, JETP Lett. **33**, 532 (1981).

[47] V. F. Mukhanov, H. A. Feldman, and R. H. Brandenberger, Theory of cosmological perturbations. Part 1. Classical perturbations. Part 2. Quantum theory of perturbations. Part 3. Extensions, Phys. Rept. **215**, 203 (1992).

[48] Y. Akrami *et al.* (Planck), Planck 2018 results. X. Constraints on inflation, Astron. Astrophys. **641**, A10 (2020), arXiv:1807.06211 [astro-ph.CO].

[49] B. D. Sherwin, *Cosmology from Secondary Anisotropies of the Cosmic Microwave Background*, Ph.D. thesis, Princeton U. (2013).

[50] C. L. Bennett *et al.* (WMAP), Nine-Year Wilkinson Microwave Anisotropy Probe (WMAP) Observations: Final Maps and Results, Astrophys. J. Suppl. **208**, 20 (2013), arXiv:1212.5225 [astro-ph.CO].

[51] N. Aghanim *et al.* (Planck), Planck 2018 results. V. CMB power spectra and likelihoods, Astron. Astrophys. **641**, A5 (2020), arXiv:1907.12875 [astro-ph.CO].

[52] N. Aghanim *et al.* (Planck), Planck 2018 results. VIII. Gravitational lensing, Astron. Astrophys. **641**, A8 (2020), arXiv:1807.06210 [astro-ph.CO].

[53] Y. Akrami *et al.* (Planck), *Planck* intermediate results. LVII. Joint Planck LFI and HFI data processing, Astron. Astrophys. **643**, A42 (2020), arXiv:2007.04997 [astro-ph.CO].

[54] S. K. Choi *et al.* (ACT), The Atacama Cosmology Telescope: a measurement of the Cosmic Microwave Background power spectra at 98 and 150 GHz, JCAP **12**, 045, arXiv:2007.07289 [astro-ph.CO].

[55] S. Aiola *et al.* (ACT), The Atacama Cosmology Telescope: DR4 Maps and Cosmological Parameters, JCAP **12**, 047, arXiv:2007.07288 [astro-ph.CO].

[56] L. Balkenhol *et al.* (SPT-3G), A Measurement of the CMB Temperature Power Spectrum and Constraints on Cosmology from the SPT-3G 2018 TT/TE/EE Data Set, (2022), arXiv:2212.05642 [astro-ph.CO].

[57] D. Dutcher *et al.* (SPT-3G), Measurements of the E-mode polarization and temperature-E-

mode correlation of the CMB from SPT-3G 2018 data, Phys. Rev. D **104**, 022003 (2021), arXiv:2101.01684 [astro-ph.CO].

[58] T. Louis *et al.* (Atacama Cosmology Telescope), The Atacama Cosmology Telescope: DR6 power spectra, likelihoods and ΛCDM parameters, JCAP **11**, 062, arXiv:2503.14452 [astro-ph.CO].

[59] G. Efstathiou and J. R. Bond, Cosmic confusion: Degeneracies among cosmological parameters derived from measurements of microwave background anisotropies, Mon. Not. Roy. Astron. Soc. **304**, 75 (1999), arXiv:astro-ph/9807103.

[60] R. Durrer, *The Cosmic Microwave Background* (Cambridge University Press, Cambridge, 2008).

[61] A. Challinor, H. Peiris, M. Novello, and S. Perez, Lecture notes on the physics of cosmic microwave background anisotropies, in *AIP Conference Proceedings* (AIP, 2009) p. 86–140.

[62] R. K. Sachs and A. M. Wolfe, Perturbations of a cosmological model and angular variations of the microwave background, Astrophys. J. **147**, 73 (1967).

[63] J. Silk, Fluctuations in the Primordial Fireball, Nature **215**, 1155 (1967).

[64] W. Hu and M. J. White, A CMB polarization primer, New Astron. **2**, 323 (1997), arXiv:astro-ph/9706147.

[65] A. Lewis and A. Challinor, Weak gravitational lensing of the CMB, Phys. Rept. **429**, 1 (2006), arXiv:astro-ph/0601594.

[66] F. J. Qu *et al.* (ACT), The Atacama Cosmology Telescope: A Measurement of the DR6 CMB Lensing Power Spectrum and Its Implications for Structure Growth, Astrophys. J. **962**, 112 (2024), arXiv:2304.05202 [astro-ph.CO].

[67] J. Carron, M. Mirmelstein, and A. Lewis, CMB lensing from Planck PR4 maps, JCAP **09**, 039, arXiv:2206.07773 [astro-ph.CO].

[68] Z. Pan *et al.* (SPT), Measurement of gravitational lensing of the cosmic microwave background using SPT-3G 2018 data, Phys. Rev. D **108**, 122005 (2023), arXiv:2308.11608 [astro-ph.CO].

[69] R. A. Sunyaev and Y. B. Zeldovich, The Observations of relic radiation as a test of the nature of X-Ray radiation from the clusters of galaxies, Comments Astrophys. Space Phys. **4**, 173 (1972).

[70] M. Birkinshaw, The Sunyaev-Zel'dovich effect, Phys. Rept. **310**, 97 (1999), arXiv:astro-ph/9808050.

[71] M. Kaplinghat, M. Chu, Z. Haiman, G. Holder, L. Knox, and C. Skordis, Probing the reionization history of the universe using the cosmic microwave background polarization, Astrophys. J. **583**, 24 (2003), arXiv:astro-ph/0207591.

[72] M. Zaldarriaga, D. N. Spergel, and U. Seljak, Microwave background constraints on cosmological parameters, Astrophys. J. **488**, 1 (1997), arXiv:astro-ph/9702157.

[73] N. Aghanim *et al.* (Planck), Planck intermediate results. LI. Features in the cosmic microwave background temperature power spectrum and shifts in cosmological parameters, Astron. Astrophys. **607**, A95 (2017), arXiv:1608.02487 [astro-ph.CO].

[74] W. Hu and M. J. White, Acoustic signatures in the cosmic microwave background, Astrophys. J. **471**, 30 (1996), arXiv:astro-ph/9602019.

[75] S. Brieden, H. Gil-Marín, and L. Verde, A tale of two (or more) h's, JCAP **04**, 023, arXiv:2212.04522 [astro-ph.CO].

[76] S. Alam *et al.* (eBOSS), Completed SDSS-IV extended Baryon Oscillation Spectroscopic Survey: Cosmological implications from two decades of spectroscopic surveys at the Apache Point Observatory, Phys. Rev. D **103**, 083533 (2021), arXiv:2007.08991 [astro-ph.CO].

[77] A. Slosar *et al.*, The Lyman-alpha forest in three dimensions: measurements of large scale flux correlations from BOSS 1st-year data, Journal of Cosmology and Astroparticle Physics **2011** (09), 001–001, arXiv:1104.5244.

[78] E. Di Valentino *et al.* (CosmoVerse Network), The CosmoVerse White Paper: Addressing observational tensions in cosmology with systematics and fundamental physics, Phys. Dark Univ. **49**, 101965 (2025), arXiv:2504.01669 [astro-ph.CO].

[79] R. Tripp, A Two-parameter luminosity correction for type Ia supernovae, Astron. Astrophys. **331**, 815 (1998).

[80] J. Guy *et al.* (SNLS), SALT2: Using distant supernovae to improve the use of Type Ia supernovae as distance indicators, Astron. Astrophys. **466**, 11 (2007), arXiv:astro-ph/0701828.

[81] D. Scolnic *et al.*, The Pantheon+ Analysis: The Full Data Set and Light-curve Release, Astrophys. J. **938**, 113 (2022), arXiv:2112.03863 [astro-ph.CO].

[82] D. Brout and D. Scolnic, It's Dust: Solving the Mysteries of the Intrinsic Scatter and Host-galaxy Dependence of Standardized Type Ia Supernova Brightnesses, Astrophys. J. **909**, 26 (2021), arXiv:2004.10206 [astro-ph.CO].

[83] A. G. Riess *et al.*, A Comprehensive Measurement of the Local Value of the Hubble Constant with 1 km s^1 Mpc^1 Uncertainty from the Hubble Space Telescope and the SH0ES Team, Astrophys. J. Lett. **934**, L7 (2022), arXiv:2112.04510 [astro-ph.CO].

[84] A. G. Riess *et al.*, A Comprehensive Measurement of the Local Value of the Hubble Constant with 1 km s^1 Mpc^1 Uncertainty from the Hubble Space Telescope and the SH0ES Team, Astrophys. J. Lett. **934**, L7 (2022), arXiv:2112.04510 [astro-ph.CO].

[85] G. S. Anand *et al.*, Tip of the Red Giant Branch Distances with JWST: An Absolute Calibration in NGC 4258 and First Applications to Type Ia Supernova Hosts, Astrophys. J. **966**, 89 (2024), arXiv:2401.04776 [astro-ph.CO].

[86] D. Brout *et al.*, The Pantheon+ Analysis: Cosmological Constraints, Astrophys. J. **938**, 110 (2022), arXiv:2202.04077 [astro-ph.CO].

[87] D. J. Fixsen, The Temperature of the Cosmic Microwave Background, Astrophys. J. **707**, 916 (2009), arXiv:0911.1955 [astro-ph.CO].

[88] N. Christensen and R. Meyer, Bayesian methods for cosmological parameter estimation from cosmic microwave background measurements, (2000), arXiv:astro-ph/0006401.

[89] R. Trotta, Bayes in the sky: Bayesian inference and model selection in cosmology, Contemp. Phys. **49**, 71 (2008), arXiv:0803.4089 [astro-ph].

[90] R. Trotta, Bayesian Methods in Cosmology (2017) arXiv:1701.01467 [astro-ph.CO].

[91] J. Torrado and A. Lewis, Cobaya: Code for Bayesian Analysis of hierarchical physical models, JCAP **05**, 057, arXiv:2005.05290 [astro-ph.IM].

[92] A. Lewis and S. Bridle, Cosmological parameters from CMB and other data: A Monte Carlo approach, Phys. Rev. D **66**, 103511 (2002), arXiv:astro-ph/0205436.

[93] H. Jeffreys, *The Theory of Probability* (Oxford University Press, Oxford, 1998).

[94] A. De Felice and S. Tsujikawa, f(R) theories, Living Rev. Rel. **13**, 3 (2010), arXiv:1002.4928 [gr-qc].

[95] E. V. Linder, Cosmic growth history and expansion history, Phys. Rev. D **72**, 043529 (2005), arXiv:astro-ph/0507263.

[96] E. V. Linder and R. N. Cahn, Parameterized Beyond-Einstein Growth, Astropart. Phys. **28**,

481 (2007), arXiv:astro-ph/0701317.

[97] T. M. C. Abbott *et al.* (DES), Dark Energy Survey Year 3 results: Constraints on extensions to ΛCDM with weak lensing and galaxy clustering, Phys. Rev. D **107**, 083504 (2023), arXiv:2207.05766 [astro-ph.CO].

[98] P. J. E. Peebles and B. Ratra, The Cosmological Constant and Dark Energy, Rev. Mod. Phys. **75**, 559 (2003), arXiv:astro-ph/0207347.

[99] V. Mukhanov, *Physical Foundations of Cosmology* (Cambridge Univ. Press, Cambridge, 2005).

[100] B. Carr, F. Kuhnel, and M. Sandstad, Primordial Black Holes as Dark Matter, Phys. Rev. D **94**, 083504 (2016), arXiv:1607.06077 [astro-ph.CO].

[101] D. S. Akerib *et al.* (LUX), Results from a search for dark matter in the complete LUX exposure, Phys. Rev. Lett. **118**, 021303 (2017), arXiv:1608.07648 [astro-ph.CO].

[102] R. J. Gaitskell, Direct detection of dark matter, Ann. Rev. Nucl. Part. Sci. **54**, 315 (2004).

[103] A. G. Riess *et al.* (Supernova Search Team), Observational evidence from supernovae for an accelerating universe and a cosmological constant, Astron. J. **116**, 1009 (1998), arXiv:astro-ph/9805201.

[104] S. Perlmutter *et al.* (Supernova Cosmology Project), Measurements of Ω and Λ from 42 high redshift supernovae, Astrophys. J. **517**, 565 (1999), arXiv:astro-ph/9812133.

[105] A. H. Guth, The Inflationary Universe: A Possible Solution to the Horizon and Flatness Problems, Phys. Rev. D **23**, 347 (1981).

[106] A. D. Linde, A New Inflationary Universe Scenario: A Possible Solution of the Horizon, Flatness, Homogeneity, Isotropy and Primordial Monopole Problems, Phys. Lett. B **108**, 389 (1982).

[107] S. Weinberg, The Cosmological Constant Problem, Rev. Mod. Phys. **61**, 1 (1989).

[108] E. J. Copeland, M. Sami, and S. Tsujikawa, Dynamics of dark energy, Int. J. Mod. Phys. D **15**, 1753 (2006), arXiv:hep-th/0603057.

[109] A. Addazi *et al.*, Quantum gravity phenomenology at the dawn of the multi-messenger era—A review, Prog. Part. Nucl. Phys. **125**, 103948 (2022), arXiv:2111.05659 [hep-ph].

[110] E. Abdalla *et al.*, Cosmology intertwined: A review of the particle physics, astrophysics, and cosmology associated with the cosmological tensions and anomalies, JHEAp **34**, 49 (2022), arXiv:2203.06142 [astro-ph.CO].

[111] E. Di Valentino *et al.*, Snowmass2021 - Letter of interest cosmology intertwined I: Perspectives for the next decade, Astropart. Phys. **131**, 102606 (2021), arXiv:2008.11283 [astro-ph.CO].

[112] E. Di Valentino *et al.*, Cosmology Intertwined III: $f\sigma_8$ and S_8, Astropart. Phys. **131**, 102604 (2021), arXiv:2008.11285 [astro-ph.CO].

[113] D. Staicova, Hints for the H0 — rd tension in uncorrelated Baryon Acoustic Oscillations dataset, in *16th Marcel Grossmann Meeting on Recent Developments in Theoretical and Experimental General Relativity, Astrophysics and Relativistic Field Theories* (2021) arXiv:2111.07907 [astro-ph.CO].

[114] E. Di Valentino, O. Mena, S. Pan, L. Visinelli, W. Yang, A. Melchiorri, D. F. Mota, A. G. Riess, and J. Silk, In the realm of the Hubble tension—a review of solutions, Class. Quant. Grav. **38**, 153001 (2021), arXiv:2103.01183 [astro-ph.CO].

[115] L. Perivolaropoulos and F. Skara, Challenges for ΛCDM: An update, New Astron. Rev. **95**, 101659 (2022), arXiv:2105.05208 [astro-ph.CO].

[116] E. Di Valentino, W. Giarè, A. Melchiorri, and J. Silk, Health checkup test of the standard

cosmological model in view of recent cosmic microwave background anisotropies experiments, Phys. Rev. D **106**, 103506 (2022), arXiv:2209.12872 [astro-ph.CO].

[117] E. Di Valentino *et al.*, Snowmass2021 - Letter of interest cosmology intertwined II: The hubble constant tension, Astropart. Phys. **131**, 102605 (2021), arXiv:2008.11284 [astro-ph.CO].

[118] M. Sajjad Athar *et al.*, Status and perspectives of neutrino physics, Prog. Part. Nucl. Phys. **124**, 103947 (2022), arXiv:2111.07586 [hep-ph].

[119] R. C. Nunes and S. Vagnozzi, Arbitrating the S8 discrepancy with growth rate measurements from redshift-space distortions, Mon. Not. Roy. Astron. Soc. **505**, 5427 (2021), arXiv:2106.01208 [astro-ph.CO].

[120] L. Verde, T. Treu, and A. G. Riess, Tensions between the Early and the Late Universe, Nature Astron. **3**, 891 (2019), arXiv:1907.10625 [astro-ph.CO].

[121] E. Di Valentino, A combined analysis of the H_0 late time direct measurements and the impact on the Dark Energy sector, Mon. Not. Roy. Astron. Soc. **502**, 2065 (2021), arXiv:2011.00246 [astro-ph.CO].

[122] A. G. Riess, The Expansion of the Universe is Faster than Expected, Nature Rev. Phys. **2**, 10 (2019), arXiv:2001.03624 [astro-ph.CO].

[123] A. G. Riess, L. Breuval, W. Yuan, S. Casertano, L. M. Macri, J. B. Bowers, D. Scolnic, T. Cantat-Gaudin, R. I. Anderson, and M. C. Reyes, Cluster Cepheids with High Precision Gaia Parallaxes, Low Zero-point Uncertainties, and Hubble Space Telescope Photometry, Astrophys. J. **938**, 36 (2022), arXiv:2208.01045 [astro-ph.CO].

[124] K. C. Wong *et al.*, H0LiCOW – XIII. A 2.4 per cent measurement of H0 from lensed quasars: 5.3σ tension between early- and late-Universe probes, Mon. Not. Roy. Astron. Soc. **498**, 1420 (2020), arXiv:1907.04869 [astro-ph.CO].

[125] C. D. Huang, A. G. Riess, W. Yuan, L. M. Macri, N. L. Zakamska, S. Casertano, P. A. Whitelock, S. L. Hoffmann, A. V. Filippenko, and D. Scolnic, Hubble Space Telescope Observations of Mira Variables in the Type Ia Supernova Host NGC 1559: An Alternative Candle to Measure the Hubble Constant 10.3847/1538-4357/ab5dbd (2019), arXiv:1908.10883 [astro-ph.CO].

[126] D. W. Pesce *et al.*, The Megamaser Cosmology Project. XIII. Combined Hubble constant constraints, Astrophys. J. Lett. **891**, L1 (2020), arXiv:2001.09213 [astro-ph.CO].

[127] E. Kourkchi, R. B. Tully, G. S. Anand, H. M. Courtois, A. Dupuy, J. D. Neill, L. Rizzi, and M. Seibert, Cosmicflows-4: The Calibration of Optical and Infrared Tully–Fisher Relations, Astrophys. J. **896**, 3 (2020), arXiv:2004.14499 [astro-ph.GA].

[128] J. Schombert, S. McGaugh, and F. Lelli, Using the Baryonic Tully–Fisher Relation to Measure H o, Astron. J. **160**, 71 (2020), arXiv:2006.08615 [astro-ph.CO].

[129] J. P. Blakeslee, J. B. Jensen, C.-P. Ma, P. A. Milne, and J. E. Greene, The Hubble Constant from Infrared Surface Brightness Fluctuation Distances, Astrophys. J. **911**, 65 (2021), arXiv:2101.02221 [astro-ph.CO].

[130] T. de Jaeger, L. Galbany, A. G. Riess, B. E. Stahl, B. J. Shappee, A. V. Filippenko, and W. Zheng, A 5 per cent measurement of the Hubble–Lemaître constant from Type II supernovae, Mon. Not. Roy. Astron. Soc. **514**, 4620 (2022), arXiv:2203.08974 [astro-ph.CO].

[131] A. J. Shajib *et al.*, TDCOSMO. XIII. Improved Hubble constant measurement from lensing time delays using spatially resolved stellar kinematics of the lens galaxy, Astron. Astrophys. **673**, A9 (2023), arXiv:2301.02656 [astro-ph.CO].

[132] D. Scolnic, A. G. Riess, J. Wu, S. Li, G. S. Anand, R. Beaton, S. Casertano, R. Anderson, S. Dhawan, and X. Ke, CATS: The Hubble Constant from Standardized TRGB and Type Ia Supernova Measurements, (2023), arXiv:2304.06693 [astro-ph.CO].

[133] R. I. Anderson, N. W. Koblischke, and L. Eyer, Reconciling astronomical distance scales with variable red giant stars, (2023), arXiv:2303.04790 [astro-ph.CO].

[134] W. L. Freedman, Measurements of the Hubble Constant: Tensions in Perspective, Astrophys. J. **919**, 16 (2021), arXiv:2106.15656 [astro-ph.CO].

[135] W. L. Freedman, B. F. Madore, T. Hoyt, I. S. Jang, R. Beaton, M. G. Lee, A. Monson, J. Neeley, and J. Rich, Calibration of the Tip of the Red Giant Branch (TRGB) 10.3847/1538-4357/ab7339 (2020), arXiv:2002.01550 [astro-ph.GA].

[136] C. Heymans *et al.*, KiDS-1000 Cosmology: Multi-probe weak gravitational lensing and spectroscopic galaxy clustering constraints, Astron. Astrophys. **646**, A140 (2021), arXiv:2007.15632 [astro-ph.CO].

[137] T. M. C. Abbott *et al.* (DES), Dark Energy Survey Year 3 results: Cosmological constraints from galaxy clustering and weak lensing, Phys. Rev. D **105**, 023520 (2022), arXiv:2105.13549 [astro-ph.CO].

[138] R. Dalal *et al.*, Hyper Suprime-Cam Year 3 Results: Cosmology from Cosmic Shear Power Spectra, (2023), arXiv:2304.00701 [astro-ph.CO].

[139] D. Brout *et al.*, The Pantheon+ Analysis: SuperCal-fragilistic Cross Calibration, Retrained SALT2 Light-curve Model, and Calibration Systematic Uncertainty, Astrophys. J. **938**, 111 (2022), arXiv:2112.03864 [astro-ph.CO].

[140] L. Knox and M. Millea, Hubble constant hunter's guide, Phys. Rev. D **101**, 043533 (2020), arXiv:1908.03663 [astro-ph.CO].

[141] K. Jedamzik, L. Pogosian, and G.-B. Zhao, Why reducing the cosmic sound horizon alone can not fully resolve the Hubble tension, Commun. in Phys. **4**, 123 (2021), arXiv:2010.04158 [astro-ph.CO].

[142] V. Poulin, T. L. Smith, and T. Karwal, The Ups and Downs of Early Dark Energy solutions to the Hubble tension: a review of models, hints and constraints circa 2023, (2023), arXiv:2302.09032 [astro-ph.CO].

[143] E. Di Valentino, Challenges of the Standard Cosmological Model, Universe **8**, 399 (2022).

[144] C. Krishnan, E. O. Colgáin, M. M. Sheikh-Jabbari, and T. Yang, Running Hubble Tension and a H0 Diagnostic, Phys. Rev. D **103**, 103509 (2021), arXiv:2011.02858 [astro-ph.CO].

[145] S. A. Adil, O. Akarsu, M. Malekjani, E. O. Colgáin, S. Pourojaghi, A. A. Sen, and M. M. Sheikh-Jabbari, S_8 increases with effective redshift in ΛCDM cosmology, (2023), arXiv:2303.06928 [astro-ph.CO].

[146] E. N. Saridakis *et al.* (CANTATA), Modified Gravity and Cosmology: An Update by the CANTATA Network, (2021), arXiv:2105.12582 [gr-qc].

[147] M. Kamionkowski and A. G. Riess, The Hubble Tension and Early Dark Energy, (2022), arXiv:2211.04492 [astro-ph.CO].

[148] E. V. Linder and A. Jenkins, Cosmic structure and dark energy, Mon. Not. Roy. Astron. Soc. **346**, 573 (2003), arXiv:astro-ph/0305286.

[149] E. V. Linder, Exploring the expansion history of the universe, Phys. Rev. Lett. **90**, 091301 (2003), arXiv:astro-ph/0208512.

[150] L.-M. Wang and P. J. Steinhardt, Cluster abundance constraints on quintessence models, Astrophys. J. **508**, 483 (1998), arXiv:astro-ph/9804015.

[151] E. V. Linder, Probing gravitation, dark energy, and acceleration, Phys. Rev. D **70**, 023511 (2004), arXiv:astro-ph/0402503.

[152] E. V. Linder and D. Polarski, End of cosmic growth, Phys. Rev. D **99**, 023503 (2019), arXiv:1810.10547 [astro-ph.CO].

[153] E. V. Linder, Dark energy, expansion history of the universe, and SNAP, AIP Conf. Proc. **655**, 193 (2003), arXiv:astro-ph/0302038.

[154] E. V. Linder, Benchmarks of Dark Energy, (2023), arXiv:2304.04803 [astro-ph.CO].

[155] E. V. Linder, Biased Cosmology: Pivots, Parameters, and Figures of Merit, Astropart. Phys. **26**, 102 (2006), arXiv:astro-ph/0604280.

[156] L. Xu, Growth Index after Planck, Phys. Rev. D **88**, 084032 (2013), arXiv:1306.2683 [astro-ph.CO].

[157] Z. Sakr, Untying the growth index to relief the σ_8 discomfort (2023) arXiv:2305.02863 [astro-ph.CO].

[158] `https://github.com/MinhMPA/CAMB_GammaPrime_Growth`.

[159] D. Hanson, A. Challinor, and A. Lewis, Weak lensing of the CMB, Gen. Rel. Grav. **42**, 2197 (2010), arXiv:0911.0612 [astro-ph.CO].

[160] A. Lewis, Efficient sampling of fast and slow cosmological parameters, Phys. Rev. D **87**, 103529 (2013), arXiv:1304.4473 [astro-ph.CO].

[161] R. M. Neal, Taking bigger metropolis steps by dragging fast variables (2005), arXiv:math/0502099 [math.ST].

[162] N. Aghanim *et al.* (Planck), Planck 2018 results. I. Overview and the cosmological legacy of Planck, Astron. Astrophys. **641**, A1 (2020), arXiv:1807.06205 [astro-ph.CO].

[163] A. Gelman and D. B. Rubin, Inference from Iterative Simulation Using Multiple Sequences, Statistical Science **7**, 457 (1992).

[164] E. Calabrese, A. Slosar, A. Melchiorri, G. F. Smoot, and O. Zahn, Cosmic Microwave Weak lensing data as a test for the dark universe, Phys. Rev. D **77**, 123531 (2008), arXiv:0803.2309 [astro-ph].

[165] E. Di Valentino, A. Melchiorri, and J. Silk, Investigating Cosmic Discordance, Astrophys. J. Lett. **908**, L9 (2021), arXiv:2003.04935 [astro-ph.CO].

[166] E. Di Valentino, A. Melchiorri, and J. Silk, Planck evidence for a closed Universe and a possible crisis for cosmology, Nature Astron. **4**, 196 (2019), arXiv:1911.02087 [astro-ph.CO].

[167] W. Handley, Curvature tension: evidence for a closed universe, Phys. Rev. D **103**, L041301 (2021), arXiv:1908.09139 [astro-ph.CO].

[168] P. A. R. Ade *et al.* (Planck), Planck 2013 results. XVI. Cosmological parameters, Astron. Astrophys. **571**, A16 (2014), arXiv:1303.5076 [astro-ph.CO].

[169] P. A. R. Ade *et al.* (Planck), Planck 2015 results. XIII. Cosmological parameters, Astron. Astrophys. **594**, A13 (2016), arXiv:1502.01589 [astro-ph.CO].

[170] A. G. Riess *et al.* (Supernova Search Team), The farthest known supernova: support for an accelerating universe and a glimpse of the epoch of deceleration, Astrophys. J. **560**, 49 (2001), arXiv:astro-ph/0104455.

[171] M. Tegmark *et al.* (SDSS), Cosmological parameters from SDSS and WMAP, Phys. Rev. D **69**,

103501 (2004), arXiv:astro-ph/0310723.

[172] R. Scranton *et al.* (SDSS), Physical evidence for dark energy, (2003), arXiv:astro-ph/0307335.

[173] J. L. Tonry *et al.* (Supernova Search Team), Cosmological results from high-z supernovae, Astrophys. J. **594**, 1 (2003), arXiv:astro-ph/0305008.

[174] R. A. Knop *et al.* (Supernova Cosmology Project), New constraints on Omega(M), Omega(lambda), and w from an independent set of eleven high-redshift supernovae observed with HST, Astrophys. J. **598**, 102 (2003), arXiv:astro-ph/0309368.

[175] U. Seljak *et al.* (SDSS), Cosmological parameter analysis including SDSS Ly-alpha forest and galaxy bias: Constraints on the primordial spectrum of fluctuations, neutrino mass, and dark energy, Phys. Rev. D **71**, 103515 (2005), arXiv:astro-ph/0407372.

[176] B. Feng, X.-L. Wang, and X.-M. Zhang, Dark energy constraints from the cosmic age and supernova, Phys. Lett. B **607**, 35 (2005), arXiv:astro-ph/0404224.

[177] A. G. Riess *et al.* (Supernova Search Team), Type Ia supernova discoveries at z $>$ 1 from the Hubble Space Telescope: Evidence for past deceleration and constraints on dark energy evolution, Astrophys. J. **607**, 665 (2004), arXiv:astro-ph/0402512.

[178] P. Astier *et al.* (SNLS), The Supernova Legacy Survey: Measurement of Ω_M, Ω_Λ and $\sqsupseteq$ from the first year data set, Astron. Astrophys. **447**, 31 (2006), arXiv:astro-ph/0510447.

[179] D. J. Eisenstein *et al.* (SDSS), Detection of the Baryon Acoustic Peak in the Large-Scale Correlation Function of SDSS Luminous Red Galaxies, Astrophys. J. **633**, 560 (2005), arXiv:astro-ph/0501171.

[180] D. J. Eisenstein, H.-j. Seo, E. Sirko, and D. Spergel, Improving Cosmological Distance Measurements by Reconstruction of the Baryon Acoustic Peak, Astrophys. J. **664**, 675 (2007), arXiv:astro-ph/0604362.

[181] M. Tegmark *et al.* (SDSS), Cosmological Constraints from the SDSS Luminous Red Galaxies, Phys. Rev. D **74**, 123507 (2006), arXiv:astro-ph/0608632.

[182] V. Sahni and A. Starobinsky, Reconstructing Dark Energy, Int. J. Mod. Phys. D **15**, 2105 (2006), arXiv:astro-ph/0610026.

[183] W. M. Wood-Vasey *et al.* (ESSENCE), Observational Constraints on the Nature of the Dark Energy: First Cosmological Results from the ESSENCE Supernova Survey, Astrophys. J. **666**, 694 (2007), arXiv:astro-ph/0701041.

[184] A. Vikhlinin *et al.*, Chandra Cluster Cosmology Project III: Cosmological Parameter Constraints, Astrophys. J. **692**, 1060 (2009), arXiv:0812.2720 [astro-ph].

[185] D. Stern, R. Jimenez, L. Verde, M. Kamionkowski, and S. A. Stanford, Cosmic Chronometers: Constraining the Equation of State of Dark Energy. I: H(z) Measurements, JCAP **02**, 008, arXiv:0907.3149 [astro-ph.CO].

[186] B. D. Sherwin *et al.*, Evidence for dark energy from the cosmic microwave background alone using the Atacama Cosmology Telescope lensing measurements, Phys. Rev. Lett. **107**, 021302 (2011), arXiv:1105.0419 [astro-ph.CO].

[187] G. Hinshaw *et al.* (WMAP), Nine-Year Wilkinson Microwave Anisotropy Probe (WMAP) Observations: Cosmological Parameter Results, Astrophys. J. Suppl. **208**, 19 (2013), arXiv:1212.5226 [astro-ph.CO].

[188] K. S. Dawson *et al.* (BOSS), The Baryon Oscillation Spectroscopic Survey of SDSS-III, Astron. J. **145**, 10 (2013), arXiv:1208.0022 [astro-ph.CO].

[189] J. T. A. de Jong, G. A. Verdoes Kleijn, K. H. Kuijken, and E. A. Valentijn (Astro-WISE, KiDS), The Kilo-Degree Survey, Exper. Astron. **35**, 25 (2013), arXiv:1206.1254 [astro-ph.CO].

[190] L. Anderson *et al.* (BOSS), The clustering of galaxies in the SDSS-III Baryon Oscillation Spectroscopic Survey: baryon acoustic oscillations in the Data Releases 10 and 11 Galaxy samples, Mon. Not. Roy. Astron. Soc. **441**, 24 (2014), arXiv:1312.4877 [astro-ph.CO].

[191] D. H. Weinberg, M. J. Mortonson, D. J. Eisenstein, C. Hirata, A. G. Riess, and E. Rozo, Observational Probes of Cosmic Acceleration, Phys. Rept. **530**, 87 (2013), arXiv:1201.2434 [astro-ph.CO].

[192] F. Beutler *et al.* (BOSS), The clustering of galaxies in the SDSS-III Baryon Oscillation Spectroscopic Survey: Testing gravity with redshift-space distortions using the power spectrum multipoles, Mon. Not. Roy. Astron. Soc. **443**, 1065 (2014), arXiv:1312.4611 [astro-ph.CO].

[193] T. Delubac *et al.* (BOSS), Baryon acoustic oscillations in the Lyα forest of BOSS DR11 quasars, Astron. Astrophys. **574**, A59 (2015), arXiv:1404.1801 [astro-ph.CO].

[194] M. Betoule *et al.* (SDSS), Improved cosmological constraints from a joint analysis of the SDSS-II and SNLS supernova samples, Astron. Astrophys. **568**, A22 (2014), arXiv:1401.4064 [astro-ph.CO].

[195] E. Aubourg *et al.* (BOSS), Cosmological implications of baryon acoustic oscillation measurements, Phys. Rev. D **92**, 123516 (2015), arXiv:1411.1074 [astro-ph.CO].

[196] A. J. Ross, L. Samushia, C. Howlett, W. J. Percival, A. Burden, and M. Manera, The clustering of the SDSS DR7 main Galaxy sample – I. A 4 per cent distance measure at $z = 0.15$, Mon. Not. Roy. Astron. Soc. **449**, 835 (2015), arXiv:1409.3242 [astro-ph.CO].

[197] M. Moresco, L. Pozzetti, A. Cimatti, R. Jimenez, C. Maraston, L. Verde, D. Thomas, A. Citro, R. Tojeiro, and D. Wilkinson, A 6% measurement of the Hubble parameter at $z \sim 0.45$: direct evidence of the epoch of cosmic re-acceleration, JCAP **05**, 014, arXiv:1601.01701 [astro-ph.CO].

[198] M. Moresco, R. Jimenez, L. Verde, A. Cimatti, L. Pozzetti, C. Maraston, and D. Thomas, Constraining the time evolution of dark energy, curvature and neutrino properties with cosmic chronometers, JCAP **12**, 039, arXiv:1604.00183 [astro-ph.CO].

[199] D. Rubin and B. Hayden, Is the expansion of the universe accelerating? All signs point to yes, Astrophys. J. Lett. **833**, L30 (2016), arXiv:1610.08972 [astro-ph.CO].

[200] S. Alam *et al.* (BOSS), The clustering of galaxies in the completed SDSS-III Baryon Oscillation Spectroscopic Survey: cosmological analysis of the DR12 galaxy sample, Mon. Not. Roy. Astron. Soc. **470**, 2617 (2017), arXiv:1607.03155 [astro-ph.CO].

[201] T. Abbott *et al.* (DES), The Dark Energy Survey: more than dark energy – an overview, Mon. Not. Roy. Astron. Soc. **460**, 1270 (2016), arXiv:1601.00329 [astro-ph.CO].

[202] B. S. Haridasu, V. V. Lukovi$\acute{c}$, R. D'Agostino, and N. Vittorio, Strong evidence for an accelerating universe, Astron. Astrophys. **600**, L1 (2017), arXiv:1702.08244 [astro-ph.CO].

[203] M. A. Troxel *et al.* (DES), Dark Energy Survey Year 1 results: Cosmological constraints from cosmic shear, Phys. Rev. D **98**, 043528 (2018), arXiv:1708.01538 [astro-ph.CO].

[204] D. M. Scolnic *et al.* (Pan-STARRS1), The Complete Light-curve Sample of Spectroscopically Confirmed SNe Ia from Pan-STARRS1 and Cosmological Constraints from the Combined Pantheon Sample, Astrophys. J. **859**, 101 (2018), arXiv:1710.00845 [astro-ph.CO].

[205] A. Gómez-Valent, Quantifying the evidence for the current speed-up of the Universe with low and intermediate-redshift data. A more model-independent approach, JCAP **05**, 026,

arXiv:1810.02278 [astro-ph.CO].

[206] Y. Yang and Y. Gong, The evidence of cosmic acceleration and observational constraints, JCAP **06**, 059, arXiv:1912.07375 [astro-ph.CO].

[207] S. Nadathur, W. J. Percival, F. Beutler, and H. Winther, Testing Low-Redshift Cosmic Acceleration with Large-Scale Structure, Phys. Rev. Lett. **124**, 221301 (2020), arXiv:2001.11044 [astro-ph.CO].

[208] B. M. Rose, D. Rubin, A. Cikota, S. E. Deustua, S. Dixon, A. Fruchter, D. O. Jones, A. G. Riess, and D. M. Scolnic, Evidence for Cosmic Acceleration is Robust to Observed Correlations Between Type Ia Supernova Luminosity and Stellar Age, Astrophys. J. Lett. **896**, L4 (2020), arXiv:2002.12382 [astro-ph.CO].

[209] E. Di Valentino, S. Gariazzo, O. Mena, and S. Vagnozzi, Soundness of Dark Energy properties, JCAP **07** (07), 045, arXiv:2005.02062 [astro-ph.CO].

[210] M. Asgari *et al.* (KiDS), KiDS-1000 Cosmology: Cosmic shear constraints and comparison between two point statistics, Astron. Astrophys. **645**, A104 (2021), arXiv:2007.15633 [astro-ph.CO].

[211] T. Tröster *et al.* (KiDS), KiDS-1000 Cosmology: Constraints beyond flat ΛCDM, Astron. Astrophys. **649**, A88 (2021), arXiv:2010.16416 [astro-ph.CO].

[212] M. Moresco *et al.*, Unveiling the Universe with emerging cosmological probes, Living Rev. Rel. **25**, 6 (2022), arXiv:2201.07241 [astro-ph.CO].

[213] M. S. Madhavacheril *et al.* (ACT), The Atacama Cosmology Telescope: DR6 Gravitational Lensing Map and Cosmological Parameters, Astrophys. J. **962**, 113 (2024), arXiv:2304.05203 [astro-ph.CO].

[214] T. M. C. Abbott *et al.* (Kilo-Degree Survey, DES), DES Y3 + KiDS-1000: Consistent cosmology combining cosmic shear surveys, Open J. Astrophys. **6**, 2305.17173 (2023), arXiv:2305.17173 [astro-ph.CO].

[215] A. G. Adame *et al.* (DESI), DESI 2024 III: Baryon Acoustic Oscillations from Galaxies and Quasars, (2024), arXiv:2404.03000 [astro-ph.CO].

[216] K. Lodha *et al.* (DESI), DESI 2024: Constraints on Physics-Focused Aspects of Dark Energy using DESI DR1 BAO Data, (2024), arXiv:2405.13588 [astro-ph.CO].

[217] T. M. C. Abbott *et al.* (Abbott, DES: T. M. C, DES), The Dark Energy Survey: Cosmology Results with ∼1500 New High-redshift Type Ia Supernovae Using the Full 5 yr Data Set, Astrophys. J. Lett. **973**, L14 (2024), arXiv:2401.02929 [astro-ph.CO].

[218] B. O. Sánchez *et al.* (DES), The Dark Energy Survey Supernova Program: Light Curves and 5 Yr Data Release, Astrophys. J. **975**, 5 (2024), arXiv:2406.05046 [astro-ph.CO].

[219] M. Vincenzi *et al.* (DES), The Dark Energy Survey Supernova Program: Cosmological Analysis and Systematic Uncertainties, Astrophys. J. **975**, 86 (2024), arXiv:2401.02945 [astro-ph.CO].

[220] N. Schöneberg, G. Franco Abellán, A. Pérez Sánchez, S. J. Witte, V. Poulin, and J. Lesgourgues, The H0 Olympics: A fair ranking of proposed models, Phys. Rept. **984**, 1 (2022), arXiv:2107.10291 [astro-ph.CO].

[221] P. Shah, P. Lemos, and O. Lahav, A buyer's guide to the Hubble constant, Astron. Astrophys. Rev. **29**, 9 (2021), arXiv:2109.01161 [astro-ph.CO].

[222] W. Giarè, CMB Anomalies and the Hubble Tension, (2023), arXiv:2305.16919 [astro-ph.CO].

[223] J.-P. Hu and F.-Y. Wang, Hubble Tension: The Evidence of New Physics, Universe **9**, 94 (2023),

arXiv:2302.05709 [astro-ph.CO].

[224] L. Verde, N. Schöneberg, and H. Gil-Marín, A Tale of Many H0, Ann. Rev. Astron. Astrophys. **62**, 287 (2024), arXiv:2311.13305 [astro-ph.CO].

[225] E. Di Valentino and D. Brout, eds., *The Hubble Constant Tension*, Springer Series in Astrophysics and Cosmology (Springer, 2024).

[226] L. Perivolaropoulos, Hubble tension or distance ladder crisis?, Phys. Rev. D **110**, 123518 (2024), arXiv:2408.11031 [astro-ph.CO].

[227] L. Breuval, A. G. Riess, S. Casertano, W. Yuan, L. M. Macri, M. Romaniello, Y. S. Murakami, D. Scolnic, G. S. Anand, and I. Soszyński, Small Magellanic Cloud Cepheids Observed with the Hubble Space Telescope Provide a New Anchor for the SH0ES Distance Ladder, Astrophys. J. **973**, 30 (2024), arXiv:2404.08038 [astro-ph.CO].

[228] Y. S. Murakami, A. G. Riess, B. E. Stahl, W. D. Kenworthy, D.-M. A. Pluck, A. Macoretta, D. Brout, D. O. Jones, D. M. Scolnic, and A. V. Filippenko, Leveraging SN Ia spectroscopic similarity to improve the measurement of H $_0$, JCAP **11**, 046, arXiv:2306.00070 [astro-ph.CO].

[229] A. Amon *et al.* (DES), Dark Energy Survey Year 3 results: Cosmology from cosmic shear and robustness to data calibration, Phys. Rev. D **105**, 023514 (2022), arXiv:2105.13543 [astro-ph.CO].

[230] X. Li *et al.*, Hyper Suprime-Cam Year 3 results: Cosmology from cosmic shear two-point correlation functions, Phys. Rev. D **108**, 123518 (2023), arXiv:2304.00702 [astro-ph.CO].

[231] J. Harnois-Deraps *et al.*, KiDS-1000 and DES-Y1 combined: Cosmology from peak count statistics, (2024), arXiv:2405.10312 [astro-ph.CO].

[232] J. Armijo, G. A. Marques, C. P. Novaes, L. Thiele, J. A. Cowell, D. Grandón, M. Shirasaki, and J. Liu, Cosmological constraints using Minkowski functionals from the first year data of the Hyper Suprime-Cam, (2024), arXiv:2410.00401 [astro-ph.CO].

[233] F. J. Qu *et al.* (ACT, DESI), The Atacama Cosmology Telescope DR6 and DESI: Structure growth measurements from the cross-correlation of DESI Legacy Imaging galaxies and CMB lensing from ACT DR6 and Planck PR4, (2024), arXiv:2410.10808 [astro-ph.CO].

[234] J. McCullough *et al.* (DES), Dark Energy Survey Year 3: Blue Shear, (2024), arXiv:2410.22272 [astro-ph.CO].

[235] E. T. Lau, A. Bogdán, D. Nagai, N. Cappelluti, and M. Shirasaki, Cosmology and Astrophysics with the Diffuse eRASS1 X-ray Angular Power Spectrum, (2024), arXiv:2410.22397 [astro-ph.CO].

[236] O. Akarsu, E. O. Colgáin, A. A. Sen, and M. M. Sheikh-Jabbari, Further support for S_8 increasing with effective redshift, (2024), arXiv:2410.23134 [astro-ph.CO].

[237] V. Sahni and A. A. Starobinsky, The Case for a positive cosmological Lambda term, Int. J. Mod. Phys. D **9**, 373 (2000), arXiv:astro-ph/9904398.

[238] S. M. Carroll, The Cosmological constant, Living Rev. Rel. **4**, 1 (2001), arXiv:astro-ph/0004075.

[239] T. Padmanabhan, Cosmological constant: The Weight of the vacuum, Phys. Rept. **380**, 235 (2003), arXiv:hep-th/0212290.

[240] R. R. Caldwell and M. Kamionkowski, The Physics of Cosmic Acceleration, Ann. Rev. Nucl. Part. Sci. **59**, 397 (2009), arXiv:0903.0866 [astro-ph.CO].

[241] M. Li, X.-D. Li, S. Wang, and Y. Wang, Dark Energy, Commun. Theor. Phys. **56**, 525 (2011), arXiv:1103.5870 [astro-ph.CO].

[242] J. Martin, Everything You Always Wanted To Know About The Cosmological Constant Problem (But Were Afraid To Ask), Comptes Rendus Physique **13**, 566 (2012), arXiv:1205.3365 [astro-ph.CO].

[243] L. M. Krauss and M. S. Turner, The Cosmological constant is back, Gen. Rel. Grav. **27**, 1137 (1995), arXiv:astro-ph/9504003.

[244] S. Weinberg, The Cosmological constant problems, in *4th International Symposium on Sources and Detection of Dark Matter in the Universe (DM 2000)* (2000) pp. 18–26, arXiv:astro-ph/0005265.

[245] V. Sahni, The Cosmological constant problem and quintessence, Class. Quant. Grav. **19**, 3435 (2002), arXiv:astro-ph/0202076.

[246] J. Yokoyama, Issues on the cosmological constant, in *12th Workshop on General Relativity and Gravitation* (2003) arXiv:gr-qc/0305068.

[247] S. Nobbenhuis, Categorizing different approaches to the cosmological constant problem, Found. Phys. **36**, 613 (2006), arXiv:gr-qc/0411093.

[248] C. P. Burgess, The Cosmological Constant Problem: Why it's hard to get Dark Energy from Micro-physics, in *100e Ecole d'Ete de Physique: Post-Planck Cosmology* (2015) pp. 149–197, arXiv:1309.4133 [hep-th].

[249] A. Joyce, B. Jain, J. Khoury, and M. Trodden, Beyond the Cosmological Standard Model, Phys. Rept. **568**, 1 (2015), arXiv:1407.0059 [astro-ph.CO].

[250] P. Bull *et al.*, Beyond ΛCDM: Problems, solutions, and the road ahead, Phys. Dark Univ. **12**, 56 (2016), arXiv:1512.05356 [astro-ph.CO].

[251] B. Wang, E. Abdalla, F. Atrio-Barandela, and D. Pavon, Dark Matter and Dark Energy Interactions: Theoretical Challenges, Cosmological Implications and Observational Signatures, Rept. Prog. Phys. **79**, 096901 (2016), arXiv:1603.08299 [astro-ph.CO].

[252] R. Brustein and P. J. Steinhardt, Challenges for superstring cosmology, Phys. Lett. B **302**, 196 (1993), arXiv:hep-th/9212049.

[253] E. Witten, The Cosmological constant from the viewpoint of string theory, in *4th International Symposium on Sources and Detection of Dark Matter in the Universe (DM 2000)* (2000) pp. 27–36, arXiv:hep-ph/0002297.

[254] S. Kachru, R. Kallosh, A. D. Linde, and S. P. Trivedi, De Sitter vacua in string theory, Phys. Rev. D **68**, 046005 (2003), arXiv:hep-th/0301240.

[255] J. Polchinski, The Cosmological Constant and the String Landscape, in *23rd Solvay Conference in Physics: The Quantum Structure of Space and Time* (2006) pp. 216–236, arXiv:hep-th/0603249.

[256] U. H. Danielsson and T. Van Riet, What if string theory has no de Sitter vacua?, Int. J. Mod. Phys. D **27**, 1830007 (2018), arXiv:1804.01120 [hep-th].

[257] I. Zlatev, L.-M. Wang, and P. J. Steinhardt, Quintessence, cosmic coincidence, and the cosmological constant, Phys. Rev. Lett. **82**, 896 (1999), arXiv:astro-ph/9807002.

[258] D. Pavon and W. Zimdahl, Holographic dark energy and cosmic coincidence, Phys. Lett. B **628**, 206 (2005), arXiv:gr-qc/0505020.

[259] H. E. S. Velten, R. F. vom Marttens, and W. Zimdahl, Aspects of the cosmological "coincidence problem", Eur. Phys. J. C **74**, 3160 (2014), arXiv:1410.2509 [astro-ph.CO].

[260] W. Giarè, M. Najafi, S. Pan, E. Di Valentino, and J. T. Firouzjaee, Robust preference for

Dynamical Dark Energy in DESI BAO and SN measurements, JCAP **10**, 035, arXiv:2407.16689 [astro-ph.CO].

[261] Z. Wang, S. Lin, Z. Ding, and B. Hu, The role of LRG1 and LRG2's monopole in inferring the DESI 2024 BAO cosmology, (2024), arXiv:2405.02168 [astro-ph.CO].

[262] G. Efstathiou, Evolving Dark Energy or Supernovae Systematics?, (2024), arXiv:2408.07175 [astro-ph.CO].

[263] V. Patel, A. Chakraborty, and L. Amendola, The prior dependence of the DESI results, (2024), arXiv:2407.06586 [astro-ph.CO].

[264] G. Liu, Y. Wang, and W. Zhao, Impact of LRG1 and LRG2 in DESI 2024 BAO data on dark energy evolution, (2024), arXiv:2407.04385 [astro-ph.CO].

[265] E. O. Colgáin, M. G. Dainotti, S. Capozziello, S. Pourojaghi, M. M. Sheikh-Jabbari, and D. Stojkovic, Does DESI 2024 Confirm ΛCDM?, (2024), arXiv:2404.08633 [astro-ph.CO].

[266] W. Giarè, Dynamical Dark Energy Beyond Planck? Constraints from multiple CMB probes, DESI BAO and Type-Ia Supernovae, (2024), arXiv:2409.17074 [astro-ph.CO].

[267] M. Cortês and A. R. Liddle, Interpreting DESI's evidence for evolving dark energy, (2024), arXiv:2404.08056 [astro-ph.CO].

[268] L. Orchard and V. H. Cárdenas, Probing dark energy evolution post-DESI 2024, Phys. Dark Univ. **46**, 101678 (2024), arXiv:2407.05579 [astro-ph.CO].

[269] A. Chudaykin and M. Kunz, Modified gravity interpretation of the evolving dark energy in light of DESI data, (2024), arXiv:2407.02558 [astro-ph.CO].

[270] A. Notari, M. Redi, and A. Tesi, Consistent Theories for the DESI dark energy fit, (2024), arXiv:2406.08459 [astro-ph.CO].

[271] I. D. Gialamas, G. Hütsi, K. Kannike, A. Racioppi, M. Raidal, M. Vasar, and H. Veermäe, Interpreting DESI 2024 BAO: late-time dynamical dark energy or a local effect?, (2024), arXiv:2406.07533 [astro-ph.CO].

[272] H. Wang, Z.-Y. Peng, and Y.-S. Piao, Can recent DESI BAO measurements accommodate a negative cosmological constant?, (2024), arXiv:2406.03395 [astro-ph.CO].

[273] H. Wang and Y.-S. Piao, Dark energy in light of recent DESI BAO and Hubble tension, (2024), arXiv:2404.18579 [astro-ph.CO].

[274] W. Giarè, M. A. Sabogal, R. C. Nunes, and E. Di Valentino, Interacting Dark Energy after DESI Baryon Acoustic Oscillation measurements, (2024), arXiv:2404.15232 [astro-ph.CO].

[275] Y. Carloni, O. Luongo, and M. Muccino, Does dark energy really revive using DESI 2024 data?, (2024), arXiv:2404.12068 [astro-ph.CO].

[276] Y. Tada and T. Terada, Quintessential interpretation of the evolving dark energy in light of DESI observations, Phys. Rev. D **109**, L121305 (2024), arXiv:2404.05722 [astro-ph.CO].

[277] W. Yin, Cosmic clues: DESI, dark energy, and the cosmological constant problem, JHEP **05**, 327, arXiv:2404.06444 [hep-ph].

[278] O. Luongo and M. Muccino, Model independent cosmographic constraints from DESI 2024 10.1051/0004-6361/202450512 (2024), arXiv:2404.07070 [astro-ph.CO].

[279] C.-G. Park, J. de Cruz Pérez, and B. Ratra, Using non-DESI data to confirm and strengthen the DESI 2024 spatially-flat w_0w_aCDM cosmological parameterization result, (2024), arXiv:2405.00502 [astro-ph.CO].

[280] D. Shlivko and P. J. Steinhardt, Assessing observational constraints on dark energy, Phys. Lett.

B **855**, 138826 (2024), arXiv:2405.03933 [astro-ph.CO].

[281] G. Ye, M. Martinelli, B. Hu, and A. Silvestri, Hints of Nonminimally Coupled Gravity in DESI 2024 Baryon Acoustic Oscillation Measurements, Phys. Rev. Lett. **134**, 181002 (2025), arXiv:2407.15832 [astro-ph.CO].

[282] T.-N. Li, P.-J. Wu, G.-H. Du, S.-J. Jin, H.-L. Li, J.-F. Zhang, and X. Zhang, Constraints on interacting dark energy models from the DESI BAO and DES supernovae data, (2024), arXiv:2407.14934 [astro-ph.CO].

[283] Y. Yang, X. Ren, Q. Wang, Z. Lu, D. Zhang, Y.-F. Cai, and E. N. Saridakis, Quintom cosmology and modified gravity after DESI 2024, Sci. Bull. **69**, 2698 (2024), arXiv:2404.19437 [astro-ph.CO].

[284] R. Calderon *et al.* (DESI), DESI 2024: reconstructing dark energy using crossing statistics with DESI DR1 BAO data, JCAP **10**, 048, arXiv:2405.04216 [astro-ph.CO].

[285] C.-G. Park, J. de Cruz Perez, and B. Ratra, Is the w_0w_aCDM cosmological parameterization evidence for dark energy dynamics partially caused by the excess smoothing of Planck CMB anisotropy data?, (2024), arXiv:2410.13627 [astro-ph.CO].

[286] W. J. Wolf, P. G. Ferreira, and C. García-García, Matching current observational constraints with nonminimally coupled dark energy, (2024), arXiv:2409.17019 [astro-ph.CO].

[287] S. Pourojaghi, M. Malekjani, and Z. Davari, ΛCDM model against cosmography: A possible deviation after DESI 2024, (2024), arXiv:2408.10704 [astro-ph.CO].

[288] M. A. Sabogal, E. Silva, R. C. Nunes, S. Kumar, E. Di Valentino, and W. Giarè, Quantifying S_8 tension and evidence for interacting dark energy from redshift-space distortion measurements, (2024), arXiv:2408.12403 [astro-ph.CO].

[289] J.-Q. Jiang, D. Pedrotti, S. S. da Costa, and S. Vagnozzi, Non-parametric late-time expansion history reconstruction and implications for the Hubble tension in light of DESI, (2024), arXiv:2408.02365 [astro-ph.CO].

[290] B. R. Dinda and R. Maartens, Model-agnostic assessment of dark energy after DESI DR1 BAO, (2024), arXiv:2407.17252 [astro-ph.CO].

[291] A. Hernández-Almada, M. L. Mendoza-Martínez, M. A. García-Aspeitia, and V. Motta, Phenomenological emergent dark energy in the light of DESI Data Release 1, Phys. Dark Univ. **46**, 101668 (2024), arXiv:2407.09430 [astro-ph.CO].

[292] N. Menci, A. A. Sen, and M. Castellano, The Excess of JWST Bright Galaxies: a Possible Origin in the Ground State of Dynamical Dark Energy in the light of DESI 2024 Data, (2024), arXiv:2410.22940 [astro-ph.CO].

[293] O. F. Ramadan, J. Sakstein, and D. Rubin, DESI constraints on exponential quintessence, Phys. Rev. D **110**, L041303 (2024), arXiv:2405.18747 [astro-ph.CO].

[294] K. V. Berghaus, J. A. Kable, and V. Miranda, Quantifying Scalar Field Dynamics with DESI 2024 Y1 BAO measurements, (2024), arXiv:2404.14341 [astro-ph.CO].

[295] F. J. Qu, K. M. Surrao, B. Bolliet, J. C. Hill, B. D. Sherwin, and H. T. Jense, Accelerated inference on accelerated cosmic expansion: New constraints on axion-like early dark energy with DESI BAO and ACT DR6 CMB lensing, (2024), arXiv:2404.16805 [astro-ph.CO].

[296] P. Adolf, M. Hirsch, S. Krieg, H. Päs, and M. Tabet, Fitting the DESI BAO data with dark energy driven by the Cohen-Kaplan-Nelson bound, JCAP **08**, 048, arXiv:2406.09964 [astro-ph.CO].

[297] S. Bhattacharya, G. Borghetto, A. Malhotra, S. Parameswaran, G. Tasinato, and I. Zavala, Cosmological constraints on curved quintessence, JCAP **09**, 073, arXiv:2405.17396 [astro-ph.CO].

[298] S. Bhattacharya, G. Borghetto, A. Malhotra, S. Parameswaran, G. Tasinato, and I. Zavala, Cosmological tests of quintessence in quantum gravity, (2024), arXiv:2410.21243 [astro-ph.CO].

[299] A. Albrecht and P. J. Steinhardt, Cosmology for Grand Unified Theories with Radiatively Induced Symmetry Breaking, Phys. Rev. Lett. **48**, 1220 (1982).

[300] A. Vilenkin, The Birth of Inflationary Universes, Phys. Rev. D **27**, 2848 (1983).

[301] A. A. Starobinsky, A New Type of Isotropic Cosmological Models Without Singularity, Phys. Lett. B **91**, 99 (1980).

[302] E. Di Valentino, S. Galli, M. Lattanzi, A. Melchiorri, P. Natoli, L. Pagano, and N. Said, Tickling the CMB damping tail: Scrutinizing the tension between the Atacama Cosmology Telescope and South Pole Telescope experiments, Phys. Rev. D **88**, 023501 (2013), arXiv:1301.7343 [astro-ph.CO].

[303] G. E. Addison, Y. Huang, D. J. Watts, C. L. Bennett, M. Halpern, G. Hinshaw, and J. L. Weiland, Quantifying discordance in the 2015 Planck CMB spectrum, Astrophys. J. **818**, 132 (2016), arXiv:1511.00055 [astro-ph.CO].

[304] F. Renzi, E. Di Valentino, and A. Melchiorri, Cornering the Planck A_{lens} anomaly with future CMB data, Phys. Rev. D **97**, 123534 (2018), arXiv:1712.08758 [astro-ph.CO].

[305] E. Di Valentino, E. V. Linder, and A. Melchiorri, Vacuum phase transition solves the H_0 tension, Phys. Rev. D **97**, 043528 (2018), arXiv:1710.02153 [astro-ph.CO].

[306] G. E. Addison, C. L. Bennett, M. Halpern, G. Hinshaw, and J. L. Weiland, Revisiting the A $_L$ Lensing Anomaly in Planck 2018 Temperature Data, Astrophys. J. **974**, 187 (2024), arXiv:2310.03127 [astro-ph.CO].

[307] C.-G. Park and B. Ratra, Using the tilted flat-ΛCDM and the untilted non-flat ΛCDM inflation models to measure cosmological parameters from a compilation of observational data, Astrophys. J. **882**, 158 (2019), arXiv:1801.00213 [astro-ph.CO].

[308] G. Efstathiou and S. Gratton, The evidence for a spatially flat Universe, Mon. Not. Roy. Astron. Soc. **496**, L91 (2020), arXiv:2002.06892 [astro-ph.CO].

[309] D. Benisty and D. Staicova, Testing late-time cosmic acceleration with uncorrelated baryon acoustic oscillation dataset, Astron. Astrophys. **647**, A38 (2021), arXiv:2009.10701 [astro-ph.CO].

[310] S. Vagnozzi, E. Di Valentino, S. Gariazzo, A. Melchiorri, O. Mena, and J. Silk, The galaxy power spectrum take on spatial curvature and cosmic concordance, Phys. Dark Univ. **33**, 100851 (2021), arXiv:2010.02230 [astro-ph.CO].

[311] S. Vagnozzi, A. Loeb, and M. Moresco, Eppur è piatto? The Cosmic Chronometers Take on Spatial Curvature and Cosmic Concordance, Astrophys. J. **908**, 84 (2021), arXiv:2011.11645 [astro-ph.CO].

[312] E. Di Valentino, A. Melchiorri, O. Mena, S. Pan, and W. Yang, Interacting Dark Energy in a closed universe, Mon. Not. Roy. Astron. Soc. **502**, L23 (2021), arXiv:2011.00283 [astro-ph.CO].

[313] W. Yang, S. Pan, E. Di Valentino, O. Mena, and A. Melchiorri, 2021-H0 odyssey: closed, phantom and interacting dark energy cosmologies, JCAP **10**, 008, arXiv:2101.03129 [astro-ph.CO].

[314] S. Cao, J. Ryan, and B. Ratra, Using Pantheon and DES supernova, baryon acoustic oscillation,

and Hubble parameter data to constrain the Hubble constant, dark energy dynamics, and spatial curvature, Mon. Not. Roy. Astron. Soc. **504**, 300 (2021), arXiv:2101.08817 [astro-ph.CO].

[315] S. Dhawan, J. Alsing, and S. Vagnozzi, Non-parametric spatial curvature inference using late-Universe cosmological probes, Mon. Not. Roy. Astron. Soc. **506**, L1 (2021), arXiv:2104.02485 [astro-ph.CO].

[316] B. R. Dinda, Cosmic expansion parametrization: Implication for curvature and H0 tension, Phys. Rev. D **105**, 063524 (2022), arXiv:2106.02963 [astro-ph.CO].

[317] J. E. Gonzalez, M. Benetti, R. von Marttens, and J. Alcaniz, Testing the consistency between cosmological data: the impact of spatial curvature and the dark energy EoS, JCAP **11** (11), 060, arXiv:2104.13455 [astro-ph.CO].

[318] O. Akarsu, E. Di Valentino, S. Kumar, M. Ozyigit, and S. Sharma, Testing spatial curvature and anisotropic expansion on top of the ΛCDM model, Phys. Dark Univ. **39**, 101162 (2023), arXiv:2112.07807 [astro-ph.CO].

[319] S. Cao and B. Ratra, Using lower redshift, non-CMB, data to constrain the Hubble constant and other cosmological parameters, Mon. Not. Roy. Astron. Soc. **513**, 5686 (2022), arXiv:2203.10825 [astro-ph.CO].

[320] A. Glanville, C. Howlett, and T. M. Davis, Full-shape galaxy power spectra and the curvature tension, Mon. Not. Roy. Astron. Soc. **517**, 3087 (2022), arXiv:2205.05892 [astro-ph.CO].

[321] J. Bel, J. Larena, R. Maartens, C. Marinoni, and L. Perenon, Constraining spatial curvature with large-scale structure, JCAP **09**, 076, arXiv:2206.03059 [astro-ph.CO].

[322] W. Yang, W. Giarè, S. Pan, E. Di Valentino, A. Melchiorri, and J. Silk, Revealing the effects of curvature on the cosmological models, Phys. Rev. D **107**, 063509 (2023), arXiv:2210.09865 [astro-ph.CO].

[323] J. Stevens, H. Khoraminezhad, and S. Saito, Constraining the spatial curvature with cosmic expansion history in a cosmological model with a non-standard sound horizon, JCAP **07**, 046, arXiv:2212.09804 [astro-ph.CO].

[324] A. Favale, A. Gómez-Valent, and M. Migliaccio, Cosmic chronometers to calibrate the ladders and measure the curvature of the Universe. A model-independent study, Mon. Not. Roy. Astron. Soc. **523**, 3406 (2023), arXiv:2301.09591 [astro-ph.CO].

[325] W. Giarè, E. Di Valentino, and A. Melchiorri, Measuring the reionization optical depth without large-scale CMB polarization, Phys. Rev. D **109**, 103519 (2024), arXiv:2312.06482 [astro-ph.CO].

[326] M. Ishak, Testing General Relativity in Cosmology, Living Rev. Rel. **22**, 1 (2019), arXiv:1806.10122 [astro-ph.CO].

[327] L. Heisenberg, A systematic approach to generalisations of General Relativity and their cosmological implications, Phys. Rept. **796**, 1 (2019), arXiv:1807.01725 [gr-qc].

[328] Y. Akrami *et al.* (CANTATA), *Modified Gravity and Cosmology. An Update by the CANTATA Network*, edited by E. N. Saridakis, R. Lazkoz, V. Salzano, P. Vargas Moniz, S. Capozziello, J. Beltrán Jiménez, M. De Laurentis, and G. J. Olmo (Springer, 2021) arXiv:2105.12582 [gr-qc].

[329] S. Nojiri, S. D. Odintsov, and V. K. Oikonomou, Modified Gravity Theories on a Nutshell: Inflation, Bounce and Late-time Evolution, Phys. Rept. **692**, 1 (2017), arXiv:1705.11098 [gr-qc].

[330] P. Zhang, M. Liguori, R. Bean, and S. Dodelson, Probing Gravity at Cosmological Scales by

Measurements which Test the Relationship between Gravitational Lensing and Matter Overdensity, Phys. Rev. Lett. **99**, 141302 (2007), arXiv:0704.1932 [astro-ph].

[331] L. Amendola, M. Kunz, and D. Sapone, Measuring the dark side (with weak lensing), JCAP **04**, 013, arXiv:0704.2421 [astro-ph].

[332] E. Di Valentino, A. Melchiorri, and J. Silk, Cosmological hints of modified gravity?, Phys. Rev. D **93**, 023513 (2016), arXiv:1509.07501 [astro-ph.CO].

[333] P. A. R. Ade *et al.* (Planck), Planck 2015 results. XIV. Dark energy and modified gravity, Astron. Astrophys. **594**, A14 (2016), arXiv:1502.01590 [astro-ph.CO].

[334] U. Andrade, A. a. J. S. Capistrano, E. Di Valentino, and R. C. Nunes, Exploring modified gravity: constraints on the μ and Σ parametrization with WMAP, ACT, and SPT, Mon. Not. Roy. Astron. Soc. **529**, 831 (2024), arXiv:2309.15781 [astro-ph.CO].

[335] G. Efstathiou, E. Rosenberg, and V. Poulin, Improved Planck Constraints on Axionlike Early Dark Energy as a Resolution of the Hubble Tension, Phys. Rev. Lett. **132**, 221002 (2024), arXiv:2311.00524 [astro-ph.CO].

[336] A. Chatrchyan, F. Niedermann, V. Poulin, and M. S. Sloth, Confronting Cold New Early Dark Energy and its Equation of State with Updated CMB and Supernovae Data, (2024), arXiv:2408.14537 [astro-ph.CO].

[337] I. J. Allali and A. Notari, Neutrino mass bounds from DESI 2024 are relaxed by Planck PR4 and cosmological supernovae, (2024), arXiv:2406.14554 [astro-ph.CO].

[338] S. Roy Choudhury and T. Okumura, Updated cosmological constraints in extended parameter space with Planck PR4, DESI BAO, and SN: dynamical dark energy, neutrino masses, lensing anomaly, and the Hubble tension, (2024), arXiv:2409.13022 [astro-ph.CO].

[339] M. Ishak *et al.* (DESI), Modified Gravity Constraints from the Full Shape Modeling of Clustering Measurements from DESI 2024, (2024), arXiv:2411.12026 [astro-ph.CO].

[340] A. G. Adame *et al.* (DESI), DESI 2024 VII: Cosmological Constraints from the Full-Shape Modeling of Clustering Measurements, (2024), arXiv:2411.12022 [astro-ph.CO].

[341] R. Caldwell, A. Cooray, and A. Melchiorri, Constraints on a New Post-General Relativity Cosmological Parameter, Phys. Rev. D **76**, 023507 (2007), arXiv:astro-ph/0703375.

[342] W. Hu and I. Sawicki, A Parameterized Post-Friedmann Framework for Modified Gravity, Phys. Rev. D **76**, 104043 (2007), arXiv:0708.1190 [astro-ph].

[343] K. Koyama and R. Maartens, Structure formation in the dgp cosmological model, JCAP **01**, 016, arXiv:astro-ph/0511634.

[344] S. Tsujikawa, Matter density perturbations and effective gravitational constant in modified gravity models of dark energy, Phys. Rev. D **76**, 023514 (2007), arXiv:0705.1032 [astro-ph].

[345] C. Bonvin and L. Pogosian, Modified Einstein versus modified Euler for dark matter, Nature Astron. **7**, 1127 (2023), arXiv:2209.03614 [astro-ph.CO].

[346] S. Tsujikawa, R. Gannouji, B. Moraes, and D. Polarski, The dispersion of growth of matter perturbations in f(R) gravity, Phys. Rev. D **80**, 084044 (2009), arXiv:0908.2669 [astro-ph.CO].

[347] R. Gannouji, B. Moraes, and D. Polarski, The growth of matter perturbations in f(R) models, JCAP **02**, 034, arXiv:0809.3374 [astro-ph].

[348] A. Gelman and D. B. Rubin, Inference from Iterative Simulation Using Multiple Sequences, Statist. Sci. **7**, 457 (1992).

[349] A. Lewis, GetDist: a Python package for analysing Monte Carlo samples, JCAP **08**, 025,

arXiv:1910.13970 [astro-ph.IM].

[350] L. Pogosian, M. Raveri, K. Koyama, M. Martinelli, A. Silvestri, G.-B. Zhao, J. Li, S. Peirone, and A. Zucca, Imprints of cosmological tensions in reconstructed gravity, Nature Astron. **6**, 1484 (2022), arXiv:2107.12992 [astro-ph.CO].

[351] H. T. Jense, M. Viña, E. Calabrese, and J. C. Hill, Choice of Planck CMB likelihood in cosmological analyses, Phys. Rev. D **113**, 043551 (2026), arXiv:2510.09430 [astro-ph.CO].

[352] E. Di Valentino, S. Gariazzo, and O. Mena, Neutrinos in Cosmology, (2024), arXiv:2404.19322 [astro-ph.CO].

[353] W. Hu, D. J. Eisenstein, and M. Tegmark, Weighing neutrinos with galaxy surveys, Phys. Rev. Lett. **80**, 5255 (1998), arXiv:astro-ph/9712057.

[354] D. Green and J. Meyers, Cosmological preference for a negative neutrino mass, Phys. Rev. D **111**, 083507 (2025), arXiv:2407.07878 [astro-ph.CO].

[355] D. Naredo-Tuero, M. Escudero, E. Fernández-Martínez, X. Marcano, and V. Poulin, Critical look at the cosmological neutrino mass bound, Phys. Rev. D **110**, 123537 (2024), arXiv:2407.13831 [astro-ph.CO].

[356] Z. Lu and T. Simon, A new multiprobe analysis of modified gravity and evolving dark energy, (2025), arXiv:2511.10616 [astro-ph.CO].

[357] P. F. de Salas, D. V. Forero, S. Gariazzo, P. Martínez-Miravé, O. Mena, C. A. Ternes, M. Tórtola, and J. W. F. Valle, 2020 global reassessment of the neutrino oscillation picture, JHEP **02**, 071, arXiv:2006.11237 [hep-ph].

[358] I. Esteban, M. C. Gonzalez-Garcia, M. Maltoni, I. Martinez-Soler, J. P. Pinheiro, and T. Schwetz, NuFit-6.0: updated global analysis of three-flavor neutrino oscillations, JHEP **12**, 216, arXiv:2410.05380 [hep-ph].

[359] F. Capozzi, W. Giarè, E. Lisi, A. Marrone, A. Melchiorri, and A. Palazzo, Neutrino masses and mixing: Entering the era of subpercent precision, Phys. Rev. D **111**, 093006 (2025), arXiv:2503.07752 [hep-ph].

[360] S. Weinberg, Baryon and Lepton Nonconserving Processes, Phys. Rev. Lett. **43**, 1566 (1979).

[361] P. Minkowski, $\mu \to e\gamma$ at a Rate of One Out of 10^9 Muon Decays?, Phys. Lett. B **67**, 421 (1977).

[362] R. N. Mohapatra and G. Senjanovic, Neutrino Mass and Spontaneous Parity Nonconservation, Phys. Rev. Lett. **44**, 912 (1980).

[363] M. Gell-Mann, P. Ramond, and R. Slansky, Complex Spinors and Unified Theories, Conf. Proc. C **790927**, 315 (1979), arXiv:1306.4669 [hep-th].

[364] S. F. King, Right-handed neutrinos: seesaw models and signatures (2025) arXiv:2502.07877 [hep-ph].

[365] K. Abe *et al.* (T2K), Measurements of neutrino oscillation parameters from the T2K experiment using 3.6×10^{21} protons on target, Eur. Phys. J. C **83**, 782 (2023), arXiv:2303.03222 [hep-ex].

[366] M. A. Acero *et al.* (NOvA), Improved measurement of neutrino oscillation parameters by the NOvA experiment, Phys. Rev. D **106**, 032004 (2022), arXiv:2108.08219 [hep-ex].

[367] F. An *et al.* (JUNO), Neutrino Physics with JUNO, J. Phys. G **43**, 030401 (2016), arXiv:1507.05613 [physics.ins-det].

[368] K. Abe *et al.* (Hyper-Kamiokande), Hyper-Kamiokande Design Report, (2018), arXiv:1805.04163 [physics.ins-det].

[369] B. Abi *et al.* (DUNE), Deep Underground Neutrino Experiment (DUNE), Far Detector Technical

Design Report, Volume II: DUNE Physics, (2020), arXiv:2002.03005 [hep-ex].

[370] S. Gariazzo, M. Archidiacono, P. F. de Salas, O. Mena, C. A. Ternes, and M. Tórtola, Neutrino masses and their ordering: Global Data, Priors and Models, JCAP **03**, 011, arXiv:1801.04946 [hep-ph].

[371] M. Aker *et al.* (KATRIN), Direct neutrino-mass measurement based on 259 days of KATRIN data, Science **388**, adq9592 (2025), arXiv:2406.13516 [nucl-ex].

[372] W. Elbers *et al.* (DESI), Constraints on Neutrino Physics from DESI DR2 BAO and DR1 Full Shape, (2025), arXiv:2503.14744 [astro-ph.CO].

[373] D. Wang, O. Mena, E. Di Valentino, and S. Gariazzo, Updating neutrino mass constraints with background measurements, Phys. Rev. D **110**, 103536 (2024), arXiv:2405.03368 [astro-ph.CO].

[374] J.-Q. Jiang, W. Giarè, S. Gariazzo, M. G. Dainotti, E. Di Valentino, O. Mena, D. Pedrotti, S. S. da Costa, and S. Vagnozzi, Neutrino cosmology after DESI: tightest mass upper limits, preference for the normal ordering, and tension with terrestrial observations, JCAP **01**, 153, arXiv:2407.18047 [astro-ph.CO].

[375] M. Loverde and Z. J. Weiner, Massive neutrinos and cosmic composition, JCAP **12**, 048, arXiv:2410.00090 [astro-ph.CO].

[376] N. Craig, D. Green, J. Meyers, and S. Rajendran, No νs is Good News, JHEP **09**, 097, arXiv:2405.00836 [astro-ph.CO].

[377] W. Elbers, C. S. Frenk, A. Jenkins, B. Li, and S. Pascoli, Negative neutrino masses as a mirage of dark energy, Phys. Rev. D **111**, 063534 (2025), arXiv:2407.10965 [astro-ph.CO].

[378] E. Ó. Colgáin and M. M. Sheikh-Jabbari, DESI and SNe: Dynamical Dark Energy, Ω_m Tension or Systematics?, (2024), arXiv:2412.12905 [astro-ph.CO].

[379] G. P. Lynch and L. Knox, What's the matter with Σm_ν?, (2025), arXiv:2503.14470 [astro-ph.CO].

[380] N. Sailer, G. S. Farren, S. Ferraro, and M. White, Dispuτable: the high cost of a low optical depth, (2025), arXiv:2504.16932 [astro-ph.CO].

[381] T. Jhaveri, T. Karwal, and W. Hu, Turning a negative neutrino mass into a positive optical depth, (2025), arXiv:2504.21813 [astro-ph.CO].

[382] G. Gu *et al.* (DESI), Dynamical Dark Energy in light of the DESI DR2 Baryonic Acoustic Oscillations Measurements, (2025), arXiv:2504.06118 [astro-ph.CO].

[383] B. R. Dinda, A new diagnostic for the null test of dynamical dark energy in light of DESI 2024 and other BAO data, JCAP **09**, 062, arXiv:2405.06618 [astro-ph.CO].

[384] M. Najafi, S. Pan, E. Di Valentino, and J. T. Firouzjaee, Dynamical dark energy confronted with multiple CMB missions, Phys. Dark Univ. **45**, 101539 (2024), arXiv:2407.14939 [astro-ph.CO].

[385] C.-G. Park, J. de Cruz Pérez, and B. Ratra, Using non-DESI data to confirm and strengthen the DESI 2024 spatially flat w0waCDM cosmological parametrization result, Phys. Rev. D **110**, 123533 (2024), arXiv:2405.00502 [astro-ph.CO].

[386] M. Malekjani, Z. Davari, and S. Pourojaghi (DESI), Cosmological constraints on dark energy parametrizations after DESI 2024: Persistent deviation from standard ΛCDM cosmology, Phys. Rev. D **111**, 083547 (2025), arXiv:2407.09767 [astro-ph.CO].

[387] J. Rebouças, D. H. F. de Souza, K. Zhong, V. Miranda, and R. Rosenfeld, Investigating late-time dark energy and massive neutrinos in light of DESI Y1 BAO, JCAP **02**, 024, arXiv:2408.14628 [astro-ph.CO].

[388] T.-N. Li, Y.-H. Li, G.-H. Du, P.-J. Wu, L. Feng, J.-F. Zhang, and X. Zhang, Revisiting holographic dark energy after DESI 2024, Eur. Phys. J. C **85**, 608 (2025), arXiv:2411.08639 [astro-ph.CO].

[389] J.-X. Li and S. Wang, A comprehensive numerical study on four categories of holographic dark energy models, (2024), arXiv:2412.09064 [astro-ph.CO].

[390] A. Notari, M. Redi, and A. Tesi, BAO vs. SN evidence for evolving dark energy, JCAP **04**, 048, arXiv:2411.11685 [astro-ph.CO].

[391] Q. Gao, Z. Peng, S. Gao, and Y. Gong, On the Evidence of Dynamical Dark Energy, Universe **11**, 10 (2025), arXiv:2411.16046 [astro-ph.CO].

[392] R. Fikri, E. ElKhateeb, E. S. Lashin, and W. El Hanafy, A preference for dynamical phantom dark energy using one-parameter model with Planck, DESI DR1 BAO and SN data, (2024), arXiv:2411.19362 [astro-ph.CO].

[393] J. Zheng, D.-C. Qiang, and Z.-Q. You, Cosmological constraints on dark energy models using DESI BAO 2024, (2024), arXiv:2412.04830 [astro-ph.CO].

[394] A. Gómez-Valent and J. Solà Peracaula, Composite dark energy and the cosmological tensions, Phys. Lett. B **864**, 139391 (2025), arXiv:2412.15124 [astro-ph.CO].

[395] A. Lewis and E. Chamberlain, Understanding acoustic scale observations: the one-sided fight against Λ, JCAP **05**, 065, arXiv:2412.13894 [astro-ph.CO].

[396] W. J. Wolf, C. García-García, and P. G. Ferreira, Robustness of dark energy phenomenology across different parameterizations, JCAP **05**, 034, arXiv:2502.04929 [astro-ph.CO].

[397] A. J. Shajib and J. A. Frieman, Evolving dark energy models: Current and forecast constraints, (2025), arXiv:2502.06929 [astro-ph.CO].

[398] W. Giarè, T. Mahassen, E. Di Valentino, and S. Pan, An overview of what current data can (and cannot yet) say about evolving dark energy, Phys. Dark Univ. **48**, 101906 (2025), arXiv:2502.10264 [astro-ph.CO].

[399] E. Chaussidon *et al.*, Early time solution as an alternative to the late time evolving dark energy with DESI DR2 BAO, (2025), arXiv:2503.24343 [astro-ph.CO].

[400] D. A. Kessler, L. A. Escamilla, S. Pan, and E. Di Valentino, One-parameter dynamical dark energy: Hints for oscillations, (2025), arXiv:2504.00776 [astro-ph.CO].

[401] Y.-H. Pang, X. Zhang, and Q.-G. Huang, The impact of the Hubble tension on the evidence for dynamical dark energy, Sci. China Phys. Mech. Astron. **68**, 280410 (2025), arXiv:2503.21600 [astro-ph.CO].

[402] S. Roy Choudhury, Cosmology in Extended Parameter Space with DESI Data Release 2 Baryon Acoustic Oscillations: A 2+ Detection of Nonzero Neutrino Masses with an Update on Dynamical Dark Energy and Lensing Anomaly, Astrophys. J. Lett. **986**, L31 (2025), arXiv:2504.15340 [astro-ph.CO].

[403] M. Scherer, M. A. Sabogal, R. C. Nunes, and A. De Felice, Challenging ΛCDM: 5σ Evidence for a Dynamical Dark Energy Late-Time Transition, (2025), arXiv:2504.20664 [astro-ph.CO].

[404] E. M. Teixeira, W. Giarè, N. B. Hogg, T. Montandon, A. Poudou, and V. Poulin, Implications of distance duality violation for the H_0 tension and evolving dark energy, (2025), arXiv:2504.10464 [astro-ph.CO].

[405] H. Cheng, E. Di Valentino, L. A. Escamilla, A. A. Sen, and L. Visinelli, Pressure Parametrization of Dark Energy: First and Second-Order Constraints with Latest Cosmological Data, (2025),

arXiv:2505.02932 [astro-ph.CO].

[406] H. Cheng, E. Di Valentino, and L. Visinelli, Cosmic Strings as Dynamical Dark Energy: Novel Constraints, (2025), arXiv:2505.22066 [astro-ph.CO].

[407] E. Özülker, E. Di Valentino, and W. Giarè, Dark Energy Crosses the Line: Quantifying and Testing the Evidence for Phantom Crossing, (2025), arXiv:2506.19053 [astro-ph.CO].

[408] I. D. Gialamas, G. Hütsi, M. Raidal, J. Urrutia, M. Vasar, and H. Veermäe, Quintessence and phantoms in light of DESI 2025, (2025), arXiv:2506.21542 [astro-ph.CO].

[409] E. Fazzari, W. Giarè, and E. Di Valentino, Cosmographic Footprints of Dynamical Dark Energy, (2025), arXiv:2509.16196 [astro-ph.CO].

[410] M. Chevallier and D. Polarski, Accelerating universes with scaling dark matter, Int. J. Mod. Phys. D **10**, 213 (2001), arXiv:gr-qc/0009008.

[411] A. Cuoco, J. Lesgourgues, G. Mangano, and S. Pastor, Do observations prove that cosmological neutrinos are thermally distributed?, Phys. Rev. D **71**, 123501 (2005), arXiv:astro-ph/0502465.

[412] Y. Farzan and S. Hannestad, Neutrinos secretly converting to lighter particles to please both KATRIN and the cosmos, JCAP **02**, 058, arXiv:1510.02201 [hep-ph].

[413] G. Dvali and L. Funcke, Small neutrino masses from gravitational θ-term, Phys. Rev. D **93**, 113002 (2016), arXiv:1602.03191 [hep-ph].

[414] N. Bellomo, E. Bellini, B. Hu, R. Jimenez, C. Pena-Garay, and L. Verde, Hiding neutrino mass in modified gravity cosmologies, JCAP **02**, 043, arXiv:1612.02598 [astro-ph.CO].

[415] M. Lattanzi and M. Gerbino, Status of neutrino properties and future prospects - Cosmological and astrophysical constraints, Front. in Phys. **5**, 70 (2018), arXiv:1712.07109 [astro-ph.CO].

[416] C. S. Lorenz, L. Funcke, E. Calabrese, and S. Hannestad, Time-varying neutrino mass from a supercooled phase transition: current cosmological constraints and impact on the Ω_m-σ_8 plane, Phys. Rev. D **99**, 023501 (2019), arXiv:1811.01991 [astro-ph.CO].

[417] C. D. Kreisch, F.-Y. Cyr-Racine, and O. Doré, Neutrino puzzle: Anomalies, interactions, and cosmological tensions, Phys. Rev. D **101**, 123505 (2020), arXiv:1902.00534 [astro-ph.CO].

[418] I. M. Oldengott, G. Barenboim, S. Kahlen, J. Salvado, and D. J. Schwarz, How to relax the cosmological neutrino mass bound, JCAP **04**, 049, arXiv:1901.04352 [astro-ph.CO].

[419] Z. Chacko, A. Dev, P. Du, V. Poulin, and Y. Tsai, Cosmological Limits on the Neutrino Mass and Lifetime, JHEP **04**, 020, arXiv:1909.05275 [hep-ph].

[420] S. Roy Choudhury and S. Choubey, Updated Bounds on Sum of Neutrino Masses in Various Cosmological Scenarios, JCAP **09**, 017, arXiv:1806.10832 [astro-ph.CO].

[421] S. Roy Choudhury and A. Naskar, Strong Bounds on Sum of Neutrino Masses in a 12 Parameter Extended Scenario with Non-Phantom Dynamical Dark Energy ($w(z) \geq -1$) with CPL parameterization, Eur. Phys. J. C **79**, 262 (2019), arXiv:1807.02860 [astro-ph.CO].

[422] S. Roy Choudhury and S. Hannestad, Updated results on neutrino mass and mass hierarchy from cosmology with Planck 2018 likelihoods, JCAP **07**, 037, arXiv:1907.12598 [astro-ph.CO].

[423] Z. Chacko, A. Dev, P. Du, V. Poulin, and Y. Tsai, Determining the Neutrino Lifetime from Cosmology, Phys. Rev. D **103**, 043519 (2021), arXiv:2002.08401 [astro-ph.CO].

[424] M. Escudero, J. Lopez-Pavon, N. Rius, and S. Sandner, Relaxing Cosmological Neutrino Mass Bounds with Unstable Neutrinos, JHEP **12**, 119, arXiv:2007.04994 [hep-ph].

[425] I. Esteban and J. Salvado, Long Range Interactions in Cosmology: Implications for Neutrinos, JCAP **05**, 036, arXiv:2101.05804 [hep-ph].

[426] I. Esteban, O. Mena, and J. Salvado, Nonstandard neutrino cosmology dilutes the lensing anomaly, Phys. Rev. D **106**, 083516 (2022), arXiv:2202.04656 [astro-ph.CO].

[427] G. Franco Abellán, Z. Chacko, A. Dev, P. Du, V. Poulin, and Y. Tsai, Improved cosmological constraints on the neutrino mass and lifetime, JHEP **08**, 076, arXiv:2112.13862 [hep-ph].

[428] G. Dvali, L. Funcke, and T. Vachaspati, Time- and Space-Varying Neutrino Mass Matrix from Soft Topological Defects, Phys. Rev. Lett. **130**, 091601 (2023), arXiv:2112.02107 [hep-ph].

[429] J. Alvey, M. Escudero, N. Sabti, and T. Schwetz, Cosmic neutrino background detection in large-neutrino-mass cosmologies, Phys. Rev. D **105**, 063501 (2022), arXiv:2111.14870 [hep-ph].

[430] J. Alvey, M. Escudero, and N. Sabti, What can CMB observations tell us about the neutrino distribution function?, JCAP **02** (02), 037, arXiv:2111.12726 [astro-ph.CO].

[431] C. S. Lorenz, L. Funcke, M. Löffler, and E. Calabrese, Reconstruction of the neutrino mass as a function of redshift, Phys. Rev. D **104**, 123518 (2021), arXiv:2102.13618 [astro-ph.CO].

[432] F. D'Eramo, E. Di Valentino, W. Giarè, F. Hajkarim, A. Melchiorri, O. Mena, F. Renzi, and S. Yun, Cosmological bound on the QCD axion mass, redux, JCAP **09**, 022, arXiv:2205.07849 [astro-ph.CO].

[433] M. Escudero, T. Schwetz, and J. Terol-Calvo, A seesaw model for large neutrino masses in concordance with cosmology, JHEP **02**, 142, [Addendum: JHEP 06, 119 (2024)], arXiv:2211.01729 [hep-ph].

[434] M. Sen and A. Y. Smirnov, Refractive neutrino masses, ultralight dark matter and cosmology, JCAP **01**, 040, arXiv:2306.15718 [hep-ph].

[435] W. Giarè, A. Gómez-Valent, E. Di Valentino, and C. van de Bruck, Hints of neutrino dark matter scattering in the CMB? Constraints from the marginalized and profile distributions, Phys. Rev. D **109**, 063516 (2024), arXiv:2311.09116 [astro-ph.CO].

[436] P. Brax, C. van de Bruck, E. Di Valentino, W. Giarè, and S. Trojanowski, New insights on ν–DM interactions, Mon. Not. Roy. Astron. Soc. **527**, L122 (2023), arXiv:2303.16895 [astro-ph.CO].

[437] P. Brax, C. van de Bruck, E. Di Valentino, W. Giarè, and S. Trojanowski, Extended analysis of neutrino-dark matter interactions with small-scale CMB experiments, Phys. Dark Univ. **42**, 101321 (2023), arXiv:2305.01383 [astro-ph.CO].

[438] I. J. Allali, D. Aloni, and N. Schöneberg, Cosmological probes of Dark Radiation from Neutrino Mixing, JCAP **09**, 019, arXiv:2404.16822 [astro-ph.CO].

[439] S. Trojanowski and L. Zu, Cosmological impact of νDM interactions enhanced in narrow redshift ranges, (2025), arXiv:2505.20396 [astro-ph.CO].

[440] C. Benso, T. Schwetz, and D. Vatsyayan, Large neutrino mass in cosmology and keV sterile neutrino dark matter from a dark sector, JCAP **04**, 054, arXiv:2410.23926 [hep-ph].

[441] L. Zu, W. Giarè, C. Zhang, E. Di Valentino, Y.-L. S. Tsai, and S. Trojanowski, Can νDM interactions solve the S_8 discrepancy?, (2025), arXiv:2501.13785 [astro-ph.CO].

[442] A. Poudou, T. Simon, T. Montandon, E. M. Teixeira, and V. Poulin, Self-interacting neutrinos in light of recent CMB and LSS data, (2025), arXiv:2503.10485 [astro-ph.CO].

[443] A. Das, P. S. B. Dev, C. Gao, S. Ghosh, and T. Kim, Impostor Among νs: Dark Radiation Masquerading as Self-Interacting Neutrinos, (2025), arXiv:2506.08085 [hep-ph].

[444] E. V. Linder, Cosmic Growth and Expansion Conjoined, Astropart. Phys. **86**, 41 (2017), arXiv:1610.05321 [astro-ph.CO].

[445] G. R. Dvali, G. Gabadadze, and M. Porrati, 4-D gravity on a brane in 5-D Minkowski space,

Phys. Lett. B **485**, 208 (2000), arXiv:hep-th/0005016.

[446] F. Bernardeau, S. Colombi, E. Gaztanaga, and R. Scoccimarro, Large scale structure of the universe and cosmological perturbation theory, Phys. Rept. **367**, 1 (2002), arXiv:astro-ph/0112551.

[447] A. Kiakotou, O. Elgaroy, and O. Lahav, Neutrino Mass, Dark Energy, and the Linear Growth Factor, Phys. Rev. D **77**, 063005 (2008), arXiv:0709.0253 [astro-ph].

[448] W. Giarè, O. Mena, and E. Di Valentino, Lensing impact on cosmic relics and tensions, Phys. Rev. D **108**, 103539 (2023), arXiv:2307.14204 [astro-ph.CO].

[449] E. Di Valentino, S. Gariazzo, W. Giarè, and O. Mena, Impact of the damping tail on neutrino mass constraints, Phys. Rev. D **108**, 083509 (2023), arXiv:2305.12989 [astro-ph.CO].

[450] M. Kaplinghat, L. Knox, and Y.-S. Song, Determining neutrino mass from the CMB alone, Phys. Rev. Lett. **91**, 241301 (2003), arXiv:astro-ph/0303344.

[451] J. Lesgourgues, L. Perotto, S. Pastor, and M. Piat, Probing neutrino masses with cmb lensing extraction, Phys. Rev. D **73**, 045021 (2006), arXiv:astro-ph/0511735.

[452] Y. Akrami *et al.* (Planck), Planck 2018 results. IV. Diffuse component separation, Astron. Astrophys. **641**, A4 (2020), arXiv:1807.06208 [astro-ph.CO].

[453] G. Domènech, X. Chen, M. Kamionkowski, and A. Loeb, Planck residuals anomaly as a fingerprint of alternative scenarios to inflation, JCAP **10**, 005, arXiv:2005.08998 [astro-ph.CO].

[454] F. Capozzi, E. Di Valentino, E. Lisi, A. Marrone, A. Melchiorri, and A. Palazzo, Global constraints on absolute neutrino masses and their ordering, Phys. Rev. D **95**, 096014 (2017), [Addendum: Phys.Rev.D 101, 116013 (2020)], arXiv:2003.08511 [hep-ph].

[455] E. Di Valentino and A. Melchiorri, Neutrino Mass Bounds in the Era of Tension Cosmology, Astrophys. J. Lett. **931**, L18 (2022), arXiv:2112.02993 [astro-ph.CO].

[456] F. Capozzi, E. Di Valentino, E. Lisi, A. Marrone, A. Melchiorri, and A. Palazzo, Unfinished fabric of the three neutrino paradigm, Phys. Rev. D **104**, 083031 (2021), arXiv:2107.00532 [hep-ph].

[457] M. Ishak *et al.*, Modified Gravity Constraints from the Full Shape Modeling of Clustering Measurements from DESI 2024, (2024), arXiv:2411.12026 [astro-ph.CO].

[458] U. Andrade *et al.* (DESI), Validation of the DESI DR2 Measurements of Baryon Acoustic Oscillations from Galaxies and Quasars, (2025), arXiv:2503.14742 [astro-ph.CO].

[459] M. Abdul Karim *et al.* (DESI), DESI DR2 Results I: Baryon Acoustic Oscillations from the Lyman Alpha Forest, (2025), arXiv:2503.14739 [astro-ph.CO].

[460] D. Rubin *et al.*, Union Through UNITY: Cosmology with 2,000 SNe Using a Unified Bayesian Framework, (2023), arXiv:2311.12098 [astro-ph.CO].

[461] M. Vincenzi *et al.* (DES), Comparing the DES-SN5YR and Pantheon+ SN cosmology analyses: Investigation based on "Evolving Dark Energy or Supernovae systematics?", (2025), arXiv:2501.06664 [astro-ph.CO].

[462] E. Di Valentino and S. Bridle, Exploring the Tension between Current Cosmic Microwave Background and Cosmic Shear Data, Symmetry **10**, 585 (2018).

[463] L. F. Secco *et al.* (DES), Dark Energy Survey Year 3 results: Cosmology from cosmic shear and robustness to modeling uncertainty, Phys. Rev. D **105**, 023515 (2022), arXiv:2105.13544 [astro-ph.CO].

[464] M. Asgari *et al.*, KiDS+VIKING-450 and DES-Y1 combined: Mitigating baryon feedback uncertainty with COSEBIs, Astron. Astrophys. **634**, A127 (2020), arXiv:1910.05336 [astro-ph.CO].

[465] S. Joudaki *et al.*, KiDS+VIKING-450 and DES-Y1 combined: Cosmology with cosmic shear, Astron. Astrophys. **638**, L1 (2020), arXiv:1906.09262 [astro-ph.CO].

[466] G. D'Amico, J. Gleyzes, N. Kokron, K. Markovic, L. Senatore, P. Zhang, F. Beutler, and H. Gil-Marín, The Cosmological Analysis of the SDSS/BOSS data from the Effective Field Theory of Large-Scale Structure, JCAP **05**, 005, arXiv:1909.05271 [astro-ph.CO].

[467] T. Tröster *et al.*, Cosmology from large-scale structure: Constraining ΛCDM with BOSS, Astron. Astrophys. **633**, L10 (2020), arXiv:1909.11006 [astro-ph.CO].

[468] S. Chen *et al.*, Analysis of DESI×DES using the Lagrangian effective theory of LSS, Phys. Rev. D **110**, 103518 (2024), arXiv:2407.04795 [astro-ph.CO].

[469] J. Kim *et al.* (ACT, DESI), The Atacama Cosmology Telescope DR6 and DESI: Structure formation over cosmic time with a measurement of the cross-correlation of CMB Lensing and Luminous Red Galaxies, (2024), arXiv:2407.04606 [astro-ph.CO].

[470] L. Faga *et al.* (DES), Dark energy survey year 3 results: cosmology from galaxy clustering and galaxy–galaxy lensing in harmonic space, Mon. Not. Roy. Astron. Soc. **536**, 1586 (2024), arXiv:2406.12675 [astro-ph.CO].

[471] A. Dvornik *et al.*, KiDS-1000: Combined halo-model cosmology constraints from galaxy abundance, galaxy clustering and galaxy-galaxy lensing, Astron. Astrophys. **675**, A189 (2023), [Erratum: Astron.Astrophys. 688, C3 (2024)], arXiv:2210.03110 [astro-ph.CO].

[472] A. H. Wright *et al.*, KiDS-Legacy: Cosmological constraints from cosmic shear with the complete Kilo-Degree Survey, (2025), arXiv:2503.19441 [astro-ph.CO].

[473] S. Tsujikawa, Quintessence: A Review, Class. Quant. Grav. **30**, 214003 (2013), arXiv:1304.1961 [gr-qc].

[474] E. Di Valentino, A. Mukherjee, and A. A. Sen, Dark Energy with Phantom Crossing and the H_0 Tension, Entropy **23**, 404 (2021), arXiv:2005.12587 [astro-ph.CO].

[475] S. A. Adil, Ö. Akarsu, E. Di Valentino, R. C. Nunes, E. Özülker, A. A. Sen, and E. Specogna, Omnipotent dark energy: A phenomenological answer to the Hubble tension, Phys. Rev. D **109**, 023527 (2024), arXiv:2306.08046 [astro-ph.CO].

[476] P. J. E. Peebles, Status of the LambdaCDM theory: supporting evidence and anomalies (2024) arXiv:2405.18307 [astro-ph.CO].

[477] E. Di Valentino *et al.*, The CosmoVerse White Paper: Addressing observational tensions in cosmology with systematics and fundamental physics (2025), arXiv:2504.01669 [astro-ph.CO].

[478] E. Di Valentino *et al.*, Snowmass2021 - Letter of interest cosmology intertwined IV: The age of the universe and its curvature, Astropart. Phys. **131**, 102607 (2021), arXiv:2008.11286 [astro-ph.CO].

[479] O. Akarsu, E. O. Colgáin, A. A. Sen, and M. M. Sheikh-Jabbari, ΛCDM Tensions: Localising Missing Physics through Consistency Checks, Universe **10**, 305 (2024), arXiv:2402.04767 [astro-ph.CO].

[480] T. Louis *et al.* (ACT), The Atacama Cosmology Telescope: DR6 Power Spectra, Likelihoods and ΛCDM Parameters (2025), arXiv:2503.14452 [astro-ph.CO].

[481] S. Birrer *et al.*, TDCOSMO - IV. Hierarchical time-delay cosmography – joint inference of the Hubble constant and galaxy density profiles, Astron. Astrophys. **643**, A165 (2020), arXiv:2007.02941 [astro-ph.CO].

[482] Q. Wu, G.-Q. Zhang, and F.-Y. Wang, An 8 per cent determination of the Hubble constant

from localized fast radio bursts, Mon. Not. Roy. Astron. Soc. **515**, L1 (2022), [Erratum: Mon.Not.Roy.Astron.Soc. 531, L8 (2024)], arXiv:2108.00581 [astro-ph.CO].

[483] D. O. Jones *et al.*, Cosmological Results from the RAISIN Survey: Using Type Ia Supernovae in the Near Infrared as a Novel Path to Measure the Dark Energy Equation of State, Astrophys. J. **933**, 172 (2022), arXiv:2201.07801 [astro-ph.CO].

[484] G. S. Anand, R. B. Tully, L. Rizzi, A. G. Riess, and W. Yuan, Comparing Tip of the Red Giant Branch Distance Scales: An Independent Reduction of the Carnegie-Chicago Hubble Program and the Value of the Hubble Constant, Astrophys. J. **932**, 15 (2022), arXiv:2108.00007 [astro-ph.CO].

[485] S. A. Uddin *et al.*, Carnegie Supernova Project I and II: Measurements of H $_0$ Using Cepheid, Tip of the Red Giant Branch, and Surface Brightness Fluctuation Distance Calibration to Type Ia Supernovae*, Astrophys. J. **970**, 72 (2024), arXiv:2308.01875 [astro-ph.CO].

[486] C. D. Huang *et al.*, The Mira Distance to M101 and a 4% Measurement of H $_0$, Astrophys. J. **963**, 83 (2024), arXiv:2312.08423 [astro-ph.CO].

[487] W. L. Freedman, B. F. Madore, T. J. Hoyt, I. S. Jang, A. J. Lee, and K. A. Owens, Status Report on the Chicago-Carnegie Hubble Program (CCHP): Measurement of the Hubble Constant Using the Hubble and James Webb Space Telescopes, Astrophys. J. **985**, 203 (2025), arXiv:2408.06153 [astro-ph.CO].

[488] A. G. Riess *et al.*, JWST Validates HST Distance Measurements: Selection of Supernova Subsample Explains Differences in JWST Estimates of Local H $_0$, Astrophys. J. **977**, 120 (2024), arXiv:2408.11770 [astro-ph.CO].

[489] C. Vogl *et al.*, No rungs attached: A distance-ladder free determination of the Hubble constant through type II supernova spectral modelling (2024), arXiv:2411.04968 [astro-ph.CO].

[490] D. H. Gao, Q. Wu, J. P. Hu, S. X. Yi, X. Zhou, and F. Y. Wang, Measuring Hubble constant using localized and unlocalized fast radio bursts (2024), arXiv:2410.03994 [astro-ph.CO].

[491] D. Scolnic *et al.*, The Hubble Tension in our own Backyard: DESI and the Nearness of the Coma Cluster, (2024), arXiv:2409.14546 [astro-ph.CO].

[492] K. Said *et al.*, DESI Peculiar Velocity Survey – Fundamental Plane (2024), arXiv:2408.13842 [astro-ph.CO].

[493] P. Boubel, M. Colless, K. Said, and L. Staveley-Smith, An improved Tully–Fisher estimate of H0, Mon. Not. Roy. Astron. Soc. **533**, 1550 (2024), arXiv:2408.03660 [astro-ph.CO].

[494] D. Scolnic, P. Boubel, J. Byrne, A. G. Riess, and G. S. Anand, Calibrating the Tully-Fisher Relation to Measure the Hubble Constant (2024), arXiv:2412.08449 [astro-ph.CO].

[495] S. Li, A. G. Riess, D. Scolnic, S. Casertano, and G. S. Anand, JAGB 2.0: Improved Constraints on the J-region Asymptotic Giant Branch-based Hubble Constant from an Expanded Sample of JWST Observations (2025), arXiv:2502.05259 [astro-ph.CO].

[496] J. B. Jensen, J. P. Blakeslee, M. Cantiello, M. Cowles, G. S. Anand, R. B. Tully, E. Kourkchi, and G. Raimondo, The TRGB-SBF Project. III. Refining the HST Surface Brightness Fluctuation Distance Scale Calibration with JWST (2025), arXiv:2502.15935 [astro-ph.CO].

[497] G. Efstathiou, A Lockdown Perspective on the Hubble Tension (with comments from the SH0ES team), (2020), arXiv:2007.10716 [astro-ph.CO].

[498] E. Mortsell, A. Goobar, J. Johansson, and S. Dhawan, Sensitivity of the Hubble Constant Determination to Cepheid Calibration, Astrophys. J. **933**, 212 (2022), arXiv:2105.11461 [astro-

ph.CO].

[499] E. Mortsell, A. Goobar, J. Johansson, and S. Dhawan, The Hubble Tension Revisited: Additional Local Distance Ladder Uncertainties, Astrophys. J. **935**, 58 (2022), arXiv:2106.09400 [astro-ph.CO].

[500] A. Sharon, D. Kushnir, W. Yuan, L. Macri, and A. Riess, Reassessing the constraints from SH0ES extragalactic Cepheid amplitudes on systematic blending bias, Mon. Not. Roy. Astron. Soc. **528**, 6861 (2024), arXiv:2305.14435 [astro-ph.CO].

[501] A. G. Riess, G. S. Anand, W. Yuan, S. Casertano, A. Dolphin, L. M. Macri, L. Breuval, D. Scolnic, M. Perrin, and R. I. Anderson, Crowded No More: The Accuracy of the Hubble Constant Tested with High-resolution Observations of Cepheids by JWST, Astrophys. J. Lett. **956**, L18 (2023), arXiv:2307.15806 [astro-ph.CO].

[502] A. Bhardwaj *et al.*, High-resolution Spectroscopic Metallicities of Milky Way Cepheid Standards and Their Impact on the Leavitt Law and the Hubble Constant, Astrophys. J. Lett. **955**, L13 (2023), arXiv:2309.03263 [astro-ph.SR].

[503] D. Brout and A. Riess, The Impact of Dust on Cepheid and Type Ia Supernova Distances, (2023), arXiv:2311.08253 [astro-ph.CO].

[504] A. M. Dwomoh, E. R. Peterson, D. Scolnic, C. Ashall, J. M. DerKacy, A. Do, J. Johansson, D. O. Jones, A. G. Riess, and B. J. Shappee, Evaluating the Consistency of Cosmological Distances Using Supernova Siblings in the Near-infrared, Astrophys. J. **965**, 90 (2024), arXiv:2311.06178 [astro-ph.CO].

[505] A. G. Riess, G. S. Anand, W. Yuan, S. Casertano, A. Dolphin, L. M. Macri, L. Breuval, D. Scolnic, M. Perrin, and I. R. Anderson, JWST Observations Reject Unrecognized Crowding of Cepheid Photometry as an Explanation for the Hubble Tension at 8σ Confidence, Astrophys. J. Lett. **962**, L17 (2024), arXiv:2401.04773 [astro-ph.CO].

[506] A. R. Khalife, M. B. Zanjani, S. Galli, S. Günther, J. Lesgourgues, and K. Benabed, Review of Hubble tension solutions with new SH0ES and SPT-3G data, JCAP **04**, 059, arXiv:2312.09814 [astro-ph.CO].

[507] N. Sailer *et al.*, Cosmological constraints from the cross-correlation of DESI Luminous Red Galaxies with CMB lensing from Planck PR4 and ACT DR6, (2024), arXiv:2407.04607 [astro-ph.CO].

[508] A. G. Adame *et al.* (DESI), DESI 2024 V: Full-Shape Galaxy Clustering from Galaxies and Quasars (2024), arXiv:2411.12021 [astro-ph.CO].

[509] K. Lodha *et al.* (DESI), Extended Dark Energy analysis using DESI DR2 BAO measurements (2025), arXiv:2503.14743 [astro-ph.CO].

[510] T. M. C. Abbott *et al.* (DES), The Dark Energy Survey: Cosmology Results with ∼1500 New High-redshift Type Ia Supernovae Using the Full 5 yr Data Set, Astrophys. J. Lett. **973**, L14 (2024), arXiv:2401.02929 [astro-ph.CO].

[511] T. M. C. Abbott *et al.* (DES), Dark Energy Survey: implications for cosmological expansion models from the final DES Baryon Acoustic Oscillation and Supernova data (2025), arXiv:2503.06712 [astro-ph.CO].

[512] M. A. C. Alvarez, L. Graef, and R. Brandenberger, Back-Reaction of Super-Hubble Fluctuations, Late Time Tracking and Recent Observational Results (2025), arXiv:2502.17395 [astro-ph.CO].

[513] E. Ozulker, Is the dark energy equation of state parameter singular?, Phys. Rev. D **106**, 063509

(2022), arXiv:2203.04167 [astro-ph.CO].

[514] K. Dutta, Ruchika, A. Roy, A. A. Sen, and M. M. Sheikh-Jabbari, Beyond ΛCDM with low and high redshift data: implications for dark energy, Gen. Rel. Grav. **52**, 15 (2020), arXiv:1808.06623 [astro-ph.CO].

[515] L. Visinelli, S. Vagnozzi, and U. Danielsson, Revisiting a negative cosmological constant from low-redshift data, Symmetry **11**, 1035 (2019), arXiv:1907.07953 [astro-ph.CO].

[516] M. Malekjani, R. M. Conville, E. O. Colgáin, S. Pourojaghi, and M. M. Sheikh-Jabbari, On redshift evolution and negative dark energy density in Pantheon + Supernovae, Eur. Phys. J. C **84**, 317 (2024), arXiv:2301.12725 [astro-ph.CO].

[517] J. A. Vázquez, D. Tamayo, G. Garcia-Arroyo, I. Gómez-Vargas, I. Quiros, and A. A. Sen, Coupled Multi Scalar Field Dark Energy (2023), arXiv:2305.11396 [astro-ph.CO].

[518] S. A. Adil, U. Mukhopadhyay, A. A. Sen, and S. Vagnozzi, Dark energy in light of the early JWST observations: case for a negative cosmological constant?, JCAP **10**, 072, arXiv:2307.12763 [astro-ph.CO].

[519] A. Gómez-Valent, A. Favale, M. Migliaccio, and A. A. Sen, Late-time phenomenology required to solve the H0 tension in view of the cosmic ladders and the anisotropic and angular BAO datasets, Phys. Rev. D **109**, 023525 (2024), arXiv:2309.07795 [astro-ph.CO].

[520] O. Akarsu, S. Kumar, E. Özülker, and J. A. Vazquez, Relaxing cosmological tensions with a sign switching cosmological constant, Phys. Rev. D **104**, 123512 (2021), arXiv:2108.09239 [astro-ph.CO].

[521] O. Akarsu, S. Kumar, E. Özülker, J. A. Vazquez, and A. Yadav, Relaxing cosmological tensions with a sign switching cosmological constant: Improved results with Planck, BAO, and Pantheon data, Phys. Rev. D **108**, 023513 (2023), arXiv:2211.05742 [astro-ph.CO].

[522] O. Akarsu, A. De Felice, E. Di Valentino, S. Kumar, R. C. Nunes, E. Ozulker, J. A. Vazquez, and A. Yadav, Λ_sCDM cosmology from a type-II minimally modified gravity, arXiv e-prints , arXiv:2402.07716 (2024), arXiv:2402.07716 [astro-ph.CO].

[523] O. Akarsu, A. De Felice, E. Di Valentino, S. Kumar, R. C. Nunes, E. Ozulker, J. A. Vazquez, and A. Yadav, Cosmological constraints on Λ_sCDM scenario in a type II minimally modified gravity, (2024), arXiv:2406.07526 [astro-ph.CO].

[524] O. Akarsu, J. D. Barrow, L. A. Escamilla, and J. A. Vazquez, Graduated dark energy: Observational hints of a spontaneous sign switch in the cosmological constant, Phys. Rev. D **101**, 063528 (2020), arXiv:1912.08751 [astro-ph.CO].

[525] O. Akarsu, E. Di Valentino, S. Kumar, R. C. Nunes, J. A. Vazquez, and A. Yadav, Λ_sCDM model: A promising scenario for alleviation of cosmological tensions, (2023), arXiv:2307.10899 [astro-ph.CO].

[526] A. Yadav, S. Kumar, C. Kibris, and O. Akarsu, Λ_sCDM cosmology: Alleviating major cosmological tensions by predicting standard neutrino properties, (2024), arXiv:2406.18496 [astro-ph.CO].

[527] L. A. Anchordoqui, I. Antoniadis, and D. Lust, Anti-de Sitter → de Sitter transition driven by Casimir forces and mitigating tensions in cosmological parameters, Phys. Lett. B **855**, 138775 (2024), arXiv:2312.12352 [hep-th].

[528] N. Menci, S. A. Adil, U. Mukhopadhyay, A. A. Sen, and S. Vagnozzi, Negative cosmological constant in the dark energy sector: tests from JWST photometric and spectroscopic observations

of high-redshift galaxies, JCAP **07**, 072, arXiv:2401.12659 [astro-ph.CO].

[529] L. A. Anchordoqui, I. Antoniadis, D. Lust, N. T. Noble, and J. F. Soriano, From infinite to infinitesimal: Using the Universe as a dataset to probe Casimir corrections to the vacuum energy from fields inhabiting the dark dimension, Phys. Dark Univ. **46**, 101715 (2024), arXiv:2404.17334 [astro-ph.CO].

[530] L. A. Anchordoqui, I. Antoniadis, D. Bielli, A. Chatrabhuti, and H. Isono, Thin-wall vacuum decay in the presence of a compact dimension meets the H_0 and S_8 tensions (2024), arXiv:2410.18649 [hep-th].

[531] J. F. Soriano, S. Wohlberg, and L. A. Anchordoqui, New insights on a sign-switching Λ, Phys. Dark Univ. **48**, 101911 (2025), arXiv:2502.19239 [astro-ph.CO].

[532] A. De Felice, S. Kumar, S. Mukohyama, and R. C. Nunes, Observational bounds on extended minimal theories of massive gravity: new limits on the graviton mass, JCAP **04**, 013, arXiv:2311.10530 [astro-ph.CO].

[533] A. Gomez-Valent and J. Solà Peracaula, Phantom Matter: A Challenging Solution to the Cosmological Tensions, Astrophys. J. **975**, 64 (2024), arXiv:2404.18845 [astro-ph.CO].

[534] L. A. Escamilla, E. Özülker, O. Akarsu, E. Di Valentino, and J. A. Vázquez, Do we need wavelets in the late Universe? (2024), arXiv:2408.12516 [astro-ph.CO].

[535] L. A. Escamilla, O. Akarsu, E. Di Valentino, and J. A. Vazquez, Model-independent reconstruction of the interacting dark energy kernel: Binned and Gaussian process, JCAP **11**, 051, arXiv:2305.16290 [astro-ph.CO].

[536] M. A. Sabogal, O. Akarsu, A. Bonilla, E. Di Valentino, and R. C. Nunes, Exploring new physics in the late Universe's expansion through non-parametric inference, Eur. Phys. J. C **84**, 703 (2024), arXiv:2407.04223 [astro-ph.CO].

[537] O. Akarsu, B. Bulduk, A. De Felice, N. Katırcı, and N. M. Uzun, Unexplored regions in teleparallel $f(T)$ gravity: Sign-changing dark energy density (2024), arXiv:2410.23068 [gr-qc].

[538] O. Akarsu, L. Perivolaropoulos, A. Tsikoundoura, A. E. Yükselci, and A. Zhuk, Dynamical dark energy with AdS-to-dS and dS-to-dS transitions: Implications for the H_0 tension (2025), arXiv:2502.14667 [astro-ph.CO].

[539] A. Bonilla, S. Kumar, and R. C. Nunes, Measurements of H_0 and reconstruction of the dark energy properties from a model-independent joint analysis, Eur. Phys. J. C **81**, 127 (2021), arXiv:2011.07140 [astro-ph.CO].

[540] V. Sahni, A. Shafieloo, and A. A. Starobinsky, Model independent evidence for dark energy evolution from Baryon Acoustic Oscillations, Astrophys. J. Lett. **793**, L40 (2014), arXiv:1406.2209 [astro-ph.CO].

[541] E. Aubourg *et al.*, Cosmological implications of baryon acoustic oscillation measurements, Phys. Rev. D **92**, 123516 (2015), arXiv:1411.1074 [astro-ph.CO].

[542] Y. Wang, L. Pogosian, G.-B. Zhao, and A. Zucca, Evolution of dark energy reconstructed from the latest observations, Astrophys. J. Lett. **869**, L8 (2018), arXiv:1807.03772 [astro-ph.CO].

[543] V. Poulin, K. K. Boddy, S. Bird, and M. Kamionkowski, Implications of an extended dark energy cosmology with massive neutrinos for cosmological tensions, Phys. Rev. D **97**, 123504 (2018), arXiv:1803.02474 [astro-ph.CO].

[544] L. A. Escamilla and J. A. Vazquez, Model selection applied to reconstructions of the Dark Energy, Eur. Phys. J. C **83**, 251 (2023), arXiv:2111.10457 [astro-ph.CO].

[545] A. A. Sen, S. A. Adil, and S. Sen, Do cosmological observations allow a negative Λ?, Mon. Not. Roy. Astron. Soc. **518**, 1098 (2022), arXiv:2112.10641 [astro-ph.CO].

[546] R. Calderón, R. Gannouji, B. L'Huillier, and D. Polarski, Negative cosmological constant in the dark sector?, Phys. Rev. D **103**, 023526 (2021), arXiv:2008.10237 [astro-ph.CO].

[547] O. Akarsu, J. D. Barrow, C. V. R. Board, N. M. Uzun, and J. A. Vazquez, Screening Λ in a new modified gravity model, Eur. Phys. J. C **79**, 846 (2019), arXiv:1903.11519 [gr-qc].

[548] G. Acquaviva, O. Akarsu, N. Katirci, and J. A. Vazquez, Simple-graduated dark energy and spatial curvature, Phys. Rev. D **104**, 023505 (2021), arXiv:2104.02623 [astro-ph.CO].

[549] O. Akarsu, E. O. Colgain, E. Özulker, S. Thakur, and L. Yin, Inevitable manifestation of wiggles in the expansion of the late Universe, Phys. Rev. D **107**, 123526 (2023), arXiv:2207.10609 [astro-ph.CO].

[550] R. R. Caldwell, A Phantom menace?, Phys. Lett. B **545**, 23 (2002), arXiv:astro-ph/9908168.

[551] C. García-García, E. Bellini, P. G. Ferreira, D. Traykova, and M. Zumalacárregui, Theoretical priors in scalar-tensor cosmologies: Thawing quintessence, Phys. Rev. D **101**, 063508 (2020), arXiv:1911.02868 [astro-ph.CO].

[552] W. J. Wolf, C. García-García, D. J. Bartlett, and P. G. Ferreira, Scant evidence for thawing quintessence, Phys. Rev. D **110**, 083528 (2024), arXiv:2408.17318 [astro-ph.CO].

[553] E. V. Linder, Interpreting Dark Energy Data Away from Λ, arXiv e-prints , arXiv:2410.10981 (2024), arXiv:2410.10981 [astro-ph.CO].

[554] R. M. Neal, Taking bigger metropolis steps by dragging fast variables (2005), arXiv:math/0502099 [math.ST].

[555] G. Hinshaw, D. Larson, E. Komatsu, D. N. Spergel, C. L. Bennett, J. Dunkley, M. R. Nolta, M. Halpern, R. S. Hill, N. Odegard, L. Page, K. M. Smith, J. L. Weiland, B. Gold, N. Jarosik, A. Kogut, M. Limon, S. S. Meyer, G. S. Tucker, E. Wollack, and E. L. Wright, Nine-year wilkinson microwave anisotropy probe (wmap) observations: Cosmological parameter results, The Astrophysical Journal Supplement Series **208**, 19 (2013).

[556] D. Collaboration, A. G. Adame, , *et al.*, Desi 2024 iii: Baryon acoustic oscillations from galaxies and quasars (2024), arXiv:2404.03000 [astro-ph.CO].

[557] D. Collaboration, A. G. Adame, *et al.*, Desi 2024 iv: Baryon acoustic oscillations from the lyman alpha forest (2024), arXiv:2404.03001 [astro-ph.CO].

[558] S. Alam *et al.* (eBOSS), Completed SDSS-IV extended Baryon Oscillation Spectroscopic Survey: Cosmological implications from two decades of spectroscopic surveys at the Apache Point Observatory, Phys. Rev. D **103**, 083533 (2021), arXiv:2007.08991 [astro-ph.CO].

[559] W. Handley, fgivenx: Functional posterior plotter, The Journal of Open Source Software **3**, 10.21105/joss.00849 (2018).

[560] Ö. Akarsu, M. Caruana, K. F. Dialektopoulos, L. A. Escamilla, E. O. Kahya, and J. Levi Said, Hints of sign-changing scalar field energy density and a transient acceleration phase at $z \sim 2$ from model-agnostic reconstructions (2026), arXiv:2602.08928 [astro-ph.CO].

[561] W. J. Wolf, C. García-García, T. Anton, and P. G. Ferreira, Assessing Cosmological Evidence for Nonminimal Coupling, Phys. Rev. Lett. **135**, 081001 (2025), arXiv:2504.07679 [astro-ph.CO].

[562] W. J. Wolf, P. G. Ferreira, and C. García-García, Cosmological constraints on Galileon dark energy with broken shift symmetry, Phys. Rev. D **113**, 023551 (2026), arXiv:2509.17586 [astro-ph.CO].

[563] S. A. Franchino-Viñas and S. Mignemi, Asymptotic freedom for $\lambda\phi^4_\star$ QFT in Snyder–de Sitter space, Eur. Phys. J. C **80**, 382 (2020), arXiv:1911.08921 [hep-th].

[564] S. A. Franchino-Viñas and S. Mignemi, The Snyder-de Sitter scalar $\varphi\star 4$ quantum field theory in D=2, Nucl. Phys. B **981**, 115871 (2022), arXiv:2104.00043 [hep-th].

[565] C. Kiefer and T. Vardanyan, Power spectrum for perturbations in an inflationary model for a closed universe, Gen. Rel. Grav. **54**, 30 (2022), arXiv:2111.07835 [gr-qc].

[566] T. Vardanyan and C. Kiefer, Quantum-gravitational corrections to the power spectrum for a closed universe, J. Phys. Conf. Ser. **2533**, 012036 (2023), arXiv:2302.07001 [gr-qc].

[567] G. Efstathiou, Is the low CMB quadrupole a signature of spatial curvature?, Mon. Not. Roy. Astron. Soc. **343**, L95 (2003), arXiv:astro-ph/0303127.

[568] J. Ryan, Y. Chen, and B. Ratra, Baryon acoustic oscillation, Hubble parameter, and angular size measurement constraints on the Hubble constant, dark energy dynamics, and spatial curvature, Mon. Not. Roy. Astron. Soc. **488**, 3844 (2019), arXiv:1902.03196 [astro-ph.CO].

[569] G. Bargiacchi, M. Benetti, S. Capozziello, E. Lusso, G. Risaliti, and M. Signorini, Quasar cosmology: dark energy evolution and spatial curvature, Mon. Not. Roy. Astron. Soc. **515**, 1795 (2022), arXiv:2111.02420 [astro-ph.CO].

[570] L. Zuckerman, E. Zuckerman, and L. A. Anchordoqui, Spatial curvature sensitivity to local H0 from the Cepheid distance ladder, JHEAp **33**, 10 (2022), arXiv:2110.05346 [astro-ph.CO].

[571] E. Di Valentino, W. Giarè, A. Melchiorri, and J. Silk, Quantifying the global 'CMB tension' between the Atacama Cosmology Telescope and the Planck satellite in extended models of cosmology, Mon. Not. Roy. Astron. Soc. **520**, 210 (2023), arXiv:2209.14054 [astro-ph.CO].

[572] Q. Vigneron and V. Poulin, Is expansion blind to the spatial curvature?, Phys. Rev. D **108**, 103518 (2023), arXiv:2212.00675 [gr-qc].

[573] R. Jimenez, A. R. Khalifeh, D. F. Litim, S. Matarrese, and B. D. Wandelt, Why is zero spatial curvature special?, JCAP **09**, 007, arXiv:2210.10102 [astro-ph.CO].

[574] T. Liu, S. Cao, X. Li, H. Zheng, Y. Liu, W. Guo, and C. Zheng, Revising the Hubble constant, spatial curvature and dark energy dynamics with the latest observations of quasars, Astron. Astrophys. **668**, A51 (2022), arXiv:2210.02765 [astro-ph.CO].

[575] N. Banerjee, P. Mukherjee, and D. Pavón, Spatial curvature and thermodynamics, Mon. Not. Roy. Astron. Soc. **521**, 5473 (2023), arXiv:2301.09823 [astro-ph.CO].

[576] K. Zhang, T. Zhou, B. Xu, Q. Huang, and Y. Yuan, Joint Constraints on the Hubble Constant, Spatial Curvature, and Sound Horizon from the Late-time Universe with Cosmography, Astrophys. J. **957**, 5 (2023), arXiv:2310.16512 [astro-ph.CO].

[577] B. Blachier, P. Auclair, C. Ringeval, and V. Vennin, Spatial curvature from super-Hubble cosmological fluctuations, Phys. Rev. D **108**, 123510 (2023), arXiv:2302.14530 [astro-ph.CO].

[578] J.-Z. Qi, P. Meng, J.-F. Zhang, and X. Zhang, Model-independent measurement of cosmic curvature with the latest H(z) and SNe Ia data: A comprehensive investigation, Phys. Rev. D **108**, 063522 (2023), arXiv:2302.08889 [astro-ph.CO].

[579] H. Foidl and T. Rindler-Daller, A ΛCDM Extension Explaining the Hubble Tension and the Spatial Curvature $\Omega_{k,0} = -0.012 \pm 0.010$ Measured by the Final PR4 of the Planck Mission, (2024), arXiv:2412.04126 [astro-ph.CO].

[580] W.-N. Deng and W. Handley, Predicting spatial curvature ΩK in globally CPT-symmetric universes, Phys. Rev. D **110**, 103528 (2024), arXiv:2407.18225 [astro-ph.CO].

[581] E. Jensko, Spatial curvature in coincident gauge f(Q) cosmology, Class. Quant. Grav. **42**, 055011 (2025), arXiv:2407.17568 [gr-qc].

[582] S. Gariazzo, W. Giarè, O. Mena, and E. Di Valentino, How robust are the parameter constraints extending the ΛCDM model?, Phys. Rev. D **111**, 023540 (2025), arXiv:2404.11182 [astro-ph.CO].

[583] S. Sanz-Wuhl, H. Gil-Marín, A. J. Cuesta, and L. Verde, BAO cosmology in non-spatially flat background geometry from BOSS+eBOSS and lessons for future surveys, JCAP **05**, 116, arXiv:2402.03427 [astro-ph.CO].

[584] L. Amendola, M. Marinucci, and M. Quartin, Cosmological Spatial Curvature with the Alcock-Paczyński Effect, Phys. Rev. Lett. **134**, 101004 (2025), arXiv:2404.13124 [astro-ph.CO].

[585] M. Shimon and Y. Rephaeli, Differing Manifestations of Spatial Curvature in Cosmological FRW Models, Universe **11**, 143 (2025), arXiv:2411.00080 [astro-ph.CO].

[586] V. E. Kuzmichev and V. V. Kuzmichev, On the generation of primordial matter by spatial curvature in the early universe, (2025), arXiv:2507.20775 [gr-qc].

[587] W.-N. Deng and W. Handley, CMB Constraints on Quantized Spatial Curvature $_K$ in globally CPT-symmetric universes, (2025), arXiv:2509.10379 [astro-ph.CO].

[588] Y.-Y. Wang, L. Lei, S.-P. Tang, and Y.-Z. Fan, Lensing amplitude anomaly and varying electron mass alleviate the Hubble and S_8 tensions, (2025), arXiv:2508.19081 [astro-ph.CO].

[589] T. Sekiguchi and T. Takahashi, Early recombination as a solution to the H_0 tension, Phys. Rev. D **103**, 083507 (2021), arXiv:2007.03381 [astro-ph.CO].

[590] N. Schöneberg and L. Vacher, The mass effect — variations of the electron mass and their impact on cosmology, JCAP **03**, 004, arXiv:2407.16845 [astro-ph.CO].

[591] Y. Toda, W. Giarè, E. Özülker, E. Di Valentino, and S. Vagnozzi, Combining pre- and post-recombination new physics to address cosmological tensions: Case study with varying electron mass and sign-switching cosmological constant, Phys. Dark Univ. **46**, 101676 (2024), arXiv:2407.01173 [astro-ph.CO].

[592] S. D. Odintsov, S. D'Onofrio, and T. Paul, Generalized entropic dark energy with spatial curvature, Phys. Dark Univ. **48**, 101920 (2025), arXiv:2504.03470 [gr-qc].

[593] Y. Hu and S. Dhawan, Constrain spatial curvature and dark energy with strong lenses and complementary probes: a forecast for next-generation surveys, Mon. Not. Roy. Astron. Soc. **535**, 3211 (2024), arXiv:2411.05082 [astro-ph.CO].

[594] D. H. Lyth and E. D. Stewart, Inflationary density perturbations with Omega < 1, Phys. Lett. B **252**, 336 (1990).

[595] B. Ratra and P. J. E. Peebles, Inflation in an open universe, Phys. Rev. D **52**, 1837 (1995).

[596] J. Asorey and J. de Cruz Pérez, Revisiting CDM extensions in light of re-analyzed CMB data, (2025), arXiv:2506.13537 [astro-ph.CO].

[597] B. Ratra, Inflation in a closed universe, Phys. Rev. D **96**, 103534 (2017), arXiv:1707.03439 [astro-ph.CO].

[598] W. Handley, Primordial power spectra for curved inflating universes, Phys. Rev. D **100**, 123517 (2019), arXiv:1907.08524 [astro-ph.CO].

[599] D.-H. Zhang and C.-Y. Sun, The Exact evolution equation of the curvature perturbation for closed universe, Chin. Phys. Lett. **21**, 1865 (2004), arXiv:astro-ph/0310127.

[600] A. Thavanesan, D. Werth, and W. Handley, Analytical approximations for curved primordial

power spectra, Phys. Rev. D **103**, 023519 (2021), arXiv:2009.05573 [astro-ph.CO].

[601] Q. Vigneron and J. Larena, A natural model for curved inflation, Class. Quant. Grav. **41**, 22LT01 (2024), arXiv:2405.04450 [gr-qc].

[602] L. F. Abbott and R. K. Schaefer, A general, gauge-invariant analysis of the cosmic microwave anisotropy, Astrophys. J. **308**, 546 (1986).

[603] U. H. Gerlach and U. K. Sengupta, Gauge-invariant perturbations on most general spherically symmetric space-times, Phys. Rev. D **18**, 1773 (1978).

[604] C. Wolf, CAN INFLATION TAKE PLACE IN A CLOSED UNIVERSE ADMITTING CREATION, Phys. Scripta **38**, 129 (1988).

[605] C. Wolf, Delayed inflation of a closed cosmological model driven by the false vacuum in five-dimensions, Austral. J. Phys. **43**, 117 (1990).

[606] J. Ponce de Leon, Inflation in a spatially closed anisotropic universe, J. Math. Phys. **31**, 371 (1990).

[607] H. J. Schmidt, Inflation within closed Friedmann universe models, Gen. Rel. Grav. **25**, 87 (1993).

[608] A. D. Linde, Inflation with variable Omega, Phys. Lett. B **351**, 99 (1995), arXiv:hep-th/9503097.

[609] S. A. Pavluchenko, N. Y. Savchenko, and A. V. Toporensky, The Generality of inflation in some closed FRW models with a scalar field, Int. J. Mod. Phys. D **11**, 805 (2002), arXiv:gr-qc/0111077.

[610] G. F. R. Ellis, W. R. Stoeger, S. J., P. McEwan, and P. Dunsby, Dynamics of inflationary universes with positive spatial curvature, Gen. Rel. Grav. **34**, 1445 (2002), arXiv:gr-qc/0109023.

[611] A. D. Linde, Can we have inflation with Omega $>$ 1?, JCAP **05**, 002, arXiv:astro-ph/0303245.

[612] J.-P. Uzan, U. Kirchner, and G. F. R. Ellis, WMAP data and the curvature of space, Mon. Not. Roy. Astron. Soc. **344**, L65 (2003), arXiv:astro-ph/0302597.

[613] S. A. Pavluchenko, Generality of inflation in closed cosmological models with some quintessence potentials, Phys. Rev. D **67**, 103518 (2003), arXiv:astro-ph/0304354.

[614] A. Lasenby and C. Doran, Closed universes, de Sitter space and inflation, Phys. Rev. D **71**, 063502 (2005), arXiv:astro-ph/0307311.

[615] D. R. Green, Reheating Closed String Inflation, Phys. Rev. D **76**, 103504 (2007), arXiv:0707.3832 [hep-th].

[616] M. Cicoli and A. Mazumdar, Reheating for Closed String Inflation, JCAP **09**, 025, arXiv:1005.5076 [hep-th].

[617] M. Kleban and M. Schillo, Spatial Curvature Falsifies Eternal Inflation, JCAP **06**, 029, arXiv:1202.5037 [astro-ph.CO].

[618] J. Ooba, B. Ratra, and N. Sugiyama, Planck 2015 Constraints on the Non-flat ΛCDM Inflation Model, Astrophys. J. **864**, 80 (2018), arXiv:1707.03452 [astro-ph.CO].

[619] L. Gordon, B.-F. Li, and P. Singh, Quantum gravitational onset of Starobinsky inflation in a closed universe, Phys. Rev. D **103**, 046016 (2021), arXiv:2010.04738 [gr-qc].

[620] T. Murata and T. Kobayashi, Dynamics of inflation with mutually orthogonal vector fields in a closed universe, Phys. Rev. D **104**, 083514 (2021), arXiv:2107.07199 [gr-qc].

[621] M. Motaharfar and P. Singh, Role of dissipative effects in the quantum gravitational onset of warm Starobinsky inflation in a closed universe, Phys. Rev. D **104**, 106006 (2021), arXiv:2102.09578 [gr-qc].

[622] B. Bonga, B. Gupt, and N. Yokomizo, Tensor perturbations during inflation in a spatially closed Universe, JCAP **05**, 021, arXiv:1612.07281 [astro-ph.CO].

[623] B. Bonga, B. Gupt, and N. Yokomizo, Inflation in the closed FLRW model and the CMB, JCAP **10**, 031, arXiv:1605.07556 [astro-ph.CO].

[624] R. D'Agostino, M. Califano, N. Menadeo, and D. Vernieri, Role of spatial curvature in the primordial gravitational wave power spectrum, Phys. Rev. D **108**, 043538 (2023), arXiv:2305.14238 [astro-ph.CO].

[625] D. Müller and A. Toporensky, Initial conditions for Starobinsky inflation with a positive spatial curvature, Eur. Phys. J. Plus **139**, 358 (2024), arXiv:2310.15377 [gr-qc].

[626] P. Peter and J.-P. Uzan, *Primordial Cosmology* (Oxford University Press, Oxford, 2009).

[627] J. A. Kable, G. E. Addison, and C. L. Bennett, Deconstructing the Planck TT Power Spectrum to Constrain Deviations from ΛCDM, Astrophys. J. **905**, 164 (2020), arXiv:2008.01785 [astro-ph.CO].

[628] J. M. Bardeen, P. J. Steinhardt, and M. S. Turner, Spontaneous creation of almost scale-free density perturbations in an inflationary universe, Physical Review D **28**, 679 (1983).

[629] D. Brizuela, C. Kiefer, and M. Krämer, Quantum-gravitational effects on gauge-invariant scalar and tensor perturbations during inflation: The slow-roll approximation, Phys. Rev. D **94**, 123527 (2016), arXiv:1611.02932 [gr-qc].

[630] P. A. R. Ade *et al.* (BICEP, Keck), Improved Constraints on Primordial Gravitational Waves using Planck, WMAP, and BICEP/Keck Observations through the 2018 Observing Season, Phys. Rev. Lett. **127**, 151301 (2021), arXiv:2110.00483 [astro-ph.CO].

[631] M. Forconi, W. Giarè, E. Di Valentino, and A. Melchiorri, Cosmological constraints on slow roll inflation: An update, Phys. Rev. D **104**, 103528 (2021), arXiv:2110.01695 [astro-ph.CO].

[632] F. O. Franco and T. S. Pereira, Tensor Perturbations in Anisotropically Curved Cosmologies, JCAP **11**, 022, arXiv:1709.00007 [gr-qc].

[633] P. A. R. Ade *et al.* (BICEP/Keck), The Latest Constraints on Inflationary B-modes from the BICEP/Keck Telescopes, in *56th Rencontres de Moriond on Cosmology* (2022) arXiv:2203.16556 [astro-ph.CO].

[634] F. J. Qu *et al.*, Atacama Cosmology Telescope DR6 and DESI: Structure growth measurements from the cross-correlation of DESI legacy imaging galaxies and CMB lensing from ACT DR6 and Planck PR4, Phys. Rev. D **111**, 103503 (2025), arXiv:2410.10808 [astro-ph.CO].

[635] F. J. Qu *et al.* (ACT, SPT-3G), Unified and Consistent Structure Growth Measurements from Joint ACT, SPT, and Planck CMB Lensing, Phys. Rev. Lett. **136**, 021001 (2026), arXiv:2504.20038 [astro-ph.CO].

[636] A. Abusleme *et al.* (JUNO), First measurement of reactor neutrino oscillations at JUNO, (2025), arXiv:2511.14593 [hep-ex].

[637] A. Abed Abud *et al.* (DUNE), Snowmass Neutrino Frontier: DUNE Physics Summary 10.2172/1873688 (2022), arXiv:2203.06100 [hep-ex].